

NASA Tech Briefs

National
Aeronautics and
Space
Administration



Thermal radiography has many commercial applications, among them the development of new products for skin care. Thermal images such as the one on the right of this photograph help researchers determine the effects of moisturizers and astringents on skin temperature. The photo was taken using an imaging system developed with NASA support. [See the bottom of page A1.]

About the NASA Technology Utilization Program

The National Aeronautics and Space Act of 1958, which established NASA and the United States civilian space program, requires that "The Administration shall provide for the widest practicable and appropriate dissemination of information concerning its activities and the results thereof."

To help carry out this objective, NASA's Technology Utilization (TU) Program was established in 1962. Now, as an element of NASA's Technology Utilization and Industry Affairs Division, this program offers a variety of valuable services to help transfer aerospace technology to nonaerospace applications, thus assuring American taxpayers maximum return on their investment in space research; thousands of spinoffs of NASA research have already occurred in virtually every area of our economy.

The TU program has worked for engineers, scientists, technicians, and businessmen; and it can work for you.

NASA Tech Briefs

Tech Briefs is published quarterly and is free to engineers in U.S. industry and to other domestic technology transfer agents. It is both a current-awareness medium and a problem-solving tool. Potential products . . . industrial processes . . . basic and applied research . . . shop and lab techniques . . . computer software . . . new sources of technical data . . . concepts . . . can be found here. The short section on New Product Ideas highlights a few of the potential new products contained in this issue. The remainder of the volume is organized by technical category to help you quickly review new developments in your areas of interest. Finally, a subject index makes each issue a convenient reference file.

Further Information on Innovations

Although some new technology announcements are complete in themselves, most are backed up by Technical Support Packages (TSP's). TSP's are available without charge and may be ordered by simply completing a TSP Request Card found at the back of this volume. Further information on some innovations is available for a nominal fee from other sources, as indicated. In addition, Technology Utilization Officers at NASA Field Centers will often be able to lend necessary guidance and assistance.

Patent Licenses

Patents have been issued to NASA on some of the inventions described, and patent applications have been submitted on others. Each announcement indicates patent status and availability of patent licenses if applicable.

Other Technology Utilization Services

To assist engineers, industrial researchers, business executives, Government officials, and other potential users in applying space technology to their problems, NASA sponsors Industrial Applications Centers. Their services are described on page A7. In addition, an extensive library of computer programs is available through COSMIC, the Technology Utilization Program's outlet for NASA-developed software.

Applications Program

NASA conducts applications engineering projects to help solve public-sector problems in such areas as safety, health, transportation, and environmental protection. Two applications teams, staffed by professionals from a variety of disciplines, assist in this effort by working with Federal agencies and health organizations to identify critical problems amenable to solution by the application of existing NASA technology.












Reader Feedback

We hope you find the information in *NASA Tech Briefs* useful. A reader-feedback card has been included because we want your comments and suggestions on how we can further help you apply NASA innovations and technology to your needs. Please use it; or if you need more space, write to the Manager, Technology Transfer Division, P.O. Box 8757, Baltimore/Washington International Airport, Maryland 21240.

NASA Tech Briefs

National
Aeronautics and
Space
Administration

SUMMER 1984
Volume 8, Number 4

NASA TU Services	A3	Technology Utilization services that can assist you in learning about and applying NASA technology.	
New Product Ideas	A9	A summary of selected innovations of value to manufacturers for the development of new products.	
Tech Briefs	443	Electronic Components and Circuits	
	465	Electronic Systems	
	479	Physical Sciences	
	491	Materials	
	501	Life Sciences	
	505	Mechanics	
	535	Machinery	
	551	Fabrication Technology	
	571	Mathematics and Information Sciences	
	Subject Index	579	Items in this issue are indexed by subject; a cumulative index will be published yearly.

COVERS: The photographs on the front and back covers illustrate developments by NASA and its contractors that have resulted in commercial and nonaerospace spinoffs. To find out more about the "Thermal Imaging System," Circle 167 on the TSP Request Card at the back of this issue. For more information on the "dc Motor Controller," Circle 168.

About This NASA Publication

NASA Tech Briefs, a quarterly publication, is distributed free to qualified U.S. citizens to encourage commercial application of U.S. space technology. For information on publications and services available through the NASA Technology Utilization Program, write to the Manager, Technology Transfer Division, P.O. Box 8757, Baltimore/Washington International Airport, Maryland 21240.

"The Administrator of National Aeronautics and Space Administration has determined that the publication of this periodical is necessary in the transaction of the public business required by law of this Agency. Use of funds for printing this periodical has been approved by the Director of the Office of Management and Budget."

Change of Address

If you wish to have NASA Tech Briefs forwarded to your new address, use the Subscription Card enclosed at the back of this volume of NASA Tech Briefs. Be sure to check the appropriate box indicating change of address, and also fill in your identification number (T number) in the space indicated.

Communications Concerning Editorial Matter

For editorial comments or general communications about NASA Tech Briefs, you may use the Feedback card in the back of NASA Tech Briefs, or write to: The Publications Manager, Technology Utilization Office (LGT-1), NASA Headquarters, Washington, DC 20546. Technical questions concerning specific articles should be directed to the Technology Utilization Officer of the sponsoring NASA Center (addresses listed on page A4).

Expanded Format

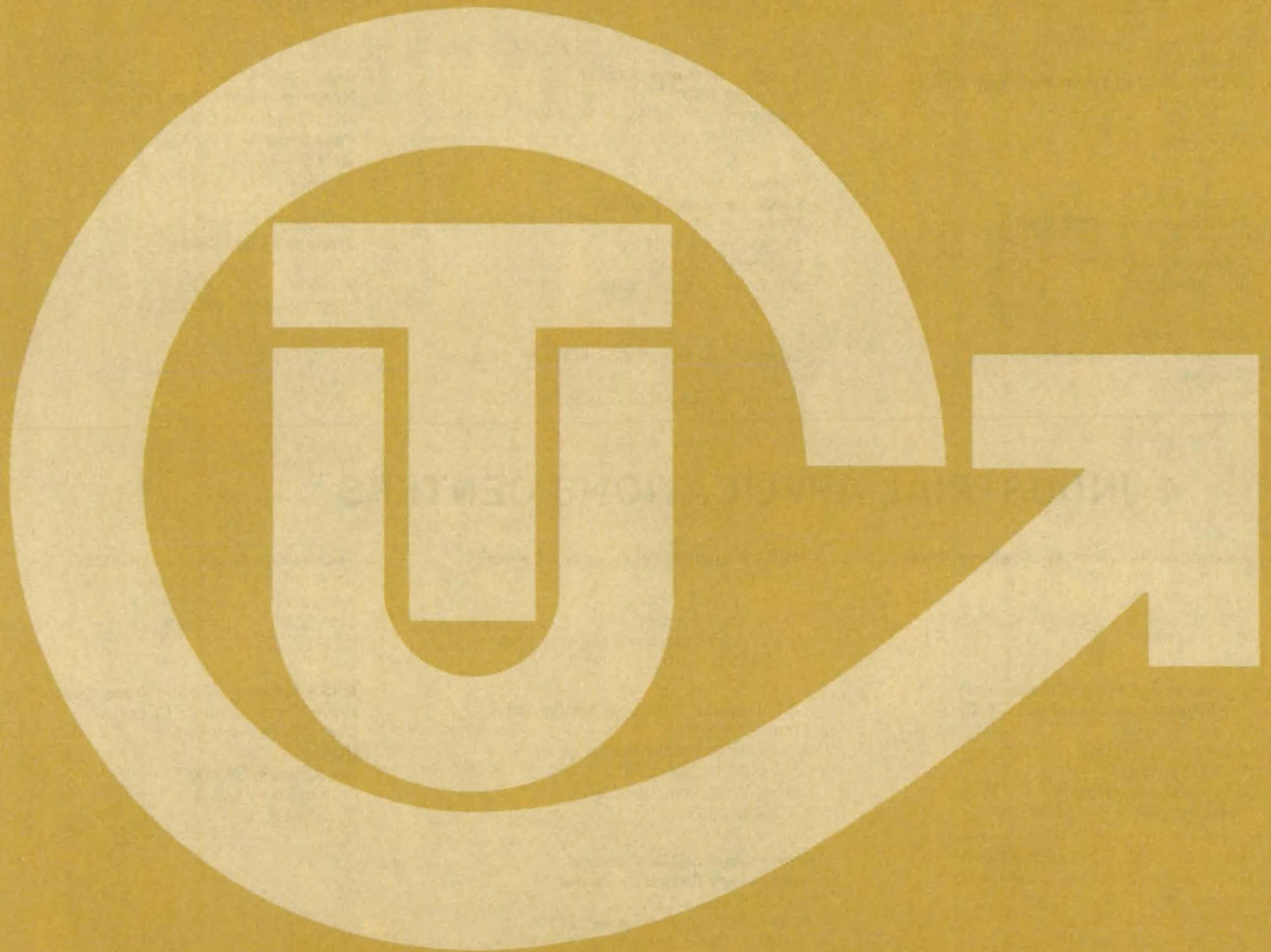
To speed the publication of our backing of Tech Brief items, we have increased our pre-issue contents by adding short articles to the end of each subject section of NASA Tech Briefs. Titled "MiniBriefs," these short articles describe NASA innovations and reports in an abbreviated format. Most are backed up by Technical Support Packages (TSP's), which are obtained by using the TSP Request Card at the back of this issue.

Acknowledgements

NASA Tech Briefs is published quarterly by the National Aeronautics and Space Administration, Technology Transfer Division, Washington, DC: Administrator: **James M. Beggs**; Director, Technology Utilization and Industry Affairs Division: **Ronald J. Philips**; Publications Manager: **Leonard A. Ault**. Prepared for the National Aeronautics and Space Administration by **Logical Technical Services Corp.**: Editor-in-Chief: **Jay Kirschenbaum**; Art Director: **Ernest Gillespie**; Managing Editor: **Jerome Rosen**; Chief Copy Editor: **Melanie Tarka**; Staff Editors: **Larry Grunberger, Paul Johnson, Jordan Randjelovich, Ted Selinsky, George Watson**; Graphics: **Andrew Abramoske, Luis Martinez, Huburn Profit**; Editorial & Production: **Camille McQueen, Richard Johnson, Sabrina Gibson, Stephanie Godino, Leslie Iwaskow, Maxine J. Kilkenny, Henry Lai, Marion Larson, Linda Lucas, Frank Ponce, Joseph Rentzler, Elizabeth Texeira**.

This document was prepared under the sponsorship of the National Aeronautics and Space Administration. Neither the United States Government nor any person acting on behalf of the United States Government assumes any liability resulting from the use of the information contained in this document, or warrants that such use will be free from privately owned rights.

NASA TU SERVICES



NASA TECHNOLOGY UTILIZATION NETWORK

★ TECHNOLOGY UTILIZATION OFFICERS

Stanley A. Miller
Ames Research Center
Code 240-10
Moffett Field, CA 94035
(415) 965-6471

Stanley A. Miller
Hugh L. Dryden Flight Research Center
Code 240-10
Moffett Field, CA 94035
(415) 965-6471

Donald S. Friedman
Goddard Space Flight Center
Code 702.1
Greenbelt, MD 20771
(301) 344-6242

William Chmylak
Lyndon B. Johnson Space Center
Code AL-32
Houston, TX 77058
(713) 483-3809

U. Reed Barnett
John F. Kennedy Space Center
Mail Stop PT-TPO-A
Kennedy Space Center, FL 32899
(305) 867-3017

John Samos
Langley Research Center
Mail Stop 139A
Hampton, VA 23665
(804) 865-3281

Harrison Allen, Jr.
Lewis Research Center
Mail Code 7-3
21000 Brookpark Road
Cleveland, OH 44135
(216) 433-4000, Ext. 6422

Ismail Akbay
George C. Marshall Space Flight Center
Code AT01
Marshall Space Flight Center, AL 35812
(205) 453-2224

Leonard A. Ault
NASA Headquarters
Code ETD-6
Washington, DC 20546
(202) 453-8424

Aubrey Smith
NASA Resident Office-JPL
4800 Oak Grove Drive
Pasadena, CA 91103
(818) 354-4849

Gilmore H. Trafford
Wallops Flight Center
Code OD
Wallops Island, VA 23337
(804) 824-3411, Ext. 201

● INDUSTRIAL APPLICATIONS CENTERS

Aerospace Research Applications Center
1201 East 38th Street
Indianapolis, IN 46205
John M. Ulrich, director
(317) 264-4644

Computer Software Management and Information Center (COSMIC)
Suite 112, Barrow Hall
University of Georgia
Athens, GA 30602
John A. Gibson, director
(404) 542-3265

Kerr Industrial Applications Center
Southeastern Oklahoma State University
Durant, OK 74701
James Harmon, director
(405) 924-0121, Ext. 413

NASA Industrial Applications Center
701 LIS Building
University of Pittsburgh
Pittsburgh, PA 15260
Paul A. McWilliams, executive director
(412) 624-5211

New England Research Applications Center
Mansfield Professional Park
Storrs, CT 06268
Daniel Wilde, director
(203) 486-4533

North Carolina Science and Technology Research Center
Post Office Box 12235
Research Triangle Park, NC 27709
James E. Vann, director
(919) 549-0671

Technology Applications Center
University of New Mexico
Albuquerque, NM 87131
Stanley Morain, director
(505) 277-3622

NASA Industrial Applications Center
University of Southern California
Denny Research Building
University Park
Los Angeles, CA 90007
Robert Mixer, acting director
(213) 743-6132

■ STATE TECHNOLOGY APPLICATIONS CENTERS

NASA/University of Florida State Technology Applications Center
500 Weil Hall
University of Florida
Gainesville, FL 32611
J. Ronald Thornton, director
Gainesville: (904) 392-6760
Boca Raton: (305) 395-5100, Ext. 2292
Fort Lauderdale: (305) 776-6645
Jacksonville: (904) 646-2478
Orlando: (305) 275-2706
Pensacola: (904) 476-9500, Ext. 426
Tampa: (813) 974-2499

NASA/University of Kentucky State Technology Applications Program
109 Kinkead Hall
University of Kentucky
Lexington, KY 40508
William R. Strong, manager
(606) 258-4632



◆ PATENT COUNSELS

Robert F. Kempf
Asst. Gen. Counsel for patent matters
NASA Headquarters
 Code GP-4
 400 Maryland Avenue, SW.
 Washington, DC 20546
 (202) 755-3954

Darrell G. Brekke
Ames Research Center
 Mail Code: 200-11A
 Moffett Field, CA 94035
 (415) 965-5104

Darrell G. Brekke
Hugh L. Dryden Flight Research Center
 Mail Code: 201-11A
 Moffett Field, CA 94035
 (415) 965-5104

John O. Tresansky
Goddard Space Flight Center
 Mail Code: 204
 Greenbelt, MD 20771
 (301) 344-7351

Marvin F. Matthews
Lyndon B. Johnson Space Center
 Mail Code: AL-3
 Houston, TX 77058
 (713) 483-4871

James O. Harrell
John F. Kennedy Space Center
 Mail Code: SA-PAT
 Kennedy Space Center, FL 32899
 (305) 867-2544

Howard J. Osborn
Langley Research Center
 Mail Code: 279
 Hampton, VA 23665
 (804) 827-3725

Norman T. Musial
Lewis Research Center
 Mail Code: 500-311
 21000 Brookpark Road
 Cleveland, OH 44135
 (216) 433-4000, Ext. 346

Leon D. Wofford, Jr.
George C. Marshall Space Flight Center
 Mail Code: CC01
 Marshall Space Flight Center, AL 35812
 (205) 453-0020

Paul F. McCaul
NASA Resident Office-JPL
 Mail Code: 180-601
 4800 Oak Grove Drive
 Pasadena, CA 91103
 (818) 354-2700

▲ APPLICATION TEAMS

Doris Rouse, director
Research Triangle Institute
 Post Office Box 12194
 Research Triangle Park, NC 27709
 (919) 541-6980

James P. Wilhelm, director
SRI International
 333 Ravenswood Avenue
 Menlo Park, CA 94026
 (415) 326-6200, Ext. 3520

TECHNOLOGY UTILIZATION OFFICERS

Technology transfer experts can help you apply the innovations in NASA Tech Briefs.

The Technology Utilization Officer

at each NASA Field Center is an applications engineer who can help you make use of new technology developed at his center. He brings you NASA Tech Briefs and other special publications, sponsors conferences, and arranges for expert assistance in solving technical problems.

Technical assistance,

in the form of further information about NASA innovations and technology, is one of the services available from the T_UO. Together with NASA scientists and engineers, he can often help you find and implement NASA technology to meet your specific needs.

Technical Support Packages (TSP's)

are prepared by the center T_UO's. They provide further technical details for articles in NASA Tech Briefs. This additional material can help you evaluate and use NASA technology. You may receive most TSP's free of charge by using the TSP Request Card found at the back of this issue.

Technical questions about articles

in NASA Tech Briefs are answered in the TSP's. When no TSP is available, or you have further questions, contact the Technology Utilization Officer at the center that sponsored the research [see page A4].



NASA INVENTIONS AVAILABLE FOR LICENSING

Over 3,500 NASA inventions are available for licensing in the United States — both exclusive and nonexclusive.

Nonexclusive licenses

for commercial use of NASA inventions are encouraged to promote competition and to achieve the widest use of inventions. They must be used by a negotiated target date.

Exclusive licenses

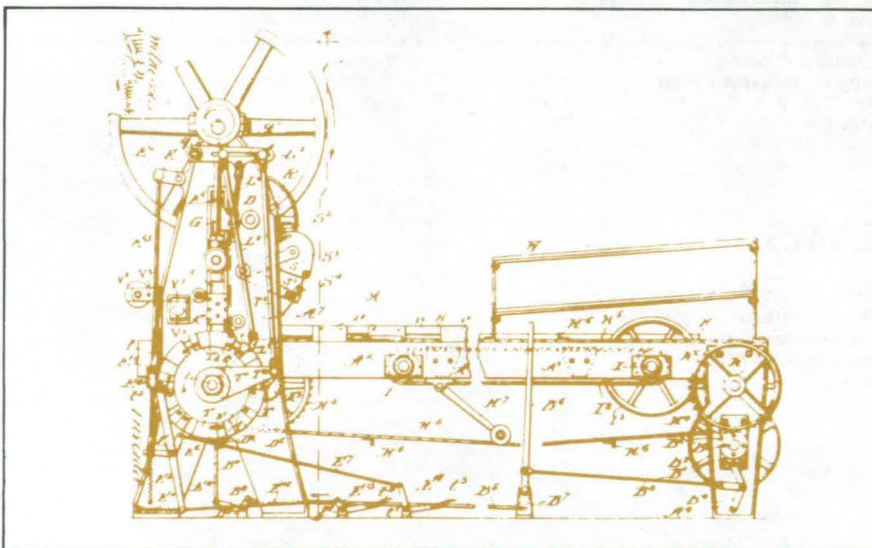
may be granted to encourage early commercial development of NASA inventions, especially when considerable private investment is required. These are generally for 5 to 10 years and usually require royalties based on sales or use.

Additional licenses available

include those of NASA-owned foreign patents. In addition to inventions described in NASA Tech Briefs, "NASA Patent Abstract Bibliography" (PAB), containing abstracts of all NASA inventions, can be purchased from National Technical Information Service, Springfield, VA 22161. The PAB is updated semiannually.

Patent licenses for Tech Briefs

are frequently available. Many of the inventions reported in NASA Tech Briefs are patented or are under consideration for a patent at the time they are published. The current patent status is described at the end of the article; otherwise, there is no statement about patents. If you want to know more about the patent program or are interested in licensing a particular invention, contact the Patent Counsel at the NASA Field Center that sponsored the research [see page A5]. Be sure to refer to the NASA reference number at the end of the Tech Brief.



APPLICATION TEAMS

Technology-matching and problem-solving assistance to public-sector organizations

Application engineering projects

are conducted by NASA to help solve public-sector problems in such areas as safety, health, transportation, and environmental protection. Some application teams specialize in biomedical disciplines; others, in engineering and scientific problems. Staffed by professionals from various disciplines, these teams work with other Federal agencies and health organizations to



identify critical problems amenable to solution by the application of existing NASA technology.

Public-sector organization

representatives can learn more about application teams by contacting a nearby NASA Field Center Technology Utilization Office [see page A4].



INDUSTRIAL APPLICATIONS CENTERS

Computerized access to over 10 million documents worldwide

Computerized information retrieval

from one of the world's largest banks of technical data is available from NASA's network of industrial Applications Centers (IAC's). The IAC's give you access to 1,800,000 technical reports in the NASA data base and to more than 10 times that many reports and articles found in nearly 200 other computerized data bases.

The major sources include:

- 750,000 NASA Technical Reports
- Selected Water Resources Abstracts
- NASA Scientific and Technical Aerospace Reports
- Air Pollution Technical Information Center
- NASA International Aerospace Abstracts
- Chem Abstracts Condensates
- Engineering Index
- Energy Research Abstracts
- NASA Tech Briefs
- Government Reports
- Announcements

and many other specialized files on food technology, textile technology, metallurgy, medicine, business, economics, social sciences, and physical science.

The IAC services

range from tailored literature searches through expert technical assistance:



- **Retrospective Searches:** Published or unpublished literature is screened, and documents are identified according to your interest profile. IAC engineers tailor results to your specific needs and furnish abstracts considered the most pertinent. Complete reports are available upon request.
- **Current-Awareness Searches:** IAC engineers will help design a program to suit your needs. You will receive selected monthly or quarterly abstracts on new developments in your area of interest.

- **Technical Assistance:** IAC engineers will help you evaluate the results of your literature searches. They can help find answers to your technical problems and put you in touch with scientists and engineers at appropriate NASA Field Centers.

Prospective clients

can obtain more information about these services by contacting the nearest IAC [see page A4]. User fees are charged for IAC information services.

STATE TECHNOLOGY APPLICATIONS CENTERS

Technical information services for industry and state and local government agencies.

Government and private industry

in Florida and Kentucky can utilize the services of NASA's State Technology Applications Centers (STAC's). The STAC's differ from the Industrial Applications Centers described on page A7, primarily in that they are integrated into existing state technical assistance programs and serve only

the host state, whereas the IAC's serve multistate regions.

Many data bases,

including the NASA base and several commercial bases, are available for automatic data retrieval through the STAC's. Other services such as document retrieval and special

searches are also provided. (Like the IAC's, the STAC's normally charge a fee for their services.)

To obtain information

about the services offered, write or call the STAC in your state [see page A4].

COSMIC®

An economical source of computer programs developed by NASA and other government agencies

A vast software library

is maintained by COSMIC — the Computer Software Management and Information Center. COSMIC gives you access to approximately 1,600 computer programs developed for NASA and the Department of Defense and selected programs for other government agencies. Programs and documentation are available at reasonable cost.

Available programs

range from management (PERT scheduling) to information science (retrieval systems) and computer operations (hardware and software). Hundreds of engineering programs perform such tasks as structural analysis, electronic circuit design, chemical analysis, and the design of fluid systems. Others determine building energy requirements and optimize mineral exploration.

COSMIC services

go beyond the collection and storage of software packages. Programs are checked for completeness; special announcements and an indexed software catalog are prepared; and programs are reproduced for distribution. Customers are helped to



identify their software needs; and COSMIC follows up to determine the successes and problems and to provide updates and error corrections. In some cases, NASA engineers can offer guidance to users in installing or running a program.

Information about programs

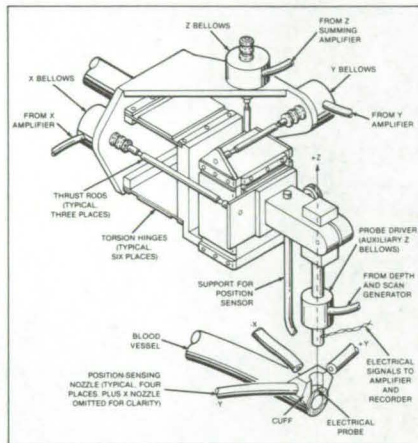
described in NASA Tech Briefs articles can be obtained by completing the COSMIC Request Card at the back of this issue. Just circle the letters that correspond to the programs in which you are interested.

NEW PRODUCT IDEAS



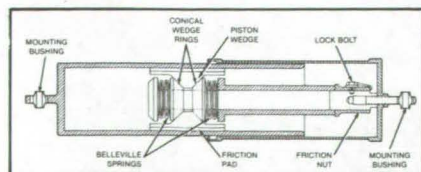
NEW PRODUCT IDEAS are just a few of the many innovations described in this issue of NASA Tech Briefs and having promising commercial applications. Each is discussed further on the referenced page in the appropriate section in this issue. If you are interested in developing a product from these or other NASA innovations, you can receive further technical information by requesting the TSP referenced at the end of the full-length article or by writing the Technology Utilization Office of the sponsoring NASA center (see page A4). NASA's patent-licensing program to encourage commercial development is described on page A6.

Probe Follower for Moving Blood Vessels



An electrical probe for medical research would be maintained at a fixed position relative to a moving blood-vessel wall to track vessel expansion and contraction. A cuff is placed on the blood vessel at the probe position. Nozzle back-pressure changes at the cuff are the basis for monitoring the position of the probe in the blood vessel. Fluidic amplifiers use these signals to control a three-axis servo that centers the measuring probe between the sensing-nozzle pairs at the cuff. (See page 503.)

Improved Coulomb-Friction Damper



An improved coulomb (sliding) friction damper resists motion equally on both the forward and reverse strokes. The damper has springs and wedge rings symmetrically placed on both ends of the piston wedge so that the friction force will be the same in both directions of travel. (See page 515.)

Integrated Exhaust-Gas-Analysis System

An integrated gas-analyzer system has been developed that is designed for nearly unattended operation. Two micro-processors range the analyzers, calibrate the system, process the raw data to units of concentration, and make all system information available to the facility research computer and to the operator. The system

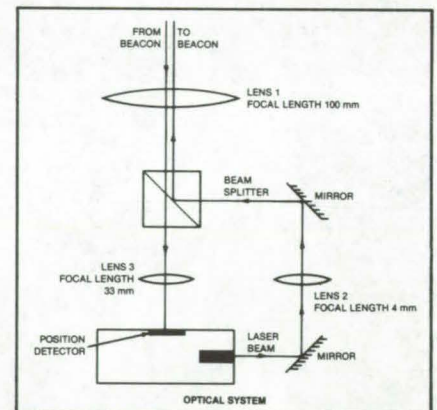


contains eight slightly modified commercially available gas analyzers: Carbon dioxide, two carbon monoxide, oxygen, water vapor, total hydrocarbons, and two nitric oxide. (See page 519.)

Integrated Laser and Light Detector

A proposed infrared optical transmitter would track a distant beacon and automatically point the transmitted beam toward the beacon. An essential part of the transmitter is an integrated gallium arsenide device containing an electronically-steerable semiconductor injection laser and a position detector that senses the

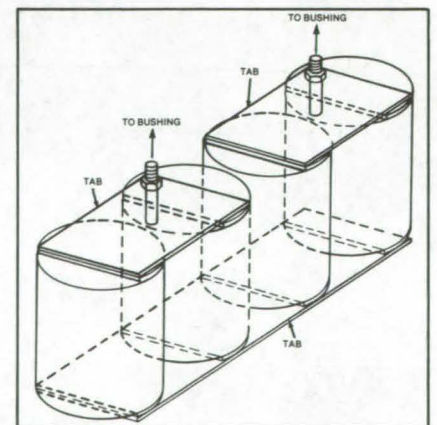
direction to the beacon. In this monolithic structure, the magnitudes and ratio of the currents to the laser stripes determine the



amount of beam deflection. The ratio of the currents from the ends of the detector indicates the direction of the beacon. (See page 450.)

High-Frequency, High-Power Capacitor

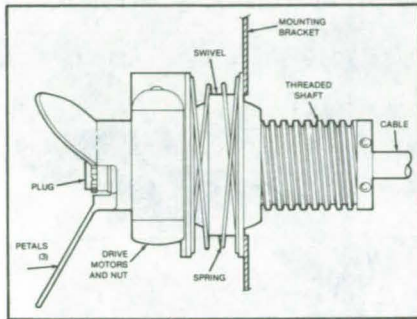
A high-energy-density, low-loss, high-power 75-kvar transfer capacitor has been designed for use at high frequencies (10 to 40 kHz) in space-power systems.



The capacitor uses a split foil and a floating foil plus multiple coils to reduce the voltage drop across the film and increase the lifetime (10 years). The efficiency of high-frequency circuits for many terrestrial applications can be increased by using this type of capacitor. (See page 445.)

Remote Coupling of Electrical Connectors

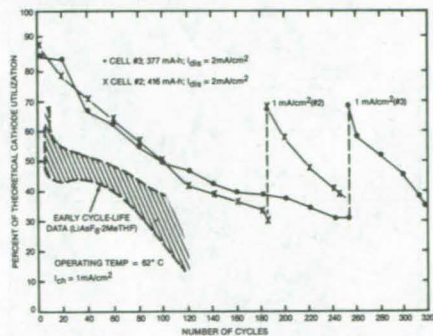
An automatic mechanism connects and disconnects a self-aligning electrical plug and receptacle. Designed for umbilical cables between the Space Shuttle and



a payload, the mechanism is adaptable to other remote or hazardous situations in which a human is not available to connect mating parts by hand — underwater or in poisonous atmospheres, for example. A standard multiple-pin plug and socket are mounted in the mechanism. As the threaded shaft moves out from its mounting bracket, the two sets of petals engage each other and correct misalignment. The misalignment is absorbed by the spring-mounted swivels. (See page 543.)

High-Cycle-Life Lithium Cell

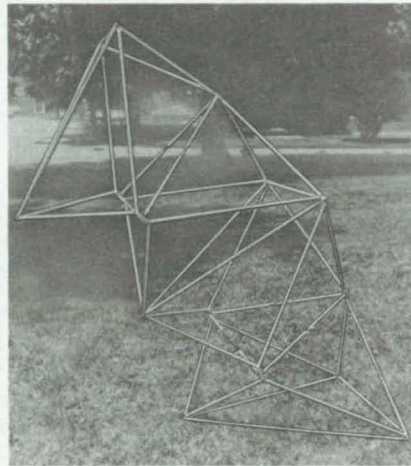
A new lithium-anode electrochemical cell offers an increased number of charge/discharge cycles. Although older types of secondary lithium cells are characterized by high energy-storage capacity, they have



poor cycle life because the cell components are physically and chemically incompatible, and the cathode tends to disintegrate after only a moderate number of cycles. The new cell uses components selected for compatibility with the electrolyte solvent: These materials are wettable and chemically stable. (See page 451.)

Deployable Geodesic Truss

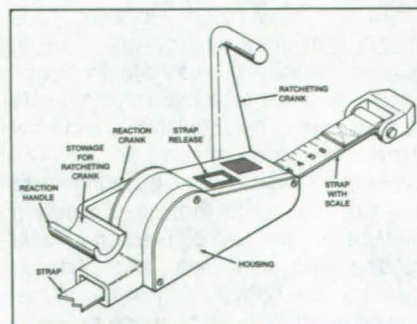
A deployable geodesic truss originally developed for satellite applications could also be used to assemble remote manipulator arms, positioners for antennas, solar-array supports, and other structures. In a two-bay structure, each bay has sets of battens connected by two longitudinal crossed members that give the bay its axial and torsional stiffness.



The crossmembers are hinged in the center to fold for packaging. The bays are deployed and stabilized by actuators connected between the center hinges of the crossmembers. (See page 532.)

Reactionless Winch

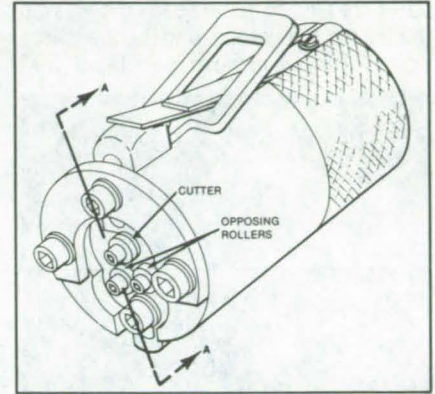
A lightweight, hand-held winch designed for use by astronauts on the Space Shuttle has a reaction crank braced against the housing in addition to a ratcheting crank. To pull on the load, the operator squeezes handles of the two cranks toward each other (as with pliers or scissors). Since all forces are thereby



reacted into the tool, there is no need to restrain or brace the operator against an external object. (See page 542.)

Stripping the Sheath From Stranded Cables

A new cable stripper uses a rotary cutter and two bearings to remove Kapton (or equivalent) plastic sheathing from



a multiwire stranded cable without damaging the insulation of the individual conductors. The sheath is cut part of the way through by the cutter, and the insulation is then "worked" off the end of the wire by hand. The cutter blade engages the cable, which is inserted between the blade and the rollers. The blade can be lifted away manually so that the cable can be inserted. An adjustable stop defines the length of the cable for stripping. (See page 561.)

Lightweight High-Temperature Thermal Insulation

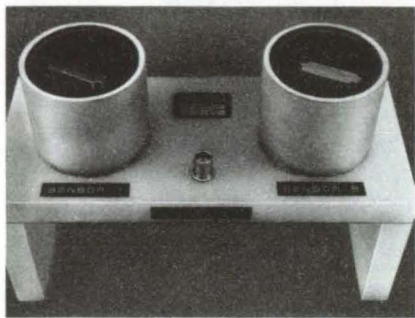
A new thermal-insulation material is constructed by partially sintering 8- μ m fibers of nickel/chromium alloy (Nichrome alloy, or equivalent) into a batt with a

Temperature °C	°F	Gas Pressure		Thermal Conductivity			
		psia	kN/m ²	Virgin		Treated	
				W/m-k	Sty-in./h-ft ² -°F	W/m-k	Sty-in./h-ft ² -°F
427	800	14.7	101	0.110	0.76	0.118	0.82
427	800	11.0	76	0.107	0.74	0.116	0.80
427	800	10.0	69	0.105	0.73	0.115	0.79
871	1,600	14.7	101	0.25	1.73	0.26	1.80
871	1,600	0.2	1.4	0.23	1.59	0.235	1.63
871	1,600	0.1	0.69	0.185	1.28	0.20	1.39
871	1,600	0.05	0.34	0.17	1.18	0.175	1.21
1,093	2,000	14.7	101	0.38	2.63	0.385	2.67
1,093	2,000	0.2	1.4	0.35	2.43	0.35	2.43
1,093	2,000	0.1	0.69	0.265	1.84	0.285	1.98
1,093	2,000	0.05	0.34	0.240	1.66	0.250	1.73
427	800	14.7	101	0.115	0.80	0.120	0.83

density only 2.5 percent that of solid alloy. Possible applications include stoves, furnaces, safes, fire clothing, draperies in public buildings, wall firebreaks, airplane walls, and jet-engine components. (See page 495.)

Differential-Coil Eddy-Current Material Sorter

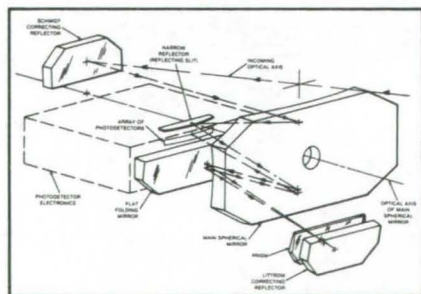
Small metal or other electrically conductive parts of the same shape but different composition are quickly sorted with a differential-coil eddy-current sorter. The parts are placed in the sensing coils with the same orientation and at the same position relative to the center of each coil.



A nonconductive holder may be used to insure the identical relative positioning of two parts. Developed to distinguish between turbine blades of different alloys, hardnesses, and residual stress, the sorter is generally applicable to parts of simple and complex shape. (See page 451.)

Reflecting Schmidt/Littrow Prism Imaging Spectrometer

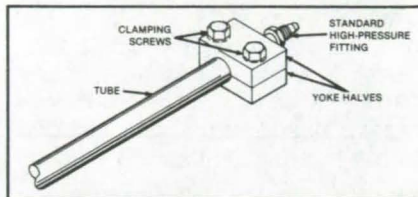
An imaging spectrometer includes off-axis optics that give an unobstructed 15° field of view and a resolution of 4.3 arc-seconds. The instrument, which operates at wavelengths from 0.4 to 2.5 μm , includes a reflecting "slit" that also serves as a field flattener. The only refracting element is the prism. The wide spectral range



is possible because the imaging optics are reflecting (as opposed to refracting) to avoid unwanted dispersion. For each image point along the spectrometer slit, a spectrum is obtained. (See page 481.)

High-Pressure Coupling for Open-Ended Tubes

New high-pressure couplings are quickly installed or removed from round metal tubes. In contrast to compression

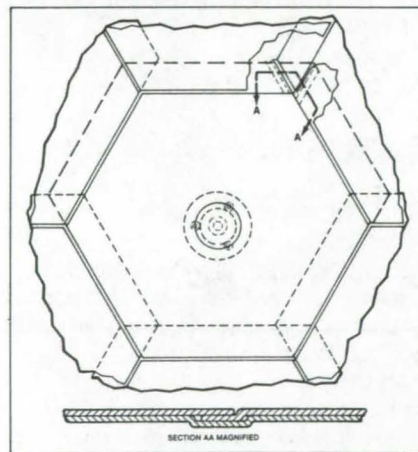


fittings, the new couplings require no wedge rings or other permanent change in the ends of the tubing. The couplings are useful mainly for such repeated temporary connections as may be necessary for high-pressure testing or prestressing of tubes with finished ends.

(See page 510.)

Prestressed Thermal-Protection Panels

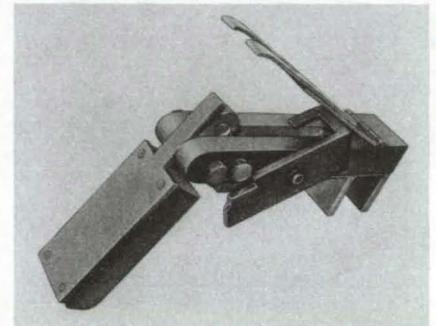
Hexagonal panels of high-temperature-resistant composite material can be prestressed to prevent vibration or distortion



under load. Each panel is held in place by a single screw that pulls it into a flat shape from its original shallow-dish shape. Although originally developed for the Space Shuttle thermal-protection system, the technique may be adaptable to industrial thermal-protection systems as well. The panel shape and mounting arrangement are not limited to thermal-protection systems but can also be used on aircraft, building walls, or wherever large surfaces must be covered with stiff, flat sheets that can be easily removed for maintenance. (See page 556.)

Safety Pedal for Foot-Operated Machinery

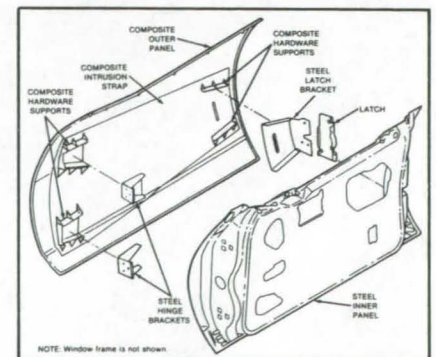
A pedal for turning on a metal-forming power brake can be moved quickly, yet resists inadvertent operation. It includes a fixed open-end wrench surface at one end to grip a bar with a hexagonal cross section. An operating cycle of the power



brake or other machine is started by applying a torque to the bar through the pedal. The new pedal improves both the productivity and safety of power brakes and such other machines as metal shearers and punch presses. (See page 537.)

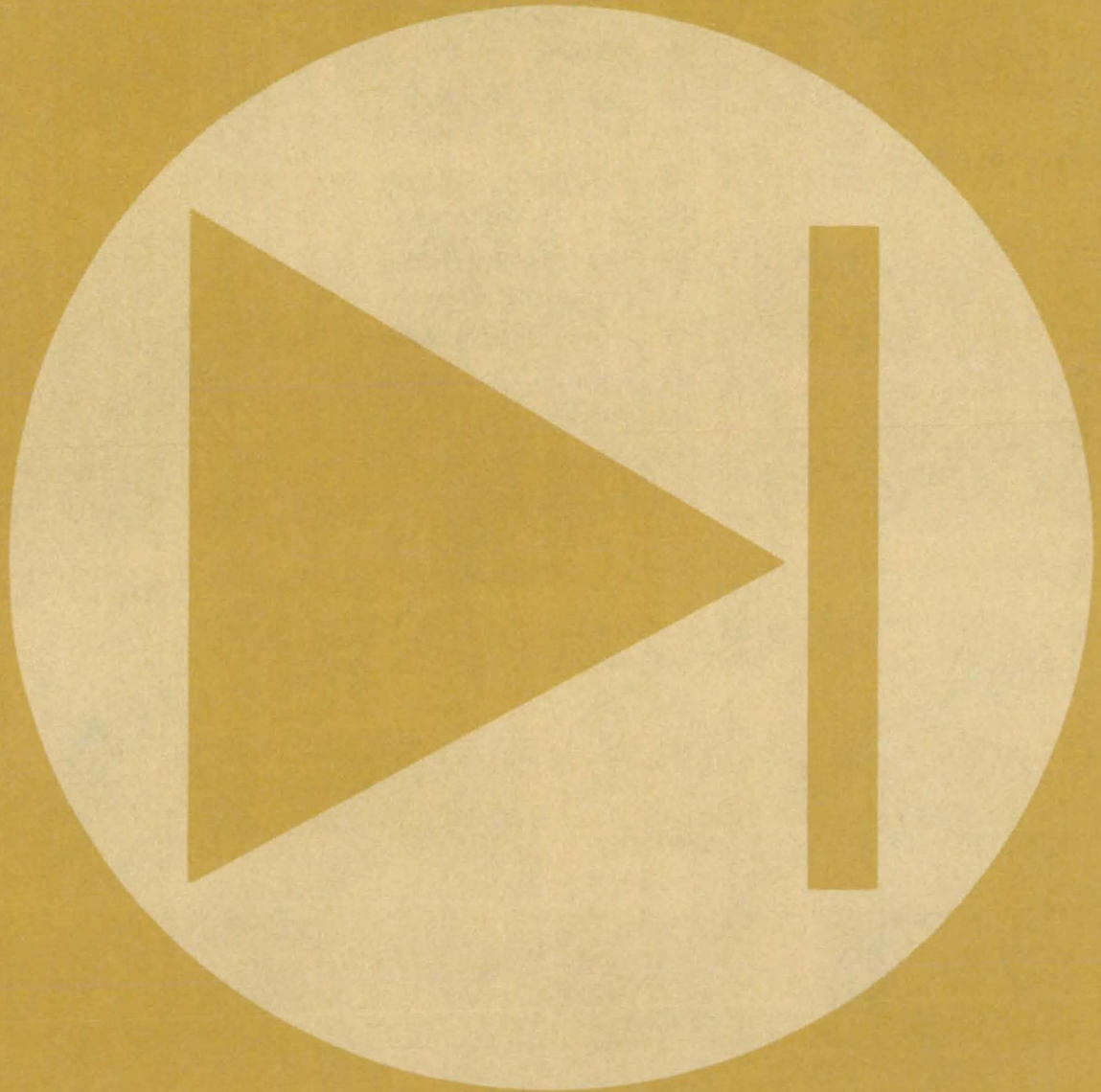
Glass/Epoxy Door Panel for Automobiles

An experimental outer panel for an automobile door, made of a glass/epoxy composite material, weighs 43 percent less than its steel counterpart, meets the same strength requirements, and is less expensive. The composite panel consists of a contoured epoxy sheet filled with chopped glass fibers and comolded with an intrusion strap of continuous glass fibers. The intrusion strap helps to protect occupants from



side collisions. It replaces the intrusion beam of the steel door and accounts for the thickness reduction and a large part of the weight reduction in the composite panel. (See page 561.)

Electronic Components and Circuits



Hardware, Techniques, and Processes

- 445 High-Frequency, High-Power Capacitor
- 446 Stable Optocoupler
- 447 Reversing Optical Damage in LiNbO₃ Switches
- 448 Real-Time Reed-Solomon Decoder
- 449 Advanced dc-Traction-Motor Control System
- 450 Integrated Laser and Light Detector
- 451 Differential-Coil Eddy-Current Material Sorter
- 451 High-Cycle-Life Lithium Cell
- 452 Discriminator Aids Phase-Lock Acquisition
- 453 Light-Activated Microwave Device
- 454 Magic-T-Coupled Magnetrons
- 455 Lightweight Regulated Power Supply
- 456 Antenna Subreflector Fed by a Line Source
- 457 Ellipsoidal Balloon Antenna
- 458 Efficient Reflector Antenna
- 459 Measuring the Contact Resistances of Photovoltaic Cells
- 460 Estimation of Grounding-Strap Resistances
- 461 Measuring Air-Ionizer Output
- 461 Guard for Fuse Caps

Books and Reports

- 462 Batteries for Electric Vehicles

Computer Programs

- 462 Theoretical Investigation of Dielectric Horn Antennas

MiniBriefs

- 463

High-Frequency, High-Power Capacitor

The capacitor will increase the efficiency of high-frequency circuits.

Lewis Research Center, Cleveland, Ohio

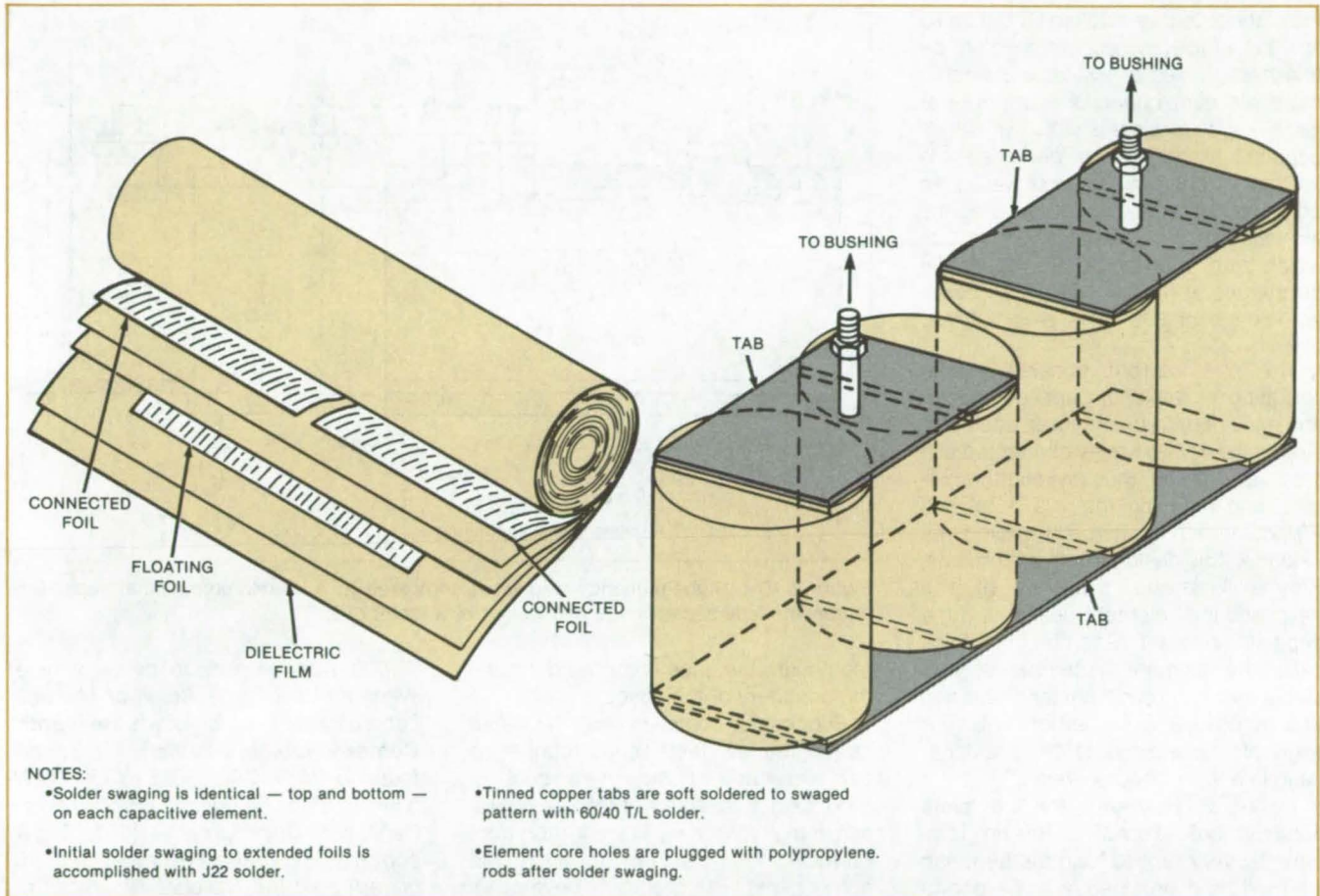


Figure 1. The **High-Power-Capacitor Design** uses a split foil and a floating foil plus multiple coils to reduce the voltage drop across the film and increase the lifetime (10 years).

A high-energy-density, high-power 75-kvar transfer capacitor has been developed that provides a very-low-loss, space-type design for use at high frequencies (10 to 40 kHz). The specifications of the capacitor developed are 0.8 μF , 600 Vrms with a 600-Vdc bias. Using a split foil and a floating foil plus multiple coils, the voltage drop across the film was reduced to a few hundred volts, which enhanced the lifetime (design life — 10 years). The outstanding features of this capacitor are its high current capability (125 A) at 40 kHz, its light weight (0.5 kg/kvar), and its very low loss (a 22-watt design loss at operating conditions).

This capacitor is one of the building blocks required for large space power

systems where light weight and small physical size are of great importance. It has a size and weight several times less than the presently available capacitors. This capacitor will enable space power systems to grow to the multikilowatt range. The efficiency of high-frequency circuits for many terrestrial applications can be increased by using this type of capacitor.

The qualities of low tan delta and high dielectric strength were paramount for superior performance of dielectric materials chosen for the capacitors being developed. Information of this nature was available from the producers of the material. Mylar, polycarbonate, Kapton, polypropylene, and polysulfone were candidate dielectric materials. The final

overall evaluation of the candidate solid dielectric materials resulted in a choice based on a system of performance rating where each factor was given a quality rating of 0 to 10, and factors were classed as minor or major. The cumulative value obtained for each material was used to classify the materials.

Polypropylene film was chosen as the superior dielectric solid material, although the temperature coefficient of capacitance was greater than for polysulfone. Even so, the total decrease in capacitance recorded at 125° C was 3 percent, but only 0.8 percent at 75° C, where the capacitor would operate. The material chosen was a surface-modified tenter film. Mineral oil, dimethyl silicone oil, diaryl alkane, monoisopropyl
(continued on next page)

biphenyl (MIPB), dioctyl phthalate, and Fluorinert were considered for the dielectric impregnant. MIPB was selected because of its dielectric strength, high-frequency tan delta, temperature stability, and radiation resistance.

To reduce the interfoil voltage of each element to a value that would provide the highest degree of reliability but could still be efficiently accommodated by thickness values of available dielectric materials, each capacitor element — or pad — was designed with two series capacitor sections. To decrease the voltage further, two elements were then connected in series, thus reducing the ac voltage to a value of 150 Vrms, at which point there would be no partial discharges at the full capacitor operating voltage of 600 Vrms plus 600-Vdc bias.

The rms current consistent with operating at maximum applied voltage and maximum frequency was dealt with by paralleling two series-connected element assemblies, thus dividing the current, and reducing the 125 A to 62.5 A/pad, which can be handled by extended-foil design of the elements. Figure 1 shows features of the "exposed-foil" element design and the capacitor-element assembly. Mechanically, the element assembly is very stable and secure to withstand vibration and shock. The assembly of four elements is secured to the capacitor base in a layer of epoxy resin.

Figure 2 illustrates the complete capacitor outline drawing. This unit is inherently very rugged, and the hermetic seal will be maintained over the operational life. The case material is 304L stainless steel and provides minimum eddy-current losses at the maximum operating frequency. The only welding accomplished after assembly of the ele-

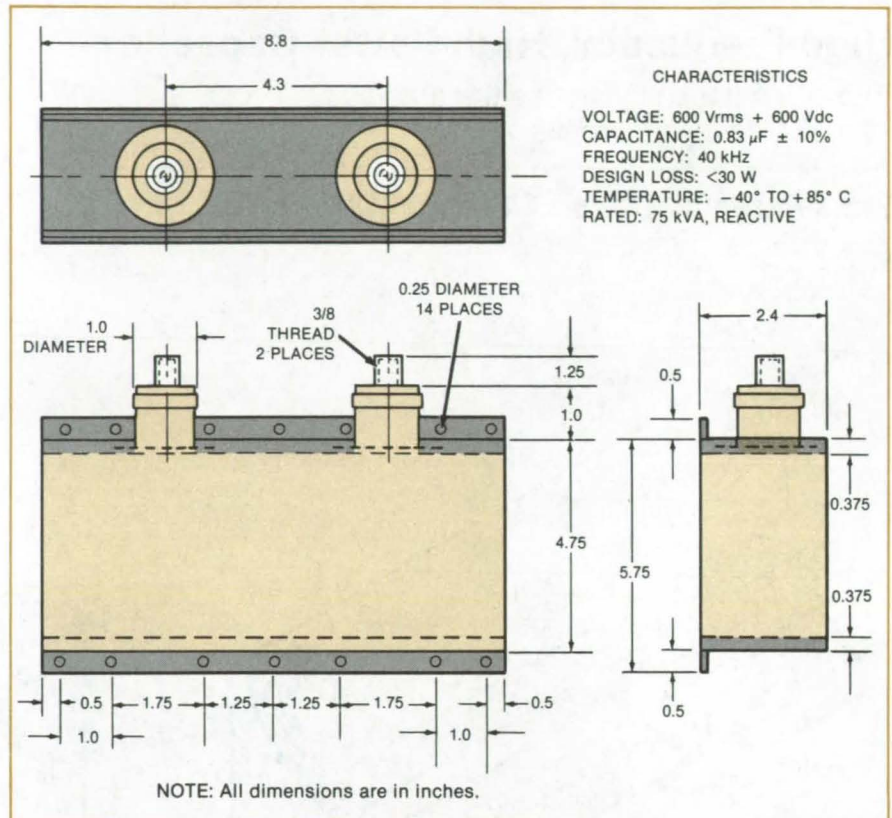


Figure 2. The **High-Frequency Capacitor**, compared to a 40-kHz commercial capacitor, represents a decrease in size and weight by a factor of 7.

ments into the case is the weld around the periphery of the cover.

Successful completion of the vacuum-endurance test series confirmed achievements of the main goal of producing a capacitor of reliable operation at high frequency in an environment normally not hospitable to electronic components. The capacitor developed, compared to a typical commercial capacitor at the 40-kHz level, represents a decrease in size and weight by a factor of 7.

This work was done by C. Wayne White and Paul S. Hoffman of Maxwell Laboratories, Inc., for Lewis Research Center. Further information may be found in NASA CR-168035 [N83-27127/NSP], "High Frequency, High Power Capacitor Development" [\$11.50]. A copy may be purchased [prepayment required] from the National Technical Information Service, Springfield, Virginia 22161. LEW-14034

Stable Optocoupler

Feedback circuit minimizes changes in current-transfer ratio.

Marshall Space Flight Center, Alabama

A circuit stabilizes the current-transfer ratio (CTR) of an optically coupled isolator used as a linear transducer. (The CTR is defined as the ratio of output current to input current.) The optocoupler produces a voltage output that is

proportional to — but electrically isolated from — the voltage input. However, the output voltage is directly affected by changes in the CTR, and the CTR can change substantially with temperature and current. To a lesser extent,

the CTR changes with time over the life of the optocoupler.

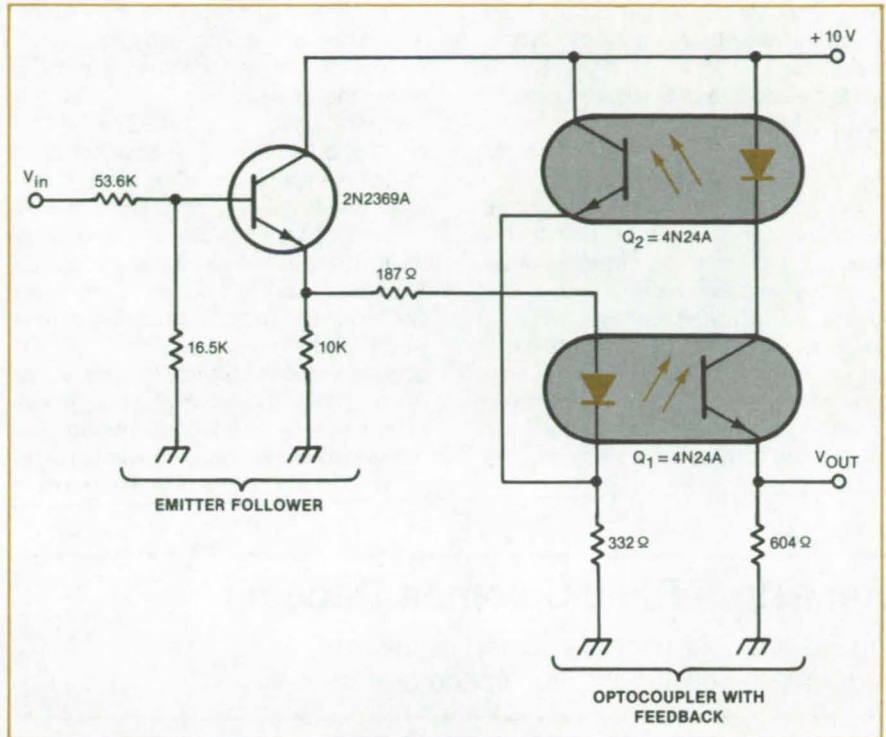
The new circuit employs a feedback circuit containing a second optocoupler (see figure). The feedback signal tends to oppose changes in the overall CTR.

Unlike other approaches to stabilization, the new circuit is inexpensive and requires little additional hardware.

Four devices of the same type were tested in a simple circuit without feedback. The CTR varied as much as 44 percent over a temperature range of -40° to $+25^{\circ}$ C. With the feedback circuit, however, the variation was only 7 percent. This variation could be reduced even further if the resistor values were changed slightly to suit the particular optocoupler type and if the temperature dependence of the emitter follower were eliminated.

The CTR for the same optocoupler type changes from 0.8 to 1.5 as diode current changes from 1 to 4 milliamperes. This CTR change would normally show up as a gain change. However, in the circuit with feedback, the gain was constant within 0.5 percent for a diode current in the range of 1.8 to 3.3 mA.

This work was done by Daniel J. Griffin of Perkin-Elmer Corp. for Marshall Space Flight Center. For further information, Circle 1 on the TSP Request Card. MFS-25927



In the CTR-Stabilizing Circuit, the optical feedback through Q₂ helps to stabilize the overall current-transfer ratio and voltage gain.

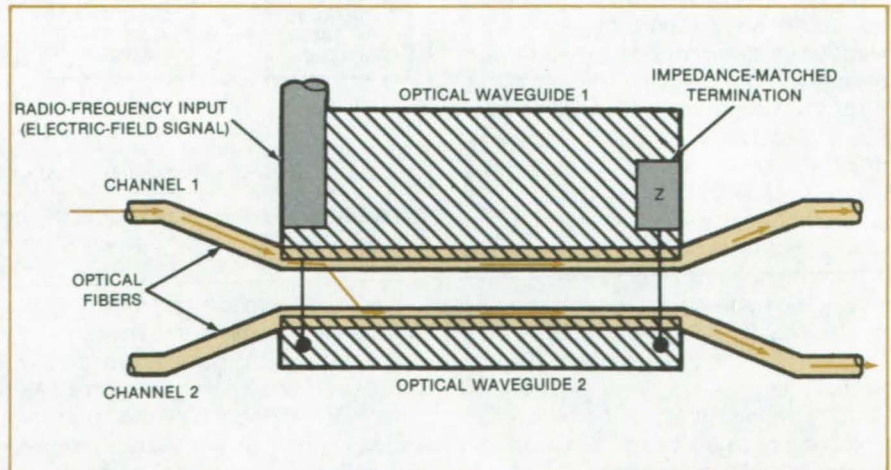
Reversing Optical Damage in LiNbO₃ Switches

Higher operating power can be tolerated after treatment.

NASA's Jet Propulsion Laboratory, Pasadena, California

One of the symptoms of optical damage in a Ti-diffused LiNbO₃ directional-coupler switch is reversed by temporarily raising the input illumination to a higher-than-normal power level. This healing phenomenon can be used to restore normal operation, to increase the operating-power rating, and to stabilize operating characteristics at lower powers. The damage-reversal principle is believed to be generally applicable to optical switches based on LiNbO₃, with consequent implications for the development of wideband data-transmission links.

A directional-coupler switch (see figure) includes two optical waveguides of Ti diffused into LiNbO₃, placed close enough to be optically coupled to each other. Light entering one waveguide is transferred to the other. The amount of
(continued on next page)



In this **Directional-Coupler Optical Switch**, the coupling between two optical channels is varied by applying an electric field to vary the relative refractive indices of two close optical waveguides. A slow drift in relative refractive indices due to optical damage is reversed by operating temporarily at an abnormally high illumination.

transfer depends on the distance between the waveguides and their indices of refraction, which in turn depend on the applied electric field. The field is varied to turn the switch on or off by inducing the appropriate propagation match or mismatch between the waveguides.

Optical damage to the LiNbO_3 material occurs during operation, manifesting itself as a change in refractive index. This change causes a drift in operating characteristics, resulting in such undesirable effects as an increase in crosstalk. Previously, optical damage was minimized by operating at power levels so low (10^{-5} W) that signal-to-noise ratios were sometimes undesirably low.

The following procedure was found experimentally to compensate for the change in relative refractive indices between the waveguides: First, the switch transfer function is recorded at the normal optical-power level, and the slow drift of the transfer function is observed. Next, one of the input ports is illuminated at about twice the normal operating level. This causes the transfer function to change markedly during the first few seconds, then to settle gradually to new values. The illumination is continued for about an hour to stabilize the new transfer function. The second input port is then similarly illuminated: Again, the transfer function changes, eventually returning to approximately the transfer

function of the initial state.

When the switch is illuminated at lower power after this treatment, the operating characteristics change very little. Hence, the technique not only reverses one of the effects of optical damage but also stabilizes the device against further damage effects.

This work was done by Caroline M. Gee and Gary D. Thurmond of Hughes Aircraft Co. for NASA's Jet Propulsion Laboratory. For further information, Circle 2 on the TSP Request Card.

Inquiries concerning rights for the commercial use of this invention should be addressed to the Patent Counsel, NASA Resident Office-JPL [see page A5]. Refer to NPO-16239.

Real-Time Reed-Solomon Decoder

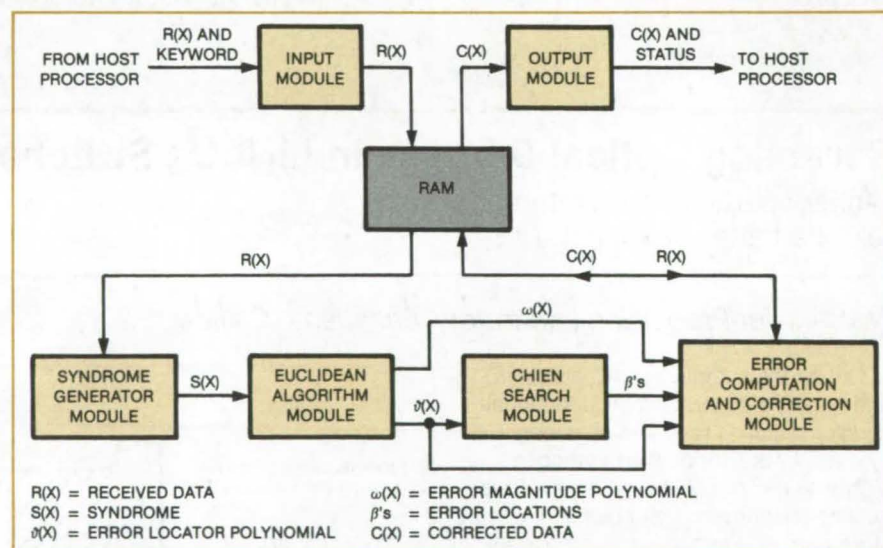
An RS decoder uses dedicated hardware and data pipelining for high-speed operation.

NASA's Jet Propulsion Laboratory, Pasadena, California

A decoder for several formats of Reed-Solomon (RS) codes is a dedicated hardware module that runs under the control of a general-purpose host computer. Data are pipelined throughout (both overall and within each stage) to achieve the high speed (1 megabit per second) required to decode messages as they are received. Parallel processing techniques provide an equivalent of over one billion operations per second at one step in the decoding. Although originally developed for NASA's Galileo mission, the decoder should find commercial application in data encoding/decoding, telemetry, and radio communications.

The Galileo format of RS encoding is a (255, 223) code over a Galois field (GF) of 256 elements. Each word comprises $8 \times 255 = 2,040$ bits, of which $8 \times 223 = 1,784$ bits carry information and $8 \times 32 = 256$ are check bits.

To enhance the efficiency of encoding, the code words are interleaved on a symbol-for-symbol basis, up to an interleaving depth of seven. The RS format can correct up to 16 erroneous (8-bit) symbols in each code word, where any or all 8 bits may be received in error and with the locations of the erroneous symbols being unknown. This same code could be adapted to correct



The **Real-Time RS Decoder** shown in this block diagram can decode a wide range of code formats. The control is by a general-purpose host computer.

32 "erased" symbols (each of 8 bits), the locations of which are known.

The internal organization of the decoder is shown in the figure. All memory is located in a central random-access-memory (RAM) storage module with multiple switchable ports. The multiple ports allow processing in overlapping fashion; that is, input, decoding, and out-

put steps have a simultaneous access to the various data sets in the RAM, accomplishing the overall pipelining. The average data rate is roughly doubled if the incoming data are in a continuous stream. By switching the ports, the decoding stage can begin operation on a first code word, while the input begins taking in a second code word.

The decoding algorithm used consists of the following five steps: (1) syndrome generation, (2) Euclidean algorithm, (3) Chien search, (4) error-magnitude computation, and (5) error correction. These steps are implemented in four separate modules.

Two other RS code formats that can be accommodated by this decoder are

the Berlekamp and Telemetry Development Lab formats. The decoder could handle still other code formats by simple reprogramming (by means of plug-in ROM's, EPROM's, or through programs stored in RAM).

The decoder communicates with a host computer via a 16-bit parallel interface and is entirely programmable by the

host computer. There are no manual controls, except for the on/off switch.

This work was done by Charles R. Lahmeyer of Caltech for NASA's Jet Propulsion Laboratory. For further information, Circle 3 on the TSP Request Card. NPO-15982

Advanced dc-Traction-Motor Control System

Features include high efficiency and regenerative braking.

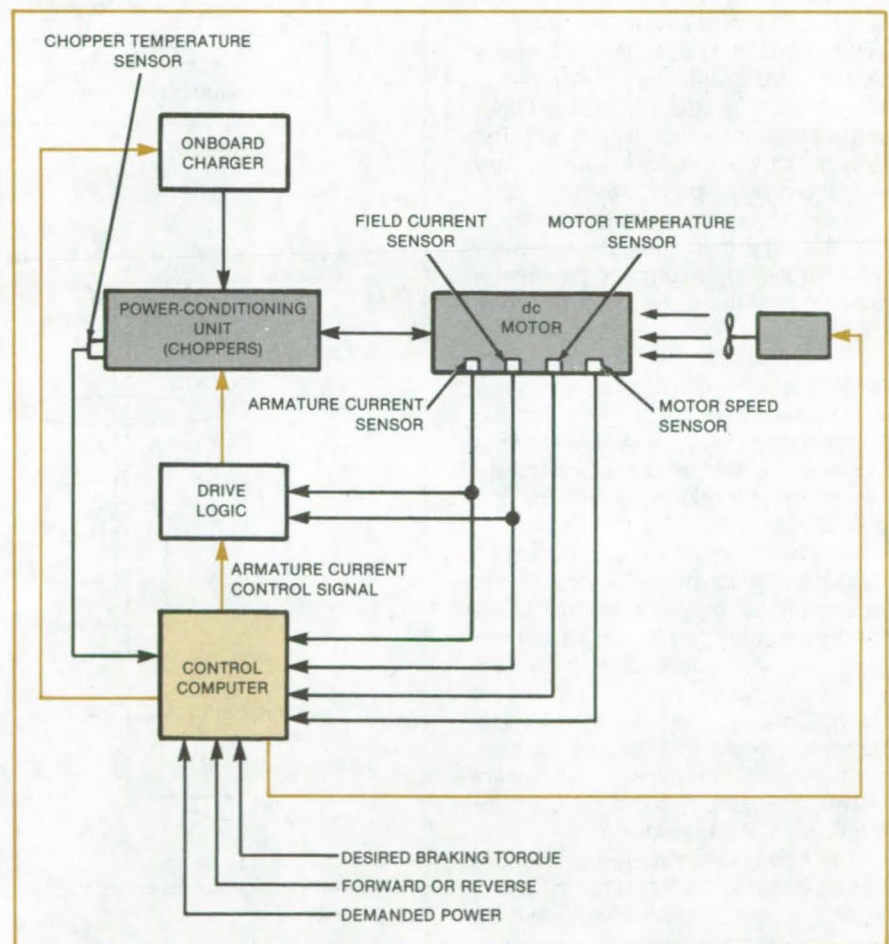
NASA's Jet Propulsion Laboratory, Pasadena, California

A motor-control concept for battery-powered vehicles includes state-of-the-art power-transistor switching and separate excitation of the motor windings in traction and in regenerative braking. The switching transistors and other components of the power-conditioning subsystem operate under the control of a computer that coordinates traction, braking, and protective functions.

The armature and field windings are connected to the battery through separate transistorized choppers. The motor is of an advanced type similar to those now used in electric vehicles, with compensation windings and auxiliary poles that enable it to operate at high efficiency in traction and braking and to accept high overloads. When combined with the advanced control and power-conditioning subsystems, the motor is capable of regenerative braking down to a full stop, with braking power comparable to traction power.

The computer controls the power-conditioning unit through a drive-logic unit (see figure). The control outputs of the computer are developed partly in response to inputs from sensors that measure the motor speed, armature and field currents, motor temperature, and chopper temperature. The other required inputs are commands that signify the demanded power, the direction of rotation (forward or reverse), the operating mode (motor or generator), and the desired braking torque.

The motor is cooled by a separately driven fan. To conserve energy, the fan is turned on only when the motor temperature exceeds a preset value. At a higher preset temperature, the arma-



A Computer Produces Control Signals in response to command and sensory inputs.

ture current is reduced. The armature current is also reduced if the armature chopper overheats. The system is shut down in case of excessive field-winding current, power-transistor failure, battery overcurrent, or armature overcurrent.

This work was done by Oreste Vittone of Centro Ricerche Fiat S.p.A for NASA's Jet Propulsion Laboratory. For further information, Circle 4 on the TSP Request Card. NPO-16118

Integrated Laser and Light Detector

A monolithic structure combines a beam deflector and position indicator.

NASA's Jet Propulsion Laboratory, Pasadena, California

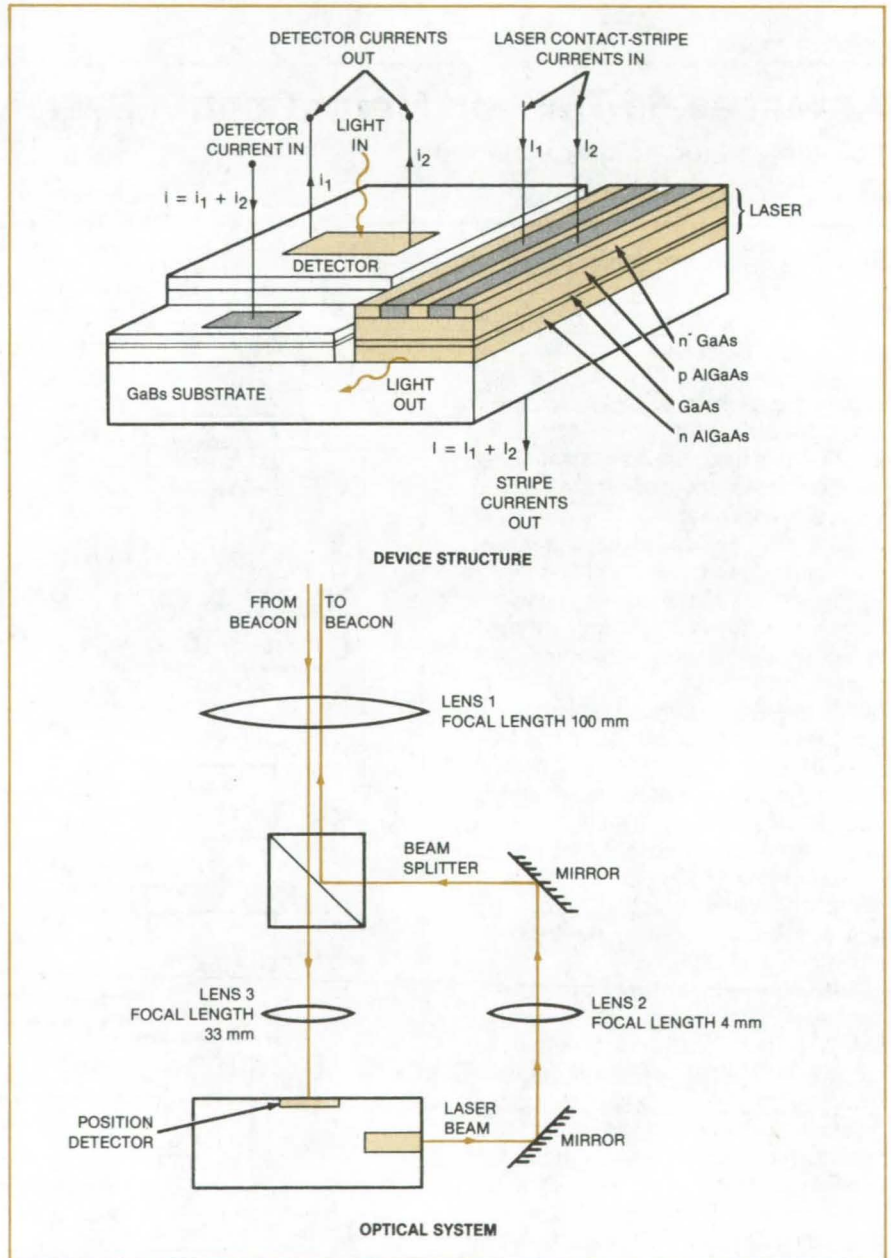
A proposed infrared optical transmitter would track a distant beacon and automatically point the transmitted beam toward the beacon. An essential part of the transmitter is an integrated gallium arsenide device containing an electronically-steerable semiconductor injection laser and a position detector that senses the direction to the beacon.

The device structure and the optical subsystem are illustrated in the figure. Light from the beacon is focused through lenses onto the position detector, which is a strip of photodetector with an output contact at each end. The detector output currents i_1 and i_2 vary with the position of the beacon image. These currents are fed to external control circuitry that uses their relative magnitudes to determine the image position (and therefore the direction to the beacon).

The laser includes two stripe contacts, the input currents of which are varied to steer the output beam. The external control circuitry varies the input currents to steer the laser beam toward the receiver position sensed by the photodetector.

This is an open-loop beam-steering system: It must be calibrated before operation by properly choosing the control-circuitry gains, lens magnifications, and lens positions. In the example of the figure, the beacon is 1 m away. This distance is typical for a laboratory-scale test setup. However, with satisfactory optics and sufficient power, the system could be used for long-distance transmission.

The combination of lenses 1 and 3 has a receiving magnification of 1/100, enabling the 500- μm -long position detector to track a beacon displacement of ± 2.5 cm. The combination of lenses 1 and 2 yields a transmitting magnification of 25; this narrows the laser-beam width from 10° to 0.4° and reduces the beam-steering range from $\pm 25^\circ$ at the chip to $\pm 1^\circ$ in the receiver space. With these parameters, the laser spot size and controllable displacement at the receiver are 7 mm and ± 2 cm, respectively.



In this **Monolithic Beam-Steerable Laser and Position Detector**, the magnitudes and ratio of the currents to the laser stripes determine the amount of beam deflection. The ratio of the currents from the ends of the detector indicates the direction of the beacon.

This work was done by Joseph Katz, James R. Lesh, and Richard M. Dickinson of Caltech for NASA's Jet Propulsion Laboratory. For further information, Circle 5 on the TSP Request Card.

Inquiries concerning rights for the commercial use of this invention should be addressed to the Patent Counsel, NASA Resident Office-JPL [see page A5]. Refer to NPO-15943.

Differential-Coil Eddy-Current Material Sorter

Identically shaped parts with different compositions are distinguished.

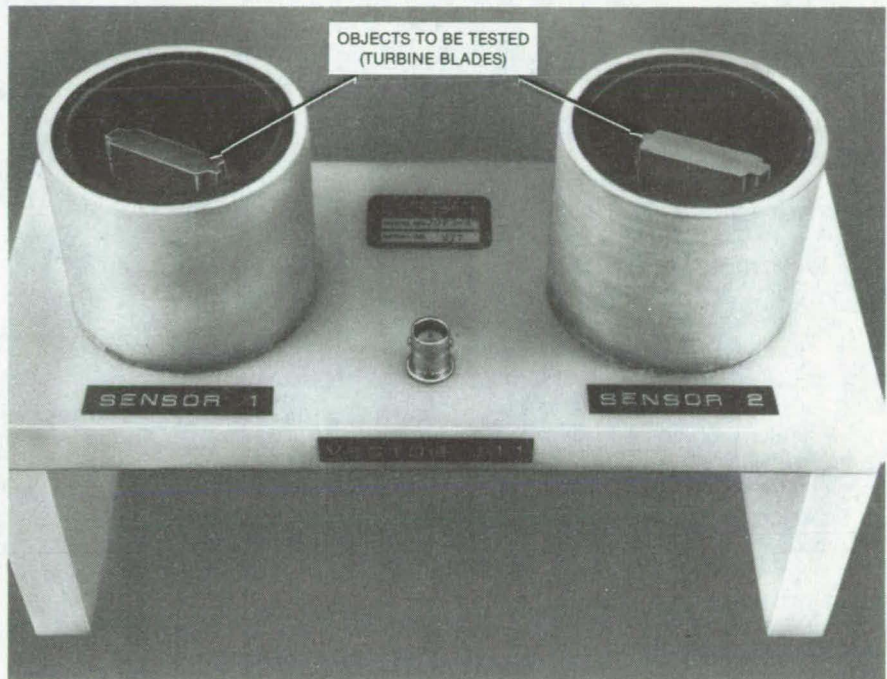
Marshall Space Flight Center, Alabama

Small metal or other electrically conductive parts of the same shape but different composition are quickly sorted with a differential-coil eddy-current sorter. Developed to distinguish between turbine blades of different alloys, hardnesses, and residual stress, the sorter is generally applicable to parts of simple and complex shape.

As in older single- and double-coil eddy-current material sorters, an alternating voltage of known amplitude and frequency is impressed on the coils. This induces eddy currents in the objects under test, which affect the currents in the coils. The amplitude and phase of each coil current is measured. Since the eddy currents depend on the conductivities of the object materials, these amplitude and phase measurements are convenient indicators of property differences that affect conductivity.

The sorter combines a commercial eddy-current instrument with two identical sensing coils (see figure) that are in different arms of an impedance bridge. The coils are large enough [in this case, 2 in. (5 cm) in diameter] to surround the objects.

The operating frequency is selected by experimentation at a value that gives readings of good sensitivity. A typical frequency is 100 kHz. Similarly, the desired phase and amplitude for a null bridge indication is set by selecting the reactive and resistive bridge-circuit impedances. When identically shaped ob-



Identically Shaped Parts Are Placed in Both Sensing Coils with the same orientation and at the same position relative to the center of each coil. A nonconductive holder (not shown) may be used to assure the identical relative positioning of the two parts.

jects are placed with one at the center of each coil, the amplitude and phase of the differential bridge reading then indicates the difference in composition between the objects.

This work was done by J. L. Nummelin and D. C. Buckley of Rockwell International Corp. for Marshall Space Flight

Center. For further information, Circle 6 on the TSP Request Card.

Inquiries concerning rights for the commercial use of this invention should be addressed to the Patent Counsel, Marshall Space Flight Center [see page A5]. Refer to MFS-19872.

High-Cycle-Life Lithium Cell

A new, stable electrolyte solvent allows many more charge/discharge cycles.

NASA's Jet Propulsion Laboratory, Pasadena, California

A new lithium-anode electrochemical cell offers an increased number of charge/discharge cycles. Although older types of secondary lithium cells are characterized by high energy-storage capacity, they have poor cycle life because the cell components are physically and

chemically incompatible and the cathode tends to disintegrate after only a moderate number of cycles.

The new cell uses components selected for compatibility with the electrolyte solvent: These materials are wettable and chemically stable. The low

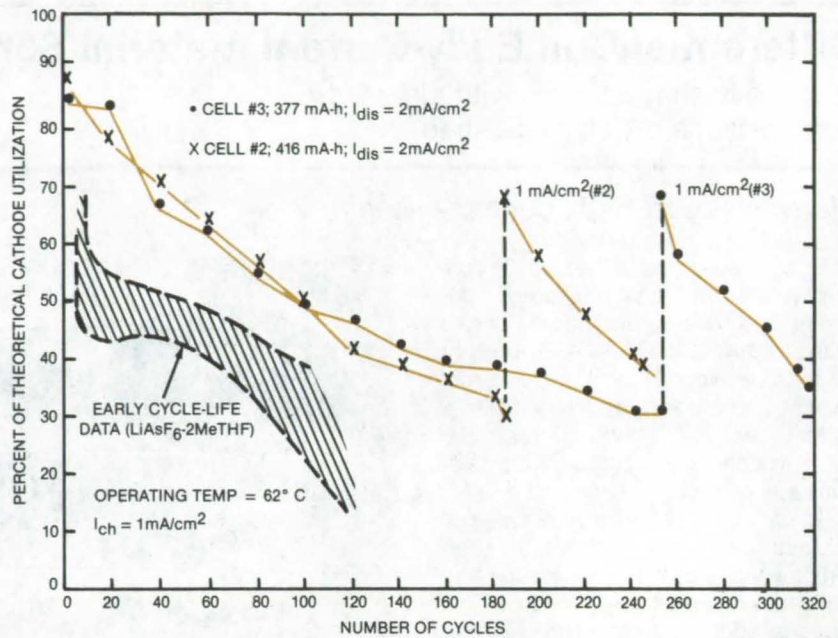
vapor pressure and high electrochemical stability of the solvent improve cell packaging, handling, and safety. Moreover, the cell operates at modest temperatures — less than 100°C — and is therefore well suited to automotive, communications, and other applications.

(continued on next page)

In addition to its lithium anode, the new cell includes a titanium disulfide (TiS_2) cathode and an electrolyte composed of $LiAsF_6$ in a sulfone-based nonaqueous organic solvent. The separator is coated with a surfactant, and a special binder formulation is included in the cathode for compatibility with the new electrolyte. The figure shows the cycle-life performance of two test cells.

The sulfone-based solvent is a heterocyclic compound, such as sulfolane or 3-methylsulfolane (3MeS). These solvents were selected because they resist oxidation and reduction much more than such commonly-used electrolyte solvents as 2-methyltetrahydrofuran (2MeTHF). In addition, with their lower melting points and higher boiling points, they offer a more convenient range of operating temperatures. However, they are highly polar and do not wet the nonpolar material used for the cell separator. Therefore, the separator is coated with imidazoline or silicon-glycol imidazoline surfactant. These materials allow the solvent to wet the separator without compromising the stability of the electrolyte.

To improve the mechanical integrity of the cathode, an ethylene/propylene copolymer is used as the binder instead of the polytetrafluoroethylene that was used



The Cycle-Life of $Li/LiAsF_6$ -3MeS/ TiS_2 Cells are shown here.

previously. Since sulfolane solvents do not wet this material, a sulfone compound is added to ensure wettability.

This work was done by Shiao-Ping S. Yen, Boyd Carter, David Shen, and Robert Somoano of Caltech for NASA's Jet Propulsion Laboratory. For further

information, Circle 7 on the TSP Request Card.

Inquiries concerning rights for the commercial use of this invention should be addressed to the Patent Counsel, NASA Resident Office-JPL [see page A5]. Refer to NPO-15921.

Discriminator Aids Phase-Lock Acquisition

The complexity of swept-frequency systems is avoided.

NASA's Jet Propulsion Laboratory, Pasadena, California

The voltage-controlled oscillator in a suppressed-carrier detector acquires the carrier frequency and phase quickly with the help of a frequency-discriminator arrangement. To obtain the discriminator function, the filter bandwidth in the quadrature (Q) leg of the detector is widened with respect to the bandwidth of the filter in the inphase (I) leg.

The input signal is mixed with the voltage-controlled-oscillator signal in the Q-leg and with a 90° -phase-shifted oscillator signal in the I-leg (see Figure 1). In the I-leg, the mixer output is low-pass-filtered, then hard-limited to produce a square wave oscillating at the frequency difference between the received and oscillator signals. The IQ-mixer output includes a dc component and a double-

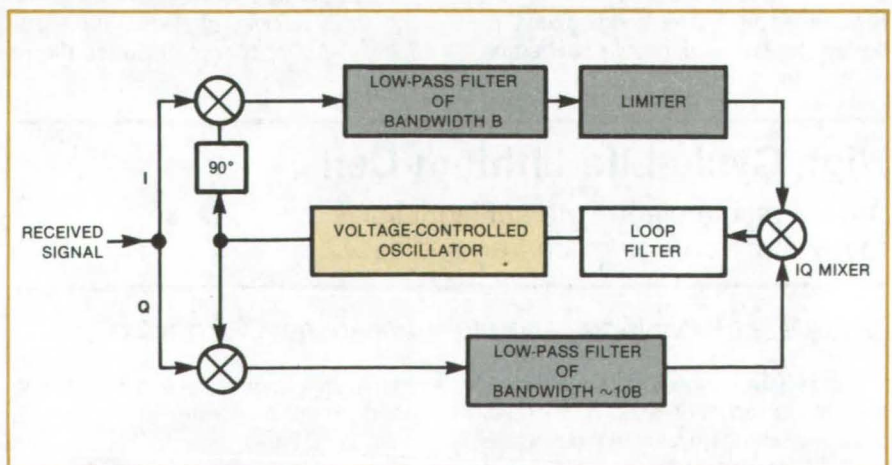


Figure 1. Different Filter Bandwidths in the I- and Q-legs cause differential phase shifts that produce a frequency-discriminator effect.

frequency component that is removed by the loop filter.

At frequency differences well within the Q-passband but in the cutoff region of the I-filter, the I-signal is phase-shifted by about 90° while the Q-signal is negligibly phase-shifted. As a result, the limiter output is in phase or 180° out of phase with the Q-leg output, and the IQ mixer acts like a full-wave rectifier for the Q-signal. The large resulting dc voltage pulls the oscillator toward the frequency of the received signal.

At frequency differences between zero and the I-filter cutoff, the phase difference between the limiter output and the Q-signal varies from 90° to either 0° or 180° . The dc component of the IQ-mixer output therefore varies from zero (at zero frequency difference) to the positive or negative of the large dc voltage mentioned previously (at large frequency differences). Figure 2 gives an example of such a voltage-versus-frequency-difference characteristic curve.

Since the noise voltages in the I and Q legs are not correlated with each other, they produce little dc component in the IQ output and therefore have little effect on the oscillator frequency. Thus, when lock is lost due to noise or to the loss of the received signal, the oscillator frequency remains near the previous value. The combination of I- and Q-leg and loop-filter bandwidths and the discrimi-

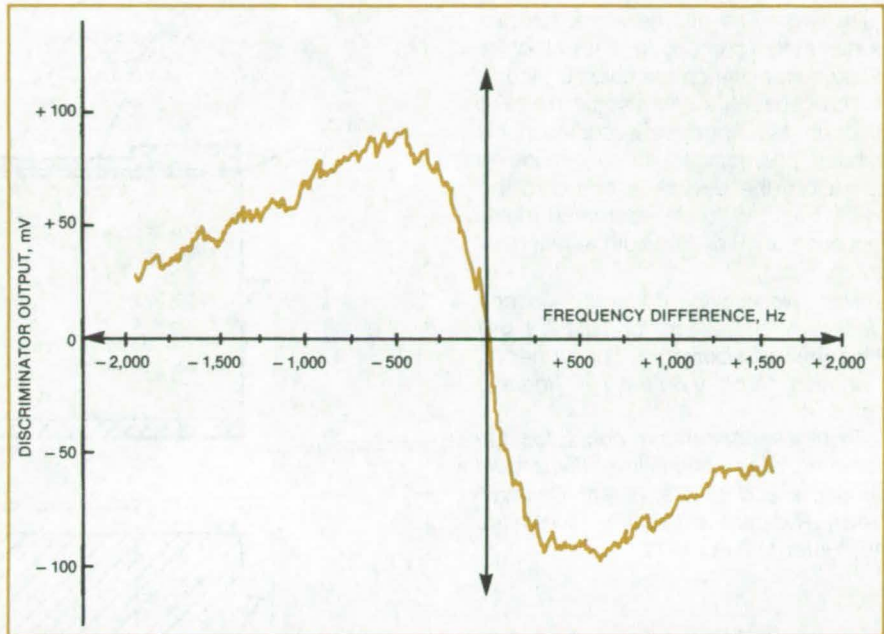


Figure 2. The dc Component of the Discriminator Output (the control voltage for the oscillator) varies with the difference between the received-signal and oscillator frequencies. In this example, the I- and Q-leg low-pass filters are of the single-pole type, with 3-dB bandwidths of 510 Hz and 5 kHz, respectively.

nator action reduce the tendency to lock on the sidebands.

This work was done by Lansing M. Carson and F. Elvin Krasin of Motorola, Inc., for NASA's Jet Propulsion Laboratory. For further information, Circle 8 on the TSP Request Card.

This invention has been patented by NASA [U.S. Patent No. 4,336,616]. Inquiries concerning nonexclusive or exclusive license for its commercial development should be addressed to the Patent Counsel, NASA Resident Office-JPL [see page A5]. Refer to NPO-14311.

Light-Activated Microwave Device

Chip would switch, generate pulses, and detect at microwave speeds.

NASA's Jet Propulsion Laboratory, Pasadena, California

A conceptual laser-activated microwave semiconductor device could switch at microwave speeds, generate pulses, or detect optical pulses with fast response. The device consists essentially of back-to-back metal/thin oxide/silicon (MTOS) capacitors on a silicon chip (see figure).

Light from a laser (which may be a semiconductor laser integrated with the microwave device) is absorbed through the thinned areas of the aluminum electrodes of the capacitors. (The aluminum is less than 10 nm thick in these areas.)

A layer of silicon dioxide about 10 nm thick under the electrodes provides a large capacitance per unit area, and this capacitance is coupled to the capacitance of the depletion layer in the silicon beneath the oxide. The oxide is thick enough to be nonconducting at voltages below 7 volts on one capacitor.

Operation of the device is based on the change in carrier-generation rate in the depletion layer caused by illuminating the MTOS capacitors. When illuminated by the laser, the depletion layer generates enough carriers to

become conducting; the path between capacitor electrodes turns on very rapidly. The device can alternate between on and off at rates in the gigahertz range.

The device can be operated as an optically-triggered pulse generator. A dc bias is applied to the back-to-back capacitors, charging the capacitors in the off state to a low level (equal to the product of the voltage and the depletion-layer capacitance). When the device is illuminated with a laser pulse, the capacitance increases to one-half the capacitance of the oxide layer, which is

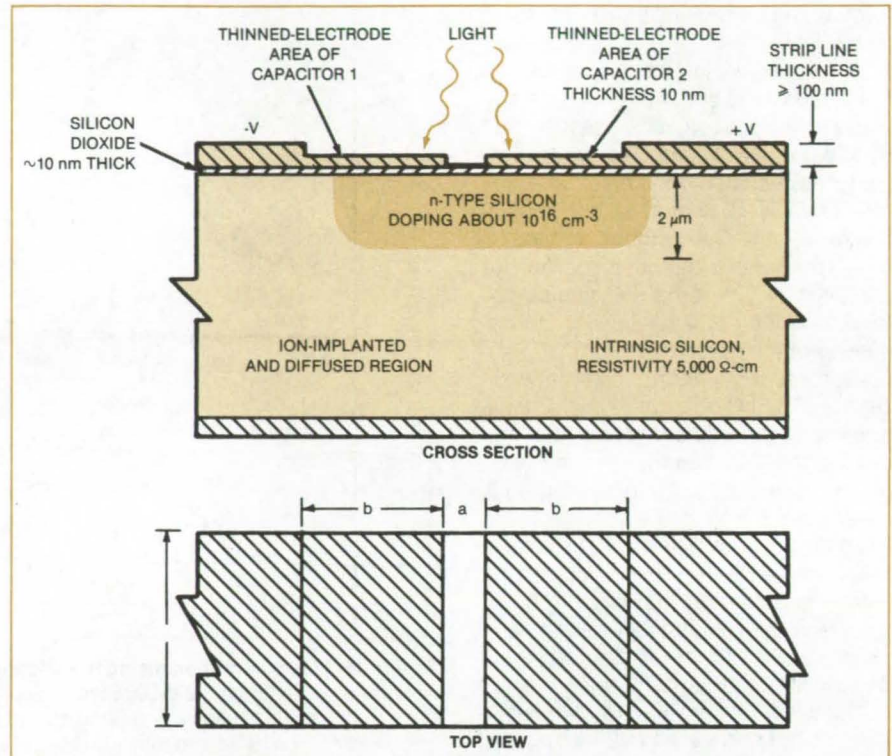
(continued on next page)

quite large. The charge increases proportionately, creating a current pulse along a strip line on the chip surface.

The capacitors can also be made to function as capacitively-coupled back-to-back photodiodes. In this mode of operation, the device responds to low light levels with an estimated pulse response of 45 ps full width at half maximum.

This work was done by Joseph Maserjian of Caltech for NASA's Jet Propulsion Laboratory. For further information, Circle 9 on the TSP Request Card.

Inquiries concerning rights for the commercial use of this invention should be addressed to the Patent Counsel, NASA Resident Office-JPL [see page A5]. Refer to NPO-16112.



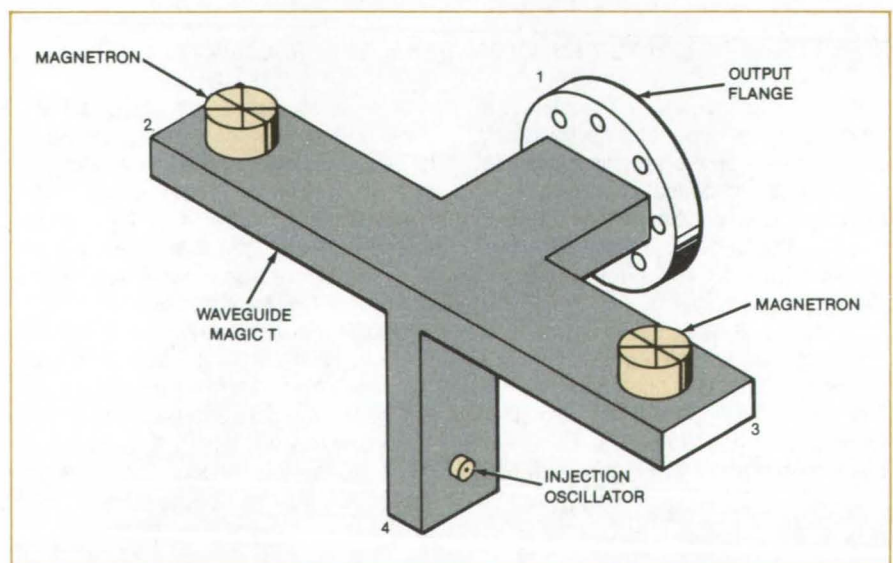
This **Light-Activated Microwave Device** contains a strip line, the two sections of which are separated by a pair of back-to-back capacitors. The 2- μm depth of the diffused region is sufficient to provide a conducting path between the capacitors at microwave frequencies. Representative strip-line dimensions are $a = 2 \mu\text{m}$, $b = 5 \mu\text{m}$, and $c = 240 \mu\text{m}$.

Magic-T-Coupled Magnetrons

Output powers are combined, and the output spectrum is clean.

The outputs of two magnetrons are added coherently in a scheme based on resonant waveguide coupling and injection phase locking. In addition, the magnetron filaments are turned off after starting. The combination of these established techniques may eliminate the need for klystron tubes in some carrier-signal generators.

As shown in the figure, the magnetrons are mounted at the ends of opposing arms of a magic-T waveguide junction. A signal of the desired output frequency is injected at port 4 to synchronize the oscillations of the magnetrons. In the magic T, the injection signal divides into two equal signals propagating to the magnetrons with opposite phases. The injection signal does not, however, propagate to output port 1.



A **Magic T** waveguide junction couples the injection signal to the magnetrons and the magnetron outputs to the output port.

If the difference in length between arms 2 and 3 is a quarter wavelength at the injection frequency, the magnetron outputs combine in phase with each other at the intersection, and the power propagates out through port 1. After initial start-up, with filaments turned off

during signal transmission, the otherwise-noisy magnetron output becomes more nearly spectrally pure. The overall effect is that relatively-inexpensive, low-power, noisy magnetrons can generate clean carrier signals of higher power that would ordinarily require the more

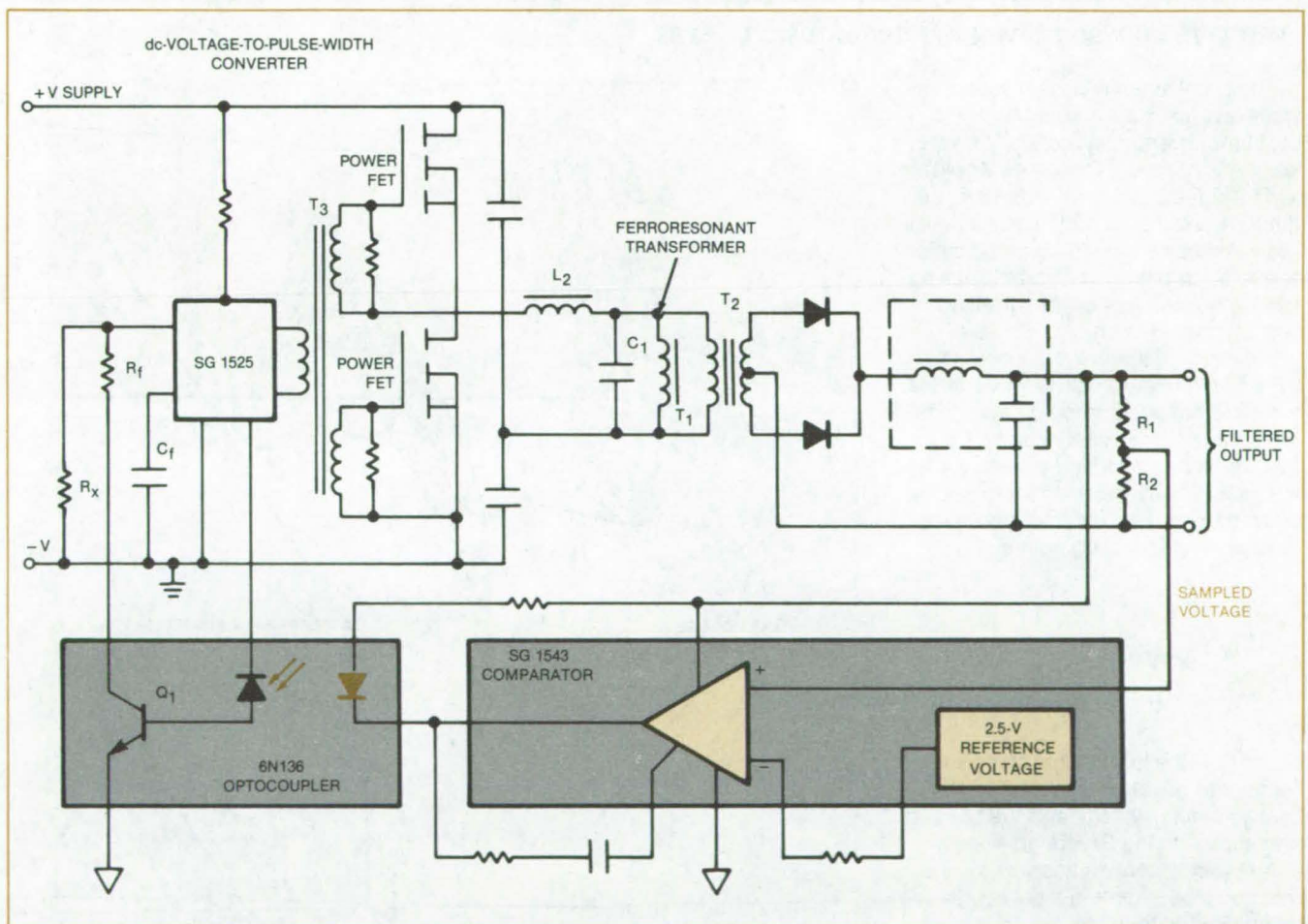
expensive klystrons.

This work was done by Richard M. Dickinson of Caltech for NASA's Jet Propulsion Laboratory. For further information, Circle 10 on the TSP Request Card. NPO-15061

Lightweight Regulated Power Supply

An error voltage alters the frequency in a ferroresonant transformer.

NASA's Jet Propulsion Laboratory, Pasadena, California



A **Frequency-Controlled Voltage Regulator** has no turn-on overshoot. Under the control of the error signal, the output voltage increases gradually to its proper value when the circuit is turned on. The effects of transients in the line voltage are also greatly reduced.

A new power-supply circuit regulates its output voltage by adjusting the frequency of a chopper circuit according to variations in the input voltage. The supply is light in weight and responds quickly to input variations. Currently installed in a battery charger for an electric wheelchair, the circuit is well suited to

other uses in which light weight is important — for example, in portable computers, radios, and test instruments.

When the output voltage varies, a sampling dc voltage also varies. The sample voltage is fed to a voltage-controlled oscillator, which changes the frequency of the oscillations in the ferrores-

onant transformer in such a way that the output voltage returns to its original value. Thus if a heavy load reduces the output voltage, the frequency increases, and the output voltage rises to compensate for the reduction.

The output voltage is sampled at voltage divider R_1 , R_2 (see figure) and is (continued on next page)

compared with a reference voltage in a comparator. A deviation in the output voltage from the nominal value causes the comparator to put out an error signal, which is applied to an optical coupler. The coupler provides electrical isolation while varying the bias on transistor Q_1 in accordance with the error voltage. This changes the resistance of the transistor, which is in parallel with

the frequency-controlling resistor R_f of the oscillator chip. The net change in resistance changes the frequency of the oscillator.

Since the ferroresonant transformer T_1 operates at saturation, the frequency change causes a change in the voltage across T_1 and the output transformer T_2 , resulting in a change in the filtered output voltage. The voltage regulation is

tight because the voltage across T_1 is a linear function of frequency, and the change in frequency is large for small error voltages.

This work was done by Colonel W. T. McLyman of Caltech for NASA's Jet Propulsion Laboratory. For further information, Circle 11 on the TSP Request Card. NPO-15977

Antenna Subreflector Fed by a Line Source

A subreflector converts cylindrical wave fronts to spherical wave fronts.

Lyndon B. Johnson Space Center, Houston, Texas

Additional antenna design options are made available by a subreflector concept for converting cylindrical waves into spherical waves. The waves would be used to feed a main reflector that shapes the radiation pattern into a pencil beam for point-to-point communication or into a fan beam for aircraft tracking, space surveillance, or directional beacon transmission.

Previous dual-reflector antennas required spherical- or plane-wave feeds, but could not accommodate cylindrical-wave (line-source) feeds. For the Cassegrainian and Gregorian systems shown in Figure 1, ray calculations yield the following equation for the subreflector surface in spherical coordinates:

$$\begin{aligned} & \rho^2 \sin^2 \theta \sin^2 \phi \\ & - 2\rho[d(\cos \theta \pm 1) + 2f_s] \\ & + 4f_s(f_s \pm d) = 0 \end{aligned}$$

where f_s = the focal length of the subreflector, the negative sign applies to the Cassegrainian system, and the positive sign applies to the Gregorian system.

A reflector configuration of the new type could be symmetric, but is preferably configured for offset feed so that the subreflector does not block the main reflector. If the subreflector is equidistant along the optical axis from the focal point of the main reflector and from the cylindrical-wave feed in the Cassegrainian system, then $d = 2f_s$, and the equation simplifies to $y^2 = 4f_s(z + f_s)$ in rectangular coordinates. This formula describes a cylindrical subreflector of parabolic cross section, as shown in Figure 2.

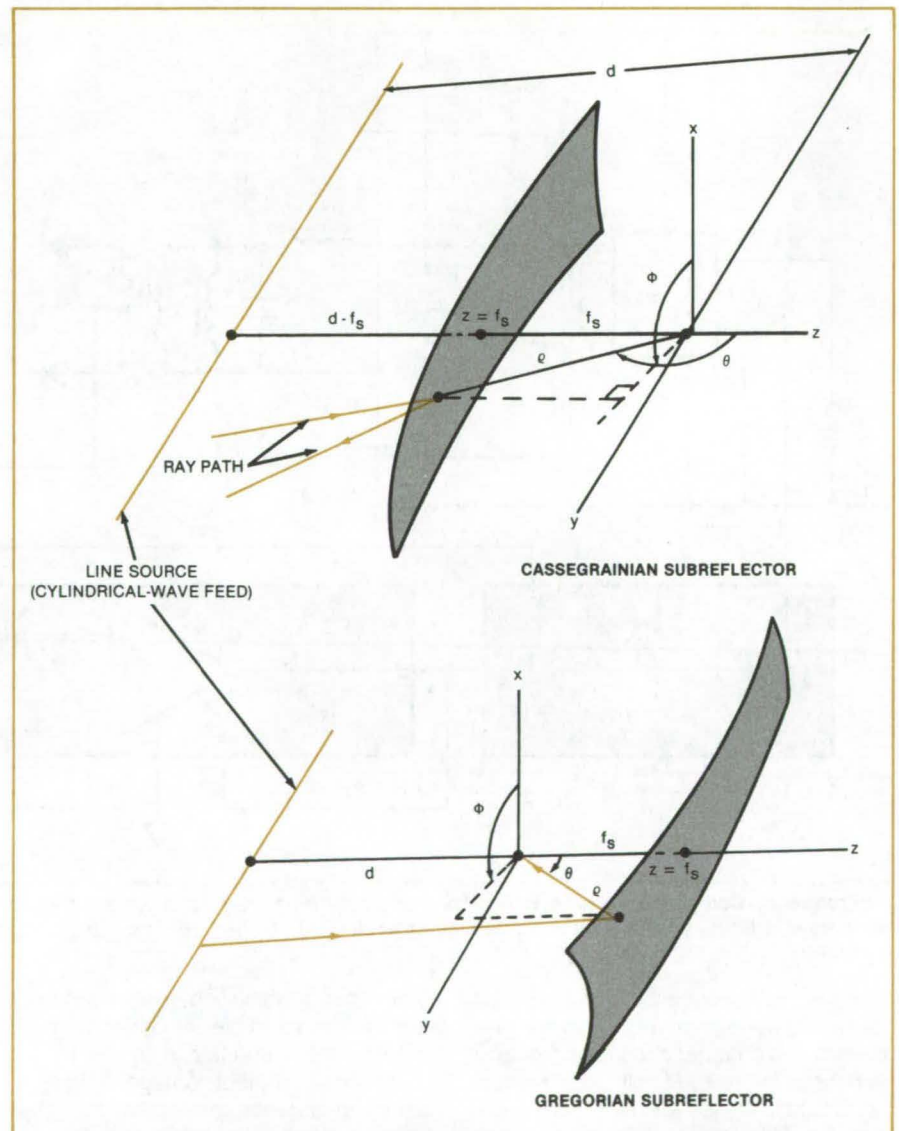


Figure 1. Cassegrainian and Gregorian Reflector Systems are shown with the coordinates used to calculate reflector surfaces.

This work was done by Alex C. Brown, Jr., and Gary D. Brunner of Goodyear Aerospace Corp. for Johnson Space Center. For further information, Circle 12 on the TSP Request Card.

Inquiries concerning rights for the commercial use of this invention should be addressed to the Patent Counsel, Johnson Space Center [see page A5]. Refer to MSC-20626.

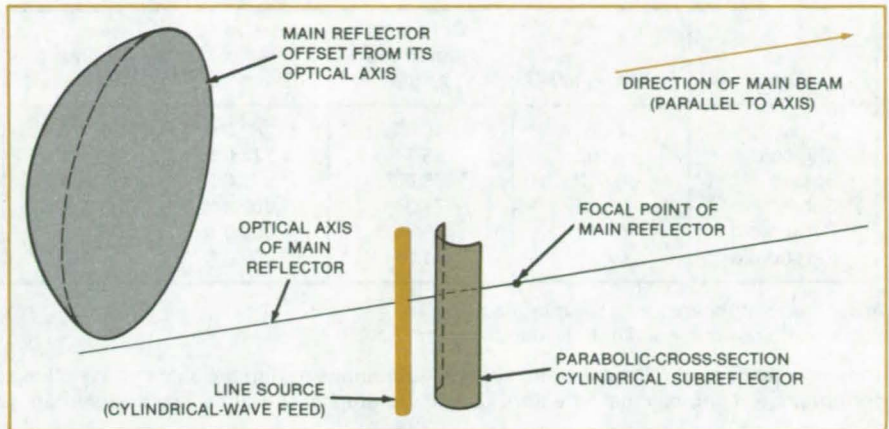
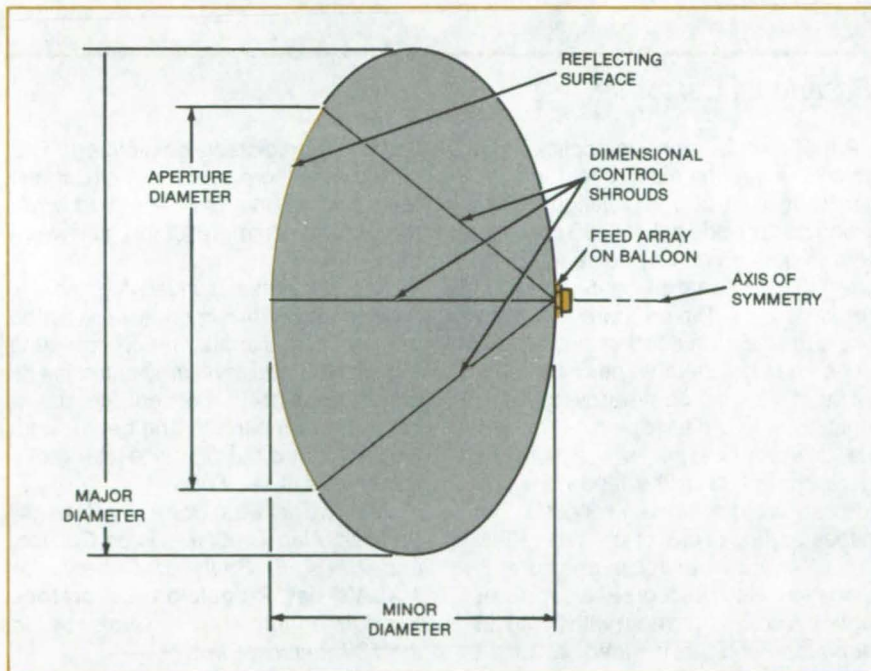


Figure 2. A Special Case of the Cassegrainian Configuration features an offset parabolic-cross-section subreflector perpendicular to a line source.

Ellipsoidal Balloon Antenna

A direct-broadcast ellipsoidal antenna would be 40 percent smaller than a spherical reflector.

NASA's Jet Propulsion Laboratory, Pasadena, California



Ellipsoidal Balloon Antenna has its feedpoint on the surface of the ellipsoid outside the balloon, simplifying balloon deployment and feed support. Dielectric shrouds may be used locally to adjust the shape of the balloon and to maintain the feed distance at its optimum value.

The geometry of an ellipsoidal balloon antenna is such that the antenna feedpoint can be located on the surface of the ellipsoid rather than inside the balloon. Conventional spherical balloon antennas, in contrast, must be energized from an interior point. Ellipsoidal antennas would thus be easier to assemble and easier to deploy if used in "self-erecting" configurations. They would require simpler feed mountings and would not have to be penetrated by signal cables.

In the antenna shown in the figure, the focus of the reflecting surface falls on the opposite side of the ellipsoid if the ratio of the major axis to the minor axis is carefully selected.

The ellipsoid is closer than a sphere to the ideal paraboloidal shape, the optimum shape for a reflector. It also offers a significant reduction in size and weight. It is at least 40 percent smaller than a spherical reflector for the equivalent performance, according to a computer simulation.

Because the feed is located on the surface of the balloon, the surface can

(continued on next page)

Type	Efficiency	Reflector Subtended Angle	Major Diameter	Minor Diameter	Feed Location	Comments
Ellipsoid	0.620	46.6°	1,280.3 ft	584.6 ft	Opposite Surface	A/B = 2.19
Ellipsoid	0.652	43.7°	1,374.0 ft	627.4 ft	Opposite Surface	A/B = 2.19
Sphere	0.612	76.0°	1,475.0 ft	1,475.0 ft	0.59 × Radius	A/B = 1.0
Sphere	0.650	71.3°	1,602.8 ft	1,602.8 ft	0.59 × Radius	A/B = 1.0
Paraboloid	0.812	43.7°	1,000.0 ft	-----	At Focus	F/D = 0.623
Paraboloid	0.828	71.3°	1,000.0 ft	-----	At Focus	F/D = 0.348

A/B = ratio of the major to the minor axis.
 F/D = ratio of the focal length to the diameter.

The **Performances of Ellipsoidal and Spherical Antennas** having the same efficiencies and aperture diameters are compared, with the performance of paraboloidal reflectors given for reference. The ellipsoidal designs can have better performance than spherical designs.

be part of the feed. For example, dipole or turnstile feeds can be easily implemented by placing foil or conductive material on the balloon surface. A bus located one-quarter wavelength from the balloon with a deployable surface ex-

tension can be the ground plane for the feed. The performances of ellipsoidal and spherical balloon antennas having the same efficiencies and aperture diameters are compared in the table.

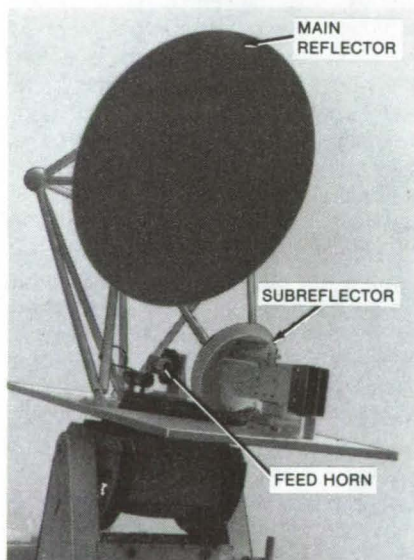
This work was done by Paul W.

*Cramer of Caltech for NASA's Jet Propulsion Laboratory. For further information, Circle 13 on the TSP Request Card.
 NPO-15931*

Efficient Reflector Antenna

An off-axis, clear-aperture design has high gain-to-noise-temperature ratio.

NASA's Jet Propulsion Laboratory, Pasadena, California



The **High-Gain, High-Efficiency Antenna** includes a horn feed to off-axis reflectors. The off-axis arrangement helps to increase efficiency by providing a clear aperture to the main reflector.

An efficient antenna is applicable to systems where the main reflector diameter is at least 500 wavelengths. This design can provide a 2- to 3-dB improvement in gain divided by noise temperature (G/T) over that of centerline symmetric designs. The aperture efficiency of a large new antenna of this type is expected to be about 90 percent.

The performance improvement is largely due to a clear-aperture, off-axis dual-reflector design. As shown in the figure, the offset of the feed horn provides an unblocked main reflector. The shapes and positions of the two reflectors offer quasi-uniform aperture illumination with a degree of spillover control. A corrugated horn with 22.40 dB gain was selected as the feed because it exhibits a nearly-perfect circular pattern

and has a predictable gain pattern. This allowed the horn to serve both as the feed and as the gain standard while measurements of reflector gain were being taken.

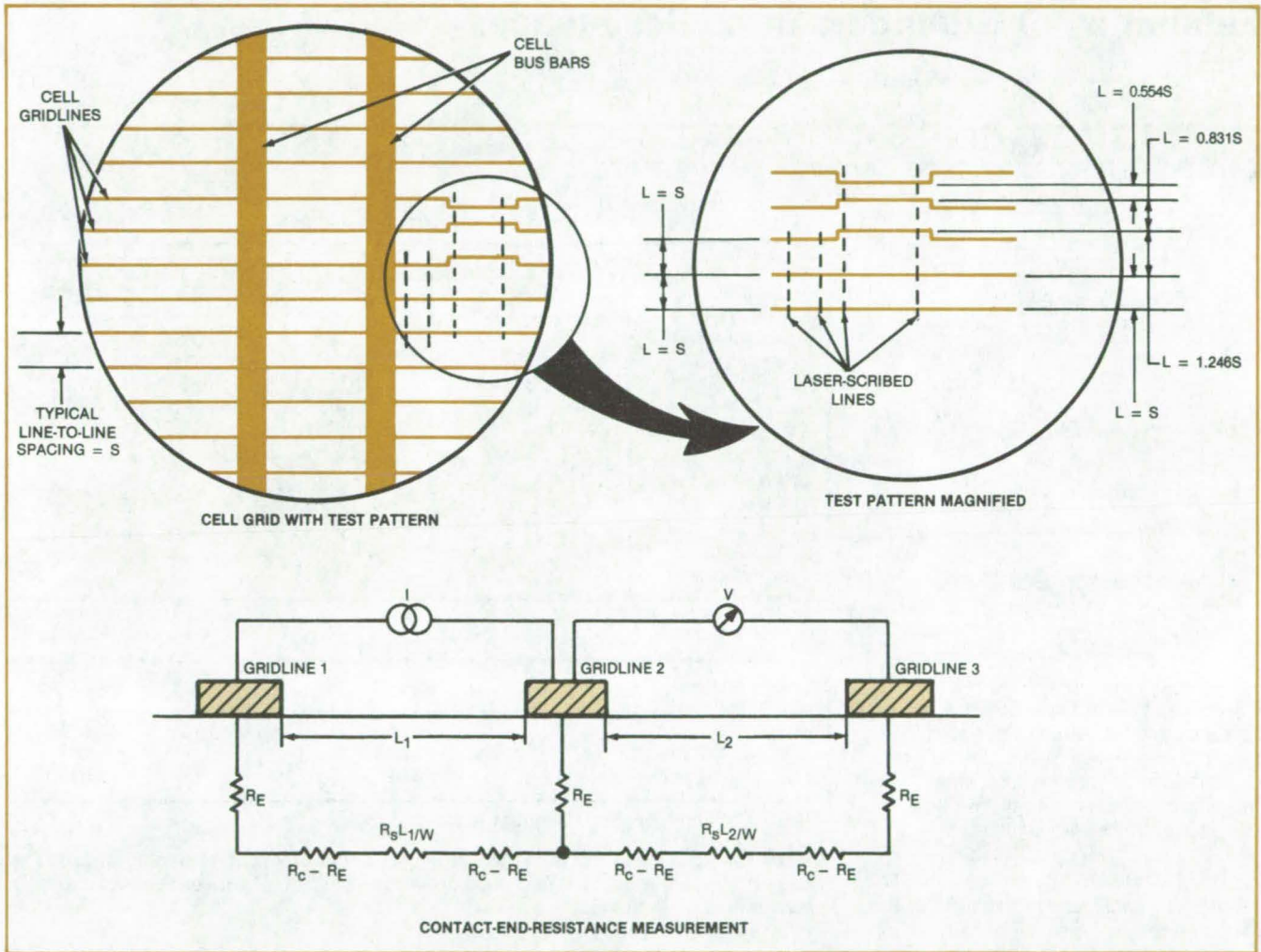
The calculations underlying the improvements in this antenna were tested using a 1.5-m-diameter model operating at 31.4 GHz. The measured antenna efficiency was 84.5 percent versus a calculated 86 percent, the beam width was 0.4°, and the first side-lobe radiation level was -19 dB.

*This work was done by Dan A. Bathker, Alan G. Cha, Victor Galindo, and Harry F. Reilly of Caltech for NASA's Jet Propulsion Laboratory. For further information, Circle 14 on the TSP Request Card.
 NPO-16262*

Measuring the Contact Resistances of Photovoltaic Cells

Test method is only slightly destructive.

NASA's Jet Propulsion Laboratory, Pasadena, California



A Pattern of Test Contacts separated from the rest of the cell by scribe lines enables the measurement of total resistance between a pair of contacts (R_c), contact-end resistance (R_E), and sheet resistivity (R_s).

A simple method has been devised to measure the contact resistances of photovoltaic solar cells. The method uses readily available equipment and is applicable at any time during the life of a cell. The method enables the evaluation of cell contact resistance (R_c), contact-end resistance (R_E), contact resistivity (ρ_c), sheet resistivity (R_s), and sheet resistivity under the contact (R_{sk}).

A test contact pattern is applied to the cell during manufacture. The test pattern consists of four or five unequally spaced contact lines. The test pattern

operates along with the rest of the contact grid to gather current during normal operation. When the contact-resistance test is to be performed, the unequally spaced portions of the test pattern are electrically isolated from the rest of the cell by laser- or diamond-wheel-scribed grooves (see figure).

Only standard pieces of test equipment are required: a low-resistance ohmmeter and a combination current source/voltmeter; alternatively, a multimeter with four-wire resistance-measurement capability. Seven inde-

pendent determinations of R_E are obtained with three of the unequally spaced test contacts. This is done by inducing a known current in a pair of contacts, then measuring the voltage at the third contact relative to the voltage at the other two, then inserting the measured values in equations relating them to R_E .

R_c and R_s are determined by measuring the total resistances between each of two pairs of unequally spaced contacts: The measured resistances are inserted along with the contact length w

(continued on next page)

and spacings L_i into equations that relate these quantities to R_c and R_s . ρ_c and R_{sk} can then be determined by a computer program, CERTLM, which allows for voltage drop in test lines.

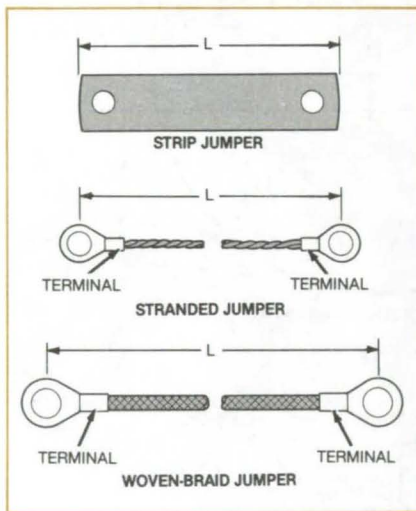
This work was done by Dale R. Burger of Caltech for NASA's Jet Propulsion Laboratory. For further information, Circle 15 on the TSP Request Card.

Inquiries concerning rights for the commercial use of this invention should be addressed to the Patent Counsel, NASA Resident Office-JPL [see page A5]. Refer to NPO-16168.

Estimation of Grounding-Strap Resistances

New tables provide more realistic values.

Lyndon B. Johnson Space Center, Houston, Texas



Grounding Connections covered by the formulas and tabulated values are strips, strands, and woven braid. Resistances calculated with these values differ from handbook values in that crimp-termination resistances are included.

Two formulas and a set of tabulated values are used for calculations of the resistances of electrical grounding straps. The tabulated values take into account the resistances of terminal crimps as well as the resistances of the straps alone. The equations apply to thin metal strips, woven braids, and stranded jumpers (see figure).

For a thin metal strip, the resistance is represented by the formula $R = \rho L/A$, where R = the total resistance, L = the length of the strip, A = the cross-

Woven-Braid and Stranded Jumpers

Type	American Wire Gage	X		Y mΩ
		mΩ/in.	mΩ/cm	
Nickel-Plated OFHC* Wire With Nickel-Plated Terminals	4	0.022	0.0087	0.1
	8	0.08	0.031	0.12
	12	0.32	0.13	0.25
	16	0.65	0.26	0.80
Nickel-Clad (Not Plated) Wire With Nickel-Plated Terminals	12	0.30	0.12	1.1

Resistivity, ρ

Material	$\rho(\mu\Omega\text{-in.})$	$\rho(\mu\Omega\text{-cm})$
Aluminum	1.46	3.71
OFHC* Copper	0.578	1.47
Beryllium Copper	4.525	11.49

*OFHC: Oxygen-Free, High-Conductivity

Values for Resistance Formulas are listed for some practical grounding straps. The values of X and Y must be determined anew for each type of wire or connector and for each method of crimping.

sectional area of the strip, and ρ = the effective electrical resistivity of the strip material. For woven braid or stranded jumpers, the equation is $R = XL + Y$. The values of X and Y (see table) depend on the nature of the protective covering on the wire, the gage of the wire, and the nature of the terminals.

These equations and the tabulated values of X and Y make it possible to

determine the grounding resistance well in advance of the installation of an electrical or electronic system. It is no longer necessary to measure resistance by trial and error at installation.

This work was done by Robert Q. Jackson of Rockwell International Corp. for Johnson Space Center. No further documentation is available.
MSC-20694

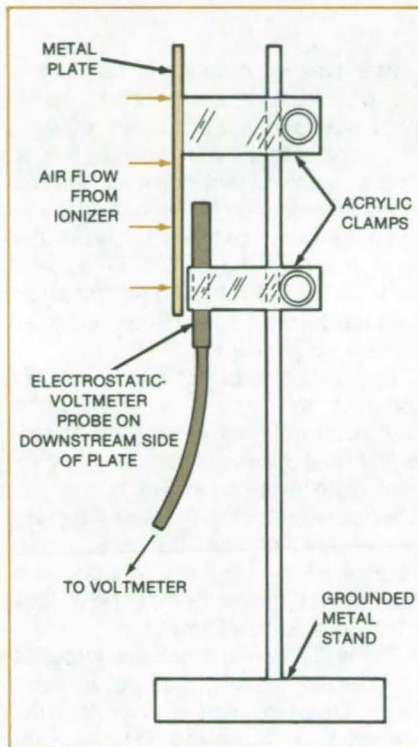
Measuring Air-Ionizer Output

Instrument is useful in monitoring the airborne static charge in electronic assembly areas.

NASA's Jet Propulsion Laboratory, Pasadena, California

A test apparatus checks the ion content of the airstream from a commercial air ionizer. The apparatus ensures that the ion output is sufficient to neutralize static charges in electronic assembly areas and that the concentrations of positive and negative ions are balanced.

The equipment includes a metal plate on an insulating mounting (see figure). The plate is charged to about 1 kV (either by means of a power supply or by induction) and then exposed to the output airstream of the ionizer. The time for the plate to discharge to an equilibrium voltage is measured with the aid of a noncontacting electrostatic voltmeter of the type used to test electrostatic copying machines. If the ionizer is producing



This Test Apparatus combines a chargeable metal plate and a noncontacting electrostatic voltmeter.

ions at the requisite rate, the discharge time does not exceed a preset value. For a typical commercial ionizer, the time is about 20 seconds, and the equilibrium voltage is in the range of -30 to $+30$ volts.

The insulation provided by the clamps should be checked when the apparatus is first assembled. Proper insulation is indicated by a discharge time of tens of minutes in un-ionized air.

This work was done by James O. Lonborg of Caltech for NASA's Jet Propulsion Laboratory. For further information, Circle 16 on the TSP Request Card.

NPO-16058

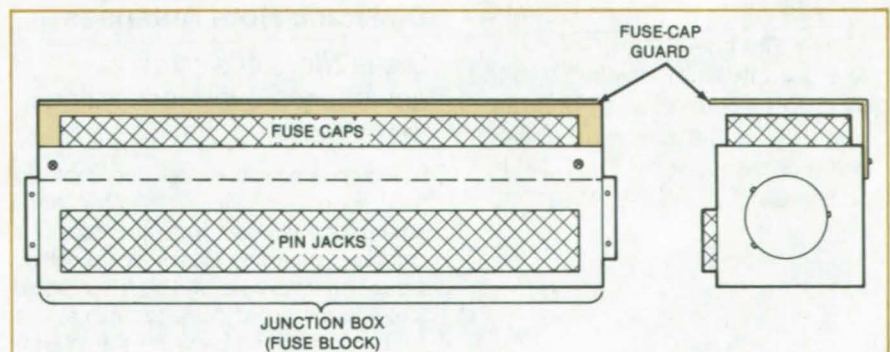


Guard for Fuse Caps

A flanged shield protects fuses from tampering and unauthorized removal and replacement.

John F. Kennedy Space Center, Florida

A simple expedient makes it difficult for people to remove electric fuses without replacing them or to replace them with fuses of the wrong current rating. An L-shaped guard is attached to the fuse holder (see figure). The guard prevents casual tampering with the fuses in an electrical junction box or fuse block. It also protects the fuses from being damaged by handling or by rope or string used to secure them.



The Fuse-Cap Guard shelters fuse caps and prevents their unauthorized removal from the fuse block.

This straightforward approach was used successfully at Kennedy Space Center to solve several recurring problems: People would remove fuses without replacing them, would replace them with fuses of incorrect rating, or

would replace them without putting through the paperwork to document the change. With the fuse-cap guard, only responsible people have access to the fuses.

This work was done by Douglas C. Atwell of McDonnell Douglas Corp. for Kennedy Space Center. No further documentation is available.
KSC-11283

Books and Reports

These reports, studies, and handbooks are available from NASA as Technical Support Packages (TSP's) when a Request Card number is cited; otherwise they are available from the National Technical Information Service.

Batteries for Electric Vehicles

Driving range is improved, but problems remain.

A report summarizes the results of tests on "near-term" electrochemical batteries — that is, batteries approaching commercial production. Nickel/iron, nickel/zinc, and advanced lead/acid batteries were included in the tests and were compared with conventional lead/acid batteries. The batteries were operated in electric vehicles, both at constant speed and on a repetitive schedule of accelerating, coasting, and braking.

The near-term batteries had significantly greater range than the conventional ones but nevertheless had certain deficiencies. The tests also identified deficiencies in the newly developed vehicles operated by the batteries.

One type of nickel/zinc cell had a positive electrode composed of nickel hydroxide and a conductive diluent, rolled and pressed with a plastic binder onto a metal current collector, and a negative electrode of zinc oxide and additives, combined and bound in the same manner. The cells were assembled into a 108-volt, 250-Ah (rated by manufacturer) battery that weighed 1,210 pounds (549 kg).

The other type of nickel/zinc cell was constructed using a more-common electrochemically-impregnated sintered-nickel positive electrode. The negative plate was bound like that in the other nickel/zinc cell. A 108-volt battery was assembled from the cells, which were rated at 300 ampere-hours. The total weight of the battery pack was 1,152 pounds (523 kilograms).

The nickel/iron cell included plates of hot-pressed nickel-plated steel wool. The positive plate was electrochemically impregnated, and the negative plate was pasted with ferrosferric oxide (Fe_3O_4). A 108-volt battery was assembled, weighing 1,080 pounds (490 kilograms). Electrolyte was circulated to provide cooling for a charging time of 3.5 hours.

The lead/acid battery was similar to conventional batteries except that its

cells were rotated 90° from the usual orientation within the battery case to increase the surface area, and the negative plate was free of antimony. The 6-volt batteries were designed within the dimensional constraints of a standard golf-car battery. A 108-volt pack, weighing 1,080 pounds (490 kilograms), was assembled from the cells.

The increased ranges of the batteries were a result of greater discharge capacity with relatively little increase in weight and volume over conventional batteries. However, the batteries — particularly the nickel/zinc batteries — suffered from short cycle lives. The effect of charging procedure on battery efficiency, performance, and life expectancy remains unclear. The nickel/iron battery requires a substantial development effort before it can be integrated satisfactorily into vehicles. Packaging the circulating electrolyte system and handling the large volume of hydrogen generated during charging warrant special attention.

This work was done by Robert A. Conover of Caltech for NASA's Jet Propulsion Laboratory. To obtain a copy of the report, Circle 17 on the TSP Request Card.
NPO-15142

Computer Programs

These programs may be obtained at very reasonable cost from COSMIC, a facility sponsored by NASA to make new programs available to the public. For information on program price, size, and availability, circle the reference letter on the COSMIC Request Card in this issue.

Theoretical Investigation of Dielectric Horn Antennas

Dielectric horns offer advantages over conventional metal horns.

A mathematical model applicable to both solid and hollow dielectric horn antennas has been implemented in a computer program. Conventional hollow metal horns have several disadvantages. Metal horns are difficult to fabricate at short wavelengths because the interior walls must be very smooth for efficient operation and the conducting properties

of metal tend to deteriorate with increasing frequency. In addition to simply avoiding the disadvantages of hollow metal horns, dielectric horns appear to provide some unique advantages such as significant improvements in directivity. This computer program permits the user to investigate the potential of various dielectric-antenna designs.

Some of the antenna performance characteristics of chief interest, such as directivity and side-lobe levels, follow from the electromagnetic radiation pattern. Also, that pattern in itself is of interest. As a central part of the mathematical model, general formulas for the

electromagnetic radiation were derived and applied in the computer program.

Input parameters consist of frequency, relative permittivity, relative permeability, and horn dimensions. Horn flare may be specified as E-plane, H-plane, or pyramidal; and either the TM or TE mode aperture fields may be selected. Choices of polarization include X-directed electric field, Y-directed electric field, theta-

directed electric field, and radially-directed Poynting vector. For parametric studies, the user can indicate that one of the input parameters is to be varied over a specified range by specified increments. Output includes radiation pattern and directivity data. Printer plots can be generated to display the radiation patterns and directivity.

This program is written in FORTRAN IV

for interactive execution and has been implemented on a DEC VAX-series computer. The program was developed in 1983.

This program was written by Jeremy K. Raines of Raines Engineering for Goddard Space Flight Center. For further information, Circle A on the COSMIC Request Card. GSC-12876

MiniBriefs describe NASA innovations and reports in an abbreviated format. Readers desiring additional information on these items should request the Technical Support Packages (TSP's), available in most cases, which can be obtained by using the TSP Request Card at the back of this issue.

Reducing Stepping-Motor Power Consumption

An input circuit design reduces the constant power consumption in stepper motors.

Direct-current stepping motors used in computer peripherals, process control, and precision remote-positioning equipment constantly dissipate power and create heat even when not moving. A circuit design energizes the stepper motor only when pulses are present on the control input. When input pulses occur, a buffer circuit transmits them to a pulse detector that produces a logic 1 output. This output enables AND gates to transmit the sequence information to the output transistors. When the input pulses cease, the pulse detector produces a logic 0 output, thereby disabling the AND gates and cutting off the input transformers.

This work was done by Charles J. Williams of The Perkin Elmer Corp. for Marshall Space Flight Center. For further information, Circle 18 on the TSP Request Card.

Inquiries concerning rights for the commercial use of this invention should be addressed to the Patent Counsel, Marshall Space Flight Center [see page A5]. Refer to MFS-25119.

Detecting the Polarity of Lightning Strikes

Strike geometries can be reconstructed.

A recording technique using an audio tape recorder determines the polarity of lightning discharges. Measurements of both the polarity and the lightning-

induced currents are necessary to characterize lightning strikes. This information is important in the design of lightning-protection equipment for powerlines and other exposed systems.

The technique involves recording the strike, then superimposing a 500-Hz signal over the magnetized tape by disabling the bias in the tape-recorder heads or by using an external oscillator. When the tape is played back, the superimposed signal cancels portions of the original recording to produce a waveform that clearly indicates N or S magnetization.

This work was done by Richard L. Grumm of Caltech for NASA's Jet Propulsion Laboratory. For further information, Circle 19 on the TSP Request Card.

NPO-16063

Calculating Strain Relief in Electronic-Component Leads

Thermomechanical design increases reliability.

Stress/strain formulas applicable to the design of electronic-component leads have been compiled in a report that is now available. Such things as factors of safety and whether or not a lead is likely to fail in service can be determined in advance. The formulas can be used to analyze the weak links in other thermomechanical systems as well.

A lead that is either straight or bent to provide strain relief is mathematically approximated by one or more straight segments, the behavior of which is described by beam- and column-type stress and strain equations. The effects of expansion, contraction, and solder creep are calculated for temperature

variations in soldering and in operation. The set of formulas is simple enough to be solved on a programable hand-held calculator.

This work was done by Henri Snytsheuvl of TRW, Inc., for Johnson Space Center. To obtain a copy of the report, Circle 20 on the TSP Request Card.

MSC-20416

Temperature Compensation for a Frequency-Modulated Oscillator

Carrier frequency and deviation ratio are maintained nearly constant.

Both the carrier frequency and the deviation ratio of a frequency-modulated oscillator are maintained nearly constant by a temperature-compensating circuit. Temperature-induced changes in circuit inductances and capacitances that would ordinarily alter the carrier frequency are compensated by feeding the varactor dc bias through a resistive voltage divider that includes a temperature-sensitive resistor.

Because the relative capacitance change per unit modulating voltage changes with the bias, the frequency deviation per unit modulating voltage would normally change also. To compensate for this effect, the modulating signal is also fed through a temperature-sensitive resistive attenuator.

This work was done by Robert H. Hesse of TRW, Inc., for Johnson Space Center. For further information, Circle 21 on the TSP Request Card. MSC-20556



Solid-State Latching Relay

It remains latched and immune to noise for a timed interval.

A latching relay requiring only a single coil is activated by a trigger pulse and remains latched for a timed interval during which it is immune to additional trigger pulses and noise. After the interval, a second trigger signal deactivates the relay. The circuit includes a relay with double-pole/double-throw contacts, a silicon-controlled rectifier, a transistor, and a few passive components. The latch time constant is set by an RC circuit at the trigger input.

This work was done by Colonel W. T. McLyman of Caltech for NASA's Jet Propulsion Laboratory. For further information, Circle 22 on the TSP Request Card.
NPO-15028

Pulsed-Current Transducers

A diode circuit linearizes the output of pulsating dc transducers.

Electric power conditioning circuits in computers and electric-vehicle drive systems frequently depend on monitoring pulsating dc. A small diode circuit linearizes the output of transducers used to measure these currents. The circuit consists of a diode in series with a sensing resistor placed across the secondary winding of a transducer transformer. Since the dc component cannot be transferred from the primary coil to the secondary coil, core saturation effects are cancelled, producing linear output.

This work was done by Satoshi S. N. Nagano of Caltech for NASA's Jet Propulsion Laboratory. For further information, Circle 23 on the TSP Request Card.
NPO-14048

Platinum-Resistor Differential Temperature Sensor

It has an accuracy of 0.01° C.

Platinum resistance elements are used in a bridge circuit for measuring the temperature difference between two

flowing liquids. Temperature errors with the circuit are less than 0.01° C over a range of 100° C. The platinum resistors form one arm of the bridge. Fixed resistors are placed in the other arm. A temperature difference between the elements in the variable arm results in a bridge imbalance voltage, which is amplified and calibrated linearly against temperature differential. The circuit has been used with a continuous-flow calorimeter for a 20-kW microwave transmitter.

This work was done by Richard B. Kolbly and Michael J. Britcliffe of Caltech for NASA's Jet Propulsion Laboratory. For further information, Circle 24 on the TSP Request Card.
NPO-15666

Determining the Life Expectancy of Photovoltaic Systems

Environmental tests yield data that help to improve this life expectancy.

Several different kinds of environmental testing are used to determine the adequacy of photovoltaic systems, their modules, and their materials to survive in real environments. The tests include outdoor testing of systems, real-time and accelerated outdoor testing of modules and materials, and laboratory testing of modules and materials. In combination, these tests identify key environmental factors and design features that could affect the system life expectancy.

Real-time and accelerated outdoor exposure testing provides a data base for determining the combinations of environmental factors and operating configurations that are most damaging. Laboratory tests, especially temperature cycling, humidity cycling, and cyclic pressure loading, are useful in detecting design, process, and workmanship deficiencies.

The effects of weathering, for example, are the worst in hot, humid environments; cold, dry environments are the most benign. System optical transmission, on the other hand, suffers most in humid, polluted environments with little rain.

This work was done by Alan R. Hoffman, John S. Griffith, and Peter Jaffe of Caltech for NASA's Jet Propulsion Laboratory. For further

information, Circle 25 on the TSP Request Card.
NPO-15683

Improved Optical Keyboard

Improved optical keyboard design uses laminations for each column of keys.

Optical keyboard surfaces used in typewriters, computer terminals, and telephones can be inexpensively fabricated using a stack of printed-circuit cards set in a laminate. The internal laminations carry all illuminating and sensing light conductors to the keys. One lamination can be used for each column of keys. When an operator's finger is placed above a particular key, an internal light beam is reflected back into a sensing photoconductor that determines which key has been covered.

This work was done by Robert S. Jamieson of Caltech for NASA's Jet Propulsion Laboratory. For further information, Circle 26 on the TSP Request Card.

Inquiries concerning rights for the commercial use of this invention should be addressed to the Patent Counsel, NASA Resident Office-JPL [see page A5]. Refer to NPO-15132.

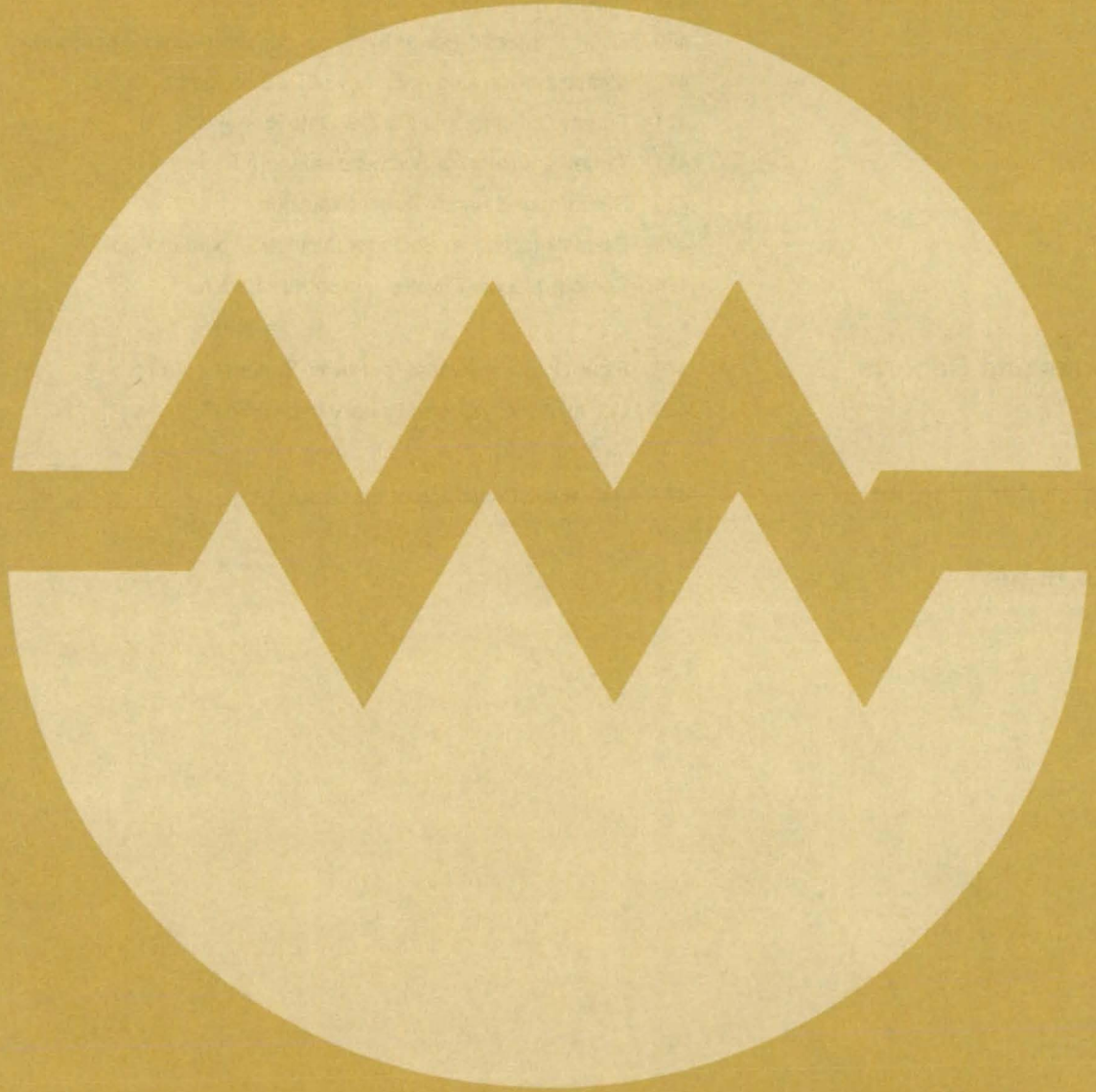
Hall-Effect Ground-Fault Interruptor

A ground-current detector has 100-mA sensitivity.

A tested ground-fault interruption circuit utilizing a Hall-effect device to sense differential current in a magnetic core trips and opens a circuit. The Hall-effect sensing element detects dc magnetic flux caused by current imbalance and feeds an operational amplifier that energizes a relay to open the circuit. Although the device currently reacts upon a simulated 100-mA fault to ground, modified circuits can be built with thresholds considerably less than 100 mA.

This work was done by Louis Okin of Underwriters Laboratories, Inc., for NASA's Jet Propulsion Laboratory. For further information, Circle 27 on the TSP Request Card.
NPO-15915

Electronic Systems



Hardware, Techniques, and Processes

- 467 Direct-Photon-Detection Communications
- 468 Estimates of Small Signal/Noise Ratios
- 468 Proximity Indicator for Remote Manipulator
- 469 Controlling Solar-Power Systems With Distributed Processors
- 470 Measuring Tracking Accuracy of CCD Imagers
- 471 Priority Queuing on a Parallel Data Bus
- 471 Target Simulator for Synthetic-Aperture Radars
- 472 Synchronized Radar-Target Simulator
- 473 Estimating Doppler Shifts for Synthetic-Aperture Radar
- 474 Contour-Mapping Synthetic-Aperture Radar

Books and Reports

- 476 Fiber-Optic Equipment for Power-System Control
- 476 Convolutionally-Coded Unbalanced QPSK Systems

Computer Programs

- 477 Interactive Digital Signal Processor

MiniBriefs

- 477

Direct-Photon-Detection Communications

Over 2.5 bits are carried by each photon, with no heterodyning at the receiver.

NASA's Jet Propulsion Laboratory, Pasadena, California

An optical communications system under development is based on direct detection of photons rather than on heterodyning of the carrier with a local oscillator. It is expected to transmit over 2.5 bits of information per photon, with its ultimate efficiency limited only by background noise. Heterodyne systems, in contrast, have a theoretical maximum efficiency of only 1.44 bits per photon, a limit imposed by the quantum uncertainty principle.

The direct-detection system uses a single laser source, pulse-position modulation, and Reed-Solomon coding to protect against burst errors. A conventional photomultiplier tube is the receiver.

The principle of transmitting bits of information per individual photon is shown in Figure 1. A time interval of t seconds is divided into 256 adjacent slots of length $t/256$ seconds. Every t seconds, an optical pulse is placed in one of the 256 slots. During the other 255 slot times, the transmitter is turned off. This modulation format is called 256-ary pulse-position modulation.

Since $256 = 2^8$, the location of the pulse can be specified by an 8-bit word. Assuming that each pulse contains (at the receiver) 3 photons of energy, 8 bits of information can be conveyed with only 3 photons of energy, for a power efficiency of 2.67 bits/photon. In actuality, the number of photons in an optical pulse is a random variable, governed by the quantum statistical nature of the laser source.

A block diagram of the optical communications system is shown in Figure 2. The transmitter contains a gallium arsenide injection laser, and the receiver uses a photomultiplier tube. The GaAs laser diode is a single spatial mode device operating at $0.85 \mu\text{m}$. The light emitted from the laser is passed through some elementary optics.

At the receiver, the attenuated optical signal is applied to the photomultiplier tube that has a high internal gain (10^6), a quantum efficiency in excess of 20 percent, and with moderate cooling, an extremely low dark current. To eliminate stray light, all of the optical components are placed in a dark enclosure.

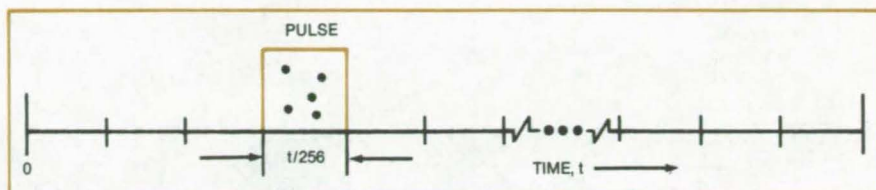


Figure 1. In the **Signal Format for Pulse-Position Modulation**, a time interval of t seconds is divided into 256 adjacent slots of duration $t/256$. Every t seconds, an optical pulse is placed in one of the 256 slots.

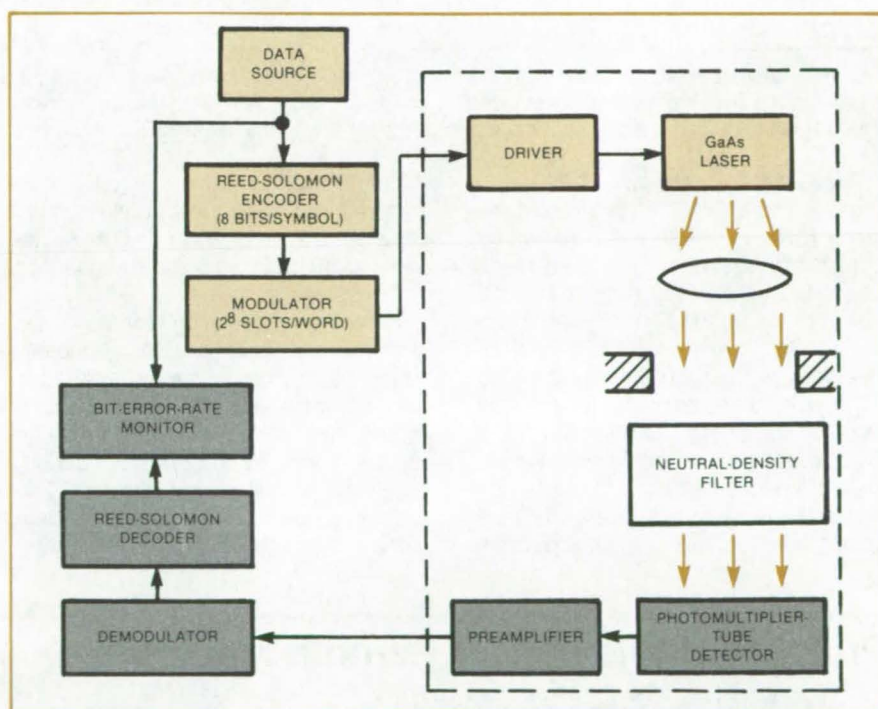


Figure 2. The **Optical Communications System** has an efficiency of 2.5 bits per detected photon, using direct photon detection and pulse-position modulation with Reed-Solomon encoding to improve the reliability of the channel against burst errors. Originally developed for deep-space applications, the technology is applicable to terrestrial communications as well.

Surrounding the optical components is the modulation and coding hardware. The laser diode is driven by a 256-slot/word modulator that decides, based on an 8-bit input word, into which slot the pulse should be placed and then provides a current pulse during that slot to turn on the laser. The inverse of this process is applied to the photomultiplier output to re-create the 8-bit word. To improve the performance of the system, an 8-bit Reed-Solomon code surrounds the modulation portion of the system. The encoder considers 8-bit segments of the

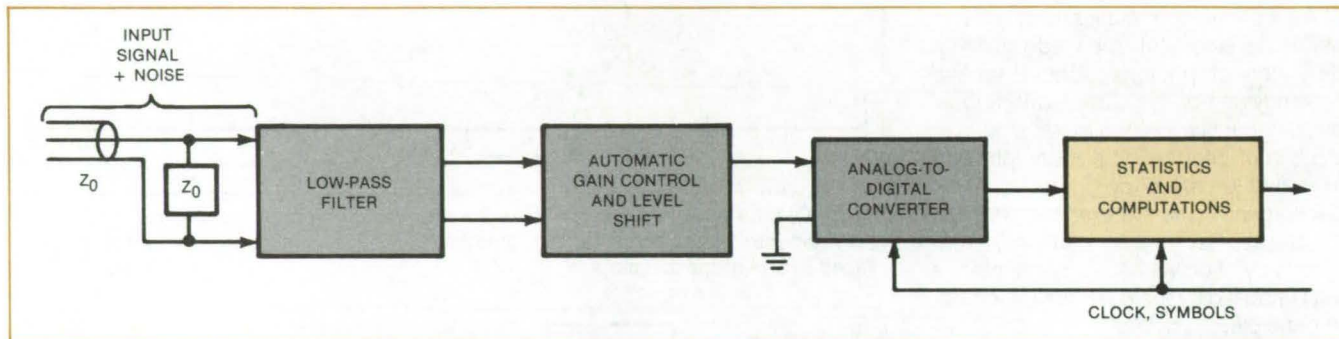
incoming (binary) data stream as individual (generalized) symbols and then performs error correction coding over strings of these generalized symbols. The data streams supplied to the encoder and delivered from the decoder are then compared for an overall bit-error-rate measurement.

This work was done by James R. Lesh and Joseph Katz of Caltech for NASA's Jet Propulsion Laboratory. For further information, Circle 28 on the TSP Request Card.
NPO-15905

Estimates of Small Signal/Noise Ratios

A split-symbol correlation technique improves precision.

NASA's Jet Propulsion Laboratory, Pasadena, California



A **Signal/Noise Ratio Meter** measures the ratio of signal power to noise power in an input that contains both signal and noise. The signal and noise are first filtered and normalized in analog circuitry, then digitized and sampled. The performance of the SNR meter is determined by the statistical algorithm chosen for the analysis of the samples.

A correlation technique promises to improve the estimation of signal/noise ratios (SNR's) in telemetry and other weak-signal systems. For SNR's much less than 1, the measurement time required to obtain the SNR to a given accuracy increases asymptotically as the inverse square of the SNR. In the best previous method, the measurement time grows as the inverse fourth power of the SNR, resulting in significantly longer measurement times.

In an SNR meter of the new type (see figure), the input signal (including noise)

is conditioned by analog circuitry, then digitized and sampled at an even multiple of the known symbol rate. The digital samples are then processed by standard statistical techniques.

In the new correlation technique, the symbol period is split into two nonoverlapping subsymbol intervals, the durations of which are fractions of the total symbol period. Normally, the fractions are each one-half of the symbol period, but this does not have to be the case. The cross-correlation of n digitized voltage samples in the pair of subsymbols is then

calculated. These cross-correlations are then used to determine the SNR. Statistically, the improvement in accuracy is due to a reduction in the variance of SNR as compared with variances obtained with previous techniques. The improvement can be 100 times or more at low signal levels.

This work was done by Larry D. Howard of Caltech for NASA's Jet Propulsion Laboratory. For further information, Circle 29 on the TSP Request Card.

NPO-15653

Proximity Indicator for Remote Manipulator

The operator receives a sensation of depth and orientation.

NASA's Jet Propulsion Laboratory, Pasadena, California

A display indicates the pitch, yaw, and distance of a remote manipulator with respect to an object to be grasped. It displays numerical values and a bar-graph simulation of the position and orientation of the hand (see figure). When the errors in position and orientation are small enough to ensure a successful grasp, the unit alerts the operator with audible and visible signals.

The display unit is intended for a four-claw hand. The hand includes four proximity sensors that measure the positions

of the claws relative to an object. The sensors feed the position data continuously to a microprocessor, which controls the display.

The numerical display presents the error information in three sets of numbers, with a resolution of 0.5° for yaw and pitch and 0.254 centimeter for distance. As the hand moves toward the object, the display is continuously updated. Once the hand is within the grasp envelope, the green light goes on, and the operator starts the grasping se-

quence. In training, a switch on the unit can be thrown to evaluate the operator's performance: The unit displays values that prevailed at the moment the operator started the grasping sequence, even after the claw has grasped or otherwise moved.

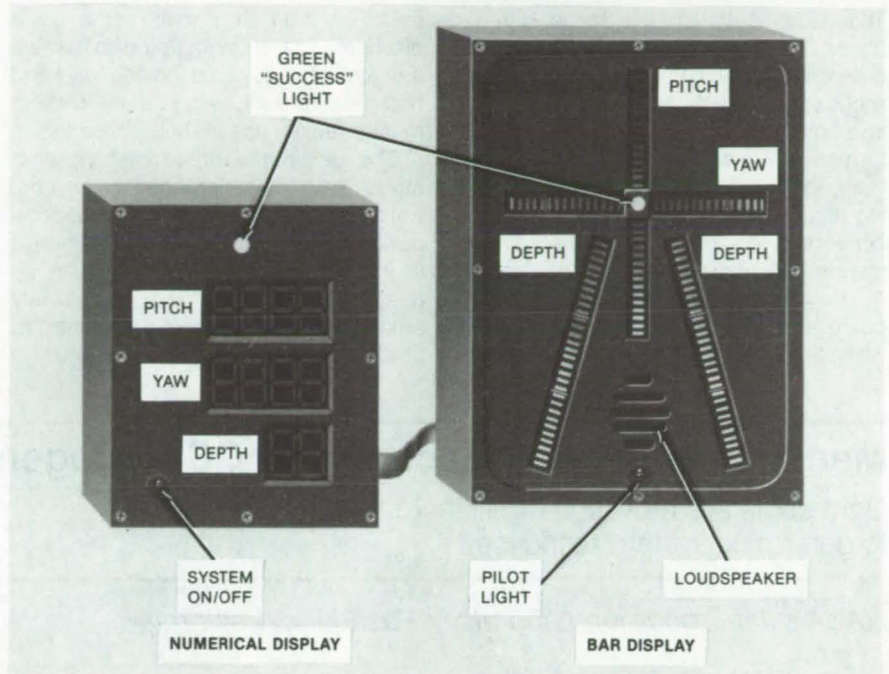
The bar-graph display is built of 10-element linear display bars. The lit element represents the magnitude of error. The distance error is displayed by two bars converging on the success light at the center, like railroad tracks

reaching to the horizon. These bars help the operator to visualize the third dimension in a two-dimensional display. The axes of the pitch and yaw bars also intersect at the center, thus focusing the operator's attention on a single goal point. The scale and resolution of the bar display are 0.508 centimeter per element in distance and 1° per element in pitch and yaw.

The bar-graph unit contains a small loudspeaker, which sounds at the same time the success lamp lights. The speaker also emits a short beep of a different frequency when the hand enters or leaves the zone in which proximity to the object can be sensed.

One of several success algorithms can be selected by a switch. The algorithms use different orientations of roll with respect to the yaw and pitch axes and various allowable error ranges.

This work was done by Antal K. Bejczy of Caltech for NASA's Jet Propulsion Laboratory. For further information, Circle 30 on the TSP Request Card. NPO-15064



Green "Success" Lamps are located on both the numerical and bar displays. The pitch, yaw, and distance bars are rows of yellow lamps.



Controlling Solar-Power Systems With Distributed Processors

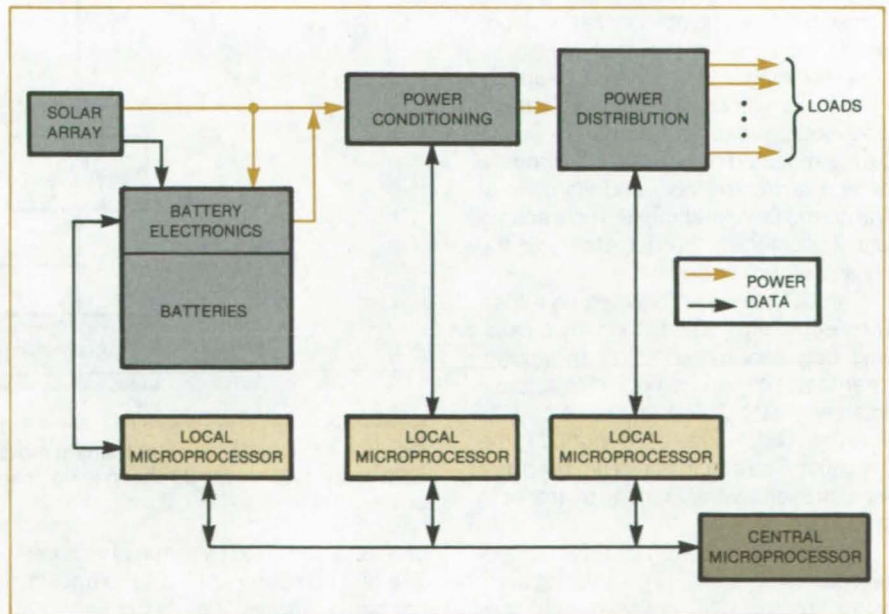
Many local processors offer advantages over a single central processor.

NASA's Jet Propulsion Laboratory, Pasadena, California

A system undergoing development at NASA's Jet Propulsion Laboratory uses distributed microprocessors to monitor and control a photovoltaic power system. The equipment increases the life expectancy and reliability of the power system and decreases costs. Originally designed for use in spacecraft, it can be adapted to vehicular, residential, and commercial solar and nonsolar power systems. Equipment of this type is especially desirable in systems with overall power levels above a few kilowatts.

A large photovoltaic/storage-battery power system needing this kind of control equipment typically includes a solar array, batteries, battery-protection electronics, a power-conditioning subsystem, and a power-distribution subsystem. The control equipment employs a central microprocessor for overall supervision and several additional microprocessors, each dedicated to one or more subsystems (see figure).

(continued on next page)



Monitoring and Control Operations are distributed among several microprocessors, all under the control of a central microprocessor. Distributed operations reduce the demands on both hardware and software.

The equipment manages loads, determines the power capacity of the array, determines battery charge, controls recharging, detects and corrects faults, and checks and diagnoses its own performance. Unique algorithms were developed for the equipment for monitoring relay positions, the status of power-conversion equipment, and the power margin (available power minus demand).

The equipment enhances overall power-system operation, especially when Sunlight is limited and power de-

mand is high. It prevents the over-discharging and damaging of batteries. It enables the design of solar arrays and batteries of reduced size by making most effective use of their capacities.

The distributed processing scheme offers several advantages over centralized processing. It reduces the computing load of the central micro-processor and allows software to be designed and developed in relatively small modules. It makes it easier to change and expand software to change

power levels, operating sequences, failure criteria, and other control features. It also decreases the risk of software errors affecting the overall equipment.

This work was done by Matthew S. Imamura and Robert L. Moser of Martin Marietta Corp. for NASA's Jet Propulsion Laboratory. For further information, Circle 31 on the TSP Request Card.
NPO-15101

Measuring Tracking Accuracy of CCD Imagers

Light spots are moved in small increments to determine system response.

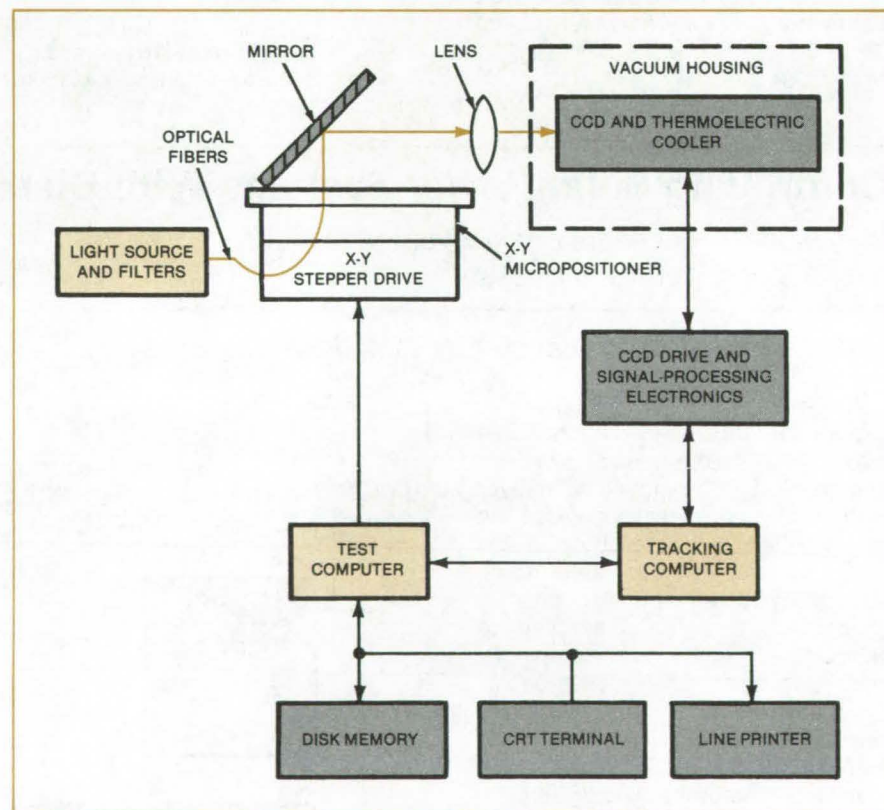
NASA's Jet Propulsion Laboratory, Pasadena, California

The tracking accuracy and resolution of charge-coupled device (CCD) imaging arrays are measured by an instrument originally developed for measuring the performance of a star-tracking telescope. It operates by projecting one or more artificial star images on the surface of a CCD array, moving the stars in controlled patterns, and comparing the star locations computed from the CCD outputs with those calculated from the step coordinates of a micropositioner (see figure). Since the star image is moved in steps of about $0.025 \mu\text{m}$, the tracking by a single pixel, or series of pixels, is measured in minute detail.

A star image is formed by a $25\text{-}\mu\text{m}$ aperture illuminated by $100\text{-}\mu\text{m}$ -diameter fiber-optic cable. The illuminated aperture is mounted on a two-axis micropositioning table. The heat and vibration of the quartz/halogen/tungsten light source and its cooler are thus isolated from the measurement apparatus.

The CCD array is mounted on a thermoelectrically-cooled, thermally isolating suspension system in a vacuum chamber, where it is cooled to approximately -40°C . The fast drive circuits for the CCD array are outside the chamber. The star image is directed by a lens through a window in the chamber to the CCD.

Two computers control the micropositioner and the CCD. The tracking computer controls CCD operation and converts the raw image data into star position measurements by calculating the centroid as the average of the pixel co-



Computer-Controlled Test Instrument moves a star image in precise increments across a CCD array. CCD pixels $30 \mu\text{m}$ on a side can track the moving image with an accuracy of one-hundredth pixel, or $0.3 \mu\text{m}$.

ordinates weighted by the pixel voltages. The test computer controls the tracking computer, moves the star image, and calculates the tracking accuracy from the differences between the measured and actual image coordinates.

This work was done by Richard H. Stanton and Edwin W. Dennison of Caltech for NASA's Jet Propulsion Laboratory. For further information, Circle 32 on the TSP Request Card.
NPO-15665

Priority Queuing on a Parallel Data Bus

Algorithms provide maximum service with a minimum number of wires.

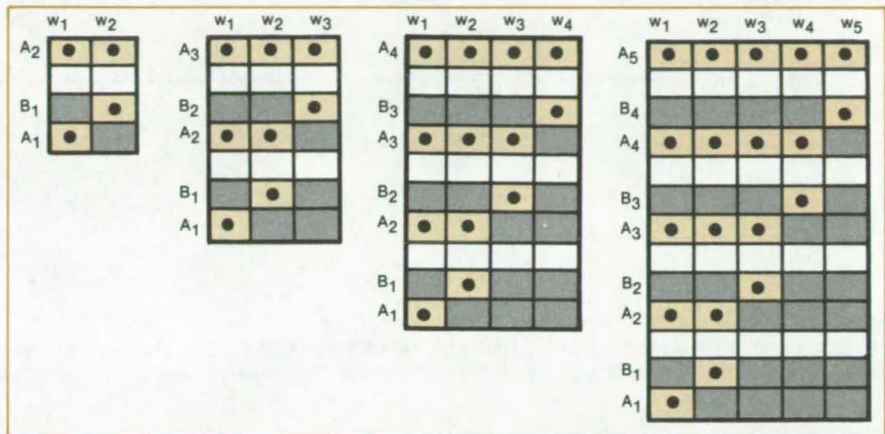
NASA's Jet Propulsion Laboratory, Pasadena, California

A queuing strategy for communications along a shared data bus minimizes the number of data lines while always assuring that the user of highest priority is given access to the bus. The new system handles up to 32 user demands on 17 data lines that previously serviced only 17 demands.

The problem solved by the strategy is defined as follows: It is assumed that m users have access to n wires along which they send one of three demands to a central terminal. User i can demand action A_i , action B_i , or no action. Each wire carries one bit of information (0 or 1) to the central terminal; namely, no user's signal is on that wire, or some user's signals are on that wire. The users may simultaneously apply demands to the n -line bus. It is the job of the central terminal to acknowledge the demand of the user of highest priority.

A black box for user i can be designed with buttons A_i and B_i causing two preselected choices of signals for the bundle of wires. Pushing neither button will contribute the Boolean zero; pushing A_i will send one Boolean word of n bits (not all 0); pushing B_i will send another Boolean word; and pushing A_i and B_i at once is prevented.

The central terminal is supposed to be able to "understand" every possible message it gets on the bundle of wires. Whatever Boolean word it gets, it must



These **Efficient Priority Codes** maximize the number of users on n wires, $n = 2, 3, 4,$ and 5 . The top-priority user is given one service request, while the other n users have a two-request capability. The rule for extension to m users on n lines is easily deduced from these illustrations.

identify the user of top priority in that word, as well as the demand of that user.

The strategy illustrated in the figure for up to five users can be generalized to m users. It allows each user two demands A_i and B_i — except for the top-priority user who has one demand A_i — and requires exactly m data lines.

In the illustration for four users, for example, users 1, 2, 3, and 4 are on four wires ($w_1, w_2, w_3,$ and w_4). Each wire is represented by a column in the figure. For each demand, there is a row representing the Boolean word of 4 bits that

the button impresses on the wires. Thus if user 3 pushes button B_3 , user 2 pushes button A_2 , and user 1 pushes button A_1 , then the word received at the central computer will be $w_1w_2w_3w_4 = 1101$. With this algorithm, it is easy to devise a decision tree that recognizes that top-priority user 3 is on the line and is specifically making demand B_3 .

This work was done by David E. Wallis of Caltech for NASA's Jet Propulsion Laboratory. For further information, Circle 33 on the TSP Request Card. NPO-15005

Target Simulator for Synthetic-Aperture Radars

The return signal contains range-curvature and Doppler-frequency information.

NASA's Jet Propulsion Laboratory, Pasadena, California

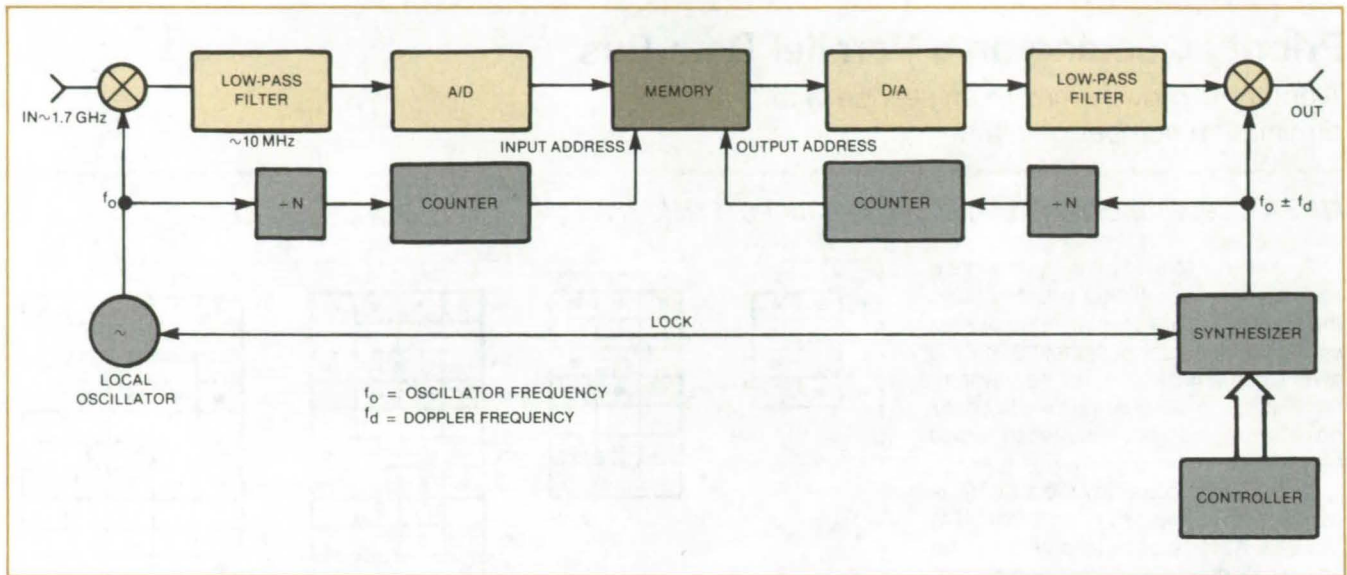
A proposed target simulator for testing synthetic-aperture radar (SAR) generates a return signal that contains range-curvature information in addition to Doppler-frequency information. Standard SAR testers simulate only the Doppler-frequency part of the return. Originally developed for testing space-

borne instruments, the target simulator should also be useful in terrestrial target-acquisition and over-the-horizon radars.

A block diagram of the proposed SAR target simulator is shown in the figure. The incoming radar signal is heterodyned down to video frequencies, converted to digital form, digitally time-

delayed, and converted back into an analog representation for subsequent up conversion. Simultaneously, a programmable frequency synthesizer, coherent with a local oscillator used for down conversion, provides the time-varying reference needed for up conversion.

(continued on next page)



In the proposed **Target Simulator for Testing Synthetic-Aperture Radars**, the radar transmitter output is received, mixed down to video frequencies, and passed through a variable digital delay. The delayed signal is mixed up to the original carrier frequency and transmitted back to the radar.

The output of the system is a delayed representation of the input at a frequency determined by the relationship between the fixed local-oscillator frequency and the instantaneous frequency of the synthesizer. Since the synthesizer can be programmed as desired, the output of the simulator can emulate the Doppler history of any point target.

The time delay generated by the target simulator is itself a function of time. This is required for complete simulation of a point target return. The mechanism for generating this time-varying delay uses a first-in/first-out (FIFO) memory

with input clocked at a rate proportional to the local oscillator frequency and with its output clocked at a rate proportional to the Doppler-shifted frequency. Thus, as the synthesizer changes frequency, the residence time of the digitized radar signal changes in precisely the manner required to simulate an SAR return.

The SAR target simulator can be used for bench testing, or it can be deployed on an antenna range to field-test the entire system. In the latter configuration, the target simulator is deployed down-range from the radar being tested. The radar antenna beam is rotated to simu-

late the motion of a point target traversing the real aperture of the SAR antenna. Thus, the phase and amplitude of the antenna are tested, as is the ability of the radar to reject azimuth ambiguities.

This work was done by Howard A. Zebker, Daniel N. Held, Richard M. Goldstein, and Thomas C. Bickler of Caltech for NASA's Jet Propulsion Laboratory. For further information, Circle 34 on the TSP Request Card.

Inquiries concerning rights for the commercial use of this invention should be addressed to the Patent Counsel, NASA Resident Office-JPL [see page A5]. Refer to NPO-15024.

Synchronized Radar-Target Simulator

A radar is presented with a test signal that varies with antenna motion.

Lyndon B. Johnson Space Center, Houston, Texas

An apparatus for testing a radar system generates signals that simulate the amplitude and phase characteristics of target returns and their variation with antenna-pointing direction. The antenna movement causes the equipment to alter the test signal in imitation of the behavior of a real signal that would be received during tracking.

The test equipment offers several advantages: An outdoor "roofhouse" test

range with a real target is unnecessary; test costs are lower because simpler facilities can be used; schedules can be compressed because the simulator equipment is ready to be used any time; and test data are more repeatable and reliable because the test environment is controllable.

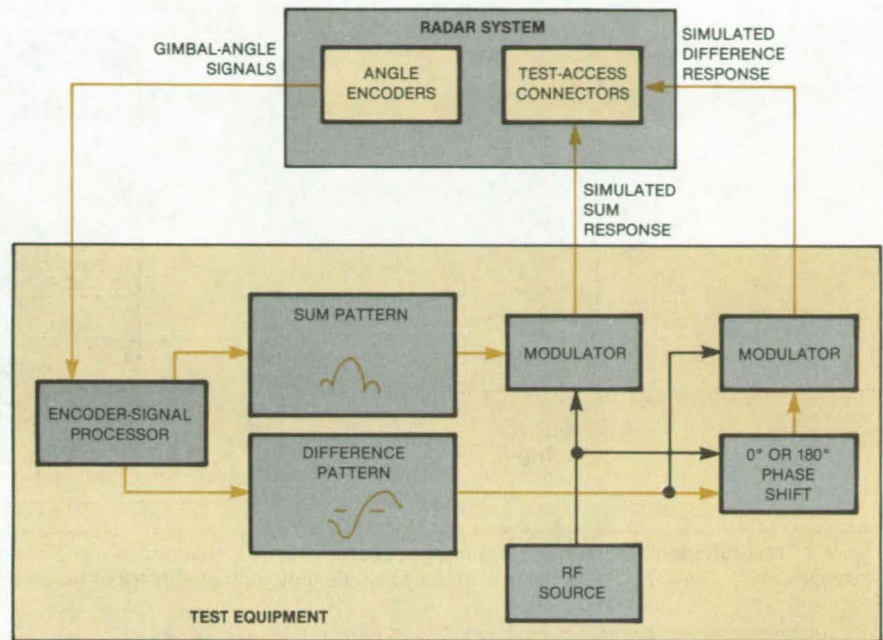
The simulated antenna pattern as a function of pointing direction is stored in advance in a random-access memory

(RAM), with the various memory locations representing different target boresight errors in increments of the 0.09° shaft-encoder resolution. The encoder outputs are processed (see figure) into absolute direction and direction relative to the target. The relative-direction data are used to address the RAM locations to obtain the sum and difference antenna responses.

The data are transmitted to modulators, which transform the data into changes in the radio-frequency signal simulating target reflections. The sum antenna response controls one modulator, and the difference antenna response controls the other. The difference branch contains an additional element: a 180° phase-shift component. This element allows the phase of the difference signal to be altered by 180° as needed.

The simulated signal is applied to the radar via test-access ports. The radar processes the signals to derive angle-error signals that control the repositioning of the antenna. The gimbal angle-encoder outputs change because of the antenna movement, and the tester-to-radar loop is closed.

This work was done by Bing C. Chin of Hughes Aircraft Co. for Johnson Space Center. For further information, Circle 35 on the TSP Request Card. MSC-20240



The Control Loop for Simulated Signals extends from a radar through a shaft-angle-encoder processor and a test-signal generator back to the radar.



Estimating Doppler Shifts for Synthetic-Aperture Radar

Return signals are preprocessed to compensate for motion.

NASA's Jet Propulsion Laboratory, Pasadena, California

The quality of synthetic-aperture-radar (SAR) imagery is enhanced by a pair of signal-processing techniques that compensate for the relative motion between the target and the vehicle. Combining vehicle trajectory data with radar-parameter and raw image data, these techniques generate Doppler estimates for use in constructing fully processed images.

In general, the relative phase between the vehicle and the target is continuously changing during the imaging period. To achieve the full resolution inherent in the SAR system, the echoes from successive radar pulses within the synthetic aperture are coherently added. This requires determination of the relative phase as a function of along-track time.

Using the known vehicle position and velocity along with the approximate measured boresight angles, a preliminary estimate is made of the target-to-vehicle position vector. From this vector and the velocity and acceleration with which it changes, preliminary estimates

are obtained for the Doppler-frequency shift, f_d , and the rate of change of the Doppler-frequency shift, \dot{f}_d . Then using the first two terms in the Taylor series for the phase history $\phi(t)$, the phase shift in the echoes from a target during a short time t is estimated from

$$\phi(t) - \phi(0) = 2\pi(f_d t + \frac{1}{2}\dot{f}_d t^2)$$

A test image is constructed using this initial estimate.

The technique for refining the f_d estimate is called "clutterlock." It is best used with a homogeneous target area (for example, ocean or desert) because it depends on the assumptions of symmetry in the azimuthal antenna-gain pattern and homogeneous scattering for each picture element across the azimuthal beam width.

The first step in the clutterlock algorithm is to process a portion of the image data into four tentative versions of that part of the image. Each version (called a "look") is generated with one-fourth of the available spectrum and with the preliminary estimates of f_d and

\dot{f}_d . Under the assumptions stated above, the Doppler spectrum must have equal energy on either side of the true Doppler centroid frequency, f_c . The lack of symmetry in the image energy about the assumed Doppler centroid is used to obtain a measure of the offset of f_d from f_c : The offset is given by

$$\Delta E = (E_1 + E_2 - E_3 - E_4) / E_t$$

where E_i = the mean image energy in the i th look and E_t = the total energy in the target area. The initial Doppler-frequency estimate is incremented and the process repeated to obtain a plot of ΔE vs. f_d (see Figure 1). The intersection of this plot with the line $\Delta E = 0$ gives the best estimate of the true f_d . (In the actual preprocessing system, an automatic regression calculation is made instead of a graphical plot.)

The autofocus technique for refining \dot{f}_d is best used on areas containing highly-reflective, well-defined targets (urban areas and mountain ranges, for example). The technique is based on the fact that a mismatch between the

(continued on next page)

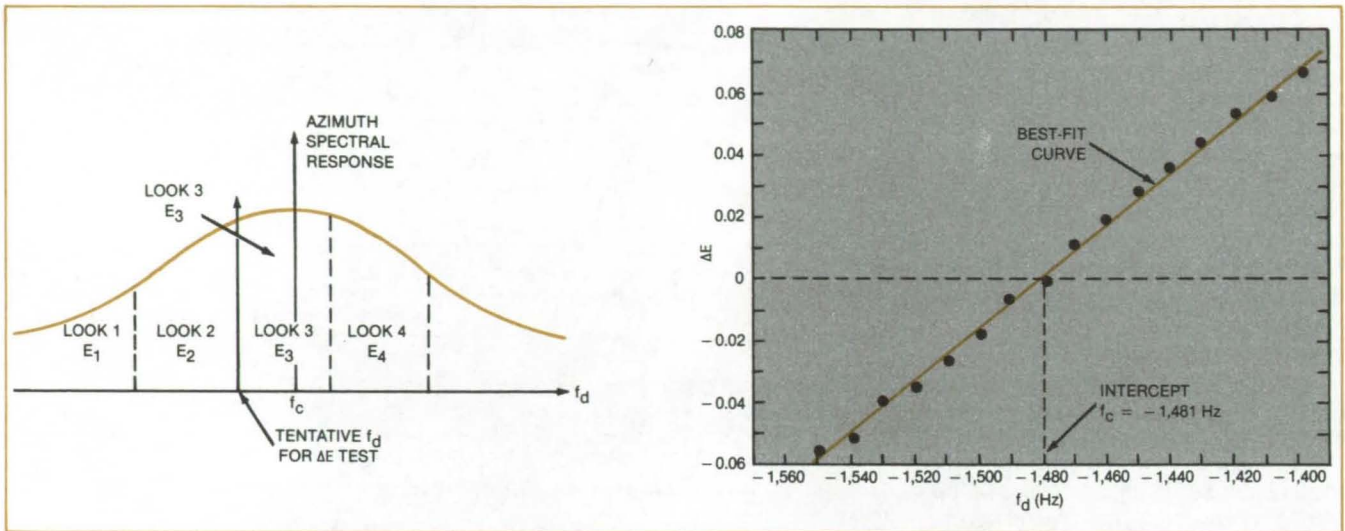


Figure 1. The **Clutterlock Technique** uses image spectral-energy measurements and a regression algorithm to obtain the best estimate of Doppler shift. The values shown here are for example only: Actual spectra differ among vehicle/target combinations.

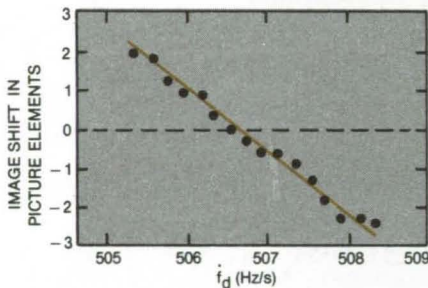


Figure 2. The **Autofocus Technique** uses linear regression: in this case, based on the cross-correlation of images. The best estimate of the rate of change of Doppler shift is the one that results in zero image offset (that is, zero misregistration of images). The \dot{f}_d values here are for example only.

estimated and true values of \dot{f}_d causes the misregistration of subsequent versions of the image and consequent blurring of the final image in the azimuthal direction.

Tentative images are prepared, each from a nonoverlapping portion of the spectral band using the preliminary estimate of \dot{f}_d . A line-by-line cross-correlation is made between two images, resulting in a correlation peak at some value of the azimuthal image shift

(measured in picture elements). The estimated \dot{f}_d is incremented and the process repeated several times to obtain a plot (or a linear-regression calculation) of shift vs. \dot{f}_d (see Figure 2). The intersection of this plot with the zero-shift line is considered the best estimate of \dot{f}_d .

This work was done by John C. Curlander of Caltech for NASA's Jet Propulsion Laboratory. For further information, Circle 36 on the TSP Request Card. NPO-15990

Contour-Mapping Synthetic-Aperture Radar

The phase difference between signals received by two antennas yields terrain height.

NASA's Jet Propulsion Laboratory, Pasadena, California

An airborne two-antenna synthetic-aperture-radar (SAR) interferometric system provides data that can be processed to yield terrain elevation as well as reflected-intensity information. Relative altitudes of terrain points can be measured to within an error of approximately 25 m.

The geometry of the SAR system is shown simplified in Figure 1. Two planar-array antennas are mounted 11.17 m

apart, one on the underside of each wing of the aircraft. At the two antennas, the arrival times of the echoes from one target point are slightly different because the range to the target point is slightly different from each antenna. The phase difference $\Delta\phi$ between the two signals varies with the look-angle θ and the average slant range R to the terrain point. Retaining the range and phase information through the entire receiving

and recording process makes it possible to compute the elevation of each element in the radar image.

The antennas are multiplexed via an antenna-selector switch (see Figure 2) to sample the echo signal first from one antenna and then the other on alternate signal pulses. The pulse-repetition rate ranges from 800 to 1,000 pulses per second: It is regulated according to the aircraft groundspeed so that the target

is illuminated by a constant number of pulses per unit distance traveled, thus keeping a constant along-track distance scale for all picture elements.

The received echoes are down-converted to video, digitized in two-dimensional vector form, and recorded with a high-density magnetic-tape recorder. On the ground, the data from the tape are processed with a digital correlator to extract the phase and intensity of each picture element as received by each antenna. The images from the two antennas are brought into registration, the phase difference information is extracted, and the altitude for each element is computed.

One effective way of displaying the terrain height is to use color. For example, the system has been used to map the Monterey Peninsula with six colors, each of which represents an altitude range of about 83 ft (25 m). The colors repeat at 500-ft (152-m) intervals. With further processing, the altitude data could be presented in such other forms as conventional equal-altitude topographical contour lines.

This work was done by Richard M. Goldstein, Edward R. Caro, and Chialin Wu of Caltech for NASA's Jet Propulsion Laboratory. For further information, Circle 37 on the TSP Request Card.

Inquiries concerning rights for the commercial use of this invention should be addressed to the Patent Counsel, NASA Resident Office-JPL [see page A5]. Refer to NPO-15939.

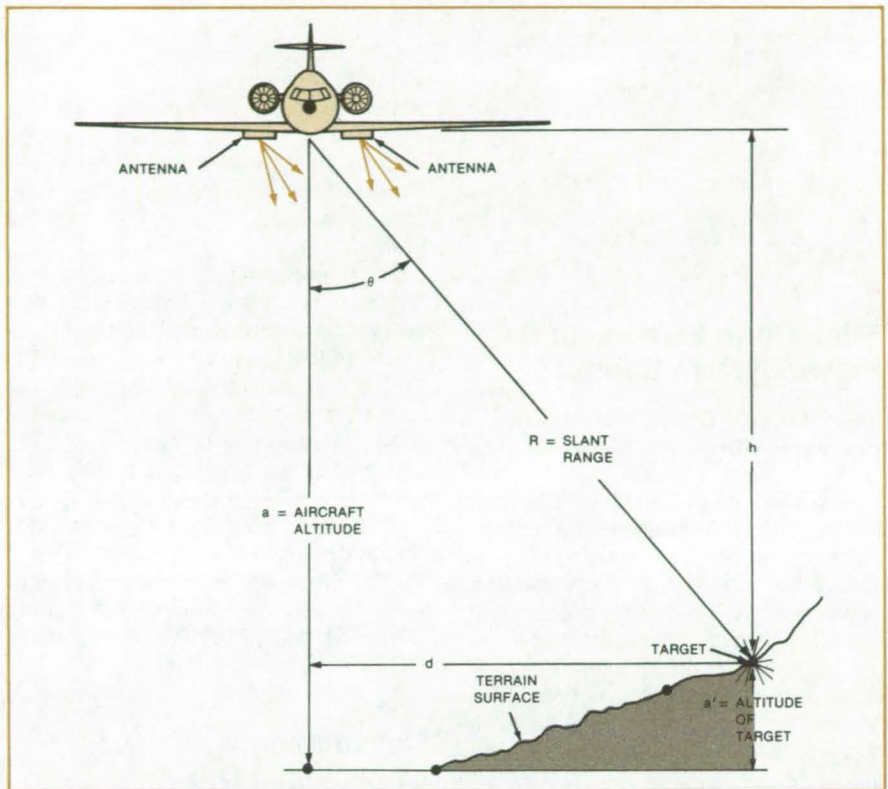


Figure 1. The Synthetic-Aperture-Radar Interferometer uses two multiplexed planar antenna arrays to obtain phase-difference information that can be processed to yield terrain altitude information.

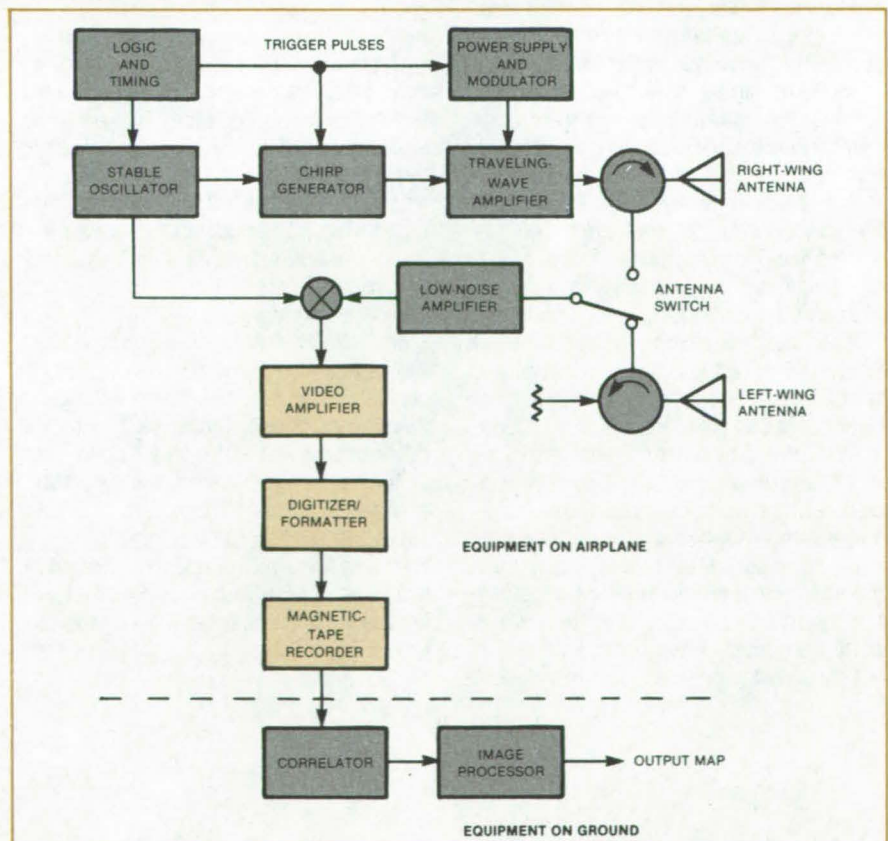


Figure 2. The Radar Transmitting, Receiving, and Data-Processing System consists mostly of standard synthetic-aperture-radar equipment. It differs from earlier systems in the use of two antennas and equipment to process phase-difference data into altitude data.

Books and Reports

These reports, studies, and handbooks are available from NASA as Technical Support Packages (TSP's) when a Request Card number is cited; otherwise they are available from the National Technical Information Service.

Fiber-Optic Equipment for Power-System Control

Digital control signals would be transmitted by light.

A report surveys the state of the art in fiber optics and explores the use of microprocessors communicating over optical fibers to control a complicated power system with many producing and consuming units. The power system of the study is that of a planetary spacecraft, and the fiber-optic technology is an extension of that now under development or used in military aircraft and ships.

The control system must operate automatically to assess power-system performance, to detect and correct equipment faults, and to manage loads. Fiber-optic equipment offers advantages for the transmission of the large amount of digital data needed to perform all these functions: Separate units can be electrically isolated if necessary; the number and mass are less than those of comparable wire connections, the susceptibility to electromagnetic interference is minimal, and the signal bandwidth (in glass fibers) can be as high as several hundred megahertz.

The study includes a cost/benefit analysis for equipping a breadboard spacecraft power system with digital fiber-optic controls instead of wire controls. Fiber optics were assumed to be used for communications between digital interface electronics and the transducers that monitor and control power, intercomputer data buses, and communications between the central power-system microcomputer and the spacecraft computer. Fiber-optic links were not assumed to be used for transmission

between units in proximity because they increase power consumption (0.1 to 0.2 W per link) and increase system complexity by requiring conversion between the various subsystem data streams and the serial bit transmission of the fibers.

According to the analysis, the mass of the fiber-optic system (including cables, connectors, transmitters, and receivers) would be 934 g, as compared to 3,596 g for the corresponding wire system. The transmitters, receivers, and parallel-to-serial encoders would consume 2.63 W. The cost of the fiber-optic system was estimated at \$72,300 (1982 prices).

This work was done by Arthur O. Bridgeforth and Lien C. Yang of Caltech for NASA's Jet Propulsion Laboratory. To obtain a copy of the report, Circle 38 on the TSP Request Card. NPO-15968

Convolutionally-Coded Unbalanced QPSK Systems

Bit-error rates are derived for three systems.

A recent report discusses the error-rate performance of three convolutionally-coded unbalanced quadrature-shift-keying (UQPSK) communication systems with noisy carriers that introduce crosstalk. The systems analyzed are unbalanced in the sense that each transmits two data streams with different bit rates and (in some cases) different powers.

In UQPSK, pulses of suppressed carrier signals are sent on one channel at phases of 0° and 180° with respect to the carrier phase reference and on the other channel at 90° and 270° . In each of the systems analyzed, the (0° , 180°) channel (channel I) has a high data rate, while the (90° , 270°) channel (channel Q) has a low data rate. Each system includes a bipolar Costas loop with a hard-limited inphase channel to track the carrier phase.

In the first system, the data streams in the I and Q channels are convolutionally coded independently and operate over a discrete-time UQPSK channel with Viterbi decoders. The two convolutional codes have different constraint lengths and different code rates.

Expressions for the bit-error rate in terms of the loop phase error and the symbol and noise energies are derived for the case of a large ratio between the data rates of the two channels. At first it is assumed that the ratio is an integer and that the two channels are synchronized. However, in the limit of a large ratio, the bit-error rates derived hold whether or not the two channels are synchronized.

In the second system, the data stream in channel I is convolutionally coded, while that in channel Q is not coded. It is advantageous to use such a system where power is limited and it is necessary to minimize the complexity of equipment.

In the third system, both the I and Q channels are coded by a common rate-1/2 coder with a constraint length of 3. It turns out that better performance can be achieved in this system by assigning one-third of the total power to the I channel and two-thirds to the Q channel. The receiver should include an integrate-and-dump circuit with a sampling rate equal to the reciprocal of the channel symbol duration in the I channel and should include a similar circuit with twice this sampling rate for the Q channel.

A Viterbi decoder designed for a constraint-length-3, rate-1/3 best convolutional code should follow the integrate-and-dump operation. The error-rate performance of this system is equivalent to that of a constraint-length-3, rate-1/3 code with only the bandwidth required for a rate-1/2 code but with a 0.3-dB gain in performance.

This work was done by Dariush Divsalar and Joseph H. Yuen of Caltech for NASA's Jet Propulsion Laboratory. To obtain a copy of the report, Circle 39 on the TSP Request Card. NPO-15566

Computer Programs

These programs may be obtained at very reasonable cost from COSMIC, a facility sponsored by NASA to make new programs available to the public. For information on program price, size, and availability, circle the reference letter on the COSMIC Request Card in this issue.

Interactive Digital Signal Processor

Analysts can "experiment" with various operations for information extraction.

The Interactive Digital Signal Processor, IDSP, consists of a set of time series analysis "operators" based on the various algorithms commonly used for digital signal analysis. The processing of digital time series to extract information is usually achieved by the application of a number of fairly standard operations. Also, it is often desirable to "experi-

ment" with various operations and combinations of operations to explore their effect on the results. IDSP is designed to provide an interactive and easy-to-use system for this type of digital time series analysis.

The IDSP operators can be applied in any sensible order, even recursively, and can be applied to single time series or to simultaneous time series. IDSP is being used extensively to process data obtained from scientific instruments on board spacecraft. IDSP is also an excellent teaching tool for demonstrating the application of time series operators to artificially generated signals.

IDSP currently includes 31 standard operators. Processing operators provide for Fourier-transform operations, design and application of digital filters, and eigenvalue analysis. Additional support operators provide for data editing, display information, graphical output, and batch operation. User developed operators can be easily interfaced with the system to provide for expansion and

experimentation. Each operator application generates one or more output files from an input file. The processing of a file can involve many operators in a non-trivial application. IDSP maintains history information as an integral part of each file so that the user can display the operator history of the file at any time during an interactive analysis.

IDSP is written in VAX FORTRAN 77 for interactive or batch execution and has been implemented on a DEC VAX-11/780 operating under VMS. The IDSP system generates graphics output for an HP2648A graphics terminal but should be adaptable to other graphics systems. The IDSP system was developed in 1982 and augmented with additional operators and updated documentation in 1984.

This program was written under direction of William H. Mish of Goddard Space Flight Center. For further information, Circle B on the COSMIC Request Card.
GSC-12862



MiniBriefs describe NASA innovations and reports in an abbreviated format. Readers desiring additional information on these items should request the Technical Support Packages (TSP's), available in most cases, which can be obtained by using the TSP Request Card at the back of this issue.

Short-Range Digital Optical Links

Concept is based on multiple optoelectronic chips.

A proposed network of semiconductor lasers could be used for communication and radar. Originally proposed for space vehicles docking at a space station, the network includes small integrated transmitters, receivers, and data processors placed at strategic points on the station and the vehicles. Within the station or vehicles, the transceiver/processor chip would be interconnected by optical fibers. Laser beams would carry the signals through free space between the station and the vehicles.

The network would allow voice communication. It would track vehicles approaching the station. It would furnish range and angle information to a space vehicle so that it can navigate to the station and dock there. Coverage would be

continuous. If the path between a chip on the station and a chip on a vehicle becomes blocked by a structural part, the network will instantly switch to an alternative path.

This work was done by Richard M. Dickinson of Caltech for NASA's Jet Propulsion Laboratory. For further information, Circle 40 on the TSP Request Card.
NPO-15999

Communication Program Emulates Switchboard

Software allows microprocessor systems to communicate with external devices.

A general-purpose input/output management program acts as a switchboard and allows microprocessing development systems (MDS) to communicate with outside electronic mail networks and information transfer via a modem. This software program called

MODEM, written in PL/M-80 and designed to execute the program in the ISIS-II environment, converts the MDS station into an interactive terminal capable of communicating with a host computer or another MDS. The flexible program is completely menu-driven, and all the local operator commands require only a single keystroke. Both ASCII and non-ASCII data may be transferred.

This work was done by D. Ron of Rockwell International Corp. for Marshall Space Flight Center. For further information, Circle 41 on the TSP Request Card.
MFS-19917

Digital Ratiometer

Ratios of two digital or analog signals are measured and recorded.

Double-beam spectrophotometers and other two-data source instruments frequently require the comparison of the
(continued on next page)

outputs of two channels. A small, low-cost comparator with 24-bit precision yields a ratio signal from a pair of analog or digital input signals. Arithmetic logic chips (bit-slice) sample two 24-bit analog-to-digital converters approximately once every millisecond and accumulate them in two 24-bit registers. Up to 4,095 individual samples can be acquired. Upon a completion of the sampling and integration, the contents of the two registers are normalized and a 24-bit quotient generated in about 5 microseconds. The result is recorded on a disk that is computer compatible. The approach is readily modified to arbitrary precision.

This work was done by Reinhard Beer of NASA's Jet Propulsion Laboratory. For further information, Circle 42 on the TSP Request Card.

Inquiries concerning rights for the commercial use of this invention should be addressed to the Patent Counsel, NASA Resident Office-JPL [see page A5]. Refer to NPO-15396.

Bistatic Synthetic-Aperture Radar

A spaceborne transmitter and ground-based receiver are required.

A report available on request describes a synthetic-aperture radar that uses a spaceborne transmitter and a ground (or airborne) receiver to obtain imaging data in real time. The spaceborne transmitter illuminates the region around the receiver. The receiver, which locks coherently on the transmitter local oscillator, detects the bistatically scattered energy and generates an image of the region surrounding the receiving station. Such a system would have applications in vessel navigation in open seas and polar ice regions, monitoring of wave and ice patterns near shores and oil platforms, and continuous monitoring of a region with a repeat time of few hours or less.

This work was done by Charles Elachi, Richard Goldstein, and Daniel Held of Caltech for NASA's Jet Propulsion Laboratory. To obtain a copy of the report, "Spaceborne Bistatic Synthetic Aperture Radar," Circle 43 on the TSP Request Card. NPO-15619

Imaging System for High-Temperature Processes

Borescope/camera images objects in furnaces.

A borescope/camera arrangement is used for viewing the silhouette image of a specimen levitated inside a furnace. The system can be adapted for monitoring other processes in enclosures.

A stainless-steel borescope, containing a series of lenses, views the sample through a sapphire window in the furnace wall. An all-quartz optical fiber projects light from an external halogen lamp on a spherical mirror to silhouette the sample on the borescope aperture. Lenses relay the image into a miniature vidicon camera.

This work was done by Thomas A. Glavich of Caltech for NASA's Jet Propulsion Laboratory. For further information, Circle 44 on the TSP Request Card. NPO-15945

Quicker Selection of CCD Images

A microprocessor limits analog-to-digital conversion to image areas of interest.

Electronic telescopes, air-traffic control systems, and object locators for robots utilize charge-coupled devices (CCD) as imaging detectors. In a typical application of CCD imaging, only a small portion of the total field of view is of direct interest. A programmed microprocessor saves time by restricting the analog-to-digital conversion process to only the desired key pixels of the CCD target image. The image region of interest can be selected in order of brightness by use of threshold detectors and their location coordinates stored by the microprocessor for tracking. Unwanted portions are rapidly scanned through.

This work was done by Phil M. Salomon and Kalman Smilowitz of Caltech for NASA's Jet Propulsion Laboratory. For further information, Circle 45 on the TSP Request Card.

This invention has been patented by NASA (U.S. Patent No. 4,430,673). Inquiries concerning nonexclusive or exclusive license for its commercial development should be addressed to the Patent Counsel, NASA Resident Office-JPL [see page A5]. Refer to NPO-15345.

High-Resolution Charge-Coupled-Device Camera

An 800-by-800-element sensor and a lens of 1.5-m focal length are used in a camera with 0.01-mrad resolution.

A camera based on an 800-line-by-800-element solid-state charge-coupled-device (CCD) image sensor was originally designed for the Jupiter-orbiting Galileo satellite. The CCD is mounted in a tantalum radiation shield and is radiatively cooled to $-60^{\circ} \pm 0.2^{\circ} \text{C}$. Its spectral range extends from 0.4 to 1.1 μm . The camera head, comprising the sensor assembly, a shutter, an eight-position filter wheel, and electronics, is coupled to a 1.5-m-focal-length, $f/8.5$, catadioptric Cassegrain telescope. The field of view is 8.1 by 8.1 mrad. Exposure times range from 0.00417 to 51.2 s.

This work was done by Maurice C. Clary, Kenneth P. Klaasen, Leonard M. Snyder, and Peter K. Wang of Caltech for NASA's Jet Propulsion Laboratory. For further information, Circle 46 on the TSP Request Card. NPO-15086

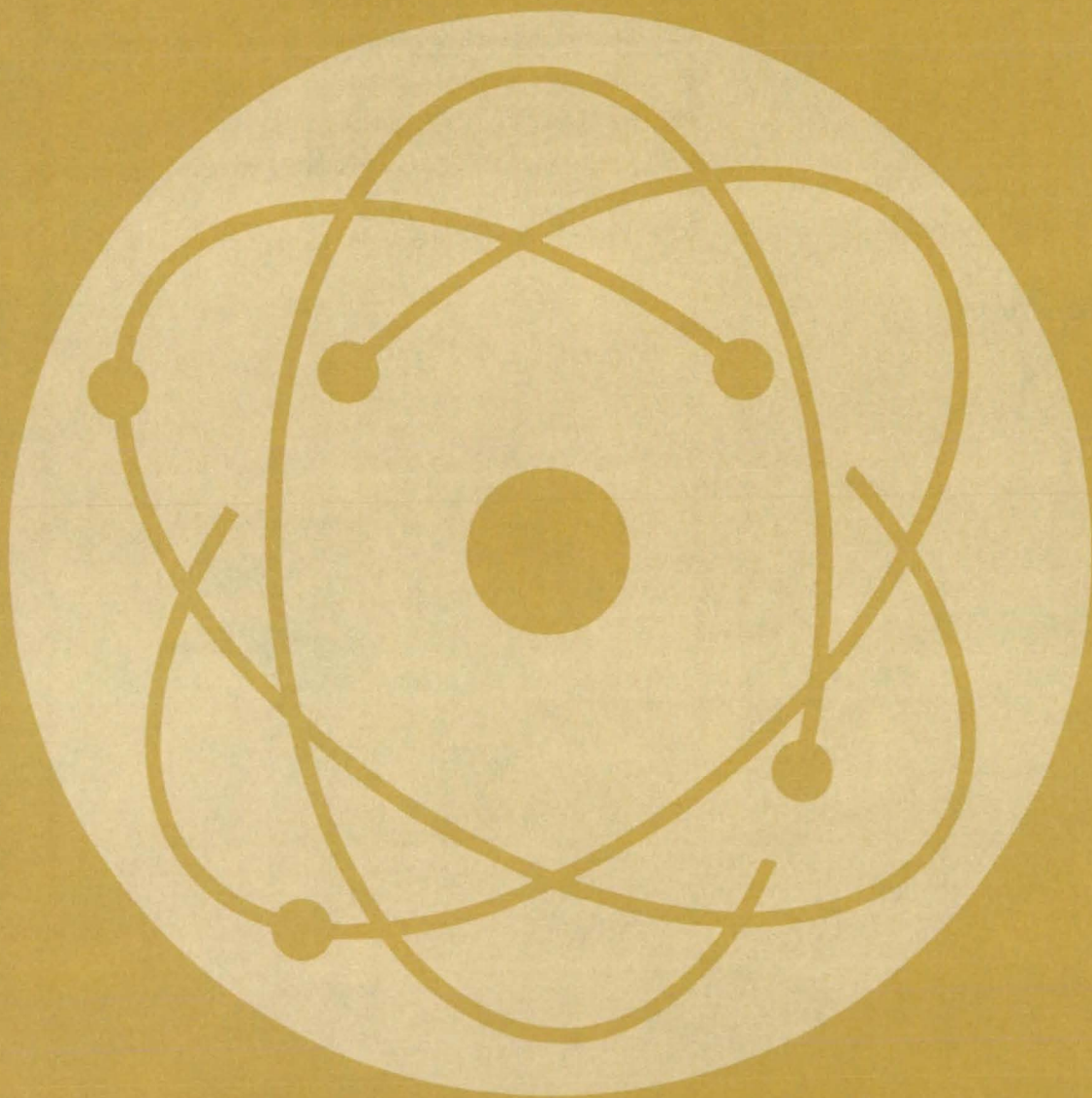
Packet Telemetry and Packet Telecommand

Standardized communication protocol covers uplink and downlink data transfers.

Two communication protocols for telemetry and telecommand reduce the amount of required hardware and software and facilitate bidirectional information exchange. One protocol covers the downlink transfer of measured data. The second covers the uplink transfer of commands from ground-support systems. Autonomous "packets" of data created using standard formatting techniques are switched through the data network using standard transfer protocols and are processed together into a single stream.

This work was done by Adrian J. Hooke and Edward Greenberg of Caltech for NASA's Jet Propulsion Laboratory. For further information, Circle 47 on the TSP Request Card. NPO-16301

Physical Sciences



**Hardware,
Techniques, and
Processes**

- 481 Reflecting Schmidt/Littrow Prism Imaging Spectrometer
- 482 Laser Rangefinder and Remote Profilometer
- 483 Rapid Freezing-Point Measurement
- 484 Determining the Slope Error of a Parabolic Reflector
- 484 Interferometer for Measuring Acoustic Signals
- 485 Roof Overhangs for Solar Houses
- 486 Telescoping Shield for Point-Focusing Solar Concentrators

Books and Reports

- 487 Maximum Outputs of Solar Photovoltaic Arrays

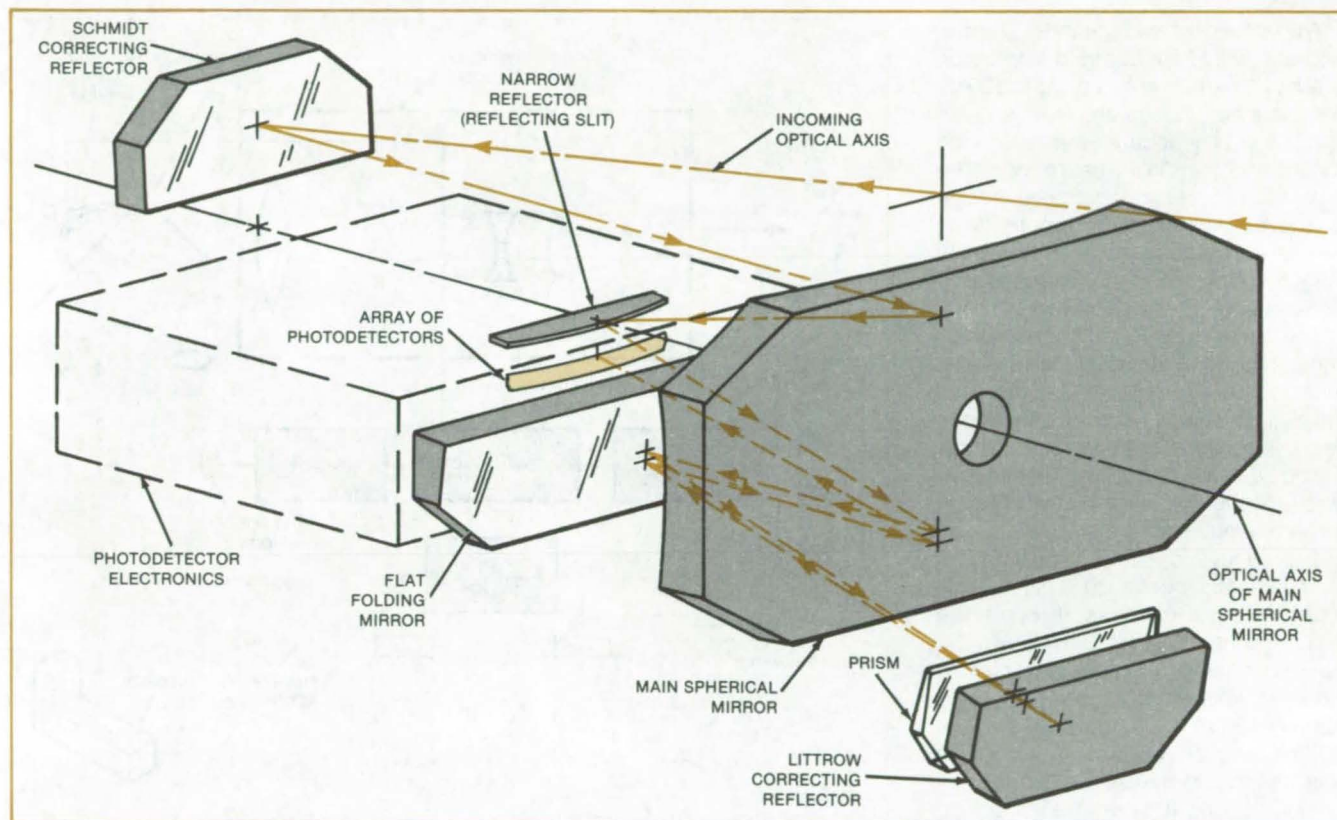
MiniBriefs

- 487

Reflecting Schmidt/Littrow Prism Imaging Spectrometer

High resolution is achieved with a wide field of view.

NASA's Jet Propulsion Laboratory, Pasadena, California



The **Imaging Spectrometer** features off-axis reflecting optics, including a reflecting "slit" that also serves as a field flattener. The only refracting element is the prism.

An imaging spectrometer includes off-axis optics that give an unobstructed 15° field of view and a resolution of 4.3 arc-seconds. The instrument operates at wavelengths from 0.4 to $2.5 \mu\text{m}$: This wide spectral range is possible because the imaging optics are reflecting (as opposed to refracting) to avoid unwanted dispersion. For each image point along the spectrometer slit, a spectrum is obtained.

The optical principle is illustrated in the figure. The entering light first strikes an off-axis Schmidt correcting reflector near the center of curvature of the main spherical mirror. The corrector is tilted by a few degrees so that the incoming optical axis lies above the edge of the main spherical reflector. From the corrector, the light travels to the upper portion of the main mirror, then to a narrow, curved reflector at the focal plane of the main mirror.

Together, the corrector and the main mirror form a Schmidt telescope system and give a curved focal surface. The narrow reflector at this surface serves as a field flattener. It also acts, in effect, as the spectrometer slit, by reflecting only a thin strip of the image into the rest of the optical system.

The light reflected from the field flattener strikes the lower portion of the main spherical mirror, is bounced off a flat folding mirror, and passes through a wedge prism on the way to an off-axis Littrow mirror. The Littrow mirror resembles the Schmidt correcting reflector and has approximately twice the aspheric correction. The light passes back through the prism to the flat folding mirror, then to the main mirror, and finally is imaged on an array of photodetectors on the focal surface, below the field flattener.

The photodetector array is two-dimensional: Each picture element along the slit axis corresponds to a spot along the line on the object that is imaged onto the slit. Each picture element along a perpendicular to the slit axis receives a portion of the spectrum emanating from one such spot. Thus, by scanning the slit across an object or scene and timing out the signal, both the spectral and spatial information in the scene are obtained.

This work was done by James B. Breckinridge, Norman A. Page, Roland V. Shack, and Robert R. Shannon of Caltech for NASA's Jet Propulsion Laboratory. For further information, Circle 48 on the TSP Request Card.

Inquiries concerning rights for the commercial use of this invention should be addressed to the Patent Counsel, NASA Resident Office-JPL [see page A5]. Refer to NPO-15801.

Laser Rangefinder and Remote Profilometer

Path lengths for pulse travel-time comparisons are controlled with optical-waveguide switches.

NASA's Jet Propulsion Laboratory, Pasadena, California

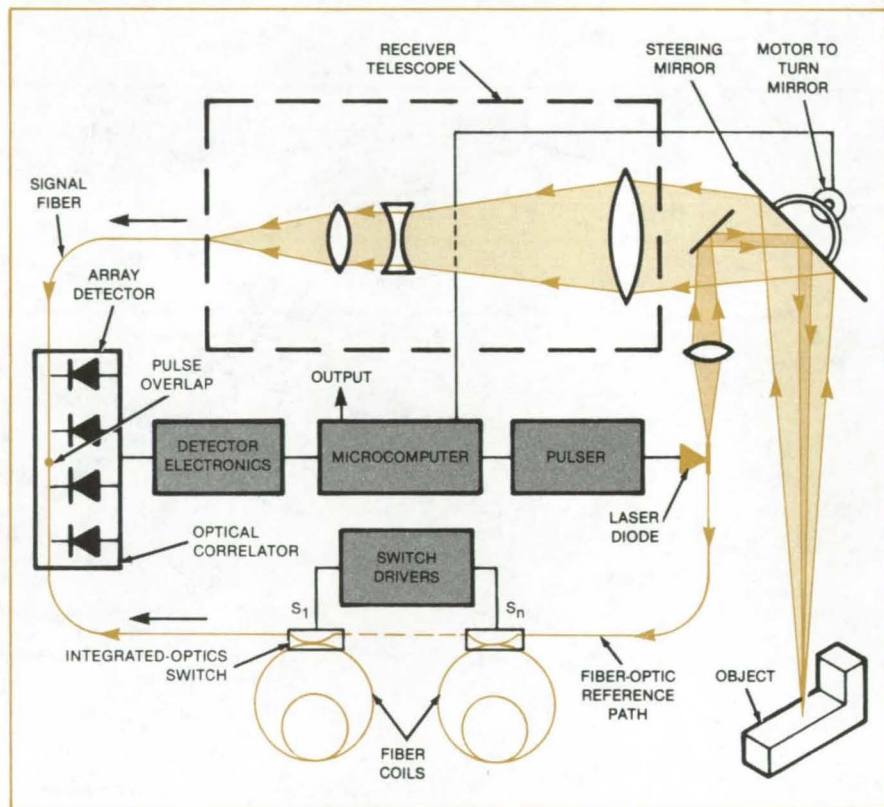
A proposed laser rangefinder and profilometer would operate with a precision of about 1 mm at ranges of up to 100 m. With scanning optics, the device could track objects or accurately measure the shapes of objects in the field of view. The new microprocessor-controlled design uses a variable-length fiber-optic delay line as a distance reference. The new ranging method could be used in vision systems for industrial robots.

The instrument (see figure) would compare the time of flight of laser pulses reflected from an object to that of pulses traveling through a reference fiber-optic delay line. Digitally-controlled optical-waveguide switches adjust the effective length of the delay line by switching in different lengths of optical fiber.

The object and reference pulses pass through each other (going in opposite directions) as they pass through the lithium niobate optical correlator. The peak instantaneous intensity occurs at the point where the two pulses meet in passing; i.e., at the point where the time of flight is equal over the two paths. This point is located by using a property of lithium niobate: It generates an optical output at half the wavelength of the original pulses. Because this property is non-linear, higher output occurs where the two pulses overlap as they pass than in the regions on either side where the two pulses pass by at different times. A charge-coupled device or other detector array locates the coincidence point.

The ultimate distance-resolution limit of the proposed instrument would be a function of laser pulse length and the resolving capability of the image-position detector. The length of a 20-ps pulse is about 6 mm. Since the change in path length to and from the object is twice the change in distance to the object, the resolution would be about 3 mm if the detector established coincidence only to the length of the overall pulse-overlap region. However, the detector array and associated electronics should be able to locate the centroid of the pulse overlap region precisely enough to improve the resolution to 1 mm.

For accurate results, the time of flight through the reference optical fibers must be accurately known. The instru-



In the **Proposed Laser Rangefinder and Remote Profilometer**, a microprocessor controls the emission of a train of 20-ps light pulses produced at a rate of 100 MHz, the states of the optical-waveguide switches $S_1 \dots S_n$ that select the lengths of fiber to be used in the reference path, and the detector electronics for the lithium niobate optical correlator. The beam can be scanned over the object to measure its shape as well as its range.

ment has two temperature dependencies that, fortunately, tend to cancel out. The laser wavelength varies with temperature, and the change in wavelength causes the time of flight in the optical fiber to vary because of dispersion (a variation of the index of refraction with wavelength). However, the second variation is opposite in sign and nearly cancels the first variation, provided that the fiber and laser can be kept at the same temperature. If so, the net error in distance due to the residual error could be as low as 0.03 mm per °C at a range of 100 m.

A signal-strength feasibility calculation considered range tracking at a distance of 100 m. It was assumed that the tracked object was fitted with small targets of retroreflective sheet covering

80 percent of the sensed target area, that it should be possible to capture 10 percent of the reflected power, and that there would be a 50-percent waveguide coupling loss. Laser output was assumed to be 30 mW during 20-ps pulses produced at a repetition rate of 100 MHz. It was also assumed that the return signals would be integrated for about 1 ms (10^5 pulses) per distance measurement.

Based on these assumptions and published data for second-harmonic-generation efficiency in lithium niobate waveguides, it is estimated that approximately 4×10^5 photons per distance measurement would be available at the detector. This is at least 10 times the number required to produce an adequate signal in a charge-coupled-array

detector. Every component required for such a rangefinder/profilometer has been demonstrated.

This work was done by John M. McLaughlan, John AuYeung, Eldred F.

Tubbs, Willis G. Goss, and Demetri Psaltis of Caltech for **NASA's Jet Propulsion Laboratory**. For further information, Circle 49 on the TSP Request Card.

Inquiries concerning rights for the commercial use of this invention should be addressed to the Patent Counsel, NASA Resident Office-JPL [see page A5]. Refer to NPO-15865.

Rapid Freezing-Point Measurement

A technique to determine the freezing point of fuels could be the basis of a portable instrument.

Lewis Research Center, Cleveland, Ohio

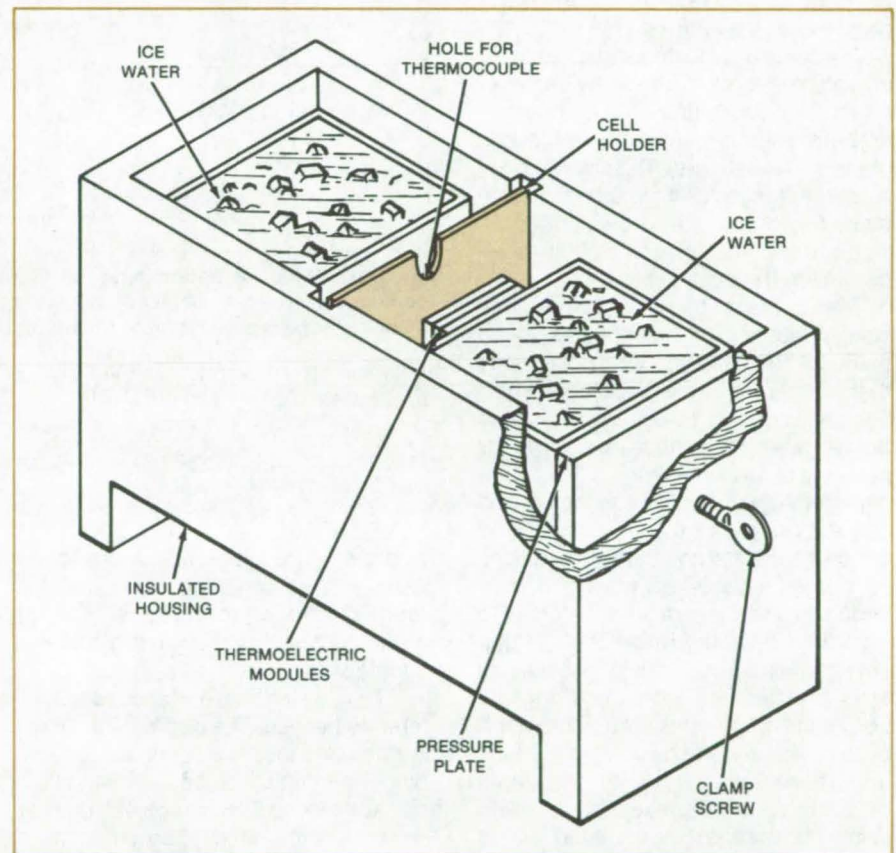
A technique has been developed for the rapid determination of the freezing-point temperature of fuels. The freezing point of aviation fuels is currently determined by the ASTM D-2386 laboratory standard. However, this method is relatively slow and not suitable for in-the-field measurements. The technique described here can determine a freezing point in under 10 minutes and is suitable for use in the design of a portable device.

Several techniques were investigated, and laboratory tests were conducted with the most promising ones. The test setup (see figure) incorporated a sample holder containing about 3 cm³ of test fuel, thermoelectric modules to cool the sample, compartments containing an ice/water mixture to act as a heat sink for the thermoelectric modules, and an external data-recording system.

The thermoelectric modules operate as a two-stage cooling unit and can be operated on portable dc batteries. The sample is cooled until it is several degrees below the freezing point and freezing has begun. The fuel is then rewarmed. The temperature, which is detected by a thermocouple with a hypodermic probe, is recorded and digitized.

During rewarming, a point of inflection in the temperature/time curve is identified, which is the freezing-point equivalent of the ASTM D-2386 measurement. This is the temperature at which the last trace of solids disappear. The test can be completed in 4 to 8 minutes, depending upon the fuel.

Eight aviation turbine and diesel fuels were tested, along with dodecane, tridecane, and tertiary-butyl alcohol. All gave good agreement with the ASTM



The **Freezing-Point Test Setup** includes a sample holder containing about 3 cm³ of test fuel, thermoelectric modules to cool the sample, compartments containing ice water to act as a heat sink for the thermoelectric modules, and an external data-recording system.

method and measurements using a differential scanning calorimeter.

No detailed design was made in the present study. A final design would incorporate the sample and cooling apparatus with the recording and readout system in an insulated portable unit. Ice would be added periodically.

This work was done by B. Mathiprakasam of Midwest Research In-

stitute for **Lewis Research Center**. Further information may be found in NASA CR-167981 [N83-10207], "Evaluation of Methods for Rapid Determination of Freezing Point of Aviation Fuels" [\$13]. A copy may be purchased [prepayment required] from the National Technical Information Service, Springfield, Virginia 22161.

LEW-14019

Determining the Slope Error of a Parabolic Reflector

The approximate slope error is determined with minimal test equipment.

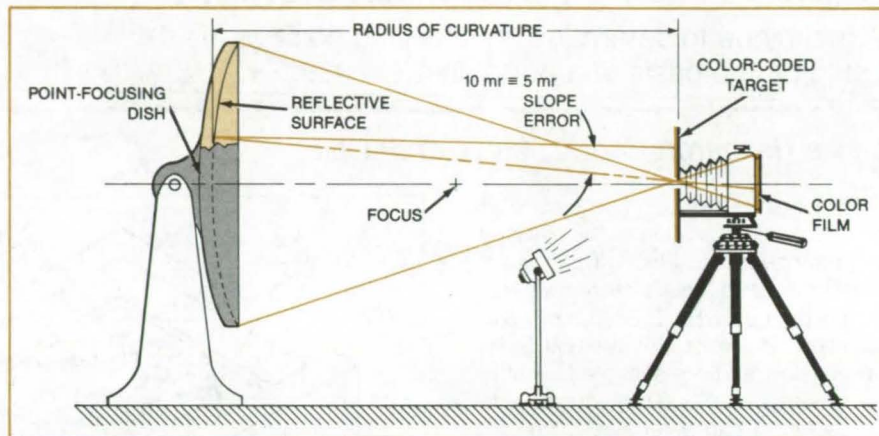
NASA's Jet Propulsion Laboratory, Pasadena, California

The slope error of a parabolic reflector is determined by using just a pinhole camera and photographic color film. Conventional determination of the slope error, in contrast, involves the use of a complex laser-scanning system to plot the deviation of a reflected beam as it is moved over the entire surface.

The pinhole is located at the center of curvature of the dish and at the center of a group of concentric colored rings on an illuminated target normal to the axis of the dish (see figure). The colored rings represent ranges of slope errors. The reflected image of the target formed by light passing through the pinhole is recorded on the color film.

The camera has a ground-glass viewer that allows adjustments to be made to the reflector while observing their effect on alignment and slope error. Such adjustments include the location of the camera/target, either side to side or nearer to or farther from the reflector, the depth of curvature of the reflector, and elevation angle of the reflector. Once the best reflector and camera positions have been established, color film is inserted in the camera and exposed to record the reflected image of the target.

A graphical integration process is used to determine the standard deviation of the slope error. The photograph of the reflected image is overlaid with graph paper, and the number of squares of each color (representing a given slope-error range) are counted. Since the deviation from zero is the concern,



The Test Setup for Determining the Slope Error of a Point-Focusing Dish includes a pinhole camera at the center of curvature and a color-coded target mounted around the pinhole. Floodlights illuminate the target to minimize exposure time.

the expression used to determine standard deviation of the slope error is

$$\sigma_1 = \frac{\sum e^2}{N}$$

where e = the recorded slope error for each square (average value for the range of error represented by the color of the square), and N = the number of squares.

This is a standard deviation of the difference between the slope of the actual surface and that of a spherical surface. Since the difference between a spherical surface and a paraboloid can be calculated, the standard deviation of the slope error of the actual surface with re-

spect to a paraboloid can be estimated by

$$\sigma_2^2 = \sigma_1^2 + \sigma_{sa}^2$$

where σ_{sa} = standard deviation of the slope error of a spherical surface with respect to a paraboloid (spherical aberration).

The new procedure, although not exact, provides a good approximation of the reflector slope error and is an excellent tool for comparative analysis of reflectors used as solar collectors and as collectors for microwave receivers.

This work was done by G. Ronald Christ of AAI Corp. for NASA's Jet Propulsion Laboratory. For further information, Circle 50 on the TSP Request Card.

NPO-15713

Interferometer for Measuring Acoustic Signals

An optical-fiber interferometer measures the wave amplitude without contacting the specimen surface.

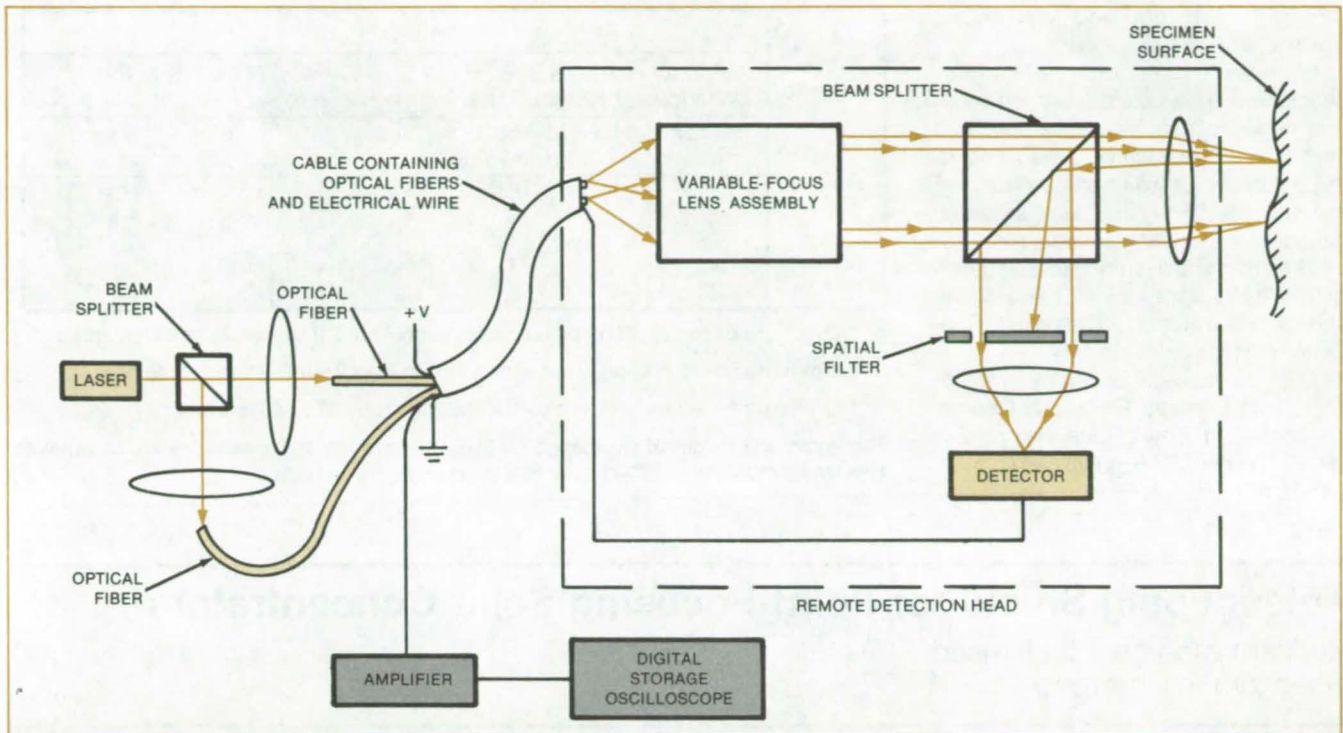
Langley Research Center, Hampton, Virginia

An optical-fiber wideband differential interferometer is a sensitive measuring instrument for broadband acoustic waves on the surfaces of materials. Acoustic waves can also be measured by mechanical transducers; however,

the interferometer offers two distinct advantages: (1) The optical-probe does not load the specimen surface and thus does not interact with system observables, and (2) the optical beams may be focused on small spots on the measured

surface so that integration effects due to large transducer area do not occur.

The interferometer uses a cabled optical fiber as the interferometer propagation path, which allows separation between the optical system and the sample.



The **Optical-Fiber Interferometer System** contains a remote detector head. The head includes a beam splitter that divides the input beam and recombines the output beams, while the spatial filter filters the interference pattern at the beam-splitter output; and a lens focuses this on a detector. The beams are focused on a specimen surface to record the acoustic signals.

A transducer on the end of the flexible fiber senses wave motion on the specimen surface and produces an output signal proportional to wave amplitude.

Polarized light from a 2.0-mW He/Ne laser source is divided and coupled to two flexible bundled single-mode optical fibers that transmit the light to a small remote detection head (see figure). The light at the output ends of the fibers is collimated and focused by a variable-focus lens system to points on the sur-

face of the specimen. Elastic waves on the specimen surface differentially modulate the relative phases of the two optical beams because of the periodic change in particle displacement at the surface. Upon reflection, the beams are superimposed, filtered, and detected to produce an output signal directly proportional to instantaneous displacement.

The acoustic sensitivity of the interferometer may be adjusted by changing the separation distance between the

spots on the surface. A 3-dB bandwidth of two frequency decades maintained at 20-dB signal-to-noise ratio is possible, using frequency-domain signal-processing techniques.

This work was done by Richard O. Claus and Avinash O. Garg of Virginia Polytechnic Institute and State University for Langley Research Center. For further information, Circle 51 on the TSP Request Card.
LAR-13030

Roof Overhangs for Solar Houses

A convenient graphical method helps in the design of overhangs at different latitudes.

Langley Research Center, Hampton, Virginia

Roof overhangs above the windows of solar houses should be narrow enough to let in the low-angle rays of the winter Sun but wide enough to keep out the high-angle rays of the summer Sun. However, the design must take into account not only the width of the overhang, but also its vertical position with respect to the windows. The width and vertical position of the overhang depend on the

size of the window and its vertical position in the south wall, the latitude, and the local climate.

A convenient graphical method determines both the width and vertical position of overhangs for a standard wall section having a "typical" window arrangement. Overhangs for this wall section were determined for two extremes of latitude in the United States. For the

southern latitude, the problem of shading for various periods of the year (to account for variations in local climate) was examined in some detail. Sun angles at different times of day for different latitudes were considered on a year-round basis for those cases requiring winter heating and summer shading and for those cases (e.g., San Diego at
(continued on next page)

32° latitude) requiring year-round shading.

For the winter heating/summer shading case, the table gives the width and height of overhangs for two wall sections at five latitudes, with one of three periods for full shading at each of the latitudes. For other wall sections, latitudes, and shading periods, the width and height of the overhang can be determined by the graphical method described in the report, "Designing Roof Overhangs for Solar Houses."

This work was done by William Gracey of Langley Research Center. To obtain a copy of the report, Circle 52 on the TSP Request Card. LAR-13140

Latitude	Wall Section			
	Window Height 6 ft, 8 in. Windowsill Height 2 ft, 6 in.		Window Height 6 ft, 8 in. Windowsill Height 0 ft, 0 in.	
	Width (in.)	Height Above Top of Window (in.)	Width (in.)	Height Above Top of Window (in.)
32°*	26	18	41	28
36°*	32	19	51	30
40°**	23	11	36	18
44°**	27	11	44	18
48°***	27	9	43	14

* Overhang based on Sun angles for noon on April 21/August 21 and December 21

** Overhang based on Sun angles for noon on May 21/July 21 and December 21

*** Overhang based on Sun angles for noon on June 21 and December 21

The **Width and Height of Overhangs** for two wall sections at five latitudes are shown with specified periods for full shading at each latitude.

Telescoping Shield for Point-Focusing Solar Concentrators

Concentrated heat is diffused when aim is incorrect.

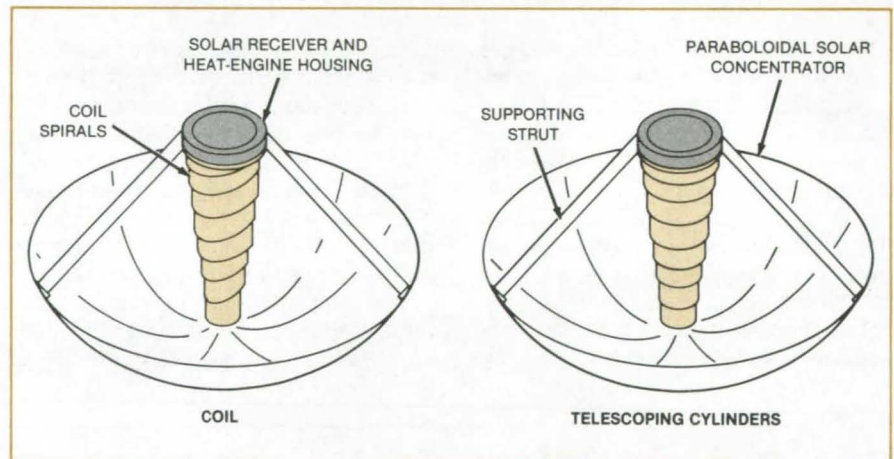
NASA's Jet Propulsion Laboratory, Pasadena, California

A telescoping shield that is normally stowed around a solar receiver protects the heat engine and supporting structure from overheating when the concentrator is aimed a few degrees away from the line to the Sun. When extended, the shield intercepts the offcenter concentrated solar radiation. The heat is spread out over the thermally conductive shield and reradiated diffusely so as not to cause structural damage.

In the version shown at the left in the figure, the shield consists of a coil of steel sheet [typically, of 1-ft (30-cm) width]. The coil is wound around the receiver or heat-engine housing — somewhat like a roll of tape wound on a hollow core. When the solar concentrator is aimed away from the Sunline, one end of the sheet is released by a heat-actuated latch and pulled out to extend the cone into a spiral of approximately conical outline. (The sheet can be pulled out either mechanically or by gravitation, depending on the concentrator design.)

The steel spiral is self-supporting when extended. The coil is drawn back into its stowed position around the heat engine by pulling up the lowered end with a motor-driven cable.

The version shown at the right in the figure is similar, except that telescoping



The **Telescoping Shield** is lowered from around the heat-engine housing to intercept and dissipate offcenter concentrated solar radiation. Without the shield, the stagnation temperature on vulnerable exposed parts could reach 1,500° F (800° C).

cylinders of sheet or screen are used instead of a single coil. The method of deployment and the heat-dissipation principle are the same. One major difference is that the retraction mechanism must include three cables spaced at equal angular intervals (120°) about the cylinders and attached to the lowest cylinder.

Shields based on a bellows concept have been proposed. These would also require three cables for retraction. The

bellows might be constructed of glass-fiber cloth or wire mesh.

This work was done by Maurice Argoud, Walter Walker, and Lloyd V. Butler of Caltech for NASA's Jet Propulsion Laboratory. For further information, Circle 53 on the TSP Request Card.

Inquiries concerning rights for the commercial use of this invention should be addressed to the Patent Counsel, NASA Resident Office-JPL [see page A5]. Refer to NPO-16236.

Books and Reports

These reports, studies, and handbooks are available from NASA as Technical Support Packages (TSP's) when a Request Card number is cited; otherwise they are available from the National Technical Information Service.

Maximum Outputs of Solar Photovoltaic Arrays

Simulated operating data are derived for different sites.

A report presents electrical data for solar photovoltaic arrays operating at different locations in the United States. The data are useful in designing power-conditioners for matching the output of an array to a load.

In a typical residential solar-cell power system, a power-conditioning subsystem converts the direct current from a photovoltaic array into alternating current for household appliances. The power-conditioning subsystem must accommodate the widely varying output of the array and must maximize energy production. In other — usually non-residential — systems, the load employs

direct current and a dc-to-dc converter, or a storage-battery and charge-control subsystem must accommodate the array output. Regardless of the type of load, a necessary ingredient in the data for the design of efficient systems is information on the long-term output characteristics of the array.

The report is based on computer simulations. It presents an overview of the general approach to system analysis. It then considers key aspects of array performance and their influence on power-conditioning subsystems. These aspects include tracking the Sun for maximum power; extreme values of array characteristics, including short-circuit current, maximum power, and open-circuit voltage; and calculating the efficiency of power-conditioning subsystems and converters. Many design examples are provided.

A computer calculated hourly electrical output based on historical weather data from a representative year at each of 26 sites in the United States. Hourly electrical performance was derived from the current/voltage curve of an actual array of silicon solar cells. This curve defines the normalized output of the array at standard reporting conditions (solar-power input of 100 mW/cm²

at 25° C) and was used to derive the appropriate current/voltage curve for each hourly irradiance level and cell temperature.

Because the shape of a current/voltage curve varies somewhat among different manufacturers and with solar-cell age, other current/voltage curves were used to define the sensitivity of the simulation results to curve shape. The shape of the current/voltage curve is quantified, for purposes of sensitivity analysis, by the "fill factor" — the ratio of maximum power to the product of open-circuit voltage and short-circuit current.

Fill factors ranging from 0.45 to 0.75 were used in the sensitivity studies simulation. The report presents most of the results of the simulation in terms of current, voltage, and power produced by an array at its maximum-power point under standard operating conditions.

This work was done by Ronald G. Ross, Jr., Gerrie M. Hill, and Charles C. Gonzalez of Caltech for NASA's Jet Propulsion Laboratory. To obtain a copy of the report, "Characterization of the Electrical Output of Flat-Plate Photovoltaic Arrays," Circle 54 on the TSP Request Card. NPO-15966



MiniBriefs describe NASA innovations and reports in an abbreviated format. Readers desiring additional information on these items should request the Technical Support Packages (TSP's), available in most cases, which can be obtained by using the TSP Request Card at the back of this issue.

Laser Pollutant-Measuring Systems

Laser optical systems for remote gas pollutant measurements are surveyed.

Remote sensing of gases based on differential absorption of two laser beams is used to determine pollutant gas concentrations. The laser systems surveyed include dye lasers for SO₂, O₃, and NO₂; carbon dioxide lasers for O₃

and C₂H₄; helium/neon lasers for CH₄; and tunable diode lasers for other gases. These laser systems, which have undergone extensive laboratory and field development, are discussed in a published report, and the choices of appropriate gas-measuring instruments and their sensitivities are evaluated.

This work was done by William B. Grant and Robert T. Menzies of Caltech for NASA's Jet Propulsion Laboratory. To obtain a copy of the report, Circle 55 on the TSP Request Card. NPO-16101

Retrieval of Geophysical Parameters From Radiometric Data

A rapid linear algorithm retrieves meteorological parameters from microwave radiometric data.

Various geophysical parameters, such as sea-surface temperatures, surface windspeed, integrated water vapor, and rainfall rate, can be rapidly calculated

(continued on next page)

from microwave radiometric data using an inversion algorithm. The versatile, 2-step, multiple-linear-regression algorithm examines all possible subsets of the available channels and selects the optimum subset for retrieving a given geophysical or meteorological parameter. A comparison of calculated sea-surface temperatures, using this algorithm and actual measured in situ water temperatures, indicates an accuracy of better than 1.5 K, which compares very well with figures quoted in earlier investigations.

This work was done by Prem C. Pandey and Ramesh K. Kakar of Caltech for NASA's Jet Propulsion Laboratory. For further information, Circle 56 on the TSP Request Card.
NPO-16266

Instrumentation for Solar-Oscillation Measurements

System works with any telescope with a spectrograph without interfering with existing use of the spectrograph.

A new instrument system for solar-oscillation measurements combines a 244- by-248-pixel charge-injection-device (CID) camera with an existing 13-foot (4-m) Littrow spectrograph at the 60-foot (18-m) solar-tower telescope at Mount Wilson. Installation of similar systems at existing telescopes around the world would make possible continuous measurements of solar photospheric and shallow subphotospheric rotation to depths up to about 20 Mm, using the frequency splitting of nonradial solar p-mode oscillations. Continuous observations of a rectangular region centered on the solar disk permit separating out eastward- and westward-traveling oscillations. Telescope aiming accuracy is 1 arc-second.

This work was done by Edward J. Rhodes, Jr., Thomas W. Andrews, and Edward J. Smith of Caltech, Robert F. Howard of Mount Wilson Observatory, and Roger K. Ulrich of UCLA for NASA's Jet Propulsion Laboratory. For further information, Circle 57 on the TSP Request Card.
NPO-15687

Solar-Power System Produces High-Pressure Steam

A triple-collector system generates high-pressure steam at 22 percent efficiency.

A combination of three multistaged solar collectors, each operating separately at maximum efficiency, produces high-pressure steam for large-scale continuously operating turbines for generating mechanical or electrical energy. Pure water serves as the working fluid throughout the cycle. In the first stage, the water is heated by inexpensive nontracking, nonconcentrating flatplate collectors. The second stage, which converts the heated water to steam, uses more sophisticated tubular or parabolic collectors to supply the latent heat of vaporization. The vapor is superheated in the third stage by a more expensive high-concentration tracking collector. The superheated water vapor drives the turbines, attaining an overall system efficiency of about 22 percent.

This work was done by Fikry L. Lansing of Caltech for NASA's Jet Propulsion Laboratory. For further information, Circle 58 on the TSP Request Card.
NPO-15434

Fresnel-Lens/Heat-Storage System

Fresnel lens system delivers 100 kilowatts.

A self-contained solar-thermal powerplant uses Fresnel lenses to deliver up to 100 kilowatts. The hexagonal honeycomblike array of thin lenses focuses and concentrates solar energy into small openings in an insulated enclosure containing a phase-change material such as magnesium fluoride. The proposed 200-volt system uses about 800 Fresnel lenses. Detailed calculations were done for the heat balance in the module.

This work was done by Robert H. Turner of Caltech for NASA's Jet Propulsion Laboratory. For further information, Circle 59 on the TSP Request Card.
NPO-16242

Ten Thousand Solar Constants Radiometer

A supplementary report on this radiometer is now available.

A report, "Radiometer for Accurate ($\pm 1\%$) Measurement of Solar Irradiances Equal to 10,000 Solar Constants," gives additional information on a radiometer described earlier. [See "Solar-Collector Radiometer" (NPO-14986) on page 46 of *NASA Tech Briefs*, Vol. 8, No. 1.]

This self-calibrating, water-cooled, thermopile radiometer measures the irradiance produced in the solar image formed by a parabolic reflector or by a multiple-mirror solar installation; it weighs about 2.2 lb (1 kg) and is 2 in. (5 cm) in diameter. Spectral response is flat from the far ultraviolet to the far infrared, with a thermal time constant of 1.3 second. It provides accurate cosine response up to 60° off axis.

This work was done by James M. Kendall, Sr., of Caltech for NASA's Jet Propulsion Laboratory. To receive a copy of the report, Circle 60 on the TSP Request Card.
NPO-15922

Heat Storage and Transport

An encapsulated phase-change material in a fluid medium stores heat efficiently.

A system for storing large amounts of heat per unit volume comprises encapsulated sealed pellets of phase-change materials dispersed and suspended in an inert fluid-transport medium. Encapsulation of the heat-storage eutectic salt in very small particles with thin, inert, corrosion-resistant outer shells allows large quantities of heat to be adsorbed in the solar-collector system as rapidly as desired. Heat transfer into and out of the phase-change storage material efficiently takes place across small distances.

This work was done by Parviz A. Bahrami of NASA's Jet Propulsion Laboratory. For further information, Circle 61 on the TSP Request Card.
NPO-15468

Solar Shutter

A solar receiver can be turned off by a movable reflective shutter.

Some material-testing facilities use solar-energy paraboloidal mirror concentrators as sources of high-temperature heat. This solar radiation can be turned off by a highly reflective shutter interposed between the reflector and receiver to block the aperture. When the reflective surface is interposed across the optical axis, the incoming solar heat will be reflected back to the concentrator for rejection into space. The reflective, water-cooled shutter may be translated linearly or pivoted about an axis to turn on or shut off the heat applied to the tested material.

This work was done by Robert R. Hale of Caltech for NASA's Jet Propulsion Laboratory. For further information, Circle 62 on the TSP Request Card. NPO-15428

Solar-Heated Gasifier

Catalytic coal and biomass gasifier system is heated by solar energy.

A catalytic reaction system using solar heat doubles the normal synthetic-gas yields from coal gasification, at lower overall temperatures and without the use of oxygen. Sunlight from a solar concentrator is focused through a quartz window onto a ceramic-honeycomb absorber surface, which raises the temperature of the reactant steam, the fluidizing gas, and the reactor walls. A recycled product-gas stream provides the fluidizing gas. Use of catalysts reduce the necessary gasification temperature to about 1,500° F.

This work was done by Shaik A. Qader of Caltech for NASA's Jet Propulsion Laboratory. For further information, Circle 63 on the TSP Request Card.

This invention has been patented by NASA (U.S. Patent No. 4,290,779). Inquiries concerning nonexclusive or exclusive license for its commercial development should be addressed to the Patent Counsel, NASA Resident Office-JPL [see page A5]. Refer to NPO-15071.

Point-Focusing Solar-Power Distributed Receivers

Modular, solar-powered generators would feed into the electric utility grid.

A two-volume annual report describes development work aimed at achieving large-scale production of modular, point-focusing distributed receivers (PFDR's) for solar-powered generation of electricity or thermal power for industrial use. A Sun-tracking parabolic reflector 30 to 50 feet (9 to 15 m) in diameter would focus solar radiation into a power-conversion unit (PCU) comprising an organic Rankine, a gas Brayton, or a Stirling heat engine and an alternator. In contrast to central solar-power systems that use a large field of reflectors to drive one large PCU, PFDR's are suitable for distributed installation near points of power usage.

This work was done by John W. Lucas of Caltech for NASA's Jet Propulsion Laboratory. To obtain a copy of the report, Circle 64 on the TSP Request Card.

NPO-15578

Purification of Solar Ponds

Flocculatory agents added to solar saltponds remove turbidity to increase the solar-energy collection efficiency.

A flocculatory agent such as aluminum sulfate at the 5-ppm level will clarify turbid salt-gradient solar ponds used as electric-energy sources. The flocculating agent or bacteriocide used to remove micro-organisms is sprayed onto the pond from an airplane and is allowed to settle to the bottom of the pond. This removes turbidity due to floating dirt, debris, or bacteria and allows more of the incident solar flux to penetrate through the water in the pond.

This work was done by Sam Carpenter of NASA's Jet Propulsion Laboratory. For further information, Circle 65 on the TSP Request Card. NPO-15397

A Ceramic Heat Exchanger for Solar Receivers

This design is intended for high-temperature service.

Recently-proposed ceramic-tube and header heat exchangers can be used for a solar-concentrating collector operating in the 25- to 150-kW power range at temperatures between 2,000° and 3,000° F (1,095° and 1,650° C). Solar flux impinges on a ceramic thermal sleeve. Between this sleeve and the hot surface of the insulation package are a number of small-diameter ceramic hairpin tubes. Each is connected to two toroidal headers with a spigot-type joint. Gas flows into one of the toroidal headers and is split between the hairpin tubes. Gas flowing through the hairpin tubes is heated, collected in the outlet header, and finally leaves through a tube and joint arrangement to deliver the heat.

This work was done by C. S. Robertson, Jr., and L. E. Stacy of General Electric Co. For further information, Circle 66 on the TSP Request Card.

NPO-15771

Calibrating for Ionospheric Phase Delays

Correlation of two transmitted signals measures frequency dispersion due to the ionosphere.

Global signal-propagation prediction as well as aerospace navigation accuracy for tracking and communications require calibration of communication equipment for phase delays caused by the ionosphere. A proposed technique determines the ionospheric phase delay on a real-time universally applicable basis in terms of electrons per meter squared by coherently modulating two L-band carrier frequencies received from two Global Positioning System satellites. As these two carriers are received at a base station, the difference in time of arrival of the two different channels

(continued on next page)



at the antenna is a function of the frequency dispersion or delay due to the ionosphere. The two pseudorandom number sequences are cross-correlated to derive the delay time. The sequences may even be encrypted, since they need not be decoded for the dispersion measurement.

This work was done by Peter F. MacDoran of Caltech for NASA's Jet Propulsion Laboratory. For further information, Circle 67 on the TSP Request Card.

Inquiries concerning rights for the commercial use of this invention should be addressed to the Patent Counsel, NASA Resident Office-JPL [see page A5]. Refer to NPO-15430.

General Design Considerations for Remote Sensors

The needs of users are considered in the light of satellite capabilities.

A report discusses the design of orbiting remote sensors. On one hand, the needs of ground-based users are expressed in terms of the frequency of revisitation, spatial resolution, spectral bands, and the speed of delivery of finished products. On the other hand, a satellite has finite capabilities in resolution and swath width, and the frequency of revisitation depends on the relationship between these and the achievable orbital parameters.

To some degree, data parameter compromises can be made. Where revisitation frequency can be traded against resolution, the data rate and quantity can be kept within bounds. A multiple-resolution sensor may satisfy several disciplines (e.g., mapping, geology, and land use) that are otherwise competing for spatial and spectral resolution.

This work was done by Frederic C. Billingsley of Caltech for NASA's Jet Propulsion Laboratory. To obtain a copy of the report, Circle 68 on the TSP Request Card.
NPO-15930

Electron-Attachment Profiles

Photoelectrons generated in situ allow measurement of electron-attachment profiles in gases.

Measurement of electron-attachment widths are important in evaluating dielectric gases for high-voltage applications. A report is available that describes the technique of photoelectron spectroscopy to measure shapes of threshold electron-attachment cross sections of various gases. The gas to be studied, for example, SF₆, is mixed with xenon. Very-low-energy (0 to 200 meV) electrons are generated in situ by photoionization of the xenon matrix gas. These photoelectrons attach to the SF₆ gas molecules to form the charged species of SF₆⁻. A plot of the SF₆⁻ ion current plotted against photon wavelength or electron energy yields the electron-attachment profile and cross section.

This work was done by Ara Chutjian and Joseph M. Ajello of NASA's Jet Propulsion Laboratory. To obtain a copy of the report, "Line Shapes for Attachment of Threshold Electrons to SF₆ and CFCL₃," Circle 69 on the TSP Request Card.
NPO-14865

Composite Spectrometer Prisms

Optical nonlinearities can be eliminated.

An efficient linear dispersive element for spectrometer instruments can be achieved using several different glasses in a multiple-element prism. The result is a disperser with low variance of dispersion with wavelength, high efficiency, and none of the order overlap or polarization problems associated with gratings.

Good results were obtained in both two- and three-element prisms using a variety of different glass materials. Maximum-to-minimum dispersion ratios as low as 1.4 to 1 were obtained over the visual and shortwave infrared bands with transmission as high as 90 percent.

This work was done by James B. Breckinridge and Norman A. Page of Caltech and John M. Rodgers of the University of Arizona for NASA's Jet Propulsion Laboratory. For further infor-

mation, Circle 70 on the TSP Request Card.

NPO-16060

Thermal Compensator for Paraboloidal Reflector

A mounting structure maintains the focus of a mirror over the temperature range of -55° to 50° C.

A mounting structure holds an off-axis paraboloidal collimating mirror so that its optical axis is constantly focused and remains stationary with respect to a fixed point over a wide temperature range. This thermal-compensation system uses a combination of iron/nickel-alloy and aluminum bars in each of the two axes of movement of the mirror. The mirror is attached to the aluminum bar. The differing coefficients of expansion of aluminum and the iron/nickel alloy provide a structure that cancels out any movement of the working surface of the mirror with respect to the field-stop aperture.

This work was done by Charles G. Stanich and Frederick G. Osterwisch of Daedalus Enterprises, Inc., for NASA's Jet Propulsion Laboratory. For further information, Circle 71 on the TSP Request Card.
NPO-16145

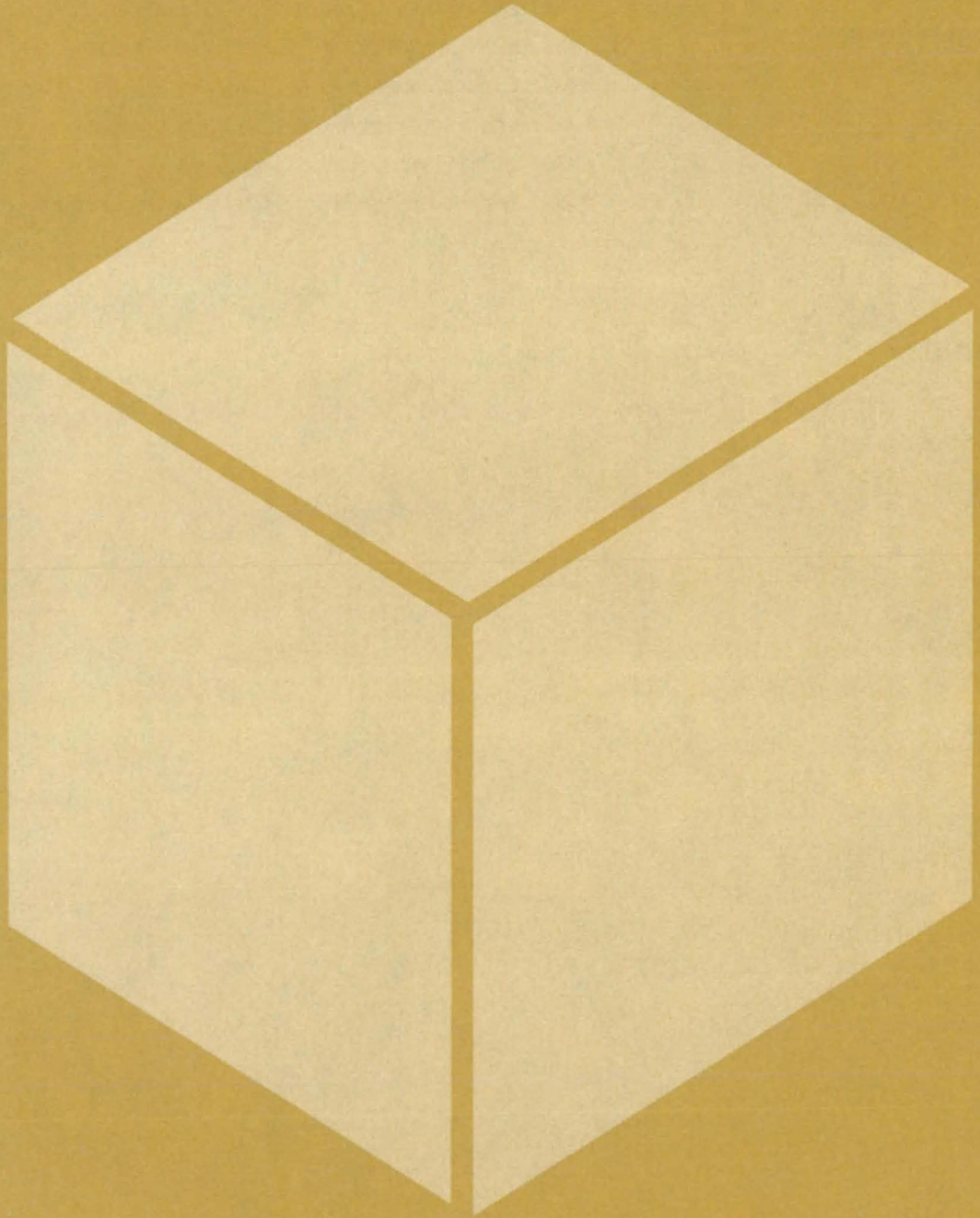
Paraboloidal-Dish Power Modules

Competing factors in power-module design are evaluated.

A study determines the configurational tradeoffs for a particular paraboloidal-dish power system for isolated-load applications. A continuous level of power can be supplied with high reliability by using a power system with modular paraboloidal-dish power units. These power units can be driven by fossil fuels as well as by heat from the Sun. First-order tradeoffs regarding optimum size of storage are investigated as a function of the number of power modules and the cost of fuel.

This work was done by William R. Revere, James M. Bowyer, Toshio Fujita, and Henry I. Awaya of Caltech for NASA's Jet Propulsion Laboratory. For further information, Circle 72 on the TSP Request Card.
NPO-16100

Materials



Hardware, Techniques, and Processes

- 493 Desulfurization of Coal in Fluidized Beds
- 494 Increasing the Ductility of Electroplated Metals
- 494 Eutectic Contact Inks for Solar Cells
- 495 Lightweight High-Temperature Thermal Insulation
- 496 Inhibiting Wet Oxidation of Ammonia
- 496 Applying Uniform Polymer Coatings to Microspheres

Books and Reports

- 497 Defect Chemistry of $\text{Hg}_{1-x}\text{Cd}_x\text{Te}$

MiniBriefs

- 498

Desulfurization of Coal in Fluidized Beds

A dry process promises to be effective and economical.

NASA's Jet Propulsion Laboratory, Pasadena, California

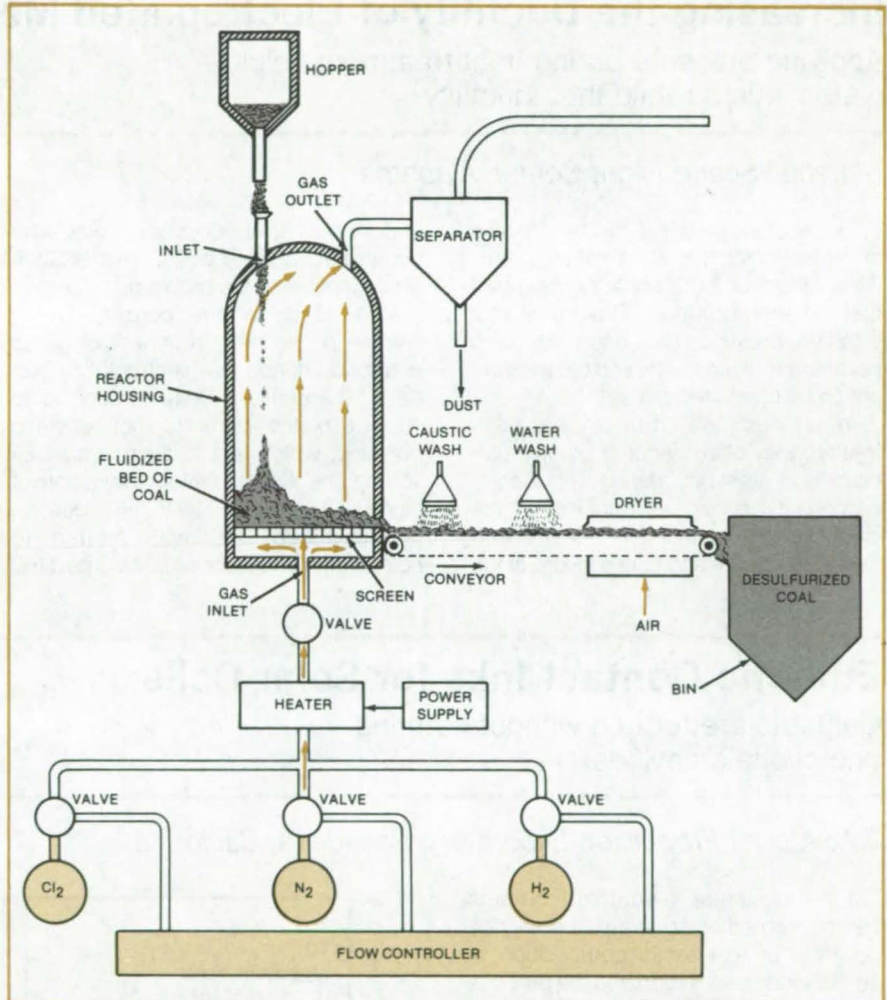
An experimental dry chemical process for removing sulfur from coal — and thereby reducing harmful sulfur emissions from coal-fired electric powerplants — promises to be more economical and effective than older wet chemical processes. The new process is faster, requires smaller amounts of chemical reagents, and produces no liquid effluents, which can pose a disposal problem.

As in older chemical coal-cleaning processes of the same type, the sulfur is removed by chemical reactions with chlorine, then with hydrogen. [A partially-wet chemical process that precedes the present one is described in "Desulfurizing Coal by Chlorinolysis and Hydrogenation" (NPO-15304), *NASA Tech Briefs*, Vol. 7, No. 3 (Spring 1983), page 279.] An important advantage of the new process is that the desulfurization reactions take place between solid and gas phases only. No liquids are involved, and the costs of handling and disposing of liquids are avoided.

The new process uses substantially less chlorine and therefore is less expensive. The reaction takes place in a fluidized-bed reactor that ensures thorough mixing and intimate contact between the coal particles and the chlorine gas. This helps react a greater proportion of the chlorine and shortens the reaction time.

The treatment begins as pulverized coal is fed to the inlet of a fluidized-bed reactor (see figure). A fluidized bed of coal forms over a screen in the reactor, created by the force of the process gas entering through the bottom inlet.

An automatic flow controller first feeds chlorine gas to the reactor for 5 to 30 minutes. The chlorine may be heated to as much as 300° C on its way to the reactor. It may also be fed in at ambient temperature, in which case the temperature in the reactor rises to about 80° C because of the exothermic reaction of the chlorine with the pyritic sulfur in the coal. The reaction produces mostly gaseous chlorine/sulfur compounds that are swept out of the reactor by the gas flow.



Dry Coal Reacts With Chlorine in a fluidized bed. Chlorine/sulfur compounds pass off as gases. The coal is then dechlorinated with hot nitrogen and further desulfurized by hydrogen.

After the chlorination, the flow controller turns off the chlorine and lets in a flow of nitrogen. The nitrogen can be used to flush out the chlorine gas prior to hydrodesulfurization; or dechlorination can be carried out with nitrogen by heating nitrogen to between 300° and 600° C, with flows for 10 to 30 minutes, without further coal treatment to dechlorinate the coal.

If hydrodesulfurization is desired for greater sulfur removal, the controller

hydrogen for 10 to 60 minutes. Heated to 500° to 700° C, the hydrogen removes much of the sulfur that remained in the coal after chlorination.

The treated coal is removed from the reactor through an outlet cooled and conveyed to storage. If a reduction in ash and mineral matter is required, the coal is carried on a conveyor past a caustic wash station, a water wash station, and a dryer before going to storage. The washes help to remove mineral and ash impurities.

(continued on next page)

The gases leave the reactor through a top outlet. A separator extracts coal dust carried along by the gases. The dust can be compressed into pellets and burned for process heat. The gases can be recycled.

This work was done by Ravindram Maddury and John Kalvinskas of Caltech for **NASA's Jet Propulsion Laboratory**. For further information, Circle 73 on the TSP Request Card.

Inquiries concerning rights for the commercial use of this invention should be addressed to the Patent Counsel, NASA Resident Office-JPL [see page A5]. Refer to NPO-15924.

Increasing the Ductility of Electroplated Metals

Applying pressure during heat treatment helps plated layers retain their ductility.

Marshall Space Flight Center, Alabama

Hot isostatic pressing may be effective in improving the ductility of metal plating, if the results of a preliminary experiment can be extrapolated. Previously, hot isostatic pressing has been used on powder-metallurgy parts and castings but not on electroplated parts.

When electroplated metals are heat-treated, they often become porous, particularly at grain boundaries. This localized porosity reduces the ductility of the electroplated metal. The electroplate may then rupture and cause failure of the

underlying metal. Copper, nickel, and cobalt electroplated layers are particularly susceptible to the problem.

One cause of the porosity is the release during heat treatment of gases entrapped during the electroplating process. Therefore, a likely solution is to subject plated parts to hot isostatic pressing, which is a heat treatment involving the simultaneous application of high pressure. To test this idea, a copper-plated part was heated to 800° C at a pressure of 23,000 psi (160

MN/m²) for 4 hours. When the part was examined metallographically, it was completely free from porosity.

This work was done by Neil Paton and Cecil Rhodes of Rockwell International Corp. for **Marshall Space Flight Center**. No further documentation is available.

Inquiries concerning rights for the commercial use of this invention should be addressed to the Patent Counsel, Marshall Space Flight Center [see page A5]. Refer to MFS-19873.

Eutectic Contact Inks for Solar Cells

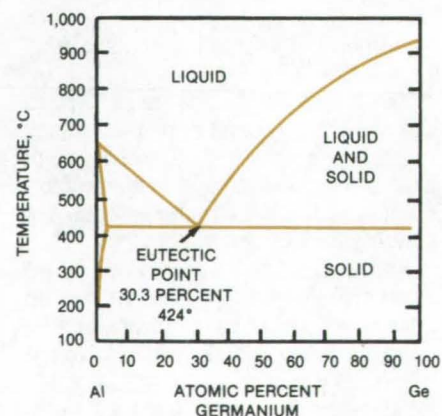
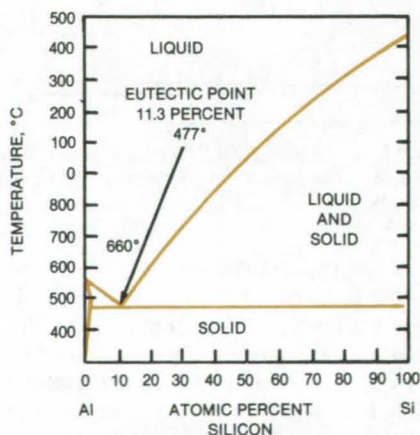
Contacts are formed without harming photovoltaic devices.

NASA's Jet Propulsion Laboratory, Pasadena, California

Low-resistance electrical contacts can be formed on solar cells by melting powders of a eutectic composition of semiconductor and dopant. The process will improve cell performance without subjecting a cell to processing temperatures high enough to degrade other characteristics.

An ink made from the powder is applied to the base of a solar cell by screening. The coated cell is heated to about 550° C, then is allowed to cool. (For a powder of silicon semiconductor and aluminum dopant, the eutectic melting point is 477° C; and for germanium and aluminum, it is 424° C.)

As the molten liquid cools back toward the eutectic melting point, it can hold less and less of the semiconductor (see figure). The silicon or germanium thus precipitates epitaxially on the cell.



Phase Diagrams for Al/Si and Al/Ge show how the concentration of the Si or Ge in the liquid decreases as the temperature decreases.

When completely solidified, the contact consists of a thin layer of aluminum on a thin epitaxial layer of semiconductor on the silicon cell. The contact resistance is somewhat lower for a germanium/aluminum contact than for a silicon/aluminum contact: 2×10^{-4}

Ω/cm^2 vs. $3 \times 10^{-4} \Omega/\text{cm}^2_{\text{cm}}$ when applied as part of a copper screening ink. In addition to a lower contact resistance, the germanium eutectic has the advantage of a lower melting point, permitting lower temperature processing.

This work was done by Bernd Ross of Bernd Ross Associates for NASA's Jet Propulsion Laboratory. For further information, Circle 74 on the TSP Request Card.
NPO-15171

Lightweight High-Temperature Thermal Insulation

Fine Ni/Cr fibers are sintered into a corrosion-resistant, fireproof batt.

Marshall Space Flight Center, Alabama

A new thermal-insulation material is constructed by partially sintering $8\text{-}\mu\text{m}$ fibers of nickel/chromium alloy (Nichrome alloy, or equivalent) into a batt with a density only 2.5 percent that of solid alloy. Possible applications include stoves, furnaces, safes, fire clothing, draperies in public buildings, wall firebreaks, airplane walls, and jet-engine components.

The new insulation takes advantage of some of the same properties of nickel/chromium alloy that make it useful in heating elements in toasters; namely, corrosion and oxidation resistance even at high temperatures. Other desirable properties include the following:

- Withstands temperatures up to about $2,000^\circ\text{F}$ ($1,100^\circ\text{C}$);
- Has low thermal conductivity;
- Is very lightweight; and
- Is resistant to solvents, oils, soaps, and water.

The insulation was manufactured in layers one-eighth in. (3.2 mm) thick and tested in a double layer one-fourth in. (6.4 mm) thick. During the thermal performance tests the insulation was retained between two layers of 100-mesh (sieve opening 0.149 mm, wire diameter about 0.1 mm) square-weave Nichrome V wire screening. The screening was included because in the initial application in an airplane engine such screening was required to hold the insulation in place.

Thermal-conductivity data are shown in the table both for a sample of the virgin material and for a sample that had been exposed to water, hydraulic-oil,

Temperature		Gas Pressure		Thermal Conductivity			
				Virgin		Treated	
$^\circ\text{C}$	$^\circ\text{F}$	psia	kN/m^2	$\frac{W}{\text{m-k}}$	$\frac{\text{Btu-in.}}{\text{h-ft}^2\text{-}^\circ\text{F}}$	$\frac{W}{\text{m-k}}$	$\frac{\text{Btu-in.}}{\text{h-ft}^2\text{-}^\circ\text{F}}$
427	800	14.7	101	0.110	0.76	0.118	0.82
427	800	11.0	76	0.107	0.74	0.116	0.80
427	800	10.0	69	0.105	0.73	0.115	0.79
871	1,600	14.7	101	0.25	1.73	0.26	1.80
871	1,600	0.2	1.4	0.23	1.59	0.235	1.63
871	1,600	0.1	0.69	0.185	1.28	0.20	1.39
871	1,600	0.05	0.34	0.17	1.18	0.175	1.21
1,093	2,000	14.7	101	0.38	2.63	0.385	2.67
1,093	2,000	0.2	1.4	0.35	2.43	0.35	2.43
1,093	2,000	0.1	0.69	0.265	1.84	0.285	1.98
1,093	2,000	0.05	0.34	0.240	1.66	0.250	1.73
427	800	14.7	101	0.115	0.80	0.120	0.83

The Thermal Conductivity of Nickel/Chromium Batt Insulation has been measured both for a virgin sample and a sample that had been exposed to water, hydraulic-oil, salt-spray, and temperature-cycle treatments. The combined effect of these treatments on the steady-state thermal conductivity at elevated temperatures was quite small.

salt-spray, and thermal-cycle treatments. The treatments caused a decrease of insulation thickness, but the consequent increase in thermal conductivity was nearly offset by a decrease in fiber-to-fiber conductance. The combined effect of all environments on the steady-state thermal conductivity at

high temperatures appears to be insignificant.

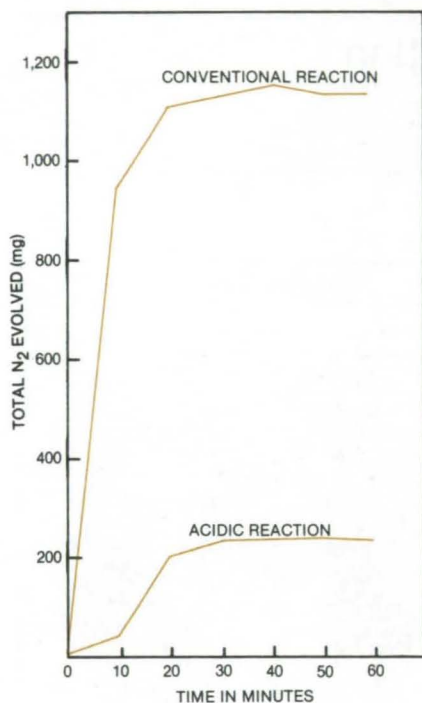
This work was done by William R. Wagner and John I. Fasheh of Rockwell International Corp. for Marshall Space Flight Center. No further documentation is available.
MFS-19754



Inhibiting Wet Oxidation of Ammonia

Loss of fixed nitrogen is reduced 80 percent by acidification.

Ames Research Center, Moffett Field, California



The **Inhibition of Ammonia Oxidation** in the wet-oxidation process for treating organic waste material can be achieved by running the reaction at a pH of 3 or less. The acidic-reaction curve (taken at a pH of 2.1) shows only about one-fifth as much NH_3 was oxidized to N_2 as in the conventional unbuffered reaction.

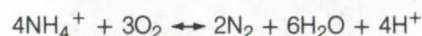
A simple modification of the wet-oxidation process for treating organic waste reduces the loss of fixed nitrogen, a potentially valuable byproduct of the process. The addition of sufficient sulfuric acid to maintain the reaction pH below 3 greatly reduces the oxidation of ammonia to free nitrogen. No equipment modification is required.

In the original patented commercial Zimpro wet-oxidation process, organic matter in a water-based suspension or solution, such as sewage, reacts with oxygen in air at 500° to 550° F (260° to 288° C) and 1,500 to 2,000 psi (10 to 14 MN/m²). The organic matter is oxidized to CO_2 and a variety of refractory organic compounds. Another patented version of the process uses lower temperature and pressure but achieves the same extent of reaction by stirring at the point of oxygen entry, maintaining acidity, and adding copper sulfate. Yet another version also uses acidity but adds nitrate and either bromide or chloride to accelerate oxidation. In all of these processes, the oxidation of carbon to carbon dioxide was the main goal: Little attention was paid to the fate of the fixed nitrogen.

The benefit of maintaining acidity became apparent in experiments monitoring N_2 evolution from $(\text{NH}_4)_2\text{SO}_4$ under conditions typical of the commercial process. The experiments were car-

ried out in an enclosed vessel made of 316 stainless steel, the material most commonly used in commercial wet-oxidation reactors. The vessel was pressurized with O_2 and heated to 527° F (275° C) while the contents were stirred. (Air containing the same amount of O_2 could have been used.) Ammonia oxidation was monitored by measuring nitrogen evolution.

During the reaction, the pH decreased from 6.2 to 2.1. The rate of N_2 production decreased rapidly with time as the reaction progressed, with the total evolution of N_2 reaching a plateau when only 30 percent of the initial NH_3 had reacted. The plateau was far from equilibrium for the system



Since the release of the H^+ ions gradually acidifies the medium, it was hypothesized that acidification might be responsible for the reduction in the nitrogen-evolution rate. To test this hypothesis, the acidity was maintained at 2.1 from the beginning by adding sulfuric acid. As shown in the figure, the overall nitrogen evolution was reduced by 80 percent.

This work was done by Dr. Bruce L. Onisko of the National Research Council for Ames Research Center. No further documentation is available. ARC-11407

Applying Uniform Polymer Coatings to Microspheres

Acoustic levitation yields an even coating on glass microspheres.

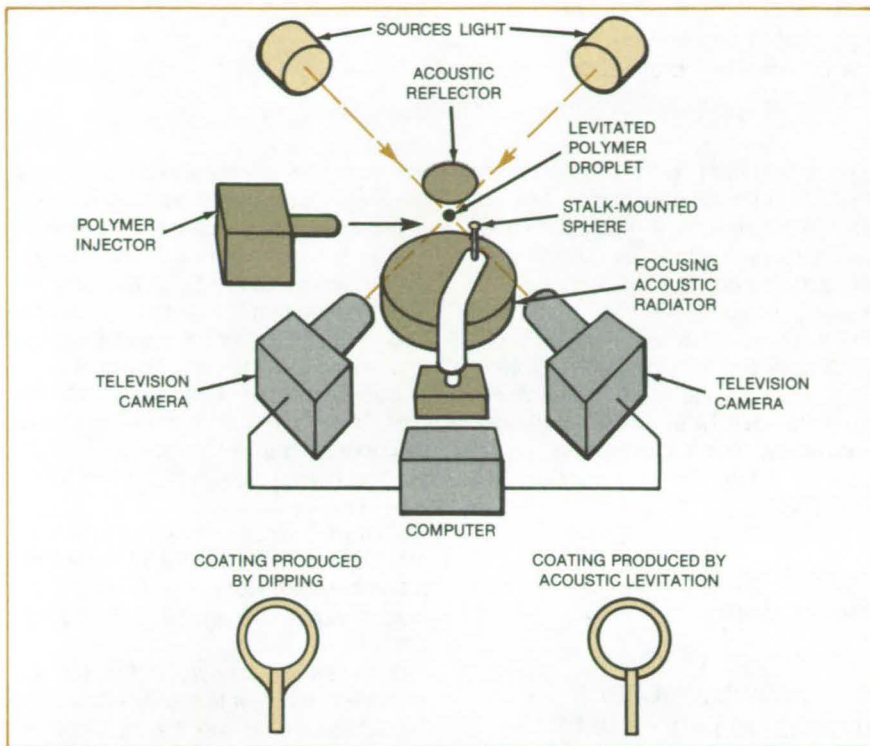
NASA's Jet Propulsion Laboratory, Pasadena, California

Acoustic levitation aids in applying uniform coatings of polymer to inertial-confinement fusion targets. The targets—stalk-mounted glass spheres containing deuterium and tritium—are used in research on fusion power generation. A sphere is about 200 microns in diameter,

and the polymer coating is 10 to 50 microns thick.

Dipping a sphere in liquid polymer is unsatisfactory because the coating becomes thicker at the bottom, where the stalk joins the sphere. The acoustic levitation method, in contrast, gives a coating of even thickness.

The polymer material, dissolved in a solvent, is sprayed into a focusing acoustic radiator (see figure), which transports the mist to the focal point and allows it to coalesce into a single droplet. The droplet is held in position by a stable acoustic levitating field.



This **Automatic Coating Apparatus** injects polymer into an acoustic levitator, moves a glass sphere into the polymer, dries the polymer, and removes the coated sphere. The apparatus then injects more polymer for coating another sphere, and the cycle repeats.

A glass sphere on its stalk is moved into the acoustic field by a three-dimensional positioner. The sphere penetrates the surface membrane of the droplet and thus becomes immersed in the levitated coating solution.

The process is controlled automatically. Two intense, narrow light beams illuminate the droplet in the field of view of two television cameras. As the sphere approaches and penetrates the droplet, the camera images are fed to a computer, which controls the manipulator to maintain the sphere at the center of the droplet until the polymer solidifies.

This work was done by Mark C. Lee of Caltech for **NASA's Jet Propulsion Laboratory**. For further information, Circle 75 on the TSP Request Card. NPO-16075

Books and Reports

These reports, studies, and handbooks are available from NASA as Technical Support Packages (TSP's) when a Request Card number is cited; otherwise they are available from the National Technical Information Service.

Defect Chemistry of $Hg_{1-x}Cd_xTe$

Control of defect concentrations is achieved by varying preparation conditions.

An investigation of defect chemistry of $Hg_{1-x}Cd_xTe$ is described in a NASA contractor report. A long-term objective is to attain the compositional uniformity, carrier concentration, and carrier lifetime required for the use of $Hg_{1-x}Cd_xTe$ in infrared imaging systems. The intermediate goal of this investigation was to correlate the nature and concentration of lattice defects with the physicochemical conditions of preparation; namely, the temperature, the partial pressures of the

constituent elements, and/or the dopant concentration.

Undoped, donor-doped, and acceptor-doped $Hg_{1-x}Cd_xTe$ samples were annealed at various temperatures in Hg atmospheres, then quenched to room temperature. Hall-effect and resistivity measurements were made at 77 K to determine the carrier concentrations and mobilities. The variation of the carrier concentrations as a function of the partial pressure of Hg and/or the dopant concentration was used to arrive at defect models.

It was found that native acceptor defects in $Hg_{0.8}Cd_{0.2}Te$ and $Hg_{0.6}Cd_{0.4}Te$ are doubly ionized and that native donor defects are negligible in concentration. These facts plus thermodynamic considerations lead to the conclusion that p-to-n conversion in undoped alloys is due only to residual foreign donors and not to native donor defects.

Incorporation mechanisms of Cu, In, I, and P were investigated. Cu and In appear to occupy only Hg lattice sites acting as single acceptor and single donor, respectively. I acts as a single donor occupying Te lattice sites. A large concen-

tration of In is incorporated as In_2Te_3 with only a small fraction acting as donors.

In crystals doped with I, a large fraction of I is paired with native acceptor defects. P acts as a donor at Hg lattice sites and as an acceptor at Te lattice sites or in the interstices. A majority of the P is present as neutral species.

Equilibrium thermodynamic constants for the intrinsic excitation reaction and for the incorporation of dopants and native acceptor defects have been established. These constants are consistent with all the experimental results on doped and undoped crystals. As a result of this investigation, it is possible to predict and control the nature and concentration of defects as a function of the preparation conditions.

This work was done by H. R. Vydyanath, D. A. Nelson, J. C. Donovan, P. Crickard, A. Barnes, R. C. Abbott, and R. A. Lancaster of Honeywell Inc. for **Marshall Space Flight Center**. To obtain a copy of the report, Circle 76 on the TSP Request Card. MFS-25851

MiniBriefs describe NASA innovations and reports in an abbreviated format. Readers desiring additional information on these items should request the Technical Support Packages (TSP's), available in most cases, which can be obtained by using the TSP Request Card at the back of this issue.

Low-Temperature Extraction of Oil From Shale

Technique increases recovery and energy efficiency.

A technique for extracting fuel from oil shale takes place at lower temperatures with higher recovery efficiencies than conventional shale processes. The process consists of pyrolysis of shale at 600° to 800° F (316° to 427° C) while the products are removed by a supercritical organic fluid. The principal product is kerogen, a bitumenlike material that can readily be refined to liquid fuels by conventional methods.

Advantages of the method are greater product yield and, because of the relatively low temperatures, minimal gas formation, smaller amounts of char byproduct, and less carbonate-rock decomposition. Up to 94 percent by weight of organic material in the shale is extracted.

The supercritical organic fluid is a dense gas created by heating an organic material above its critical temperature (that is, the temperature at which it can exist only as a gas regardless of pressure). Such fluids readily dissolve high-molecular-weight hydrocarbons.

This work was done by Leslie E. Compton of Caltech for NASA's Jet Propulsion Laboratory. For further information, Circle 77 on the TSP Request Card.

Inquiries concerning rights for the commercial use of this invention should be addressed to the Patent Counsel, NASA Resident Office-JPL [see page A5]. Refer to NPO-15656.

High-Temperature Coating for Titanium

Graphite reduces electrical resistivity.

An inorganic electrically conductive coating for protecting titanium substrates is thermally stable to 800° F (427° C) and has a solar absorbance and emittance greater than 0.80. The wet coating mixture is composed of a

graphite pigment with a potassium silicate binder solution and distilled water. The mixture is applied to the titanium surface with an air-driven spray gun and cured for 24 hours. The resulting coating has an electrical resistivity of less than 10^6 ohm-cm.

This work was done by Richard J. Mell and Yoshiro Harada of IIT Research Institute for NASA's Jet Propulsion Laboratory. For further information, Circle 78 on the TSP Request Card. NPO-16222

Predicting Polymer/Liquid Interactions

Calculations of liquid absorption by rubber vulcanizates agree with experimental results.

Elastomer seals that absorb fluid in hydraulic systems can expand and lose their original properties, such as rupture stress and rupture strain. Such changes can be predicted with a simple equation that calculates the quantity of liquid absorbed by a polymer. No experimental data are required. The equation allows calculation of the swelling of rubber vulcanizates by liquids, based on the knowledge of the chemical structure of the polymer and solvent. The calculated values agree favorably with the experimental data.

This work was done by Robert F. Fedors of Caltech for NASA's Jet Propulsion Laboratory. For further information, Circle 79 on the TSP Request Card. NPO-14874

Silicon Formation for Solar Cells

Reaction of sodium and SiF₄ yields silicon and sodium fluoride.

Highly pure silicon can be obtained for solar cells by a proposed technique that sprays liquid-sodium droplets into SiF₄ gas. The resulting freely flowing powder of silicon and sodium fluoride will not adhere to the reactor walls and

can be easily transferred to a melt separator to recover the silicon. Various approaches are suggested for initiating the reaction by either heating the sodium liquid or the SiF₄. The only requirement is that the reactor system be large enough so that the sodium droplets react completely and have a chance to cool before the solid product hits the reactor walls. The chamber walls should be cooled to prevent the sodium fluoride product from melting and building up on the walls.

This work was done by K. M. Sancier of SRI International for NASA's Jet Propulsion Laboratory. For further information, Circle 80 on the TSP Request Card.

Inquiries concerning rights for the commercial use of this invention should be addressed to the Patent Counsel, NASA Resident Office-JPL [see page A5]. Refer to NPO-14973.

Integrated Fuel Cell/Coal Gasifier

Fuel efficiency is maximized.

A conceptual powerplant design with a low-temperature coal gasifier coupled to a highly-exothermic fuel cell for the efficient production of dc power eliminates the need for oxygen in the gasifier and achieves high fuel efficiency with the recycling of waste heat from the fuel cell.

In the process, coal and fresh catalyst are fed to the fluidized-bed gasifier, which operates at 1,200° F (650° C) and produces coal gas containing methane, hydrogen, carbon monoxide and dioxide, and small amounts of hydrogen sulfide. After cleaning, the gas then enters the fuel cell where the electrochemical potential of hydrogen is used to produce dc power and high-level waste heat. Part of this heat is used in the catalytic reformation of methane to produce more hydrogen, and the rest is used to heat the gasifier.

This work was done by Joseph F. Ferrall of Caltech for NASA's Jet Propulsion Laboratory. For further information, Circle 81 on the TSP Request Card. NPO-16062

Elastomeric Cathode Binder

Porous flexible cathodes can be prepared using a polymer binder.

A soluble copolymer binder mixed with cathode material and a solvent forms a flexible porous cathode that can be used in lithium and Ni/Cd batteries. The cathode material such as TiS_2 is uniformly dispersed in the viscous ethylene/propylene copolymer solution at room temperature to form a paste. The paste is smeared onto a conducting cathode substrate and dried in vacuum to remove the cyclohexane or toluene solvent. Cathodes prepared by this process have a lower density due to the expanding rubbery binder and have greater flexibility than conventional cathodes. Preliminary tests show that these cathodes discharge above 80 percent of theoretical capacity, compared to 30 to 50 percent capacity with conventional cathodes. These cathodes cycle well and maintain mechanical integrity. The fabrication procedure is readily adaptable to scaled-up processes.

This work was done by Shiao-Ping S. Yen, David S. Shen, and Robert B. Somoano of Caltech for NASA's Jet Propulsion Laboratory. For further information, Circle 82 on the TSP Request Card.
NPO-15424

Activated Internal Gettering

Lifetimes of minority carriers in silicon wafers can be improved by annealing.

Dislocations due to liquid entrapment during silicon ribbon growth normally arise near the strip edges. These dislocations propagate into the web as it is pulled out of the melt. However, these dislocation arrays can be used as internal gettering centers following heat treatment to improve minority-carrier lifetime distributions. Heat treatment of silicon web ribbons, such as annealing in oxygen at 1,000° to 1,200° C for 1 hour considerably improves the efficiency of solar cells.

This work was done by James K. Liu, Guenter H. Schwuttke and Krishna M. Koliwad of Caltech for NASA's Jet Propulsion Laboratory. For further information, Circle 83 on the TSP Request Card.

This invention has been patented by NASA (U.S. Patent No. 4,401,505). Inquiries concerning nonexclusive or exclusive license for its commercial development should be addressed to the Patent Counsel, NASA Resident Office-JPL [see page A5]. Refer to NPO-15530.

Preparing InSb Substrates

Molecular-beam epitaxial substrates can be passivated by chloride film growth.

Substrates of InSb used for molecular-beam epitaxial preparation can be cleaned by forming a surface passivation layer followed by in situ thermal desorption at ~350° C. Formation of an indium chloride rather than an oxide passivating layer reduces the carbon contamination by 60 percent, cleans the surface more reproducibly, and enables the film to be thermally volatilized at lower temperatures. The chloride layer can be produced by direct chlorination, by chloride radicals in solutions, or by formation of a preliminary oxide layer followed by chloride substitution.

This work was done by Richard P. Vasquez, Blair F. Lewis, and Frank J. Grunthaler of Caltech for NASA's Jet Propulsion Laboratory. For further information, Circle 84 on the TSP Request Card.
NPO-16127

Cleaning the Walls of a Silane Reactor

A scraper is supported by a gas bearing.

A scraper removes silicon deposits from the inner walls of a silane reactor vessel. The scraper, which is held close to but not touching the reactor walls, is supported on a high-velocity gas stream. The cleaning action is accomplished by scraping high spots from the walls and

by blowing the silicon powder away. Previous scrapers made of stainless steel left traces of iron in the silicon. The new scraper can be made of such non-contaminating materials as quartz or even silicon.

This work was done by Kazuo A. Yamakawa of Caltech for NASA's Jet Propulsion Laboratory. For further information, Circle 85 on the TSP Request Card.

Inquiries concerning rights for the commercial use of this invention should be addressed to the Patent Counsel, NASA Resident Office-JPL [see page A5]. Refer to NPO-15851.

Stabilized Aluminum Titanate

Improved ceramic maintains its crystal type to 1,700 K.

A stable, potentially-inexpensive, cubic crystalline alpha aluminum titanate that shows no phase change to 1,700 K could be used in heat exchangers. The aluminum titanate high-temperature ceramic may be prepared by adding such stabilizing metal oxides as CaO, MgO, or Fe_2O_3 during formation to produce a cubic crystal structure. When properly stabilized, the resulting aluminum titanate will have a zero coefficient of thermal expansion. The particular stabilizing species must be selected with careful attention to crystal dimensions and bond angles of the alpha and beta phases of aluminum titanate.

This work was done by James E. Schroeder of Caltech for NASA's Jet Propulsion Laboratory. For further information, Circle 86 on the TSP Request Card.
NPO-16227

Molten-Salt Electrolysis

Hydrogen sulfide can be electrolyzed into hydrogen and gaseous sulfur.

The concept of electrolytic decomposition of gaseous hydrogen sulfide to yield gaseous sulfur at the anode and hydrogen gas at the cathode is considered.

(continued on next page)



The effectiveness and degree of separation of hydrogen and sulfur from hydrogen sulfide would be optimized as a function of various parameters, such as porosity of the carbon or graphite cathode, electrode overvoltages, temperature, and pressure.

The separator, which can be made of alumina or zirconia to fit into compartments between the anodes and cathodes, should be a porous nonconductor that would permit hydrogen sulfide permeation, but prevent mixing of hydrogen and sulfur. The separator should also be

resistant to corrosion or degradation by the gases.

*This work was done by D. Cubicciotti of SRI International for **NASA's Jet Propulsion Laboratory**. For further information, Circle 87 on the TSP Request Card.*

NPO-15535

Life Sciences



**Hardware,
Techniques, and
Processes**

- 503 Probe Follower for Moving Blood Vessels
- 504 Photographic Screening for Eye Defects

Probe Follower for Moving Blood Vessels

Probes would track vessel expansion and contraction with minimal perturbation.

NASA's Jet Propulsion Laboratory, Pasadena, California

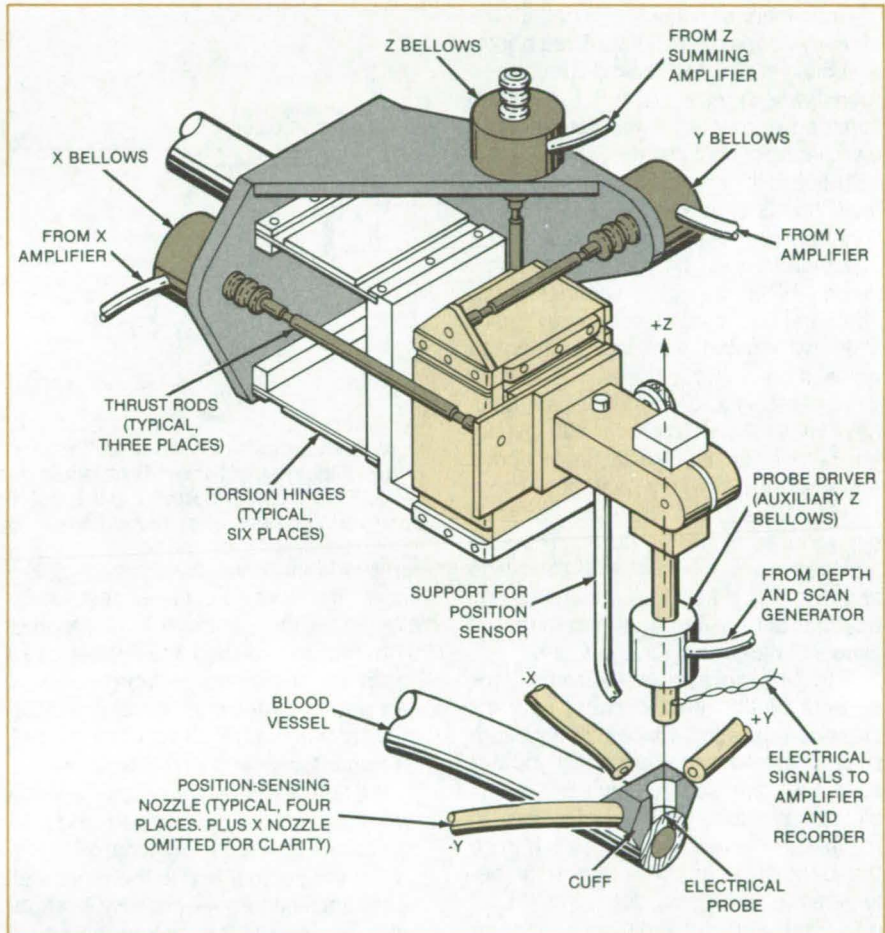
An electrical probe for medical research would be maintained at a fixed position relative to a moving blood-vessel wall by the proposed system shown in the figure. The objective is to keep the probe in contact with a region of tissue as the tissue moves, while minimizing the mechanical load on the tissue. The system would follow radial and axial blood-vessel motions.

As shown in the figure, a cuff is placed on the blood vessel at the probe position. Adjacent to the cuff, four small nozzles direct streams of distilled water, plasma, or other sterile liquid at 45° to the probe axis. The probe (z) axis is perpendicular to the wall at the probe entry point. Two of the streams oppose each other along the longitudinal (x) vessel axis, and two oppose each other across the vessel (on the y-axis).

The back pressure in each of the four fluid lines is fed to a fluidic amplifier. When a pressure imbalance is sensed between the two lines on the x (or y) axis, the amplifier feeds liquid into or out of a metal bellows that moves the probe along the affected axis back to a null position between the nozzles.

A radial (z-axis) motion of the vessel wall produces a symmetrical pressure change in all four lines. The symmetrical component of pressure is obtained by summing the pressure in all four lines. This pressure signal is fed to the bellows that controls the z-axis probe motion, thereby enabling the probe to track the vessel expansion or contraction.

The probe depth (z) could be varied at will with a stepping-motor-driven pump that feeds liquid into or out of an auxiliary z-axis bellows independently of the follower control system. Thus, the probe could be made to follow the vessel motion while scanning along a range of depths in response to an externally-generated control signal. The depth-control signal could also be used as the reference for a phase-lock amplifier to reject noise.



Nozzle Back-Pressure Changes at the Cuff on the blood vessel are the basis for monitoring the position of the probe in the blood vessel. Fluidic amplifiers use these signals to control a three-axis servo that centers the measuring probe between the sensing-nozzle pairs at the cuff.

While fluidic sensors are noncontacting, they impart distorting forces to the vessels through the pressure of the sensing liquid. If this is intolerable, an optical sensor could be substituted, especially if the surgical-insertion site could be kept immersed in a clear sterile fluid. In the optical-sensor version, position is sensed by the reflection of light from a reflecting reference surface attached to the blood vessel at the probed site. A fiber-optic

cable conducts the light to the site and transmits the reflected light to a photodiode. The photodiode signals are amplified to drive hydraulic signal generators, which then act on the hydraulic servos.

This work was done by Robert E. Frazer and Thomas W. Andrews of Caltech for NASA's Jet Propulsion Laboratory. For further information, Circle 88 on the TSP Request Card. NPO-15898

Photographic Screening for Eye Defects

Images of retinas are examined for characteristic patterns.

Marshall Space Flight Center, Alabama

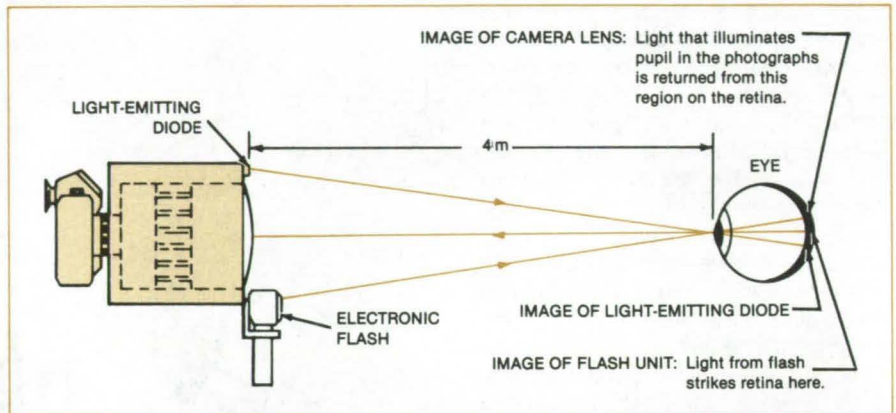
Ocular abnormalities are detectable in many cases by a standardized photographic test. The test, called "generated retinal reflex image system" (GRRIS), is intended primarily for the screening of elementary-school children.

The GRRIS exploits the "red-eye effect" that is caused by the reflection of light from the retina and that is usually a nuisance in color portrait photography. In the GRRIS, the eye is illuminated and photographed in color, making a 35-mm slide with sufficient magnification to reveal some of its features.

The testing apparatus consists basically of a 35-mm camera with a telephoto lens, an electronic flash, and a 4-m spacing bar with a head-positioning hood for the subject. The subject is asked to open his/her eyelids wide and to look at a flashing light-emitting diode that is mounted on the camera, as shown schematically in the figure.

The photograph is examined for defects of the lens, cornea, anterior chamber, or retina. Since both eyes are photographed simultaneously, ocular alignment can also be studied. The use of color film is necessary for detecting minimal refractive errors, determining the difference in refractive error between the two eyes, detecting retinal diseases, and determining alignment defects.

Abnormalities are revealed in the photograph through characteristic pat-



Color Photographs of Retinas are taken with an apparatus having this configuration. The proper alignment of the eye is obtained by asking the subject to gaze at the light-emitting diode. The "red-eye" patterns in the resulting color photographs are examined by trained observers for signs of ocular defects.

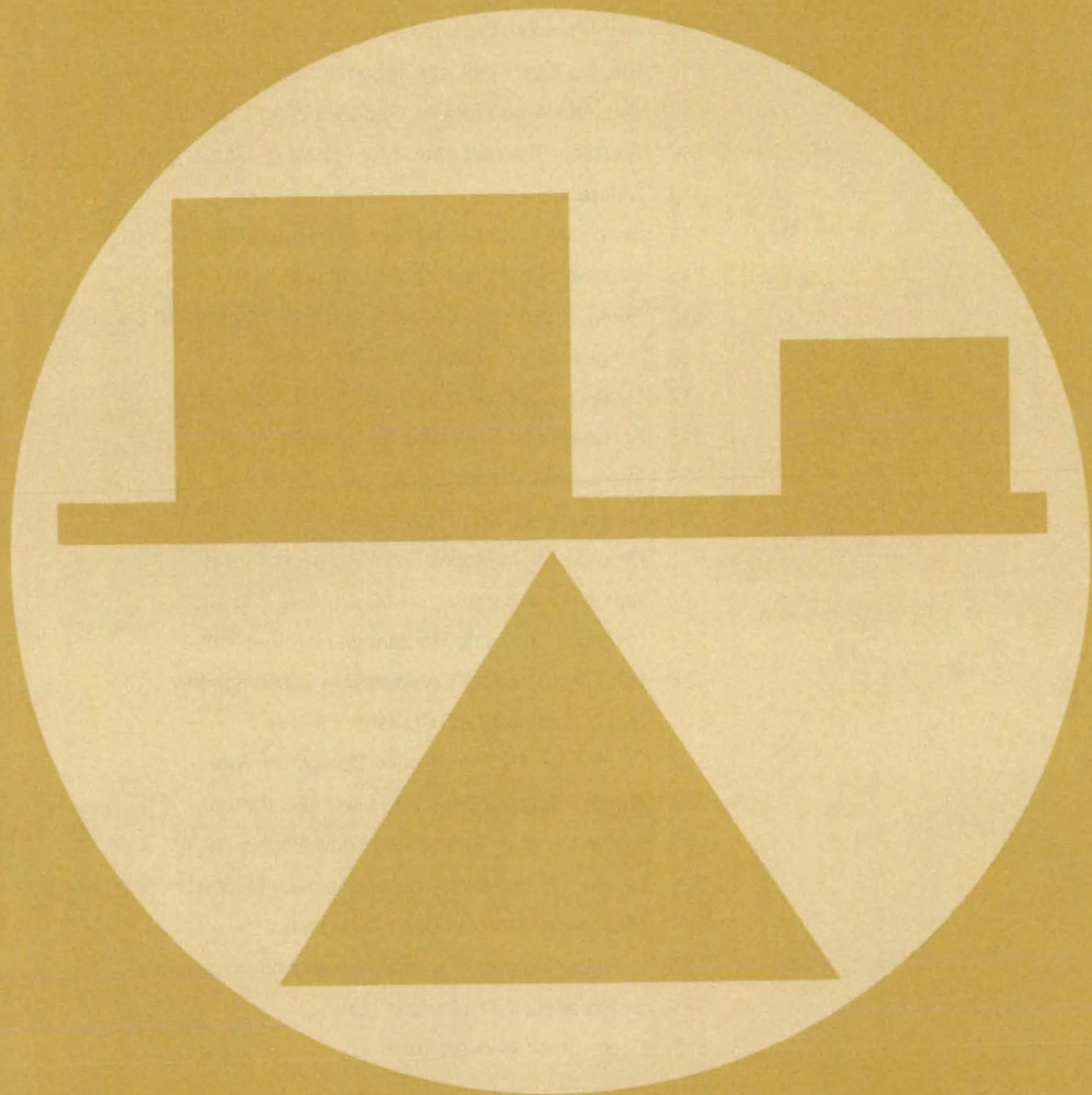
terns of light, dark, and color that are known from previous investigations. By examining the photograph (preferably with the aid of correctly diagnosed samples), a trained semiprofessional can detect hyperopia, myopia, strabismus, retinal-pigmentation color or pattern anomalies, and lens obstructions.

The GRRIS offers other advantages as well. It is portable, noninvasive, and non-hazardous. It requires minimal cooperation of the subject and is therefore well suited for children — possibly even infants. The cost of the photographic slide for each person is about 30¢ (1983 prices), or less if film is purchased in bulk. The system can also be used to check the

power of contact lenses and eyeglasses by taking the photographs with these items in place.

This work was done by John Richardson of Marshall Space Flight Center. Further information may be found in NASA TM-82359 [N83-34565/NSP], "Ocular Screening Tests of Elementary School Children" [\$8.50]. A paper copy may be purchased [prepayment required] from the National Technical Information Service, Springfield, Virginia 22161. The document is also available on microfiche at no charge. To obtain a microfiche copy, Circle 89 on the TSP Request Card. MFS-27045

Mechanics



Hardware, Techniques, and Processes

- 507 X-Ray Determination of Weld Misalignment
- 508 Insulation Debond Detection
- 509 Determining Thermal Diffusivities of Radiating Specimens
- 510 High-Pressure Coupling for Open-Ended Tubes
- 511 Brazing Alloys Indicate Turbomachinery Temperatures
- 512 Over-the-Wing Propeller Reduces Wing Drag
- 512 Reusable Thermal Barrier for Insulation Gaps
- 513 Differential Pressure Helps Seal Ball Valve
- 514 Specimen Holder for Analytical Electron Microscopes
- 515 Improved Coulomb-Friction Damper
- 515 Fuel-Conservative Descents Using a Programmable Calculator
- 516 Sting-Mounted Flow Survey Apparatus
- 517 Dynamic Calibration of Pressure Transducers
- 518 Acousto-optic Extensometer for Bolts
- 519 Integrated Exhaust-Gas-Analysis System
- 520 Multipurpose Photonic Transducers
- 521 Deriving Strain Modes From Vibrational Tests
- 522 Active Pulse Suppression of Structural Vibrations
- 523 Constant-Operating-Resistance Hot-Wire Probe
- 524 Hot-Wire Probe for Compressible Subsonic Flow
- 525 Measuring the Liquid Content of a Gas
- 526 Continuous-Filament Isogrid Composite Panel
- 527 Thermal-Balance Strip for Fluted LFC Panels
- 527 Silicone-Rubber Tooling for Hollow Panels
- 528 Quick-Change Holder for Aeronautical-Research Microphones
- 529 Microphone Detects Boiler-Tube Leaks
- 530 In-Place Calibration of Instrumentation Microphones
- 531 Synchronously Deployable Truss
- 532 Deployable Geodesic Truss

MiniBriefs

534

X-Ray Determination of Weld Misalignment

A simple technique uses ordinary X-ray equipment.

Lyndon B. Johnson Space Center, Houston, Texas

Misalignment between two hidden welded parts can be checked in many cases with the help of industrial X-ray equipment. The inspection technique was developed for spherical thin-wall nickel-alloy or aluminum pressure vessels that are fabricated by welding hemispheres together, then surrounded by insulation and encased in outer protective shells.

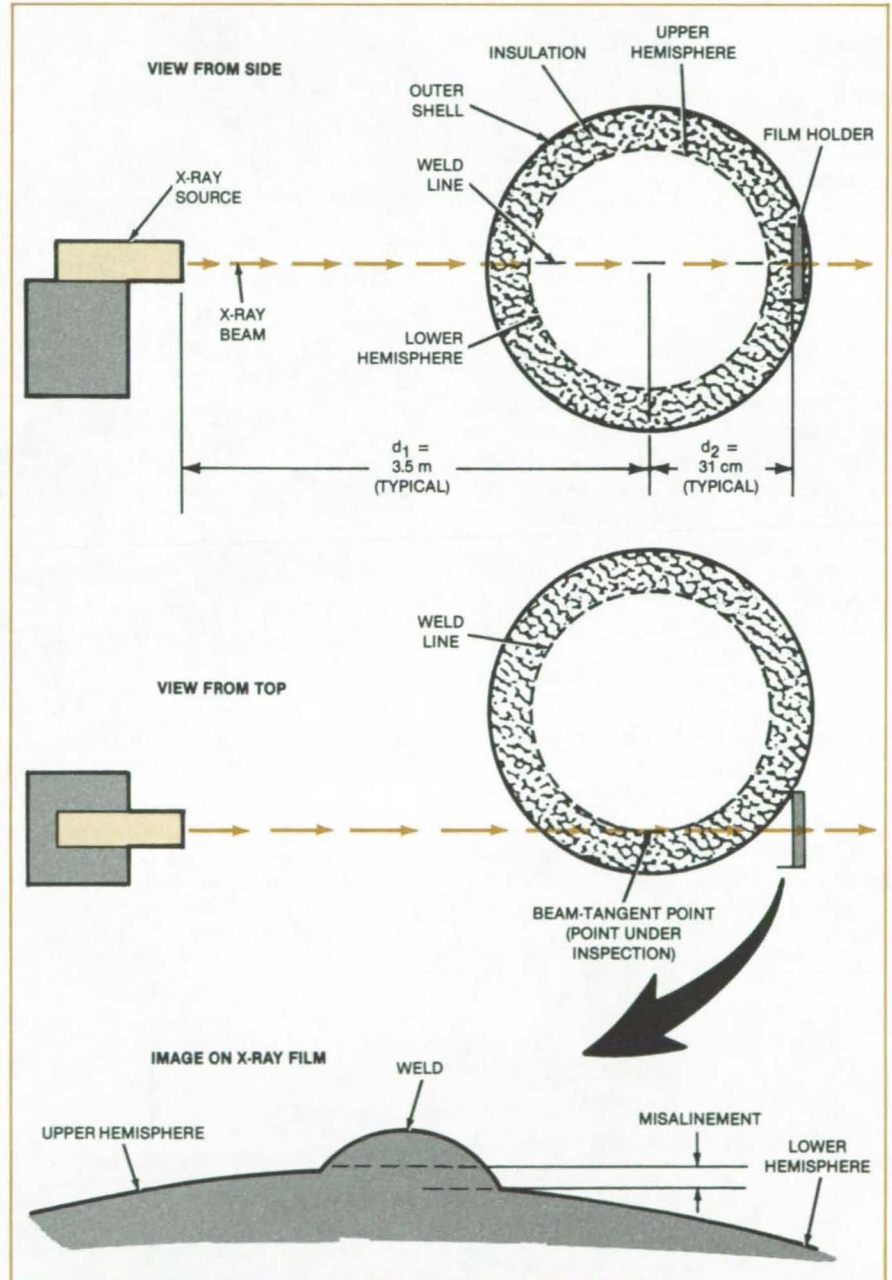
The pressure vessel is placed in a holder so that the central ray of the X-ray beam can be aimed tangent to the inner weld line at the point to be inspected (see figure). Beam aiming is done optically by reference to external features on the assembly that have known positions relative to the weld line. The X-ray filmholder is placed as close as possible to the tangent point. The center of the film is placed at or near the central ray, with the plane of the film perpendicular to the central ray.

An example with representative exposure parameters is provided by the original aluminum-pressure-vessel application. The inner and outer spheres have inside and outside diameters of about 1 m and 1.1 m, respectively. Wall thicknesses are about 3 mm. With the parts positioned as shown in the figure, an X-ray source of 260 kV and 9.5 mA, and an industrial X-ray film, the exposure time was 4 minutes.

The shadow on the X-ray film image has the appearance shown at the bottom of the figure. Misalignment between the top and bottom hemispheres is conveniently measured on an optical comparator. The measured misalignment is corrected for the X-ray magnification.

The technique is not limited to spheres. It can also be used, for example, to check alignment between insulated sections of pipelines or chemical-reaction vessels without removing the insulation or interrupting the flow or process.

This work was done by Charles W. Nelson of Beech Aircraft Corp. for Johnson Space Center. For further information, Circle 90 on the TSP Request Card.



A Weld Line Between Hemispheres of a hidden spherical pressure vessel is examined for misalignment between the hemispheres. The central X-ray is tangent to the pressure vessel at the weld line. A typical X-ray image of misaligned hemispheres would have the appearance shown at the bottom.

This invention is owned by NASA, and a patent application has been filed. Inquiries concerning nonexclusive or ex-

clusive license for its commercial development should be addressed to the Patent Counsel, Johnson Space Center [see page A5]. Refer to MSC-20418.

Insulation Debond Detection

Load-cell and acoustic responses indicate the bonding condition nondestructively.

Marshall Space Flight Center, Alabama

A nondestructive test for determining whether insulating material is bonded to its substrate or debonded involves measuring sound and load-cell responses to an impact. The technique was used to confirm the bonding of thermal-protection insulation to the Space Shuttle orbiter external tank.

In the new test, the sound and load-cell responses to a controlled impact on a small area of the insulation surface are analyzed for their frequency content. The load-cell measurement is the primary determinant of proper bonding, with the sound measurement used for confirmation. If the frequency response is above a certain threshold, the insulation is properly bonded; below this threshold, the insulation is either debonded or only partially bonded.

Figure 1 shows a version of the bond detector. The calibrated load cell, which measures the impact force, is mounted on the tip of a spring-driven plunger. The plunger is released when the operator presses the trigger. A microphone measures the sound of the impact.

Both signals are processed by a fast-Fourier-transform analyzer. It takes the amplitude-versus-time responses from the load cell and microphone and converts them in about 2 seconds to their respective amplitude-versus-frequency plots.

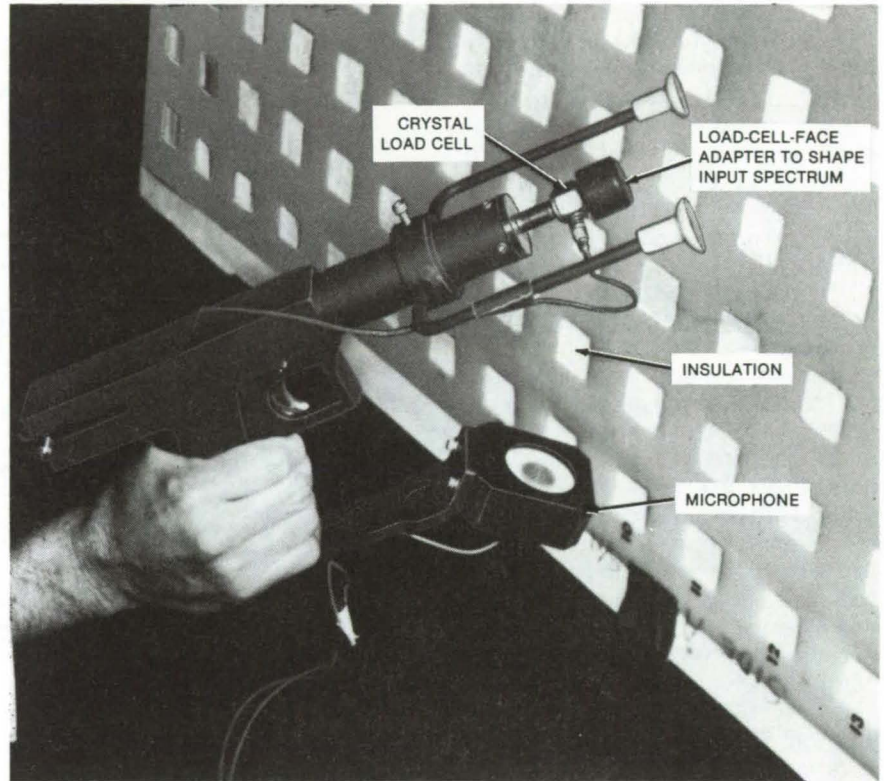


Figure 1. The **Load Cell and Microphone** measure the response of the insulation to a force pulse. The microphone measures sound created during the force period of vibration and during the subsequent period of free vibration. It is positioned at a 45° angle to the point of impact at a distance of 6 to 12 inches (15 to 30 cm) from the point of impact. The greater distance minimizes the structural modes of the substrate and allows the insulation response to be the dominant acoustic energy measured.

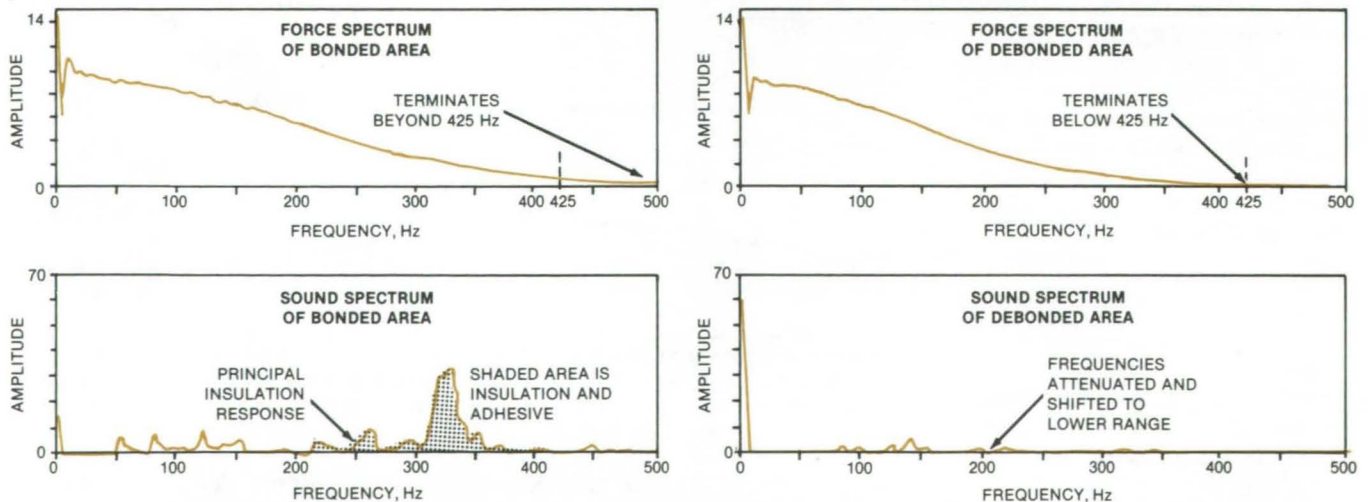


Figure 2. The **Signal Recorded by the Load Cell** is a direct and instantaneous measure of the local stiffness of the material at the point of impact. It is a separate and distinctly different measurement than that sensed by the microphone. The spectrum analysis of the pulse obtained from a debonded point will only show frequencies below 425 Hz because the insulation alone does not have the stiffness to support energy at higher frequencies.

For each spectrum, the operator observes the point at which the force spectrum terminates (see Figure 2). In the case of the insulation used on the Space Shuttle, it is 425 Hz. This is the first indication of bonding. To confirm this indication, the operator glances at the sound spectrum in the region of the insulation frequency. For the Space Shuttle

insulation this is in the range of 300 to 400 Hz for proper bonding.

This work was done by Garland D. Johnston, Archie D. Coleman, Joseph N. Portwood, Jerry M. Saunders, and Allan J. Porter of **Marshall Space Flight Center**. For further information, Circle 91 on the TSP Request Card.

This invention is owned by NASA, and a patent application has been filed. Inquiries concerning nonexclusive or exclusive license for its commercial development should be addressed to the Patent Counsel, Marshall Space Flight Center [see page A5]. Refer to MFS-25862.

Determining Thermal Diffusivities of Radiating Specimens

Two heat-pulse techniques eliminate uncertainties due to radiation losses.

NASA's Jet Propulsion Laboratory, Pasadena, California

Two heat-pulse techniques have been proposed for the measurement of thermal diffusivity and heat capacity in solid specimens at 700° C or hotter. These special techniques are needed because the radiation heat losses in this temperature range introduce uncertainties into conventional heat-flux measurements.

In the heat-pulse method, thermal energy is suddenly deposited in a thin surface layer on one side of a specimen

while the temperature is monitored as a function of time on the opposite surface. From the dimensions of the specimen and the time constant that characterizes the propagation of the heat pulse to the opposite side, the thermal diffusivity of the specimen can be calculated. If the

energy in the heat pulse is known or if the temperature is also monitored on the pulsed side, the specimen heat capacity can also be determined.

In one technique (see Figure 1), the heat pulse is applied by a flashlamp that illuminates the surface through a short-
(continued on next page)

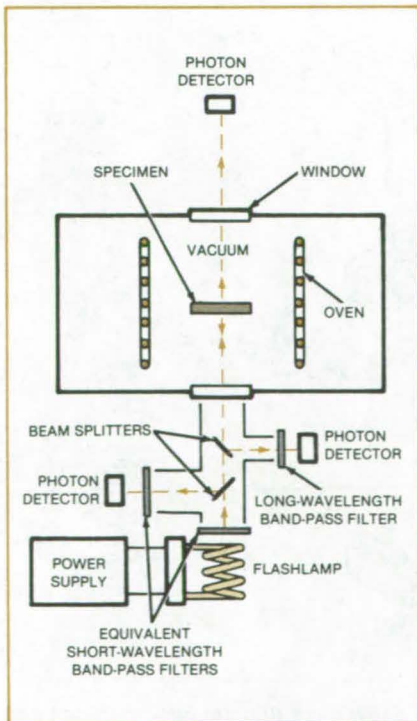


Figure 1. A Flashlamp Supplies a Pulse of Heat to one side of a specimen. The temperatures of the illuminated surface and of the opposite surface are then monitored photometrically.

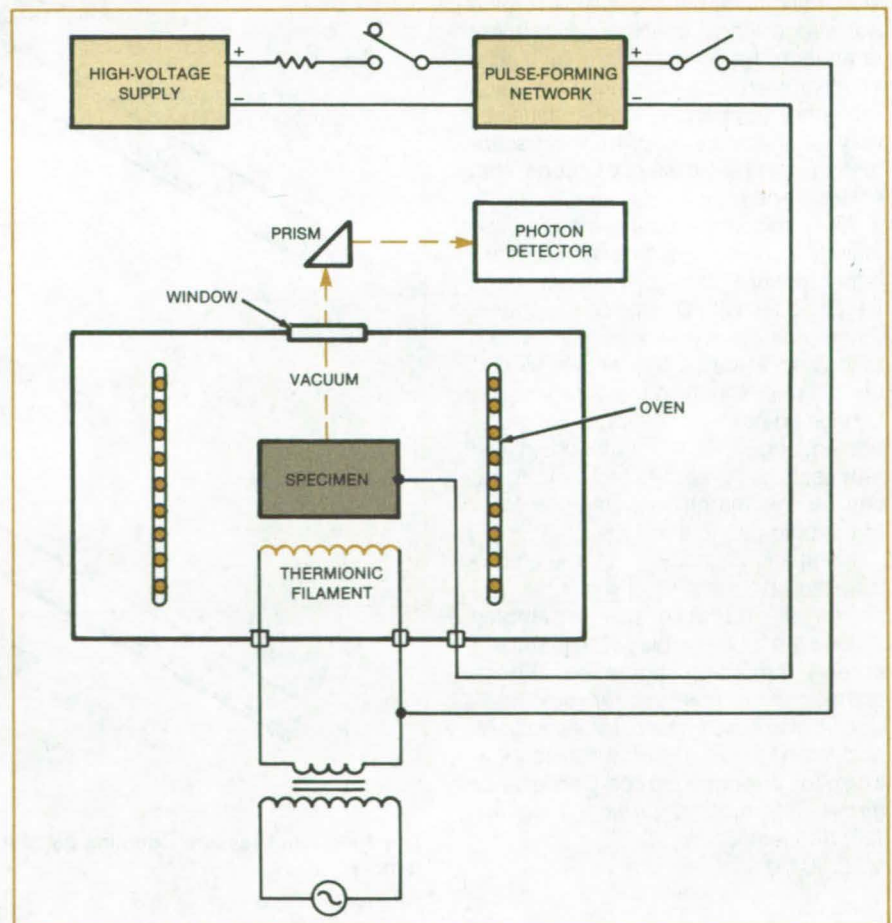


Figure 2. A Pulse of Electrons Supplies Heat to one side of a specimen. The temperature of the opposite side is monitored by a photon detector as in Figure 1.

wavelength band-pass filter. The thermal radiation from the specimen surface is monitored photometrically through a long-wavelength band-pass filter. A second photon detector measures the thermal radiation from the opposite specimen surface to determine its temperature.

The radiant energy reflected from the specimen is measured by a third photon detector. This is compared with the energy received by the same detector when placed directly in the path of the flashlamp to determine the energy ab-

sorbed by the sample. The optical filter in front of this detector has the same spectral characteristics as those of the flashlamp filter.

In the other method (see Figure 2), the heat pulse is applied by electron bombardment. The electrons originate at a filament near the specimen. A voltage pulse is applied between the filament and specimen to accelerate the electrons into the specimen.

The current and voltage versus time are measured to determine the energy deposited in the specimen. The heat

pulse is shaped by a pulse-forming network. The magnitude of the heat pulse can be set at any desired value from about 0.1 to 100 joules by adjusting the voltage. As in the first method, the temperature of the opposite specimen surface is monitored photometrically.

This work was done by Charles Wood, R. Addis Lockwood, and Katsunori Shimada of Caltech for NASA's Jet Propulsion Laboratory. For further information, Circle 92 on the TSP Request Card.
NPO-15436 and NPO-15441

High-Pressure Coupling for Open-Ended Tubes

A temporary fitting is easily installed and removed without damage to tubes.

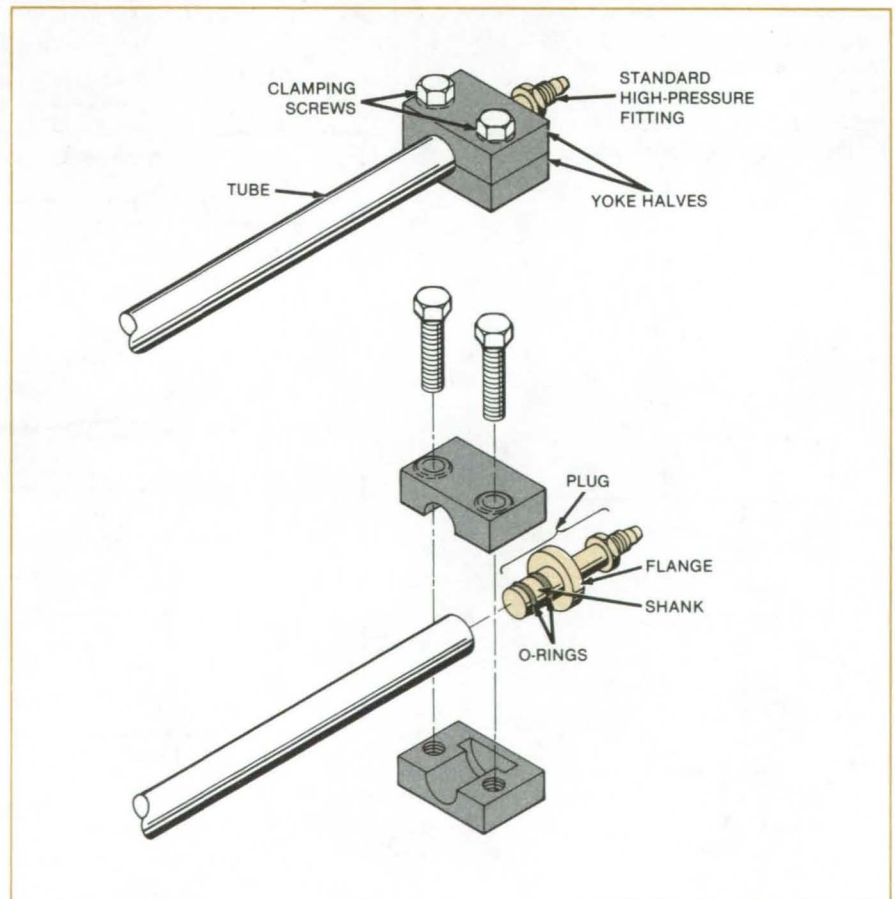
Lyndon B. Johnson Space Center, Houston, Texas

New high-pressure couplings are quickly installed or removed from round metal tubes. In contrast to compression fittings, the new couplings require no wedge rings or other permanent change in the ends of the tubing. The couplings are useful mainly for such repeated temporary connections as may be necessary for high-pressure testing or prestressing of tubes with finished ends.

As shown in the figure, the coupling includes a plug consisting of a standard high-pressure fitting installed in a flanged body with O-rings on the shank. The O-ring grooves and the shank are machined to close tolerances so that the plug fits snugly in the tube and the O-rings do not extrude under pressure. A clamping yoke is machined in two halves, each with semicylindrical cavities that match the outer diameters of the plug flange and tube.

Installation is easy. First, the plug is inserted into the end of the tube. The halves of the yoke are assembled around the tube and plug. The clamping screws are then tightened. These operations are reversed for removal.

This work was done by August N. Anderson of Rockwell International Corp. for Johnson Space Center. For further information, Circle 93 on the TSP Request Card.
MSC-20451



The **Tube-End Pressure Coupling** consists of a few parts that are easy to install and remove.

Brazing Alloys Indicate Turbomachinery Temperatures

Foils serve as consumable thermometers.

Marshall Space Flight Center, Alabama

Alloy Trade Name	Composition	Liquidus	Temperature	Solidus	Temperature
		°F	°C	°F	°C
Easy Flo	50 Ag/15.5 Cu/16.5 Zn/18 Cd	1,175	635	1,160	627
Easy Flo 45	45 Ag/15 Cu/16 Zn/24 Cd	1,145	618	1,125	607
Easy Flo 3	50 Ag/15.5 Cu/15.5 Zn/16 Cd	1,270	688	1,170	632
Bt	72 Ag/28 Cu	1,436	780	1,436	780
Silcoro 60	60 Au/20 Cu/20 Ag	1,553	845	1,535	835
Silcoro 75	75 Au/20 Cu/5 Ag	1,643	895	1,625	885
Nioro	82 Au/18 Ni	1,742	950	1,742	950
Nicoro	35 Au/62 Cu/3 Ni	1,886	1,030	1,832	1,000
Palniro 1	50 Au/25 Pd/25 Ni	2,050	1,121	2,016	1,102
Palniro 4	30 Au/34 Pd/36 Ni	2,136	1,169	2,075	1,135

Figure 1. **Commercial Brazing Alloys** have a range of melting points. No, partial, or complete melting of an alloy is used to indicate whether the temperature reached in a test was below, within, or above the liquidus-to-solidus temperature range of that alloy.

Foils of brazing alloy are used in a new technique for measuring temperatures in hot gas turbines. The technique can be used for temperature measurements on moving engine parts, in industrial process equipment, or at other locations where more complex instrumentation cannot be installed or the expense of such instrumentation is not justified.

The technique does not give precise or time-resolved temperature, but rather indicates approximately the maximum temperature reached during a test. The measurement is done with foils of brazing alloys having known melting temperatures (see Figure 1) in the range of 1,160° to 2,136° F (627° to 1,169° C).

To prepare a set of samples, foils of the various alloys 0.001 to 0.002 in. (0.025 to 0.051 mm) in thickness are cut into 1/8-in. (3.20-mm) squares. The samples are held in place behind tabs of stainless-steel foil that are spot-welded onto the object to be tested (see Figure 2).

A hole in the middle of each stainless-steel tab allows access to the sample. After the spot welding, a line is scribed in the exposed portion of each sample. The high-temperature test is then performed.

The samples are examined visually after the high-temperature test. If the scribed line has widened, narrowed, or disappeared, then partial melting has taken place, and the temperature must have reached a point in the solidus-to-liquidus range of the particular alloy. If the foil material is in a ball or lump or is

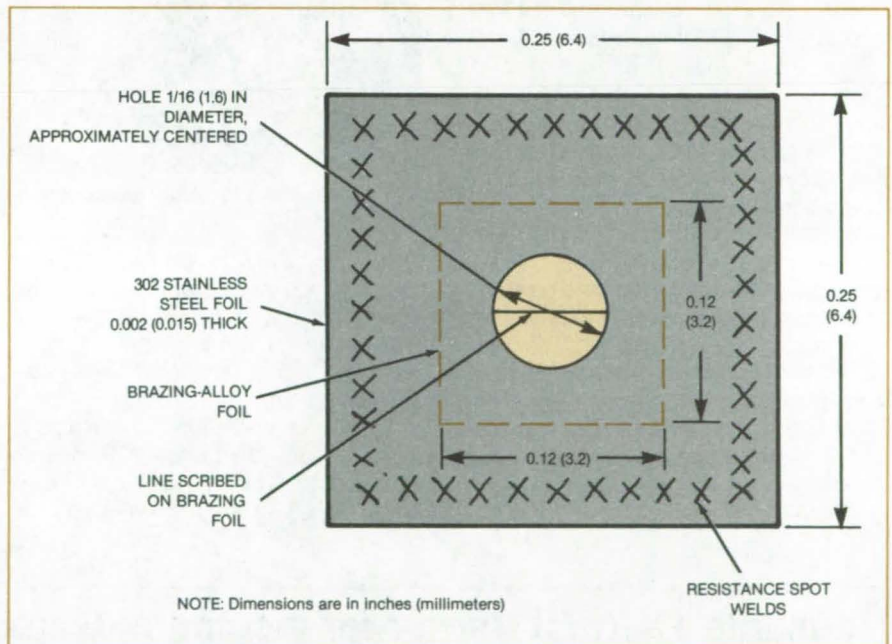


Figure 2. A **Stainless-Steel Tab With a Circular Window** holds a brazing-foil sample in place. The tab is tacked to the object to be tested with a capacitive-discharge spot welder operating in the range of 10 ± 1 joules.

welded to the object under test, then full melting has occurred, and the temperature must have risen above the liquidus point of the alloy. By examining the degree of melting in a set of samples with solidus-to-liquidus ranges that span the operating range, the approximate maximum temperature achieved can thus be found.

After the measurements, the tabs and samples can be chiseled off, leaving the

tested object fairly well intact. The technique can be used on objects made of alloys that can be resistance-spot-welded; for example, alloys with iron, nickel, or cobalt as principal ingredients.

This work was done by John W. Schlaff of Rockwell International Corp. for Marshall Space Flight Center. No further documentation is available. MFS-19792

Over-the-Wing Propeller Reduces Wing Drag

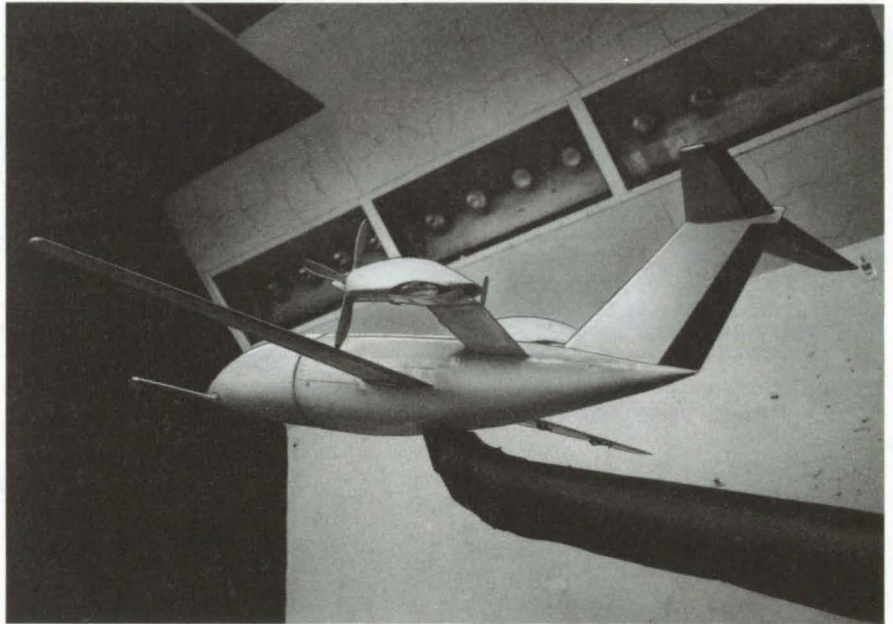
Airflow is favorably altered if the propeller is placed above and behind the wing.

Langley Research Center, Hampton, Virginia

A relocation of the engine/propeller on a propeller-driven airplane to above and behind the wing so that the rotating plane of the propeller is slightly behind the leading edge of the wing alters the airflow around the wing in such a way as to reduce the wind drag. The concept reduced drag significantly on an aircraft model in a 12-foot (3.7-meter) wind tunnel. This relocation may also help to reduce cabin noise.

Relocating the propeller induces flow over the wing airfoil leading edge, which in turn produces leading-edge suction forces not usually attainable by a wing in a free-stream flow. The result is a reduction in wing drag, which translates into improved aircraft performance and efficiency. Application of this concept to transport aircraft could result in significant improvement in performance during flight conditions involving high power settings such as during climbout.

Wind-tunnel tests were conducted with the three-surface commuter model shown in the photograph. The optimum propeller position was found to be such that the propeller plane was located at a wing chord station (x/c) of 0.2. This position provided maximum potential performance gains. The data indicate that propeller efficiency is not reduced at the climb flight condition due to the presence of the wing and that it is actually improved in the cruise regime.



An Over-the-Wing Propeller Model is shown here.

Another possible configuration for this concept is a forward-swept wing commuter aircraft to provide the wing-drag reduction and to permit a further-aft engine location for cabin noise considerations.

This work was done by Joseph L. Johnson, Jr., of Langley Research Center and Richard White of Kentron International, Inc. For further informa-

tion, Circle 94 on the TSP Request Card.

This invention is owned by NASA, and a patent application has been filed. Inquiries concerning nonexclusive or exclusive license for its commercial development should be addressed to the Patent Counsel, Langley Research Center [see page A5]. Refer to LAR-13134.

Reusable Thermal Barrier for Insulation Gaps

Filler is composed of resilient, heat-resistant materials.

Lyndon B. Johnson Space Center, Houston, Texas

A thermal barrier for tile gaps can be attached to its supporting structure by mechanical fasteners instead of with an adhesive. The barrier can therefore be removed and replaced without damage. Developed for filling spaces between tiles on the Space Shuttle in areas where occasional access to the interior is needed, the improved barrier may also be used in furnaces and kilns.

The barrier (see figure) includes an outer layer of a nickel-alloy wire mesh wrapped in ceramic cloth and an inner layer of fibrous bulk insulation. Both layers are bound in a ceramic cloth. A strip of aluminum 0.040 inch (1 mm) thick lies between the insulation and the outer cloth wrapping and is bonded with adhesive to the inside of the wrapping. Nut plates are installed at intervals along

the strip so that the barrier can be attached to a supporting frame by screws.

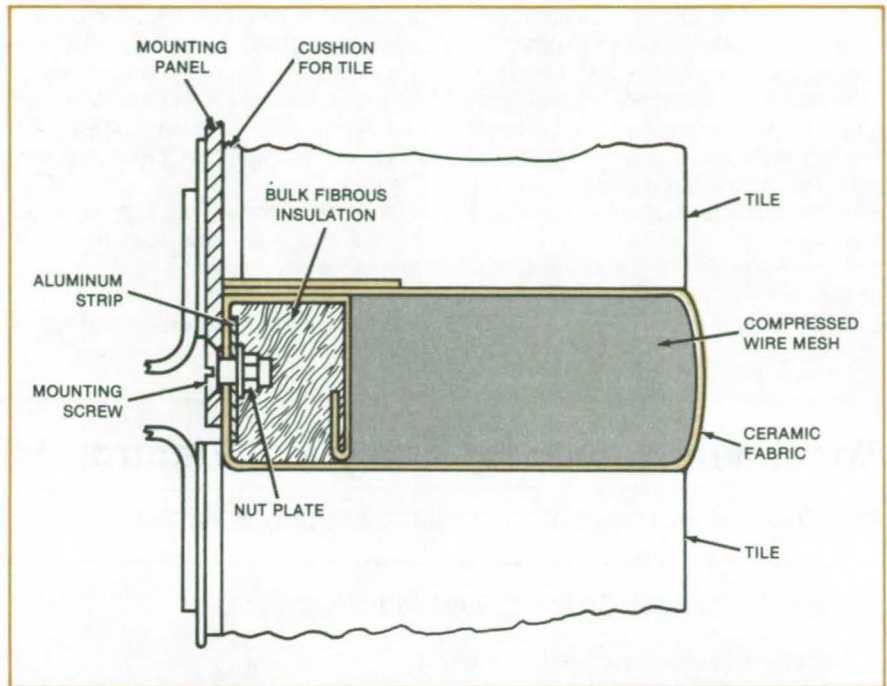
The wire mesh is compressible so that it conforms to the gap contours and remains essentially flush with the surfaces of the adjacent tiles. The fibrous layer provides a high thermal resistance so that the supporting structure does not become overheated.

The two-layer barrier described above can withstand maximum temperatures of about 750° to 1,000° F (400° to 540° C). For service at maximum temperatures of 350° to 750° F (175° to 400° C), the inner layer of insulation can be eliminated.

The ceramic cloth must be handled carefully during fabrication to prevent fraying of the edges. The fabric is cut to size by a laser beam that fuses the cut ends and is sewn with quartz thread. For protection during sewing, the fabric may be sandwiched between polyethylene films 0.002 in. (0.05 mm) thick. The films are removed when sewing is completed.

This work was done by Charles E. Saladee of Rockwell International Corp. for Johnson Space Center. For further information, including a detailed specification for fabricating the thermal barrier, Circle 95 on the TSP Request Card.

Inquiries concerning rights for the commercial use of this invention should be addressed to the Patent Counsel, Johnson Space Center [see page A5]. Refer to MSC-20519.



The **New Thermal Barrier** nestles snugly in the gap between two tiles with minimal protrusion beyond the surfaces of the surrounding tiles. When removed from the gap, the barrier springs back to nearly its original shape.

Differential Pressure Helps Seal Ball Valve

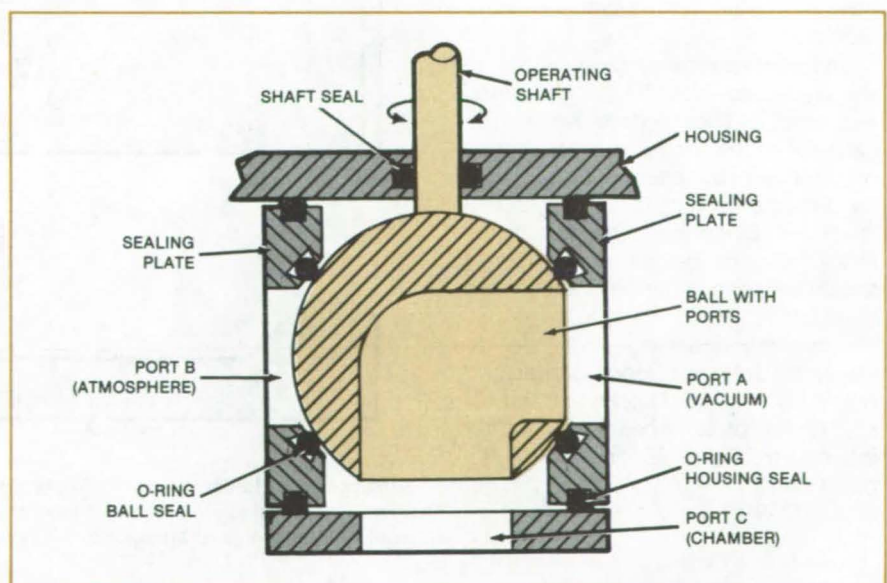
Leakage is suppressed despite O-ring wear.

Lyndon B. Johnson Space Center, Houston, Texas

An improved three-way ball vacuum valve uses atmospheric pressure to force the sealing parts together. The new design eliminates leakage in a vacuum selector valve on the Space Shuttle waste-control subsystem. It could be applied to improve sealing in laboratory and industrial vacuum systems and other plumbing that involves switching among lines with pressure differentials of the order of 1 atmosphere (0.1 MPa).

As shown in the figure, the valve connects the system at port C to either of the systems at ports A and B. In the case of a laboratory vacuum system, for example, the chamber would be reached through port C, the atmosphere through port B, and the vacuum through port A.

In contrast with prior vacuum ball valves, the seals do not depend on spring loading, elastic packing, or the maintenance of precise dimensions on wearing parts. Instead, the ball seals (continued on next page)



The **Sealing Plate at Port B** is pushed by atmospheric pressure toward the sealing plate at port A. This compresses the O-rings against the ball, thereby effecting a tight seal.

against standard O-rings seated in ring grooves in floating sealing plates. The floating design allows the plates and ball to move axially and press against each other. The pressure differential between the atmospheric and vacuum sides provides the steady force needed to compress the ball seals between the ball and the plates.

Since the sealing force depends only on the atmospheric pressure, it remains constant, causing the O-rings to com-

press even when they are worn or have taken a permanent set from prolonged squeezing. The O-rings therefore seal effectively until they are completely worn out. A prototype valve was cycled 1,400 times with no sign of degradation in sealing capacity.

In addition to long life with no detectable leakage, the new valve design offers other advantages:

- The seals are easy to design and fabricate. No special parts or techniques

are required.

- Manual operation is facilitated by low torques.

- The O-ring material can be selected without special regard for resilience or compression setting.

- The seals are easily replaced.

This work was done by John K. Mangialardi of General Electric Co. for Johnson Space Center. No further documentation is available.

MSC-20615

Specimen Holder for Analytical Electron Microscopes

It reduces spectral contamination by spurious X-rays.

Lyndon B. Johnson Space Center, Houston, Texas

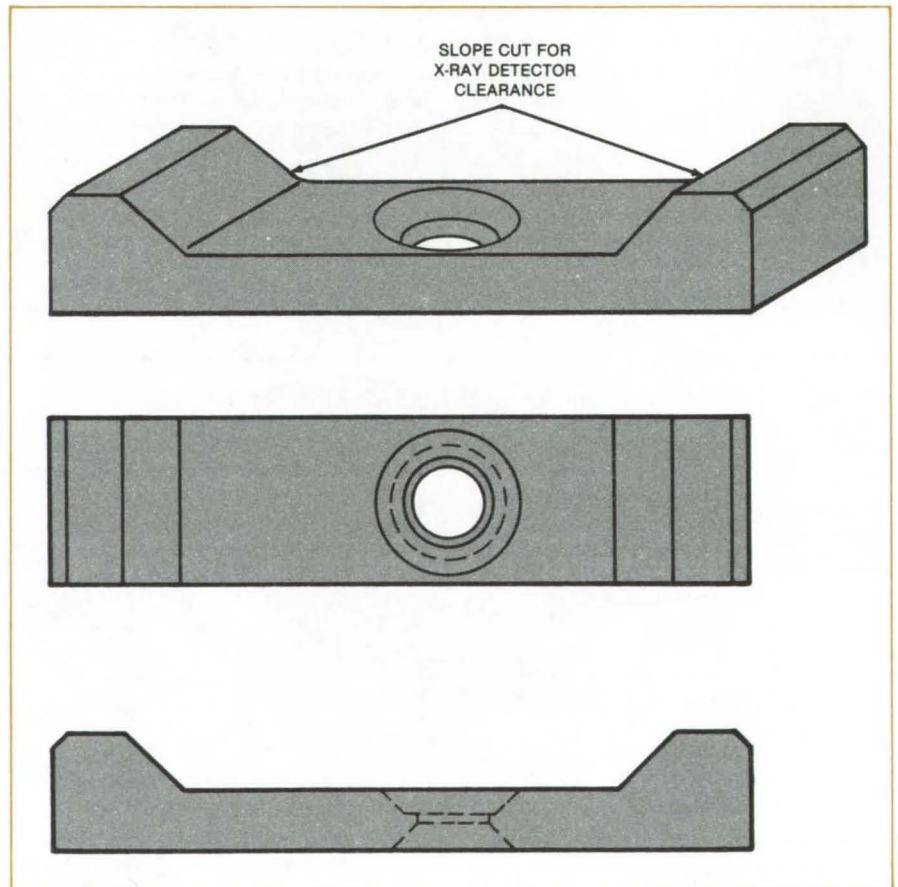
A specimen holder machined from a single block of compressed carbon retains a standard electron-microscope grid and reduces the formation of spurious X-rays near the specimen.

Most commonly, electron-microscope data are obtained by analyzing the X-rays generated in a sample exposed to a beam of electrons. Secondary fluorescence is induced in objects near the sample by X-rays generated in the sample and by electrons backscattered from the sample. This secondary fluorescence can refluoresce the sample or enter the X-ray detector directly, thus interfering with quantitative data reduction.

The new specimen holder, shown in the figure, absorbs the backscattered electrons and low-energy X-rays. Because of its low atomic number, it does not produce high-energy line radiation that would contribute to the X-ray detector output. Since the holder is inexpensive, it can be dedicated to a single specimen when numerous samples are to be examined.

This work was done by Uel S. Clanton of Johnson Space Center, and Andrew M. Isaacs of Lockheed, and Ian MacKinnon of Microbeam. For further information, Circle 96 on the TSP Request Card.

MSC-20398



The **Specimen Holder**, made of compressed carbon, securely retains a standard electron microscope grid (disk) 3 mm in diameter and absorbs the backscattered electrons that would otherwise generate spurious X-rays.

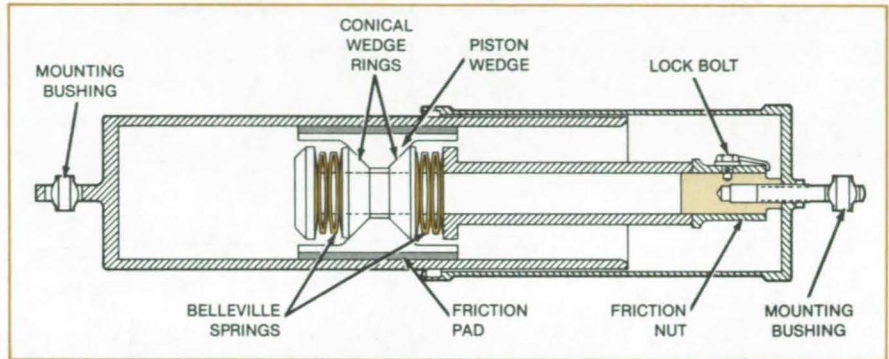
Improved Coulomb-Friction Damper

Equal damping is provided on forward and reverse strokes.

Lyndon B. Johnson Space Center, Houston, Texas

An improved coulomb (sliding) friction damper resists motion equally on both the forward and reverse strokes. An earlier version with unbalanced friction is described in "Coulomb Friction Damper" (MSC-20179), *NASA Tech Briefs*, Vol. 7, No. 2, p. 196. Unlike conventional automotive shock absorbers, which they resemble on the outside, both versions require no viscous liquid and operate over a wide temperature range of -110° to $+250^{\circ}$ F (-80° to $+120^{\circ}$ C).

The improved version (see figure) has two Belleville springs — one on either end of the piston wedge. The wedge therefore pushes the friction pad outward against the cylinder with equal force in both directions of travel, resulting in equal sliding friction in both directions. The earlier version included only one spring, with the result that the friction force was lower when the direc-



The **Improved Damper** has springs and wedge rings symmetrically placed on both ends of the piston wedge, so that the friction force will be the same in both directions of travel.

tion of motion was such as to increase the spring compression.

This work was done by George E. Campbell of Rockwell International Corp. for Johnson Space Center. For further information, Circle 97 on the TSP Request Card.

This invention is owned by NASA, and a patent application has been filed. Inquiries concerning nonexclusive or exclusive license for its commercial development should be addressed to the Patent Counsel, Johnson Space Center [see page A5]. Refer to MSC-20505.

Fuel-Conservative Descents Using a Programmable Calculator

An airborne descent algorithm may be used with or without time constraints.

Langley Research Center, Hampton, Virginia

An algorithm compatible with time-based metering and profile-descent procedures accurately delivers an airplane to a metering fix at a time designated by the air traffic control system. This algorithm provides open-loop guidance for an airplane to make an idle-thrust clean-configured descent to arrive at the metering fix at a predetermined time, altitude, and airspeed. The algorithm may also be used for planning fuel-conservative descents when time is not a consideration.

The descent algorithm is configured for the Federal Aviation Administration automated time-based metering form of air traffic control with profile descent procedures for arrivals into the terminal area. These concepts provide fuel savings by matching the airplane arrival

flow to the airport acceptance rate through time control computations and by allowing the pilot to descend at his discretion from cruise altitude to a designated metering fix in an idle-thrust clean (landing gear up, flaps zero, and speed brakes retracted) configuration.

Substantial fuel savings have resulted from these procedures, but air traffic control workload is high since the radar controller maintains time management for each airplane through either speed control or path stretching with radar vectors. Pilot workload is also high since the pilot must plan for an idle-thrust descent to the metering fix using various rules of thumb.

The new algorithm was programmed on a small, hand-held, programmable calculator. In a time-metered mode, the air-

borne algorithm computes the specific mach number, airspeed, and point for the pilot to begin the descent to arrive at a metering fix at a predetermined airspeed, altitude, and time assigned by air traffic control. In the nonmetered mode, the algorithm computes the point to begin the descent based on the mach number and airspeed descent speed schedule input by the pilot.

Flight-test results indicate that the open-loop guidance, provided to the pilot in the form of an indication of the approximate point to start the idle-thrust descent and the approximate mach and airspeed values to be used during descent, could be used to execute the descent. The resulting mean distance and time errors to achieve the predicted speed and altitude conditions at the end
(continued on next page)

of the descent profile for the T-39A Sabreliner were 1.2 nautical miles (2.2 km) long and 1.4 seconds early.

This work was done by Charles E. Knox of **Langley Research Center**. Fur-

ther information may be found in NASA TP-2085 [N83-17535/NSP], "Planning Fuel-Conservative Descents With or Without Time Constraints Using a Small Programmable Calculator" [\$8.50]. A

copy may be purchased [prepayment required] from the National Technical Information Service, Springfield, Virginia 22161. LAR-13138

Sting-Mounted Flow Survey Apparatus

The flow survey instrumentation is an integral part of the model support system.

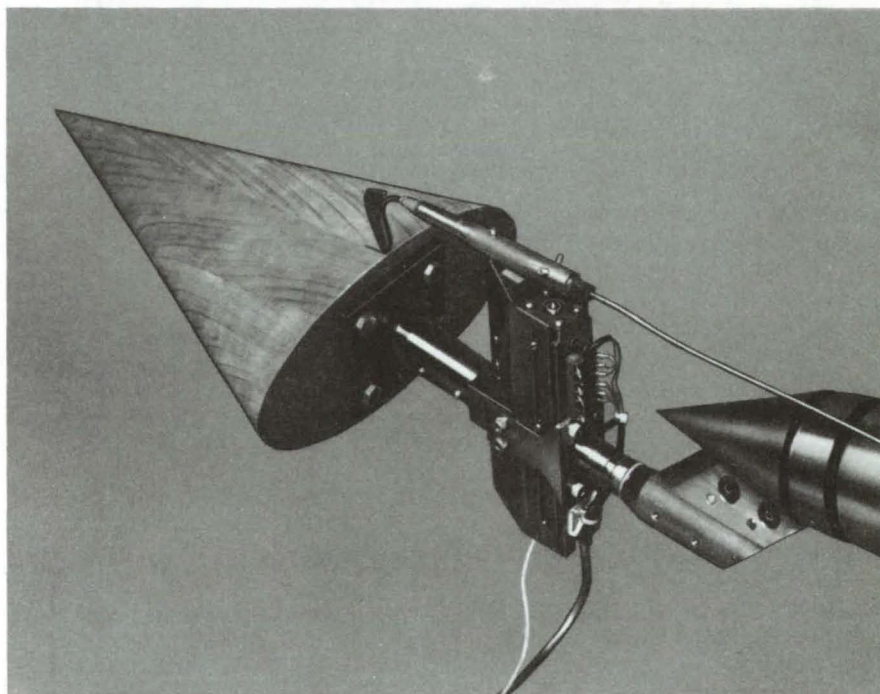
Langley Research Center, Hampton, Virginia

A sting-mounted flow-field apparatus in the Langley Research Center 22-inch (55.8-cm) Hypersonic Helium Facility can be positioned at any radial angle from 0° to 360° and can traverse a distance of 2 inches (5 cm). The drive motor, limit switches, and position transducer are all contained within the streamlined housing and are operable in the near vacuum of the wind-tunnel environment. Because the 22-inch facility uses helium at room temperature as its test gas, no water cooling is required.

The sting-mounted system has several advantages over the conventional wall-mounted flow-field survey equipment, including more efficiently utilized run time, higher position accuracy, and fewer runs to map the flow field.

By being an integral part of the model support system, there is no relative motion between the probe and the model support system during a run. This allows the tunnel to be started with the probe physically in contact with the model surface. The conventional survey system, which is attached to the tunnel wall allowing relative motion between the probe and model, requires the tunnel to be started with the probe away from the surface and then driven to the surface before the actual flow-field survey can begin. In a blowdown facility like the 22-inch tunnel, where run time is on the order of 30 to 40 seconds, run time is utilized more efficiently by the sting-mounted system.

The streamlined compactness of the sting-mounted unit and its shielding by



The **Streamlined, Sting-Mounted Apparatus** contains the drive motor, limit switches, and probe-position transducer.

the model make the flow blockage less than that of the wall-mounted system. Also, the unity of the model and survey apparatus through the sting makes the measurement of the probe position relative to the model surface more accurate.

The capability of the sting-mounted apparatus to traverse perpendicularly to the model axis requires fewer runs to map the flow field than the wall-mounted system. Assuming each system surveys

from the same points on the model surface, both would have the same number of runs until the lateral extremity of the model is reached. To map the flow field beyond that point requires additional runs for the wall-mounted system.

This work was done by George C. Ashby, Jr., of **Langley Research Center**. No further documentation is available.

LAR-13157

Dynamic Calibration of Pressure Transducers

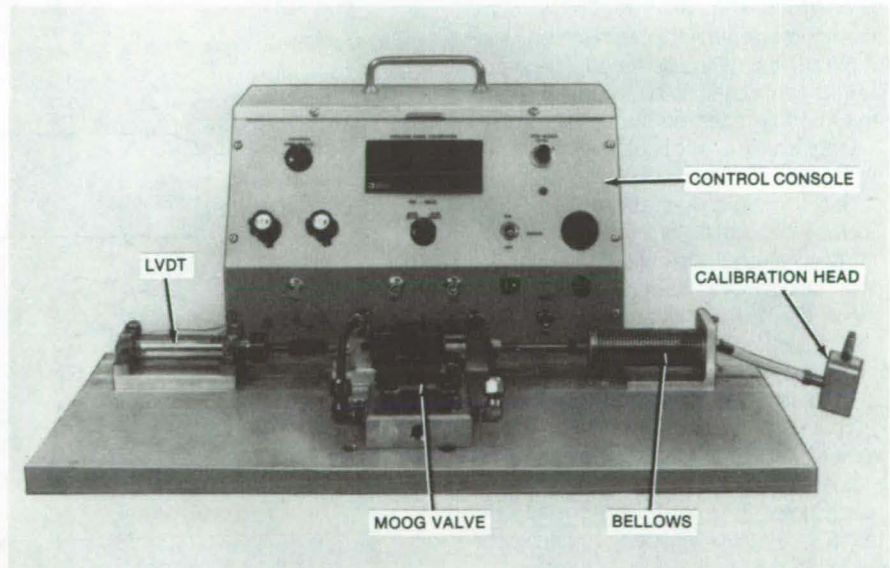
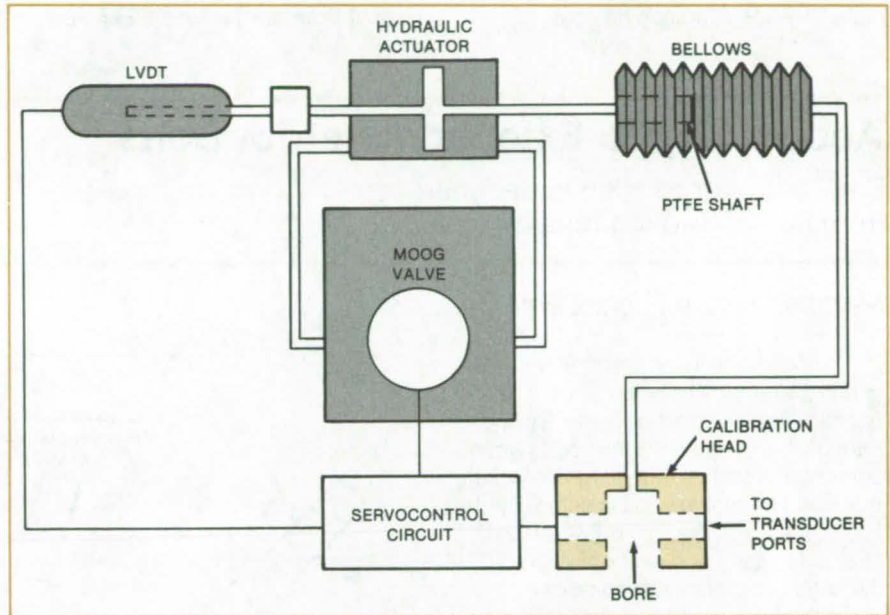
Sinusoidal calibration signal is produced in 4- to 100-Hz range.

Langley Research Center, Hampton, Virginia

A portable oscillating-pressure device measures the dynamic characteristics of pressure transducers installed in models or aircraft at the frequency and oscillating-pressure ranges encountered during unsteady-pressure-measurement tests. In unsteady aerodynamic pressure measurements, a dynamic measurement of the transducer sensitivity is needed to establish that the static and dynamic sensitivities are the same and to determine if the installation configuration affects the amplitude and phase response corresponding to conditions on the model surface. The pressure and frequency ranges of interest in unsteady aerodynamic pressure measurements are 0.1 to 2 psi (0.7 to 14 kN/m²) and 4 to 100 Hz, respectively. Previous techniques have been limited in that dynamic calibration could not be performed in situ at these frequencies and oscillating pressures.

The apparatus consists of a hydraulic actuator, a linear variable-displacement transformer (LVDT), a bellows with an internal polytetrafluoroethylene (PTFE) shaft, a Moog valve, a calibration head, and a control console (see the figure). A surface plate with a flush-mounted transducer is used in the initial checkout of the tube calibration-head configuration. One end of the hydraulic actuator shaft is attached to the free end of the bellows; the other end, to the LVDT, the output of which is a linear function of displacement; and one of the inputs, to the servocontrol circuit. The expansion and contraction of the bellows provides the oscillating pressure.

The cylindrical shaft attached internally to the moving end plate of the bellows makes the pressure output more linear with bellows deflection and serves as a guide to keep the bellows axially aligned in compression. A flexible tube 30 in. (75 cm) long, 1/4 in. (6 mm) I.D. connects the fixed end of the bellows to the calibration head. The reference pressure cell is flush-mounted to the bore of the calibration head that is the same diameter as the tube. The efficiency of the system is directly related to the volume of the tube between the bellows and the calibration head. A short tube extending from the bottom face of the



A Portable Transducer Calibrator, designed to operate in the difficult 4- to 100-Hz frequency range, is used for dynamic and static calibration of pressure transducers in model and real aircraft. The calibration head shown in the block diagram on the top supplies selected pressures at set frequencies to the transducer. The photograph on the bottom shows the assembled calibrator.

calibration head serves as a seal around the transducer orifice in the wing surface.

The servo feedback system that controls the Moog valve operates on the signal from either the LVDT (position of

bellows free end) or the signal from the reference transducer (reference pressure). Depending on the operating mode, the digital display registers either the bellows position or the pressure. Both peak and mean pressure values
(continued on next page)

are controlled, permitting both static and dynamic calibration of an in situ pressure transducer. Audible and visual alarm signals are preset to pressure amplitudes that would not damage the system from overextension or over-compression of the bellows. The calibration is over a range of frequencies and amplitudes not available with commercial acoustic calibration devices.

This work was done by Robert W. Hess, William T. Davis, and Pamela A. Davis of **Langley Research Center**. Further information may be found in NASA TM-85687 [N84-10538/NSP], "Portable Dynamic Pressure Generator for Static and Dynamic Calibration of In Situ Pressure Transducers" [7]. A copy may be purchased [prepayment required] from the National Technical In-

formation Service, Springfield, Virginia 22161.

This invention is owned by NASA, and a patent application has been filed. Inquiries concerning nonexclusive or exclusive license for its commercial development should be addressed to the Patent Counsel, Langley Research Center [see page A5]. Refer to LAR-13094.

Acousto-optic Extensometer for Bolts

Bolt torque or tension is deduced from noncontacting measurements.

Marshall Space Flight Center, Alabama

A noncontacting extensometer determines the length of a bolt with the help of optically-induced sound waves. By comparing the length of the bolt when tightened with the length when loose, the axial strain of the bolt is determined. From the relationship between axial strain, tension, and tightening torque, the latter two quantities can be deduced.

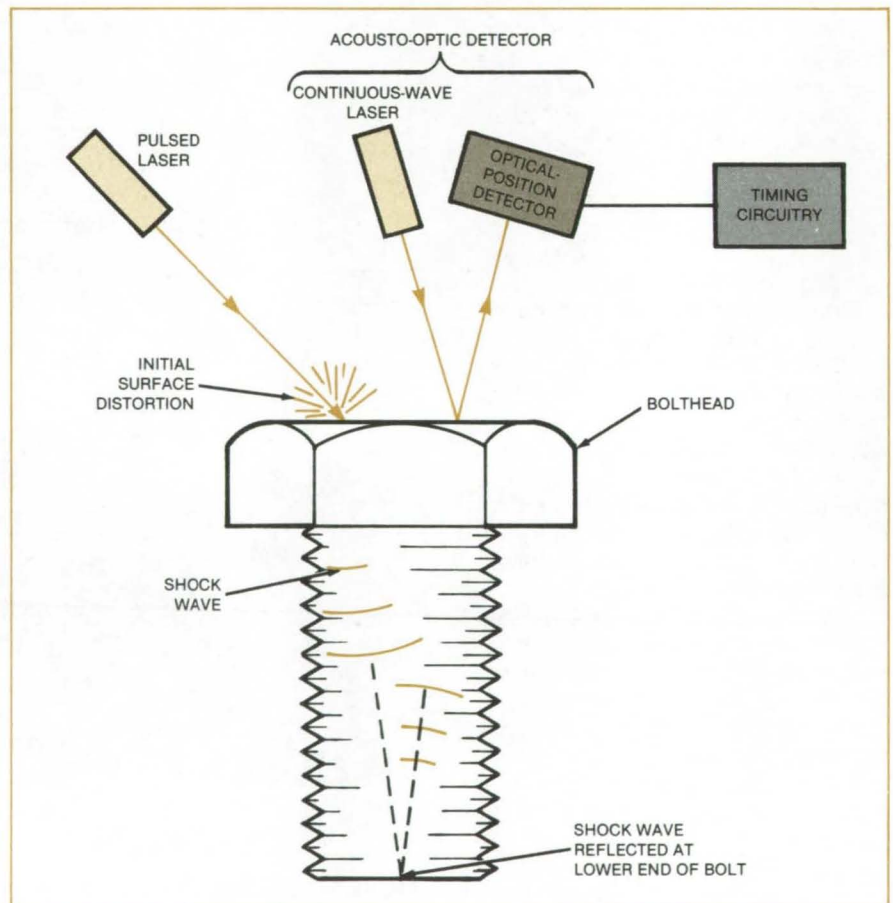
As shown in the figure, a pulse from a laser (for example, ruby or yttrium/aluminum/garnet) induces a shock wave at the surface of the bolthead. The shock travels along the bolt to the opposite end, then is reflected back to the head.

Light from a continuous-wave solid-state laser is reflected from the bolthead surface onto a solid-state light detector. Surface distortions produced by the initial and return shock waves deflect the continuous-wave laser beam, thereby giving rise to a position-change output from the detector. The time between the initial and return position-change signals is measured to obtain the bolt length.

This totally noncontacting extensometer for measuring bolt tension or extension can be applied to difficult-to-reach bolts. The solid-state position detector is relatively inexpensive and keeps down the cost of the extensometer.

This work was done by J. Maram and G. Kuhr of Rockwell International Corp. for **Marshall Space Flight Center**. No further documentation is available.

Title to this invention has been waived under the provisions of the National Aeronautics and Space Act (42 U.S.C. 2457(f)) to the Rocketdyne Division of Rockwell International Corp., 6633 Canoga Ave., Canoga Park, CA 91304. MFS-19914



A Pulsed Laser Induces a Shock Wave in the bolthead, while a continuous-wave acousto-optic detector monitors the distortion produced by the shock. The shock travel time along the bolt is measured to determine the bolt length.

Integrated Exhaust-Gas-Analysis System

Self-contained unit includes data processing and automatic calibration.

Lewis Research Center, Cleveland, Ohio

The output of continuous-sample-flow gas analyzers is a function of many variables. As a result, frequent adjustments are needed in many cases before every reading. When eight analyzers are operated together in one system, manual operation becomes unwieldy and automation is needed to insure reliability and accuracy.

An integrated gas-analyzer system has been developed that is designed for nearly unattended operation. Two microprocessors range the analyzers, calibrate the system, process the raw data to units of concentration, and make all system information available to the facility research computer and to the operator.

After initial setup, the system can operate for several hours without significant operator attention. The system is providing data for computing bulk temperature in the high-temperature combustor test facility at the Lewis Research Center, Cleveland, Ohio.

The system shown in Figure 1 contains eight slightly modified commercially available gas analyzers: carbon dioxide, two carbon monoxide, oxygen, water vapor, total hydrocarbons, and two nitric oxide. Two carbon monoxide analyzers are needed to cover the large CO measurement range with acceptable accuracy and two nitric oxide analyzers are needed so the system can simultaneously measure both nitric oxide and oxides of nitrogen.

The unique pneumatic design offers many advantages. As shown in Figure 2, the most important feature of this design is the vent to atmosphere so that all gases supplied to the analyzers are supplied at atmospheric pressure. The vent to atmosphere makes the system insensitive to variation in source flowrate and source pressure because any variation in those parameters simply results in variation of the flowrate in the vent. This atmospheric inlet feature also provides a known and relatively constant inlet pressure, and it allows inlet control valves to operate with zero pressure difference between ports. This eliminates leakage problems. A venturi pump pulls gas through the analyzer with a fixed

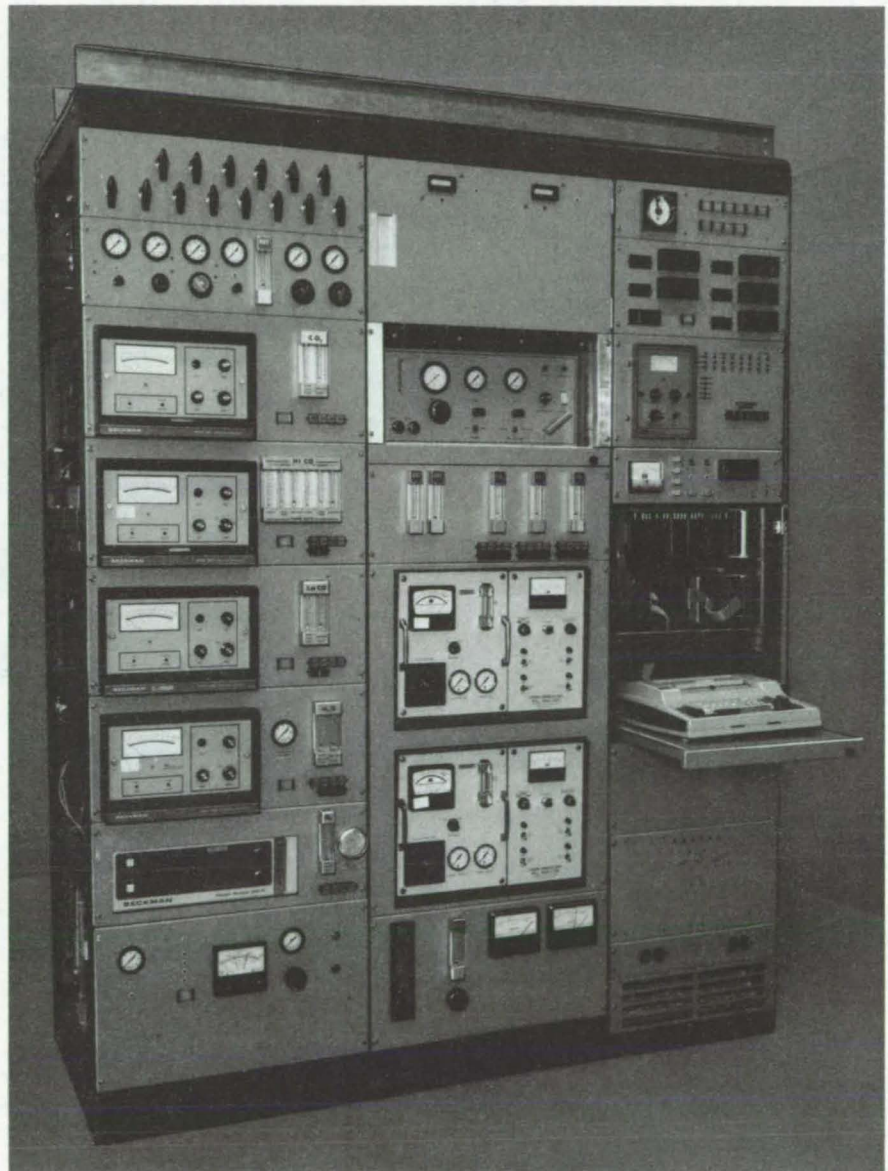


Figure 1. The **Gas-Analysis System** includes eight commercial gas analyzers and data-processing and calibration electronics.

restrictor inserted to control the flowrate.

The basic flow scheme is used in all the analyzers. There are, however, some deviations necessary because of the often large differences between analyzers and measurement techniques.

There are two calibration gases for each analyzer: a zero gas that in every case is dry nitrogen and a span gas with

a known concentration near full scale of the range used for calibration. The span gas for the water analyzer is generated within the system.

The system is modular: Throughout the design of both the hardware and the software, there is a high level of standardization. The resulting system is easy to test and to maintain. All major

(continued on next page)



components or groups of components can operate alone.

Computer-managed calibration saves considerable operator time by correcting for zero and sensitivity drift. Significant operator time is also saved with corrected analyzer output available at the data-processing computer-output terminal. A six-fold reduction has been observed in the time necessary to do a formerly manual multipoint analyzer calibration when the terminal output is used to read analyzer output given a known input.

This work was done by R. C. Anderson and R. L. Summers of **Lewis Research Center**. Further information may be found in NASA TM-81592 [N81-23435/NSP], "An Integrated Exhaust Gas Analysis System with Self-Contained Processing and Automatic Calibration" [7]. A copy may be purchased [prepayment required] from the National Technical Information Service, Springfield, Virginia 22161.

Inquiries concerning rights for the commercial use of this invention should be addressed to the Patent Counsel, Lewis Research Center [see page A5]. Refer to LEW-14062.

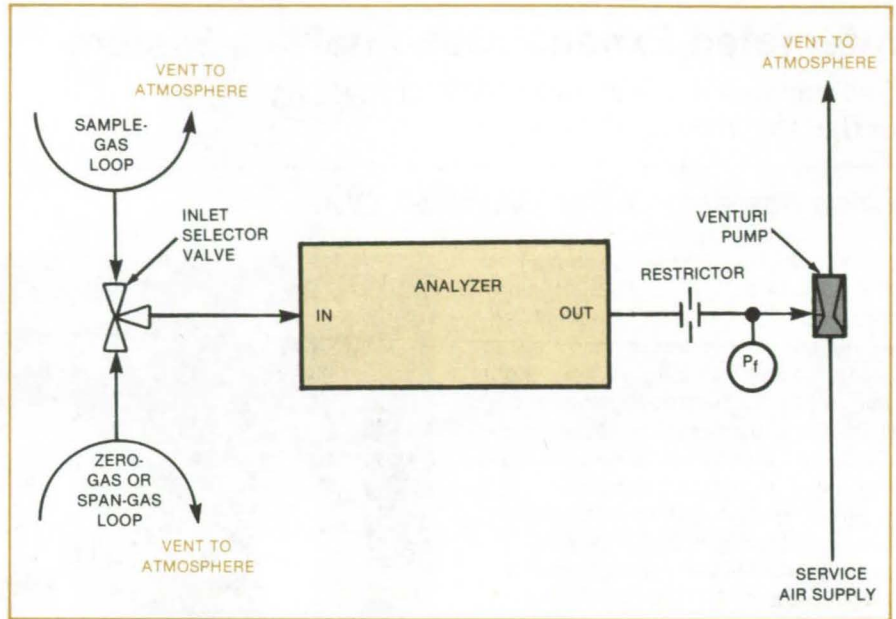


Figure 2. This **Flow Schematic** illustrates the basic flow geometry of the gas analyzer. The vent to atmosphere makes the system relatively insensitive to variations in source flowrate.

Multipurpose Photonic Transducers

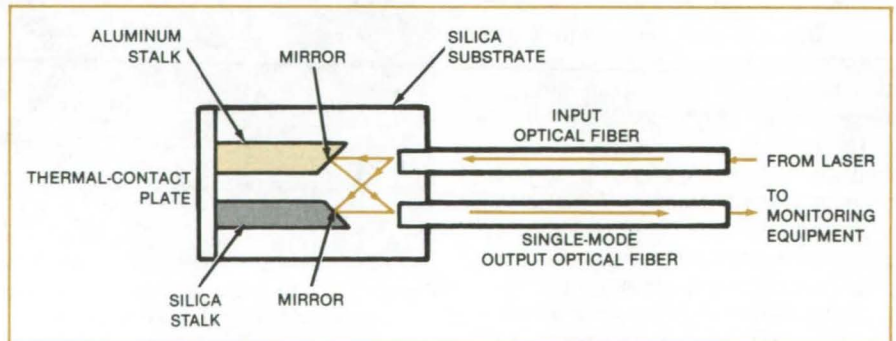
Their features include smallness and noise immunity.

NASA's Jet Propulsion Laboratory, Pasadena, California

Proposed transducers for measuring temperature, acceleration, and other physical properties are based on changes in optical interference patterns produced by small displacements. The new transducers differ from conventional electromechanical units in that they are smaller (typical size less than 1 cm) and are coupled to monitoring equipment with optical fibers instead of wires.

The figure gives a simplified view of a temperature-change transducer. Coherent light from a laser enters through the input fiber and traverses the interior space to two mirrors. One of the mirrors is mounted on a stalk of relatively high thermal expansivity (for example, aluminum). The other mirror is mounted on a stalk of relatively low thermal expansivity (for example, silica).

The coherent light reflected from the mirrors forms interference fringes.



The **Photonic Transducer** is an interferometer with two arms. Small relative axial motions of the mirrors are detected as shifts in the interference pattern. This version measures temperature changes via differential expansion or contraction of the stalks.

Changes in the relative lengths of the two stalks due to differential thermal expansion produce changes in the fringe pattern: These changes are detectable as fluctuations in the output light as the fringes pass across the output-fiber

aperture. The output light emerging from the fiber at the far end is fed to a photodetector so that the fringe changes can be electronically counted and converted to equivalent temperature-change readings.

(continued on next page)

A device based on the same interferometric principle might be used to measure acceleration. Instead of two fixed stalks of different material, both would be of the same material, and one might be lightly sprung and free to move along its axis, thereby producing fringe shifts.

Similarly, the measurement of small differential elastic displacements could be detected for the measurement of strain, force, and pressure. The small size of the photonic transducers should suit them well to biomedical instrumentation.

This work was done by Eugene R. du Fresne and Warren L. Dowler of Caltech for NASA's Jet Propulsion Laboratory. For further information, Circle 98 on the TSP Request Card. NPO-15135

Deriving Strain Modes From Vibrational Tests

Measurements and theoretical analysis complement each other.

Lyndon B. Johnson Space Center, Houston, Texas

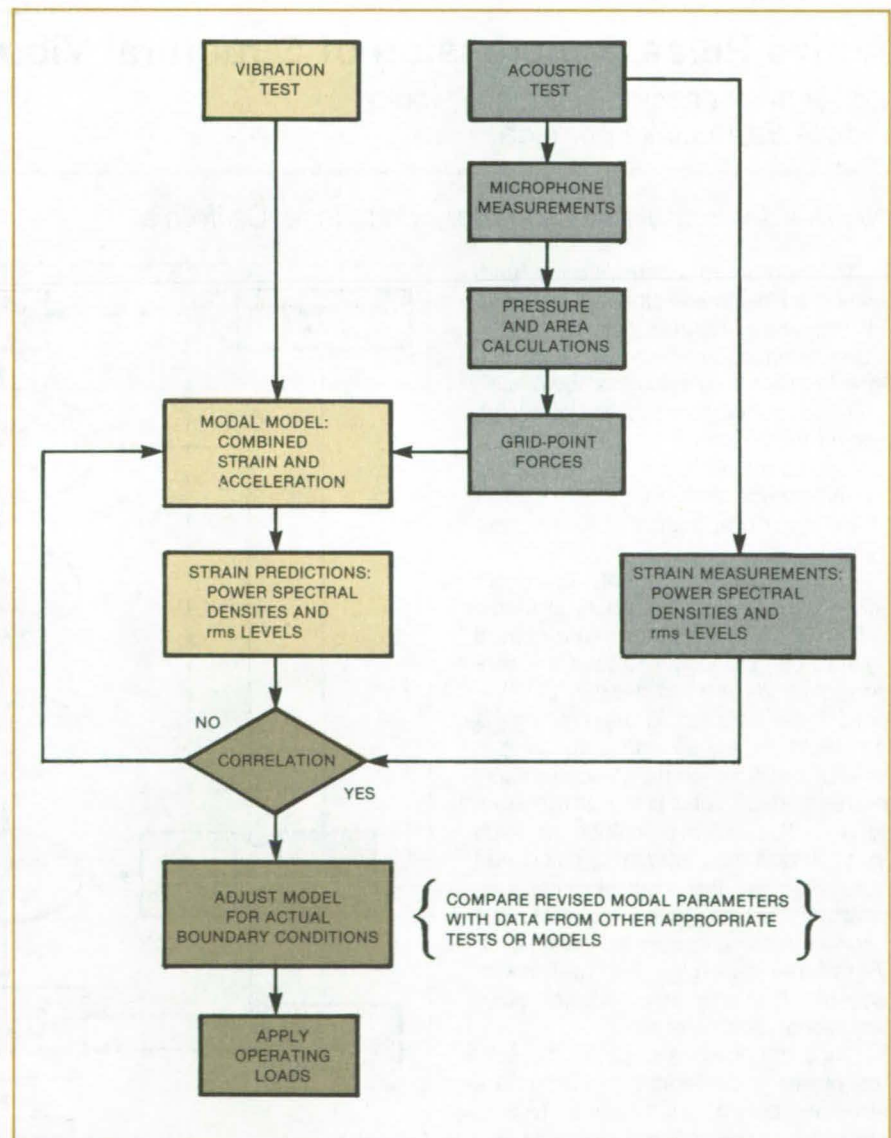
A hybrid method of vibration analysis combines experimental and theoretical techniques to find the strains due to the normal vibrational modes of an object. The method should be useful in fatigue-life and reliability analyses of buildings, pumps, engines, vehicles, and other systems subject to vibrations and loud noises during operation.

The experimental data for the hybrid model are obtained from acoustical-frequency vibration tests (see figure). The object in question is vibrated at many frequencies in the range of interest (typically, several hundred) while readings are taken simultaneously with accelerometers and strain gages placed at many points.

For machinery or other objects with complicated structures, this approach offers advantages over fine-mesh finite-element analysis of the normal modes and the associated strains. The method requires no analytical prediction of strain at welds, corners, fasteners, and other stress-concentration points: It is simpler to measure the strains at these locations and insert them into the analytical equations wherever they call for strains.

Vibration data are taken with the object excited at a single driving point. The frequency, amplitude, and phase of the forcing function and of each acceleration and strain measurement are recorded. Converted to complex numbers, the ensemble of amplitude and phase data at different frequencies constitutes the vector of forcing-function and response spectra. The spectrum at each gage location is a component of the acceleration- or strain-response vector.

Modal coefficients (eigenvectors) for displacement are extracted from the accelerometer data using modal-analysis (continued on next page)



Experimental Acceleration and Strain Data are used to calculate the coefficients of the low-frequency vibrational modes of the object under test. An iterative comparison of experimental and calculated strains gives a modal model of improved accuracy that can be used to predict strains under operating conditions.

techniques. The unusual feature of this method is that a similar analysis is also performed on the strain-gage data to obtain the modal coefficients for strain. The modal coefficients are used to calculate the acceleration and strain frequency-response functions in the form of $m \times n$ matrices. The acceleration- or strain-response spectrum for a general excitation can then be calculated from:

$$\vec{R}(\omega) = \vec{G}(\omega) \cdot \vec{F}(\omega)$$

where $\vec{R}(\omega)$ = the $m \times 1$ column vector representing the response spectrum at each of m points of interest, $\vec{G}(\omega)$ = the

$m \times n$ matrix representing the acceleration or strain frequency-response function of the object, $F(\omega)$ = the $n \times 1$ column vector that represents the forcing-function spectrum at each of n excitation points, and ω = the angular frequency.

For greatest accuracy, the method is applied iteratively. Modal coefficients calculated from vibrational tests are used to predict the strains at the gage points. These strains are compared with the measured strains. The model is adjusted for actual boundary conditions, and modal coefficients are revised as needed to give a better approximation of

actual strains. Once the finite-element theoretical and test-derived models are in reasonable agreement, the finite-element model is used to predict strains throughout the object at points other than the gage locations.

This work was done by Jeffrey W. Young of Structural Dynamics Research Corp. and Jack C. Joanides of Rockwell International Corp. for **Johnson Space Center**. For further information, Circle 99 on the TSP Request Card.

Inquires concerning rights for the commercial use of this invention should be addressed to the Patent Counsel, [see page A5]. Refer to MSC-20587.

Active Pulse Suppression of Structural Vibrations

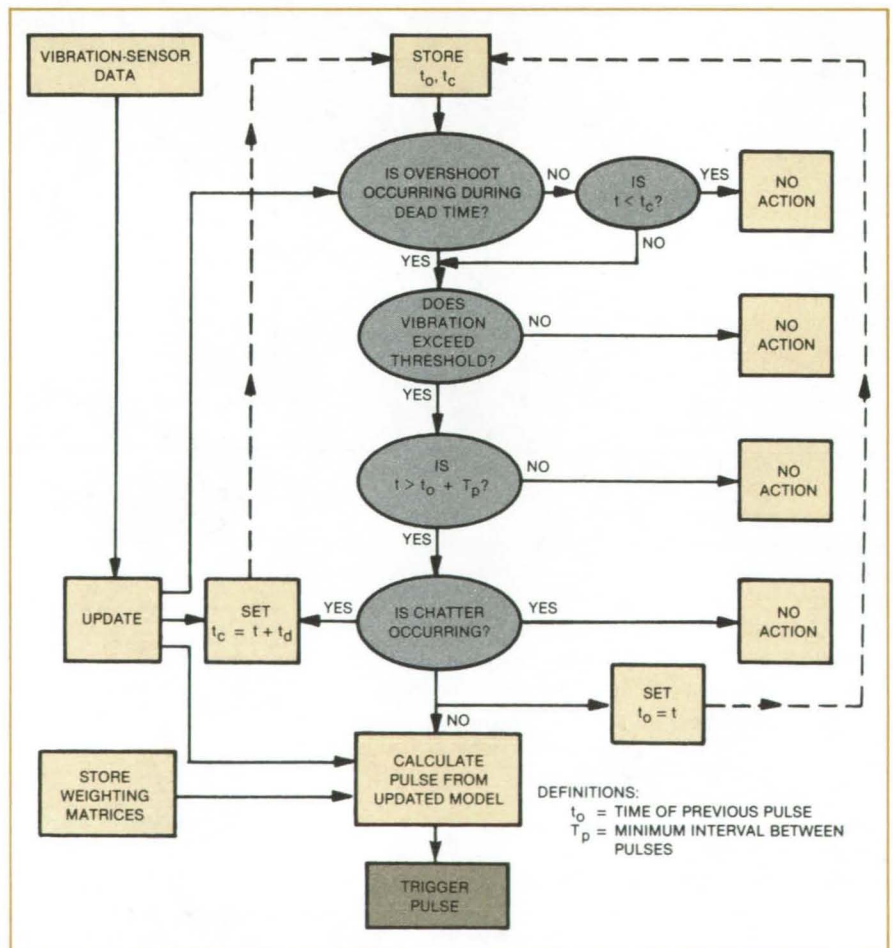
Corrective opposing vibrations would reduce Earthquake damage.

NASA's Jet Propulsion Laboratory, Pasadena, California

An algorithm for controlling the reactions of buildings and other structures to Earthquakes initiates counterpulses when incoming shock pulses exceed a threshold level. By using this "go/no-go" criterion rather than continuously adjusting the response to every input excitation no matter how small, the control system needs less computation effort than do comparable closed-loop systems.

According to the concept, vibration or strain sensors are placed at strategic positions on the structure. The control system continuously analyzes the sensor data and identifies stresses or vibrations above a threshold value. When the threshold is exceeded, actuators at several positions on the structure apply corrective vibrational pulses at preset intervals: The pulse amplitude at each location and time interval is calculated according to the control algorithm, which is designed with regard to the known structural modes to minimize the vibrational energy, the root-mean-square vibrational amplitude, or other vibrational parameter(s).

Since the power source for the control pulses is preferably located in the structure, economy is essential. To conserve the energy in this source until it is needed, the threshold is determined by the nature of the system, its structural resistance, and the acceptable level of damage.



A Flow Chart Shows the Logic used to determine whether correcting pulses are necessary.

Control-system chatter can arise when system motion is continued by control-pulse oscillations. This chatter phenomenon can be reduced by incorporating a control feature that sets the pulse amplitude to zero when chatter is detected (see figure). First, the values of t (present time) and t_c (a critical control time) are stored. The algorithm asks whether the measured vibrations exceed the predetermined threshold(s). If

the vibration exceeds the threshold(s), the system seeks to know whether chatter is occurring. If there is no chatter, it calculates the correcting-pulse amplitudes to counteract the measured vibrations, then triggers the correcting pulses. If chatter is present, the computations are repeated to determine whether the pulses should be shut off for a "dead" time, t_d , or continued to counteract large stochastic excitations.

This control concept was demonstrated in a computer simulation of a four-degree-of-freedom vibrating structure. It is preferable to incorporate such a control system into a design before construction, but it could be fitted into an existing structure.

This work was done by F. E. Udwadia of Caltech for NASA's Jet Propulsion Laboratory. For further information, Circle 100 on the TSP Request Card. NPO-15788

Constant-Operating-Resistance Hot-Wire Probe

Effects of lead-wire-resistance changes with temperature are nullified.

Langley Research Center, Hampton, Virginia

In hot-wire anemometry, it is desirable that all changes in resistance be in the sensing element. Unfortunately, the resistance of the leads to the probe changes with temperature. A proposed constant-operating-resistance hot-wire probe uses two sets of leads, one to the sensing element, the second to a temperature-invariant resistance. Since the two sets of leads are exposed to identical conditions, a comparison of resistance gives the change in the sensing element itself.

The proposed probe (see figure) consists of an active wire for measuring fluctuations in gas flow and a second, auxiliary, wire that has nearly constant resistance over a given ambient temperature range. The auxiliary wire maintains the "overheat" or resistance ratio of the active probe to the desired value. When this probe, with the two wires, is used with a symmetrical bridge (1:1 bridge ratio) of a standard hot-wire anemometer, the resistance of the active probe has essentially a constant resistance over some range of ambient temperatures. This mode of operation eliminates the constant need to check the resistance of the lead wires and to balance out this resistance change with a potentiometer on standard anemometer units.

In its simplest form, the probe would have one active wire and one or more auxiliary wires to maintain the resistance of the active wire at constant resistance over a large range of temperatures. If the temperature range is small, only one auxiliary wire is required.

In its most complex form, the probe would have six active wires and six or

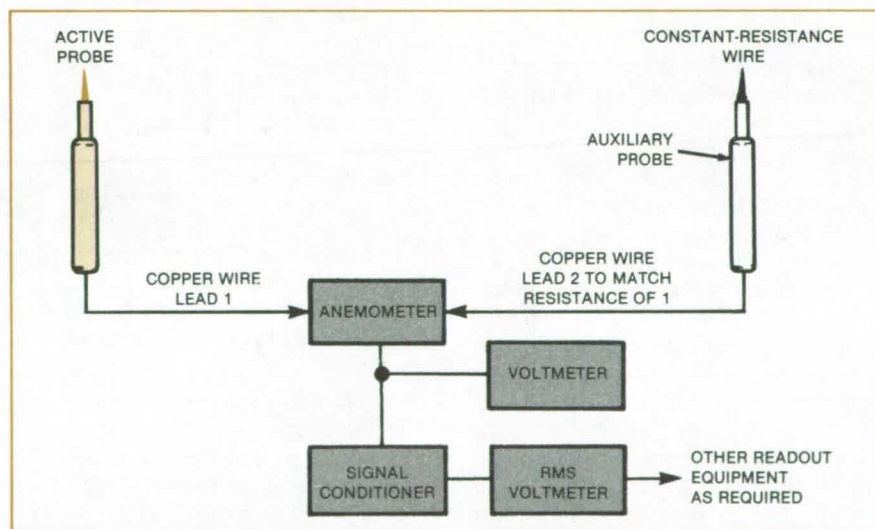
more auxiliary wires. The six active wires would be made up of four wires mounted normal to the mean flow velocity and two wires slanted about 45° to the flow velocity. The slant wires would be normal to each other in two planes so that the wires would measure the two velocity components normal to the flow velocity and normal to each other. Probably the most useful configuration would be a probe with three active wires mounted normal to the mean velocity with three or more auxiliary wires. For probes with multiple active wires, it would probably be more convenient to mount the auxiliary wires on a separate probe.

When the probe is used with a standard hot-wire anemometer and sym-

metrical bridge, the resistance of the active probe is held constant automatically at the required overheat by the electronics of the anemometer to ensure accurate data. Therefore, data can be taken in a more convenient manner, with all the advantages of not having to constantly check for possible changes in lead resistance and to consequently readjust the potentiometer.

This work was done by P. Calvin Stainback of Langley Research Center. No further documentation is available.

Inquiries concerning rights for the commercial use of this invention should be addressed to the Patent Counsel, Langley Research Center [see page A5]. Refer to LAR-13144.



The Constant Resistance Wire on the Auxiliary Probe and the matched lead 2 may be placed on a separate probe, as shown, or on the active probe itself.



Hot-Wire Probe for Compressible Subsonic Flow

A probe measures velocity, density, and total temperature fluctuations.

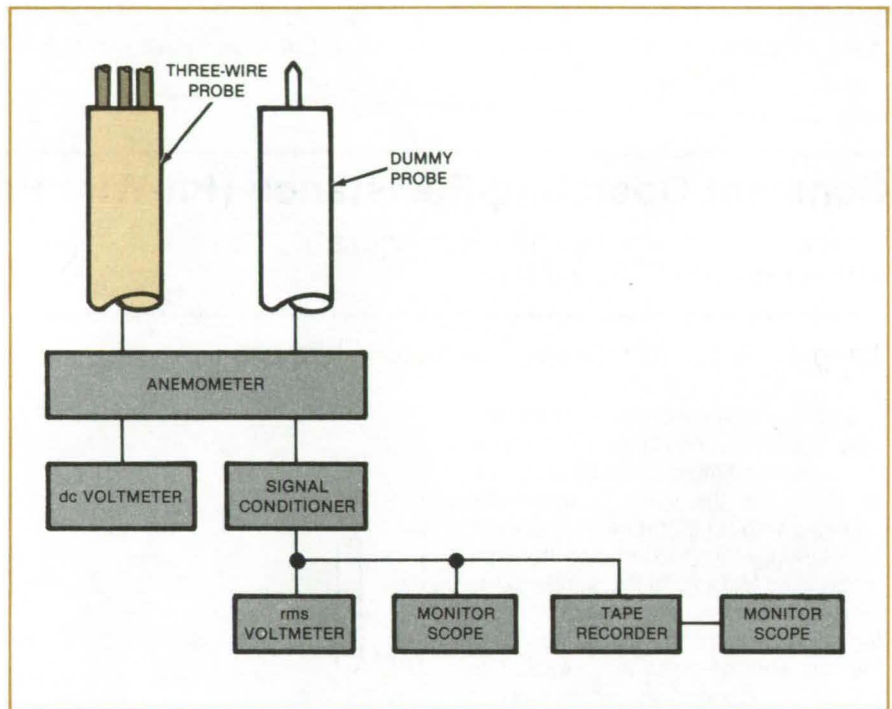
Langley Research Center, Hampton, Virginia

A hot-wire probe and calibration and data-reduction techniques measure the velocity, density, and total temperature fluctuation in compressible subsonic flows.

Until recently, very few measurements were reported for compressible subsonic, transonic, and low supersonic flows. One of the reasons is that, for a given probe, the heat transfer from a heated wire oriented normal to the flow is a function of the three fluid variables: velocity, density, and total temperature. Calibration of the hot-wire probe, therefore, is very time consuming. Also, because the heat transfer from the hot wire is a function of the combined effect of the three fluid variables, interpretation of the data is difficult. Finally, because the dynamic pressures are high, the wire often breaks due to the aerodynamic loads on the wire and particles in the flow striking the wire.

The new hot-wire probe was calibrated, and the test-section free-stream fluctuations were measured in the Langley 0.3-m Transonic Cryogenic Tunnel (TCT). The probe has six "needles" made from piano wire that support three wires. The needles, each about 1 in. (2.5 cm) long, are glued into a section of six-hole ceramic tubing. The ceramic tubing, with the needles and lead wires, is glued into a section of 0.250-in. (6.35-mm) stainless-steel tubing. Platinum-coated tungsten wires having a diameter of 0.4 mil (0.01 mm) are mounted between the needles with about 1/4-circle slack in each wire. The wires are about 0.10 in. (2.5 mm) long and about 0.040 in. (1.02 mm) apart. Each of the three wires on the probe was operated with its own constant-temperature hot-wire anemometer and signal-conditioner system.

The hot-wire probe is calibrated by mounting it in the test section of the 0.3-m TCT on the forward mounting position normally used for the drag rake. A dummy probe with shorted needles is mounted below the active probe on the aft mounting position of the drag rake. The dummy probe with leads going to the anemometer is used to balance out



A Three-Wire Probe is used with each wire operating at a different overheat ratio.

any lead-resistance changes that occur because of changes in temperature. The resistances of the dummy probe and leads are matched to those of the active probe, and both sets of leads follow the same path to the anemometer, ensuring that each set of leads is subjected to the same temperature environment.

During the tests, the tunnel velocity is varied in five evenly spaced steps, and the mean and fluctuating voltages are recorded at each speed. As the speed is reduced, the total pressure is decreased to maintain a constant density. The density is reduced in three steps, the speed is varied for each step, and data are recorded for the probe. The total temperature is then set at different values and the above procedure is repeated.

Again, the total pressures are changed to maintain a constant density as the temperatures are changed. This calibration procedure is not required if a multiple-regression technique is used to correlate the data. The constant-parameter method, however, is useful for de-

termining the form of the correlation equation to be used for the multiple-regression method.

In the tests performed in the 0.3-m TCT (see figure), the mean flow calibration of the probe indicated that the mean voltage measured across the hot wire, at a given wire resistance, was a function of velocity, density, and total temperature. The sensitivity coefficients with respect to density were, in general, higher than those for velocity.

The probe was used to measure the disturbance levels in the 0.3-m TCT, which were very high where the velocity and density fluctuations ranged from about 0.3 to 4.5 percent; the total temperature fluctuations ranged from about 0.05 to 0.5 percent. Various data-reduction methods indicated that the major disturbances, at the higher mach numbers, were a result of upstream moving sound.

The disturbances were, in general, mostly broadband with some discrete frequencies existing between 100 and

1,000 Hz. This technique should be extendable into the transonic and low-supersonic flow regimes without difficulty except for those problems usually

associated with lengthy calibration and possible wire breaking.

This work was done by P. Calvin Stainback and Charles B. Johnson of Langley Research Center and

Constance B. Basnett of SDC. For further information, Circle 101 on the TSP Request Card.
LAR-13051

Measuring the Liquid Content of a Gas

Instrument is an adaptation of the hot-wire anemometer.

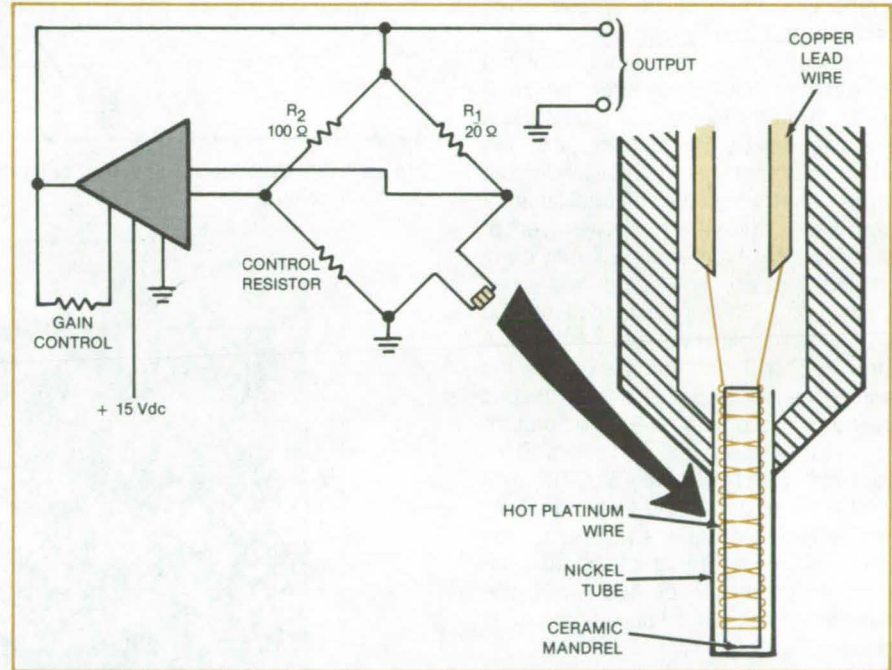
Marshall Space Flight Center, Alabama

A hot-wire anemometer — ordinarily used to measure the speed of flowing gas — can be used to detect droplets of liquid entrained in the gas. The instrument might be used in steam turbines to check for condensation that could damage the blades or to detect entrained droplets in liquefied natural gas when tankers are being filled. It might also be used to detect fog at airports and highways, generating a control signal to turn on fog lights.

The key element of the instrument is a platinum wire wrapped on a ceramic mandrel contained in a probe. The probe forms one leg of a bridge circuit (see figure). Gas flowing over the probe removes heat from it at a rate dependent on the gas velocity. The wire cools slightly and its resistance decreases as a result. A controller senses the resistance change and increases the current in the wire to raise its temperature and compensate for the heat loss. The current is therefore a measure of the gas velocity.

If liquid droplets are entrained in the gas stream, they collect on the probe, increasing the heat-transfer coefficient of the probe up to as much as 12 times that of droplet-free gas at the same temperature and velocity. The resulting sharp increase in bridge current thus indicates that droplets are present in the flow.

If the anemometer is expected to measure the velocity of a dry gas, it is necessary only to set the temperature of the platinum wire above the minimum gas temperature. For droplet detection, however, the wire temperature must not be too high or else droplets will not collect on the probe, and the current-producing capability of the controller may be exceeded during periods of gas-only flow. Analysis or experimentation will indicate the proper amount of



A Hot-Wire Anemometer is used to detect liquid droplets entrained in a flowing gas. Droplets impinge on the probe and carry away heat as they are vaporized. The power required to maintain the probe at a constant resistance and elevated temperature gives a measure of the amount of liquid present.

“overheat” — that is, the difference between the temperatures of the wire and the gas. Usually about one-fourth the maximum overheat capacity of the controller will suffice.

Droplet detection with an anemometer requires that several components be selected with care. The value of the control resistor, which establishes a reference for the platinum wire, is critical, and a “precision” resistor or a decade box should be used for it. The connection from the controller to the platinum wire is also important. Ideally, a four-wire, temperature-compensated connection should be used to prevent changes in the lead-wire temperature from shifting the set temperature. At the very least, low-

resistance wire should be used and should be installed in such a way as to minimize temperature changes in the leads.

In service as a droplet detector in a liquid-oxygen supply, the hot-wire anemometer has proven to be fast and dependable. It responded to less than 1 percent liquid by mass.

This work was done by Douglas H. Beekman and Lothar H. Methner of Martin Marietta Corp. for Marshall Space Flight Center. For further information, Circle 102 on the TSP Request Card.

Inquiries concerning rights for the commercial use of this invention should be addressed to the Patent Counsel, Marshall Space Flight Center [see page A5]. Refer to MFS-25990.

Continuous-Filament Isogrid Composite Panel

Damaged panels do not fail catastrophically when fabricated this way.

Langley Research Center, Hampton, Virginia

In a new fabrication method for composite structural panels, the isogrid stiffener is formed in a slotted silicon-rubber tool. At grid intersections, the slots are offset to prevent excessive buildup of the composite material and are widened to give room for the overlapping filaments to spread when compressed (see Figure 1).

An isogrid-stiffened panel designed for a moderately loaded structure, such as an aircraft fuselage, was built using graphite/epoxy material. Material for the isogrid stiffener was first preplied into a large sheet consisting of one layer of biwoven cloth covered with two layers of unidirectional tape, then vacuum compacted. This prepolymer was cut into strips 0.389-cm (0.153-inch) wide to fit into the grid-pattern slots in the rubber tool. One strip was laid into each slot running across the tool. After five strips were laid in each direction, a wooden grid-pattern tool was placed into the slots. This assembly was heated to 93° C (200° F) for 10 minutes while under vacuum. This process compressed and spread the fibers at the grid intersections, and the procedure was repeated until the designated 87 plies had been laid in place.

The panel skin was formed separately with 24 plies of unidirectional tape, compacted under vacuum, and trimmed to size. The skin and grid were joined by placing the rubber tool containing the grid on the skin and curing the epoxy in an autoclave at 177° C (350° F) for 2 hours under 689,500 pascal (100 psi) pressure.

Tests showed that a stronger attachment was needed between the skin and stiffener to prevent skin/stiffener separation. To prevent this failure mode, strip reinforcements composed of two layers of graphite cloth and an adhesive film were laid over the isogrid stiffeners and onto the skin between the grid intersections. A high-elongation silicon-rubber sheet was sealed over the panel. The reinforcement cloth was tightly pressed under vacuum against the isogrid and panel skin, and heat was applied to cure the reinforcement. The completed panel is shown in Figure 2.

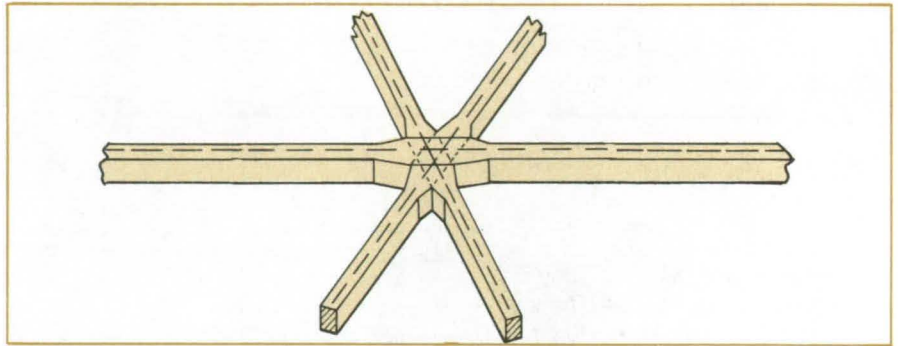


Figure 1. The Grid Width is Doubled at intersections and one overlap is offset to maintain constant height.

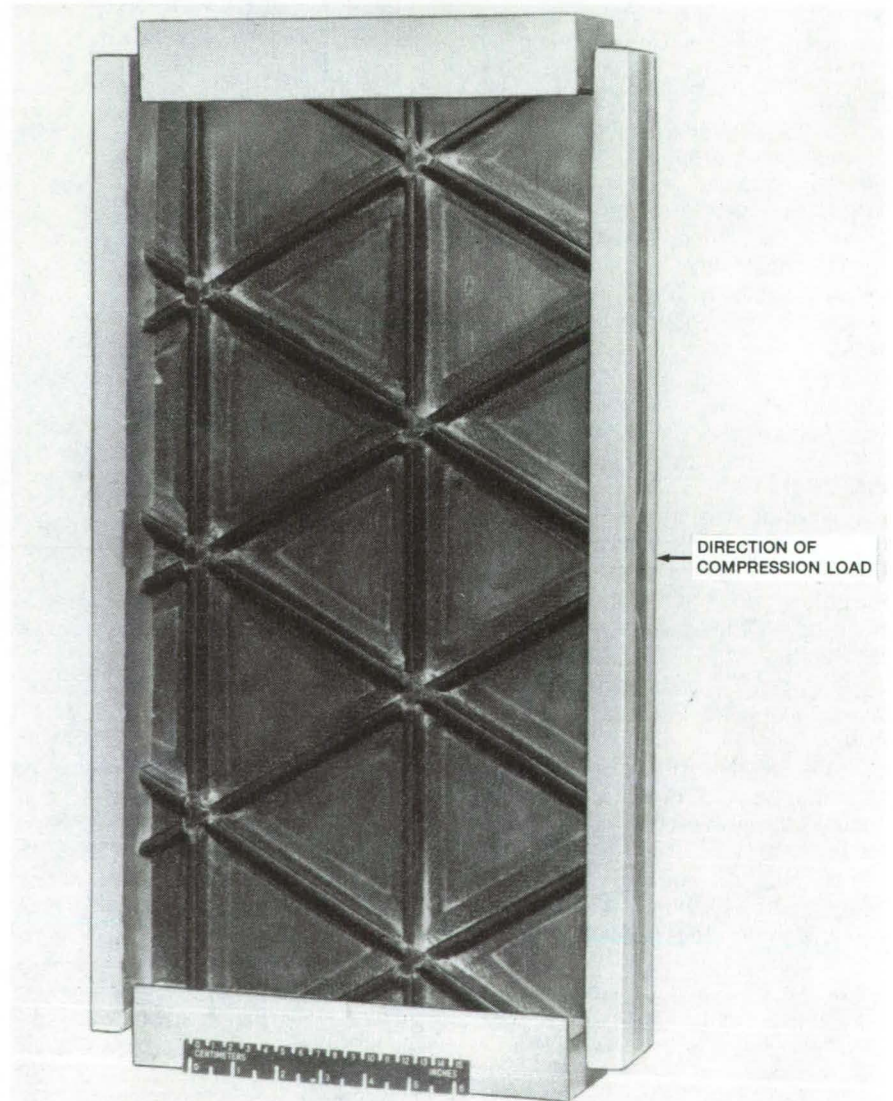


Figure 2. The Isogrid-Stiffened Panel with grid reinforcement wrap is shown here.

This panel was loaded in compression to 1.43 MN/m (6,526 lb/in.) without evidence of damage. A panel that did not have the additional reinforcement wrap over the isogrid failed catastrophically at 890 kN/m (5,082 lb/in.) when the isogrid separated from the skin.

After the successful compression test, the skin was deliberately punctured near the center of a triangular section

between the isogrid. As this panel was loaded in compression, the skin failed by progressive growth with increasing load in a narrow band that spread across the panel perpendicular to the direction of the applied load. The damage in the skin had propagated completely across the panel at a load of 676 kN/m (3,860 lb/in.). However, following the total failure of the skin, the isogrid stiffener still carried

350 kN/m (2,000 lb/in.) and remained intact.

This work was done by Jerry G. Williams of **Langley Research Center** and Raymond J. Palmer and Allan T. Tucci of **McDonnell Douglas Corp.** For further information, Circle 103 on the TSP Request Card. LAR-12975

Thermal-Balance Strip for Fluted LFC Panels

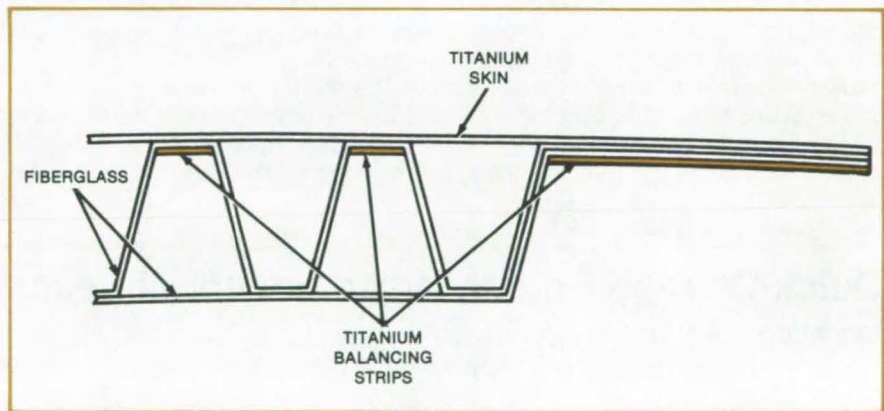
Waviness of less than 0.004 inch is achieved using titanium strips.

Langley Research Center, Hampton, Virginia

The surface waviness of laminar-flow control (LFC) panels must be less than 0.004 inch (0.102 cm). In bonding the titanium skin to the fluted fiberglass panel substructure, unequal expansion of the titanium and the fiberglass causes waviness greater than 0.004 inch to appear in the titanium skin.

A process was developed that uses titanium balancing strips to keep the waviness within the 0.004-inch limit. The balancing strips reduce thermal bonding stresses on the lower fiberglass fluted sections and are placed so that the fiberglass ends up sandwiched between the porous titanium skin and the titanium balance strip (see figure).

An alternate method to reduce waviness consists of wrapping each individual trapezoidal mandrel with carbon-fiber cloth to allow for even stress release during cure. The internal stress is contained within each single unit, thus preventing dishing and waviness on the titanium skin surface.



Balance Strips Reduce Thermal Bonding Stresses in laminar-flow control wing panels.

Both methods use a multiple-grooved silicone female lower form and removable silicone rubber mandrels to fabricate the fluted composite substructure for the hollow LFC wing panels (see the preceding article). However, the thermal-balancing-strip method appears to require less skill and is less labor in-

tensive than the composite-wrapped-mandrel method.

This work was done by Philip Bono of **McDonnell Douglas Corp.** for **Langley Research Center.** For further information, Circle 104 on the TSP Request Card.

LAR-12991



Silicone-Rubber Tooling for Hollow Panels

A wave-free contour surface is obtained by using a flexible mold.

Langley Research Center, Hampton, Virginia

A technique that uses a flexible silicone-rubber mold produces fluted composite substructures for porous titanium wing panels. The flexible rubber sheet contains a trapezoidal rib pattern. A rigid submold provides the overall contour. The release of the finished part

from the mold is facilitated by the flexible rubber material.

Laminar flow control for leading-edge and wing-surface applications requires a hollow panel made of trapezoidal fluted fiberglass webbing separating two contoured panel surfaces. Previously,

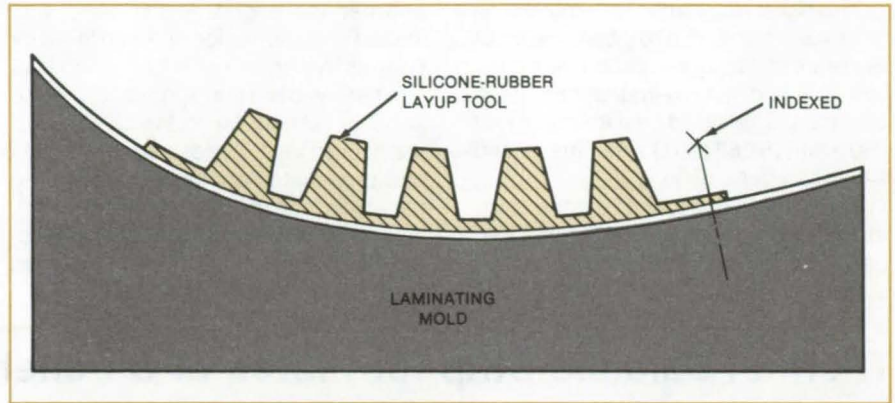
three layers of "B" type fiberglass were formed around a single trapezoidal mandrel. Each flute was then sewn through the webbing plies and the base plies by an industrial sewing machine, but a problem developed in maintaining

(continued on next page)

uniform spacing between the fluted webbing. The center distance between flutes was difficult to maintain because of mandrel locations in the sewing operation, and individual molding and sewing of each flute was very labor intensive.

The silicone-rubber tooling technique overcomes these difficulties. In addition to providing a porous hollow-panel wing structure that acts as a duct for transporting the sucked boundary layer, the tooling can be used to fabricate high-strength lightweight door panels and any single- or compound-contour panel. The resulting panels are lighter than similar honeycomb panels.

The silicone mold (see figure) is flexible and therefore easy to remove from the cured composite material and is the only type of mandrel that can be removed from curved or compound-curved panels. It replaces expensive trapezoidal contoured aluminum or steel dies produced by numerical-control milling machines. Even pressure is applied to all surfaces during cure, ensuring



The **Silicone-Rubber Layup Tool**, when used in conjunction with a hard plastic laminating mold defining the desired contour, produces a panel with a wave-free surface that accurately reproduces the shape of the mold.

void-free parts with acceptable dimensional accuracy. The flexibility of the silicone mold allows it to be formed to any desired flat, radial, or compound surface.

This work was done by Frank H. Gallimore of McDonnell Douglas Corp. for **Langley Research Center**. For further information, Circle 105 on the TSP

Request Card.

This invention is owned by NASA, and a patent application has been filed. Inquiries concerning nonexclusive or exclusive license for its commercial development should be addressed to the Patent Counsel, Langley Research Center [see page A5]. Refer to LAR-12974.

Quick-Change Holder for Aeronautical-Research Microphones

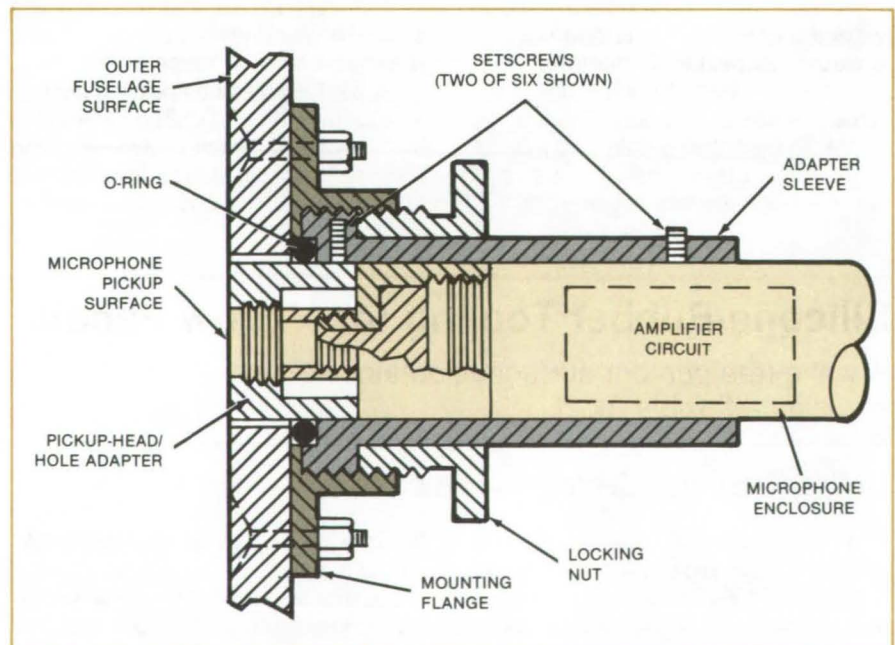
Mounting holds microphone flush with aircraft surface and maintains a pressure seal.

Dryden Flight Research Center, Edwards, California

A mounting for microphones used in aeronautical research reduces erroneous output caused by airframe vibration. The microphones, which measure dynamic pressure and shock waves as they pass over an aircraft fuselage or other experimental body, are mounted through the fuselage so that they are flush with the outside surface. The mounting also allows the microphones to be changed quickly.

Previously, the microphones were clamped in place, and a potting or sealing compound was placed around them. To remove a microphone for calibration or replacement, the sealant had to be cut and scraped from the microphone and the fuselage. Cleaning, reapplying sealant for reinstallation, and curing required 8 to 24 hours, and tests could not be resumed during that time.

With the new mounting method, a microphone can be removed and replaced, ready for use, in 15 minutes. The cylindrical microphone-circuit enclosure, with the pickup head and pickup-



Mating Threaded and Flanged Cylindrical Parts hold a microphone flush with the outer aircraft surface while providing a pressure seal. Besides being faster and easier to use than are older mounts, this new mount prevents damage to the microphone on removal because there is no sealant to be cut and scraped away.

head/hole adapter attached, is placed in a flanged sleeve and held there by set-screws (see figure). The sleeve is screwed into a mounting flange until the microphone pickup surface is flush with the outer fuselage surface. An O-ring at the junction of the sleeve, mounting

flange, fuselage, and pickup-head/hole adapter provides a pressure seal between the inside and outside of the fuselage.

This work was done by Robert Cohn of Dryden Flight Research Center. For further information, Circle 106 on the TSP Request Card.

This invention has been patented by NASA (U.S. Patent No. 4,388,502). Inquiries concerning nonexclusive or exclusive license for its commercial development should be addressed to the Patent Counsel, Dryden Flight Research Center [see page A5]. Refer to FRC-11072.

Microphone Detects Boiler-Tube Leaks

Unit is simple, sensitive, rugged, and reliable.

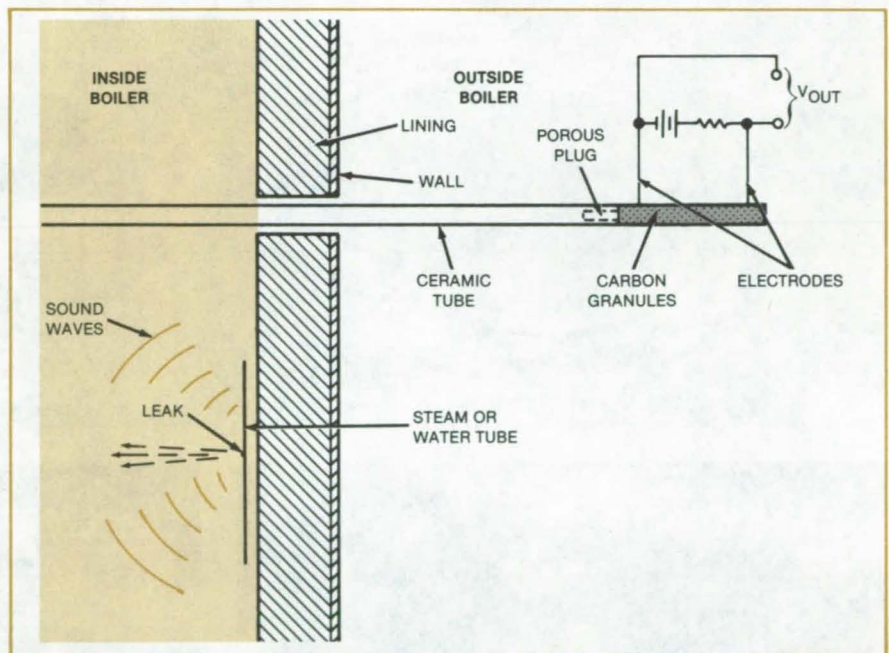
NASA's Jet Propulsion Laboratory, Pasadena, California

A leak detector for boiler fireboxes senses leaks in boiler tubes by their characteristic sound. Such leaks eject jets of water or steam at high pressure. The jets emit sound at peak frequencies ranging from 2 kHz for a 5-mm leak to 10 kHz for a 1-mm leak. When the unit detects the leak sound above the low-frequency background noise of combustion, it sounds an alarm.

The sensor is housed in a ceramic tube of small diameter (about 1 cm) that projects into the boiler (see figure). The outside end of the tube is packed with carbon granules between a pair of electrodes to form a crude microphone. Connected to the electrodes, outside the ceramic tube, are a battery and a resistor in series. The sound of the leak in the boiler creates small audiofrequency pressure changes on the carbon granules, alternately packing and releasing them and thereby changing the resistance of the granules. As a result, the current through the external resistor varies, and the variation is detected by measuring circuitry.

A small flow of air directed toward the boiler end of the ceramic tube keeps dust and fumes away from the granules if necessary. The airflow also absorbs some of the combustion noise.

Unlike previous microphone-type leak detectors, the new unit contains no



This **Diaphragmless Microphone** detects leaks from small boiler tubes. It can be used in a variety of hot, corrosive atmospheres. A porous plug retains carbon granules in the tube while allowing pressure changes to penetrate to the granules.

metal diaphragm. It has greater life expectancy than the previous detectors, in which the diaphragms each corroded after only about a month of service.

This work was done by Shakkottai P. Parthasarathy of Caltech for NASA's Jet Propulsion Laboratory. For further

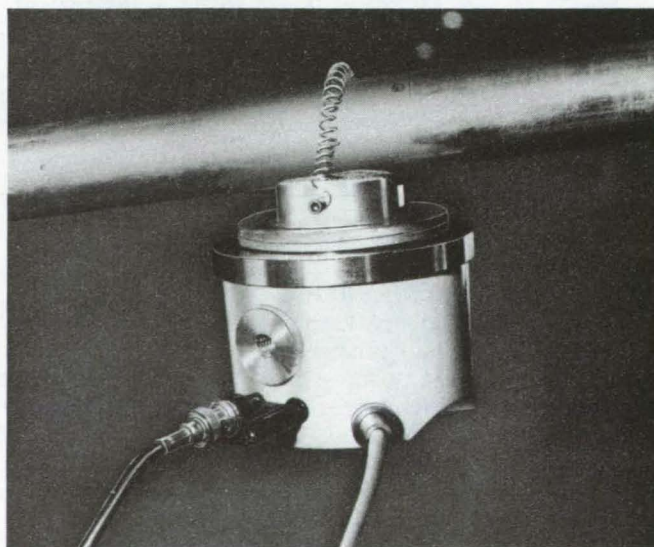
information, Circle 107 on the TSP Request Card.

Inquiries concerning rights for the commercial use of this invention should be addressed to the Patent Counsel, NASA Resident Office-JPL [see page A5]. Refer to NPO-16027.

In-Place Calibration of Instrumentation Microphones

Accidental damage and decalibration are prevented.

Ames Research Center, Moffett Field, California



An **Artificial Voice** (a calibrated sound source) is provided with adapters for flush mounting against surfaces of various shapes. For example, the artificial voice is held by a spring against a tube containing a flush-mounted microphone.

Flush-mounted instrumentation microphones and dynamic-pressure transducers can be calibrated without being removed from their mountings. The linearity, sensitivity, and frequency

response of a microphone are measured with a commercial sound generator that has been modified so that it can be placed directly over or under the microphone.

The sound generator provides a known sound level in the enclosed space formed by the microphone, the generator, and the mounting surface. Besides being convenient, in-place

calibration prevents damage to the microphone that might otherwise occur when it is removed. It also precludes the decalibration that might occur when the microphone is reinstalled.

A Bruel and Kjaer "artificial voice" was selected as the sound generator because its sound intensity can be readily measured and controlled via an internal control microphone (equivalent units by other manufacturers can be substituted). The top of the artificial-voice

enclosure is replaced by any of a number of different aluminum adapters. The outer surface of each adapter is shaped to mount flush with the surface in which the microphone is installed (see figure). A thin layer of foam seals the adapter to the surface around the periphery of the microphone.

The control microphone is calibrated by a pistonphone or other laboratory standard. For the test, the artificial voice is connected to an oscillator and

measuring amplifier. The requisite frequencies and sound pressures are applied to the microphone, and the microphone output is recorded. The new calibration method has been used on aircraft and wind-tunnel microphones.

This work was done by Robert B. Cohn of Dryden Flight Research Facility for Ames Research Center. No further documentation is available.

ARC-11463

Synchronously Deployable Truss

Double-layered truss structure is compactly packaged and synchronously deployed.

Langley Research Center, Hampton, Virginia

The synchronously deployable truss (see Figure 1) is constructed of two surface layers of struts, arranged in triangles, connected by "tripods" of equal-length core struts. Face struts are hinged at each strut end and center and may fold inward or outward. Core struts are hinged only at each end. A deployment and synchronization mechanism is located at each node for inward-folding face struts. The mechanism is powered by a passive spring and damped by a hydraulic-damping cylinder. When released, the spring drives a slider that is linked to core and surface struts.

Proper design of the kinematic mechanism results in the synchronization of the face and core struts during deployment. The formation of kinematic loops between truss faces using the struts and synchronizer mechanism (see Figure 2) causes the truss faces to deploy in a prescribed, controlled synchronous manner from a position in which all struts are parallel to the position required by the final geometric form of the truss structure.

This concept provides a method for constructing, folding, and deploying a mechanism into a double-layered, curved, or flat truss structure. This structure may be used to support a reflector surface for an antenna or may be used as a platform to which other functional equipment are attached. Synchronous deployment minimizes structural anomalies during deployment and "lock-up" of component parts before complete deployment. The result is a compactly

(continued on next page)

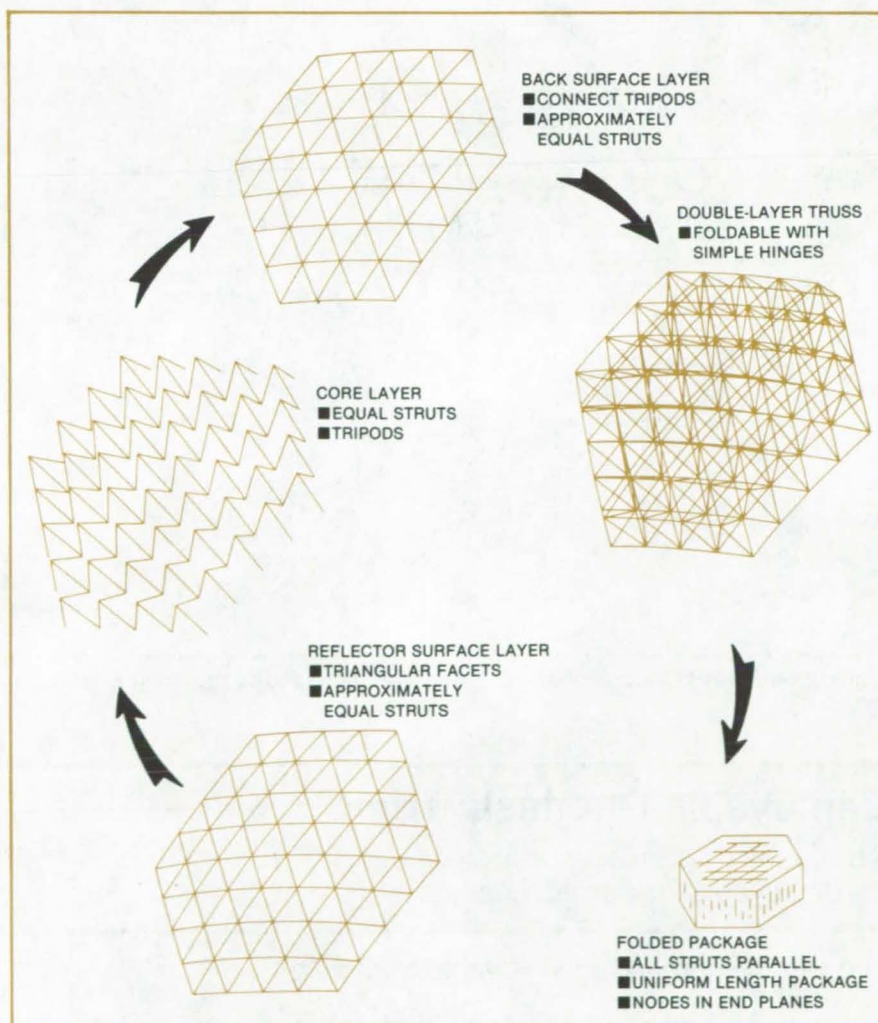


Figure 1. A Synchronously Deployed Truss can be folded into compact package.

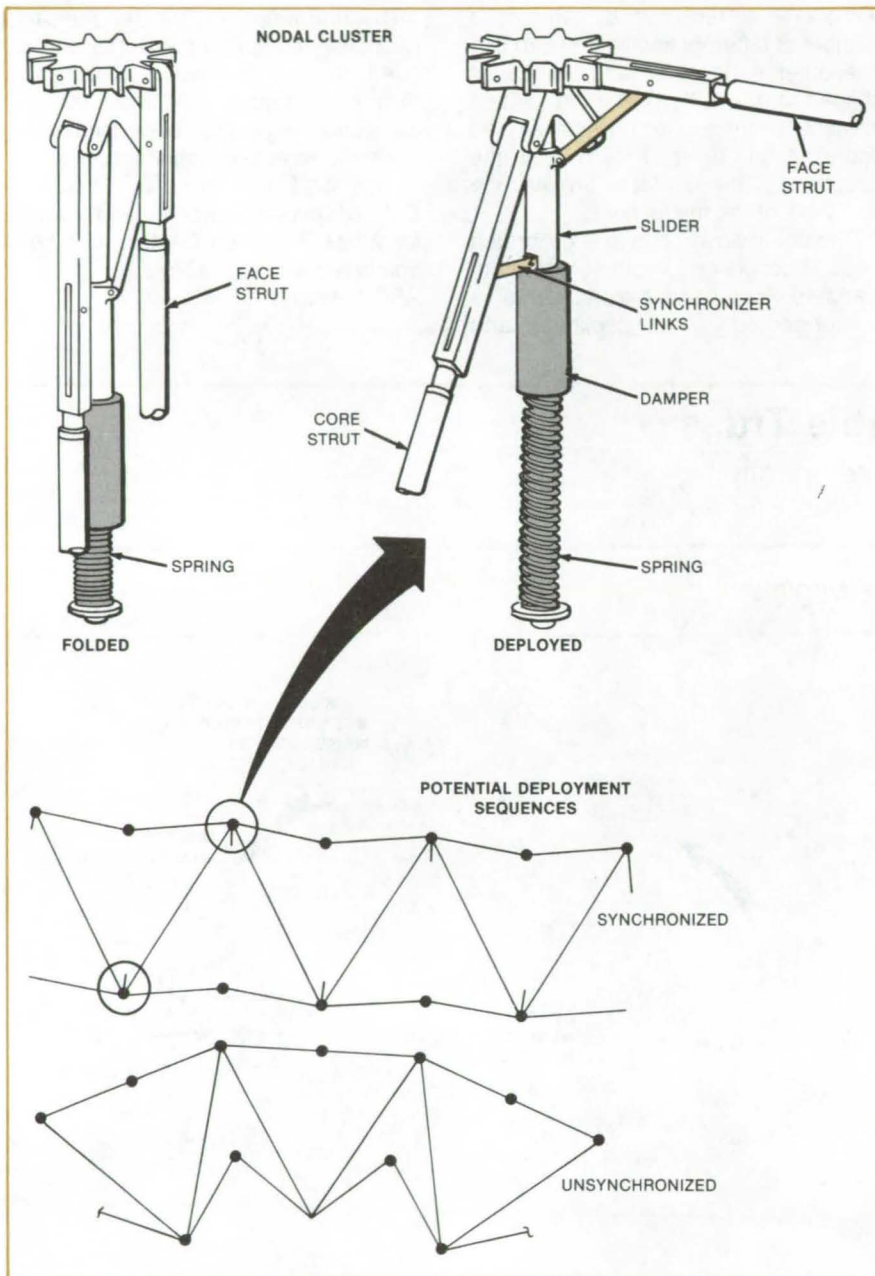


Figure 2. **Strut Synchronizer** is powered by a passive spring and damped by a hydraulic cylinder.

Deployable Geodesic Truss

An efficiently packaged structure can be deployed or retracted easily.

Langley Research Center, Hampton, Virginia

A deployable geodesic truss originally developed for space satellite applications could also be used to assemble remote manipulator arms, positioners for antennas, solar-array supports, and other structures.

A preliminary two-bay model is shown in the figure. Each bay has sets of battens connected by two longitudinal crossed members that give the bay its axial and torsional stiffness. The cross-members are hinged in the center to fold

packageable truss that slowly and synchronously deploys once in orbit. A variety of truss geometries, including curved structures, are contemplated.

This work was done by Harold G. Bush and Martin K. Mikulas, Jr., of **Langley Research Center** and Richard E. Wallsom of *Kentron International, Inc.* For further information, Circle 108 on the TSP Request Card.

This invention is owned by NASA, and a patent application has been filed. Inquiries concerning nonexclusive or exclusive license for its commercial development should be addressed to the Patent Counsel, Langley Research Center [see page A5]. Refer to LAR-13117.

Tapered Ring Seal

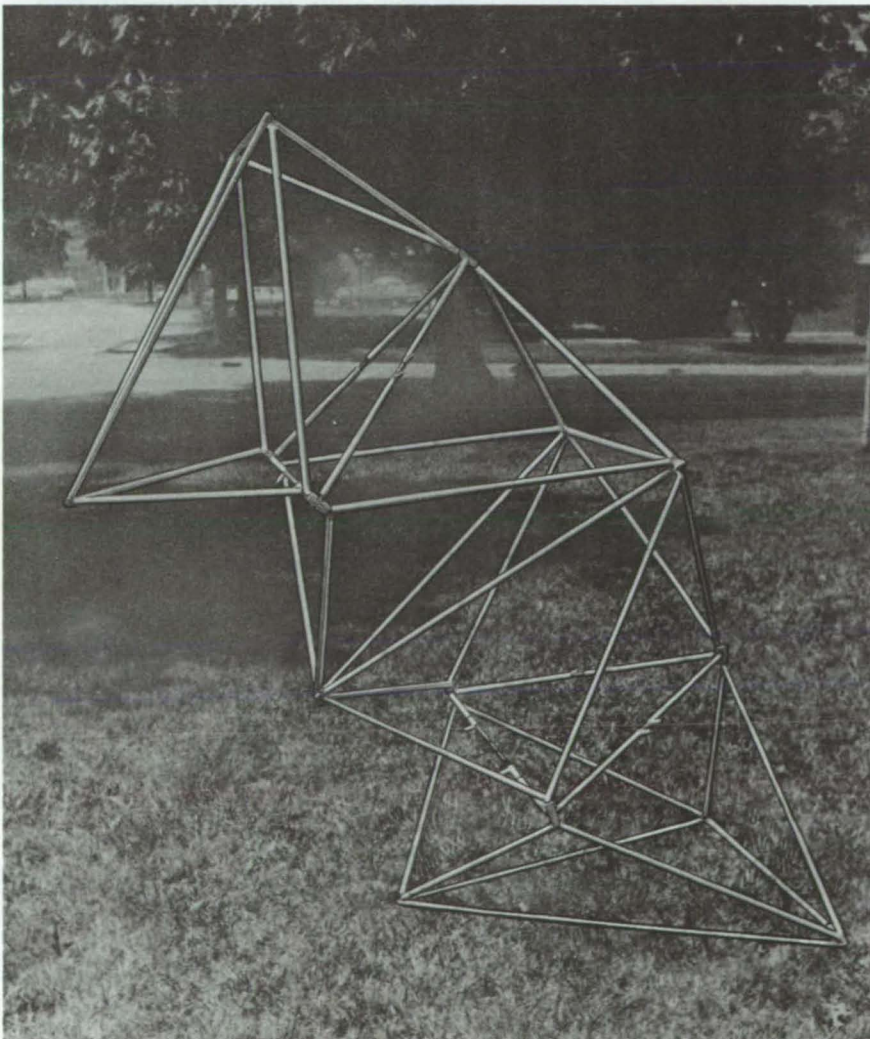
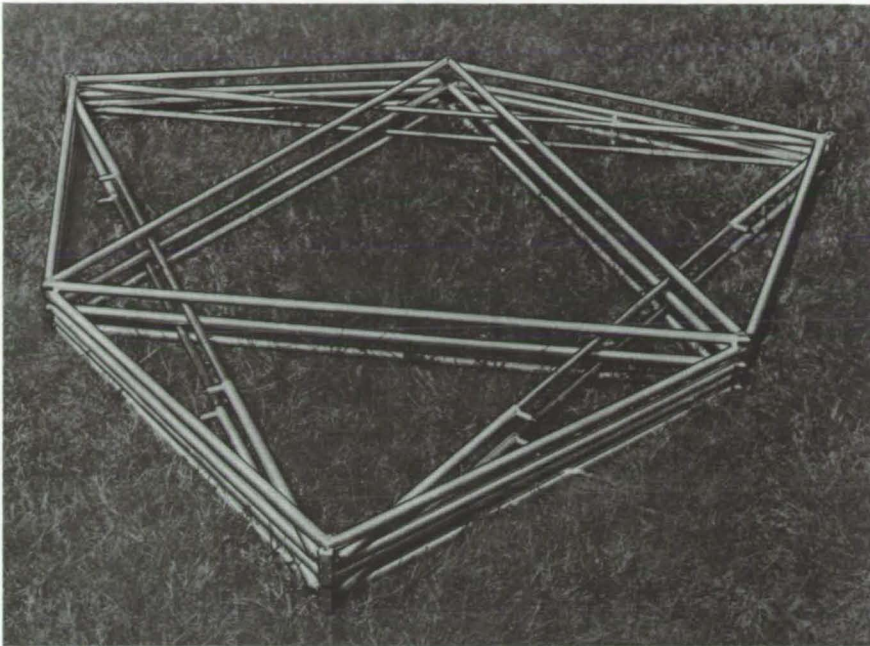
A convenient tapered ring seal maximizes the centering force generated by the sealed fluid, preventing contact between the seal and a shaft. The seal clearance decreases in the direction of flow. Fluid flow through the clearance produces a force that keeps the shaft centered.

(See page 541.)

Garter Valves

A proposed valve would control many inlets or outlets dispersed around the periphery of a cylindrical vessel. Radial or conical influx or efflux could be controlled evenly for combustion mixing and sampling. The essential parts of the valve are two rings machined to precise dimensions, with holes to form the flow passages, control surfaces, and channels.

(See page 540.)



The **Deployable Geodesic Truss** is shown collapsed for storage at the top and deployed at the bottom. Packaging efficiencies of 20 or greater are possible.

triangular relations. The necessary mobility of the crossmembers is obtained through ball-and-socket joints, and the actuators are hinged off the socket body.

Component members and joints for the deployable geodesic truss may be fabricated from conventional metallic materials or nonmetallic materials such as graphite/epoxy. The packaging efficiency (ratio of deployed height to stowed height) is a function of design requirements and may vary somewhat; however, packaging efficiencies of 20 or greater should be obtainable easily.

One alternate design of the concept is a truss that deploys automatically along the axis and does not articulate. This structure can be deployed repeatedly in a gravity-free environment, and the position of the tip will be at precisely the same location each time. Its unique geometric configuration permits the use of stored elastic energy in the actuators, thus eliminating the need for powered deployment aids or canisters frequently required for deployable space structures.

*This work was done by Martin M. Mikulas, Jr., Marvin D. Rhodes, and J. Wayne Simonton of **Langley Research Center**. For further information, Circle 109 on the TSP Request Card.*

This invention is owned by NASA, and a patent application has been filed. Inquiries concerning nonexclusive or exclusive license for its commercial development should be addressed to the Patent Counsel, Langley Research Center [see page A5]. Refer to LAR-13113.



Probe Follower for Moving Blood Vessels

An optical or pneumatic feedback system would maintain a probe for medical research at a fixed position relative to a blood-vessel wall. The objective is to keep the probe in contact with a region of tissue as the tissue moves, while minimizing the mechanical load on the tissue. The system would follow radial and axial blood-vessel motions

(See page 503.)

MiniBriefs describe NASA innovations and reports in an abbreviated format. Readers desiring additional information on these items should request the Technical Support Packages (TSP's), available in most cases, which can be obtained by using the TSP Request Card at the back of this issue.

Adjustable Mount

A remotely-controlled adjustable mount operates in vacuum environments.

A precision mount used in electro-optical transducers for measuring trace gas species in the stratosphere features a remote mechanical adjustment of five degrees of freedom (three translational, pitch, and azimuth) in one mechanism. The mount consists of a jacking-screw arrangement to control vertical direction and one horizontal direction. A gear-driven lead screw controls the other horizontal direction, while rack-and-pinion gears control the azimuth and pitch. All adjustments can be made independently of each other.

A fiberglass support provides structural stability and thermal and vibration isolations. Mount temperature is controlled by cooling through thermal exchange by means of a flexible thermal strap connected to a refrigerator unit. All appropriate joints have vacuum seals to maintain vacuum both statically and during readjustment.

This work was done by Edward A. Crossley, Howard C. Jones, David P. Haynes, and Irby W. Jones of Langley Research Center. For further information, Circle 110 on the TSP Request Card.

Inquiries concerning rights for the commercial use of this invention should be addressed to the Patent Counsel, Langley Research Center [see page A5]. Refer to LAR-13100.

Gas-Density Gage

Gas density is accurately and rapidly measured over large pressure ranges.

Atmospheric electron-beam experiments frequently depend on the density of gas at the injector point and require

quantitative knowledge of its instantaneous value. A lightweight density gage that operates over a broad pressure range accurately measures gas pressures.

A hot filament within the gage produces a regulated stream of 130-eV electrons that ionize the neutral gas inside a grid-cage structure. The emission current is kept constant by a control circuitry that maintains the filament temperature at constant levels. The formed ions are accelerated through an aperture and measured by a Faraday cup. The measured ion current is proportional to the density of gas. The instrument typically operates in the pressure range of 10^{-3} to 10^{-8} torr (133×10^{-3} to 133×10^{-8} N/m²).

This work was done by William Bernsterin and John McGarity of William Marsh Rice University for Marshall Space Flight Center. For further information, Circle 111 on the TSP Request Card.

Inquiries concerning rights for the commercial use of this invention should be addressed to the Patent Counsel, Marshall Space Flight Center [see page A8]. Refer to MFS-28011.

Capture-Range Indicator

A position indicator allows rapid positioning and linkage of payloads.

A positioning system can be used in the capture and linkup with a payload even when the payload is as far away as 1/2 in. (1.3 cm) from being berthed. As the payload is moved into berthing position, it impinges upon the device plunger. As the plunger is forced downward, a set of microswitches is activated by the operator to engage the payload. The 1/2-in. (1.3-cm) leadway provided by the wide-capture indicating

device shortens capture time and provides a less-stressful linkage on the operator.

This work was done by Clarence Heller of Marshall Space Flight Center. For further information, Circle 112 on the TSP Request Card.

Inquiries concerning rights for the commercial use of this invention should be addressed to the Patent Counsel, [see page A5]. Refer to MFS-28008.

Measuring Clearance Indirectly

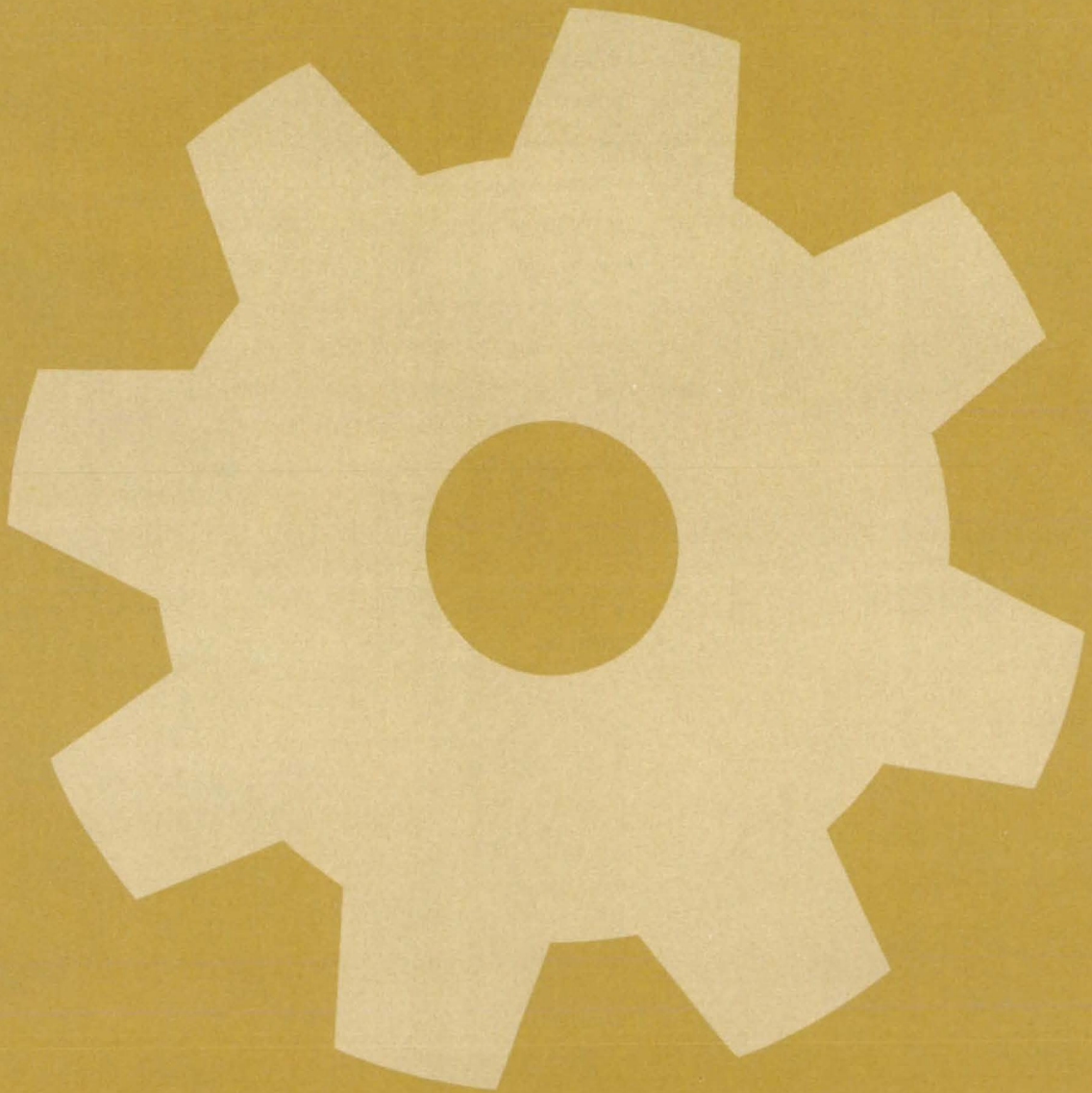
A plot of deflection versus load indicates clearance between internal pins and a wall.

A tool measures clearance in inaccessible areas. The tool was developed for measuring the clearance between dynamic damping pins and the liner of a hot-gas manifold. The tool relies on the principle that if a varying load is applied to a pin and its deflection is measured, the load-versus-deflection curve will have a different slope after the pin contacts the liner because of the added stiffness provided by the liner.

An operator positions a pneumatic cylinder inside the manifold with its ram on the top of the pin to be checked. A deflection sensor is positioned to contact a lip on the ram. The operator manually cycles the ram while an x-y plotter records a load-versus-deflection curve. The point on the curve where the slope changes abruptly indicates the clearance.

This work was done by Wayne C. Johnson and Bert O. Westberg of Rockwell International Corp. for Marshall Space Flight Center. For further information, Circle 113 on the TSP Request Card. MFS-19875

Machinery



Hardware, Techniques, and Processes

- 537 Safety Pedal for Foot-Operated Machinery
- 538 Bridle Attachment for Aircraft Spin-Recovery Parachute
- 539 Compact Antispin Parachute System
- 540 Garter Valves
- 541 Degreaser Reduces Solvent Loss
- 541 Tapered Ring Seal
- 542 Reactionless Winch
- 543 Remote Coupling of Electrical Connectors
- 544 Tool for Inserting and Removing Tube Plugs
- 544 Ignition-Spark Detector for Engine Testing
- 545 Hinged Shields for Machine Tools
- 546 Holding Cargo in Place With Foam
- 546 Automatic Robot Safety Shutdown System
- 547 EDM Electrode for Internal Grooves
- 548 Setup Aid for Electrical-Discharge Machining

Computer Programs

- 548 Propeller Design Program

MiniBriefs

- 549

Safety Pedal for Foot-Operated Machinery

A hinged structure prevents inadvertent use.

Lyndon B. Johnson Space Center, Houston, Texas

A pedal for turning on a metal-forming power brake can be moved quickly, yet resists inadvertent operation. Previously, power-brake pedals had to be covered by safety screens to prevent inadvertent use. The screens had to be removed to permit pedal operation. The new pedal thus improves both the productivity and safety of power brakes and such other machines as metal shears and punch presses.

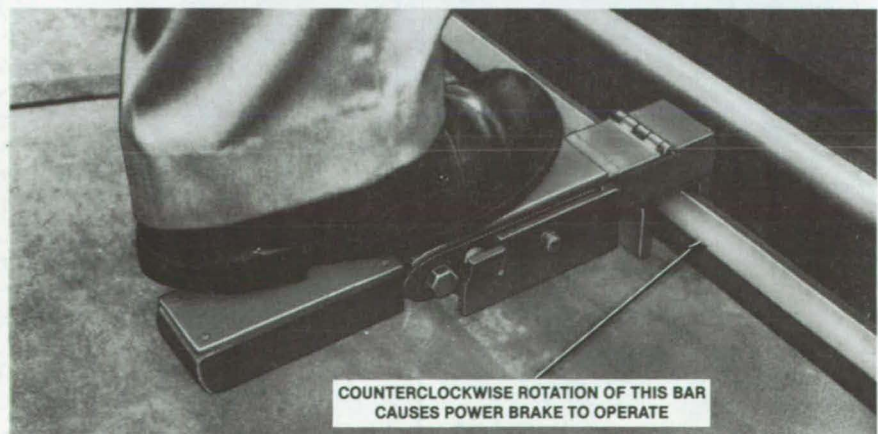
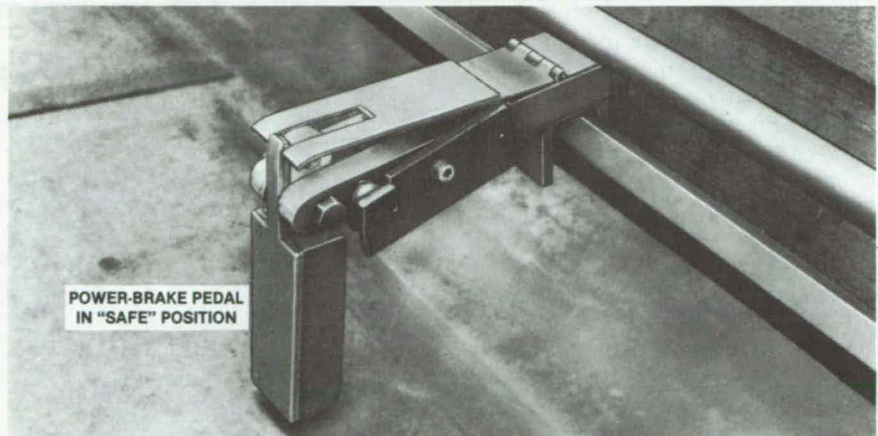
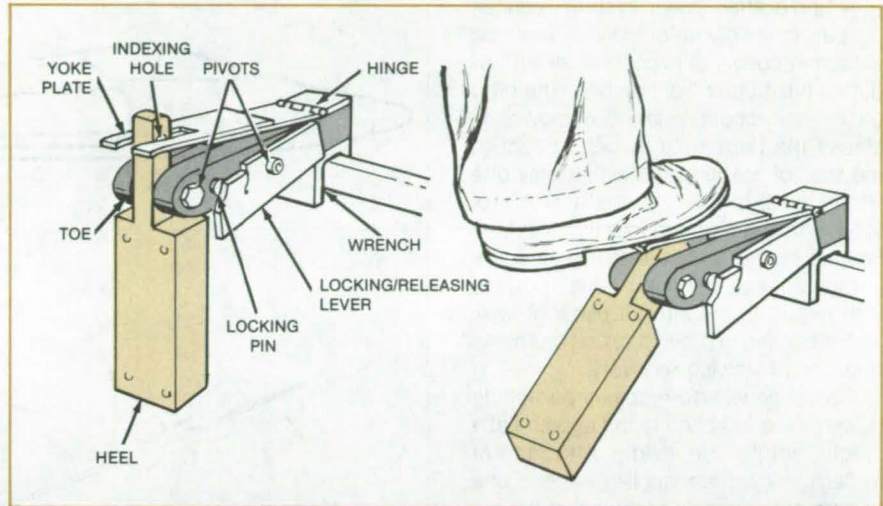
As shown in the figure, the pedal includes a fixed open-end wrench surface at one end to grip a bar with a hexagonal cross section. An operating cycle of the power brake or other machine is started by applying a torque to the bar through the pedal.

When the pedal is not being used and the machine is off, the hinged heel of the pedal hangs vertically, touching the floor and thereby preventing operation. To operate the machine, the operator presses a foot down and forward on the yoke plate and on the protruding tip of the heel. This action depresses the yoke plate slightly and simultaneously pivots the lower end of the heel upward until it is flush with the yoke plate.

Depressing the yoke plate also rotates a locking/releasing lever, which forces a spring-loaded pin into an indexing hole in the heel, locking the heel and toe together in line. The pedal is then a single composite unit that can be depressed with the full force of the operator's foot to operate the machine.

To release the brake, the operator removes the foot from the pedal. With no pressure on the yoke plate, the pin is disengaged, and the heel member collapses to its vertical position.

This work was done by Gilberto D. Garcia of Rockwell International Corp. for Johnson Space Center. No further documentation is available.
MSC-20535



A Forward Motion of the Foot on the yoke plate is necessary to operate the brake pedal. The downward force on the yoke plate turns the locking/releasing lever, which then pushes the locking pin into the indexing hole.

Bridle Attachment for Aircraft Spin-Recovery Parachute

Antispin rolling moment is produced by chute drag force.

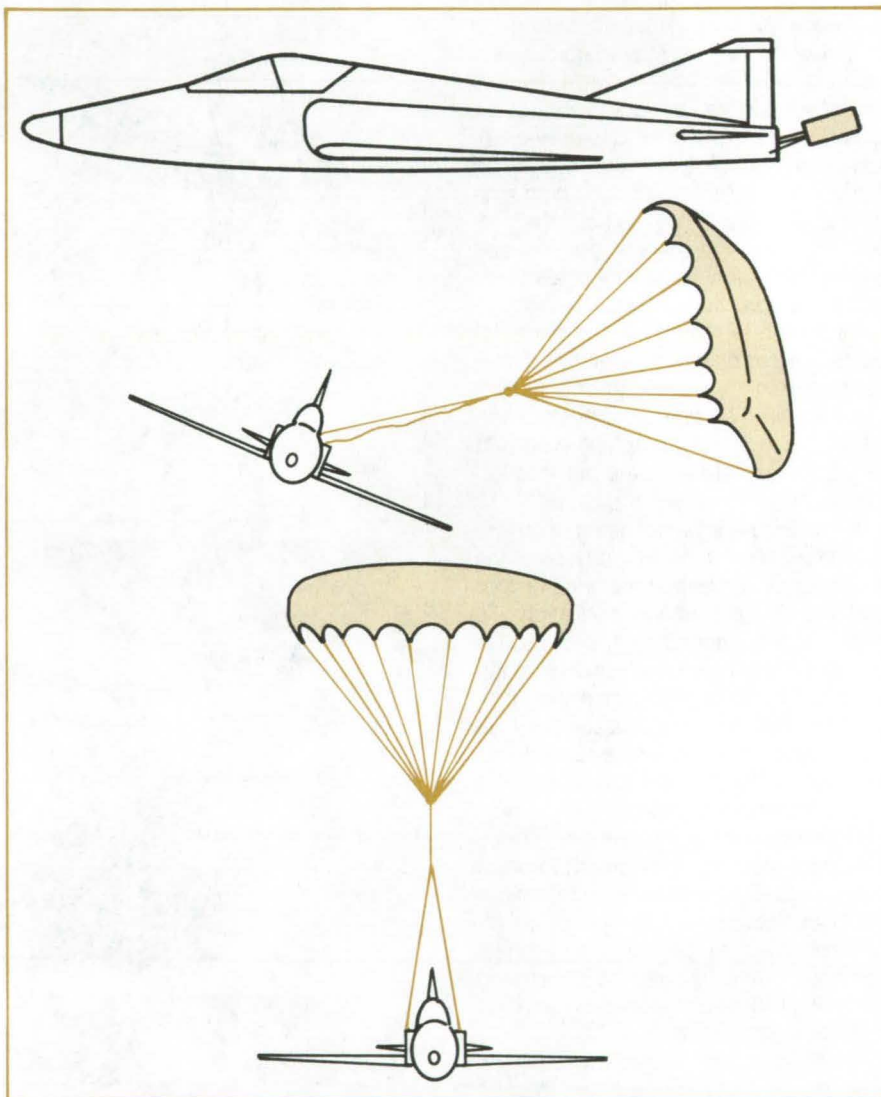
Langley Research Center, Hampton, Virginia

A bridle attachment system reduces the parachute diameter typically required for spin recovery of experimental aircraft during hazardous flight testing. The drag on the parachute, prior to deployment, places the parachute at deployment to the side of the aircraft so that only one line of the bridle is taut, that which provides a rolling moment into the spin (see figure). As the spin rate decreases, the parachute assumes a normal position with regard to the aircraft plane of symmetry, helping to prevent rolling moments prior to or following recovery.

Conventional spin-recovery parachute systems are attached to the airplane at a single point. The bridle attachment system, in contrast, applies force to one or both of two points at the tail of the aircraft. The bridle distributes the parachute drag force to produce a rolling moment appropriate to spin recovery. Data from model tests are presented in the table.

This work was done by William L. White of Langley Research Center. For further information, Circle 114 on the TSP Request Card.

This invention is owned by NASA, and a patent application has been filed. Inquiries concerning nonexclusive or exclusive license for its commercial development should be addressed to the Patent Counsel, Langley Research Center [see page A5]. Refer to LAR-13076.



Parachute Is Stowed prior to deployment. At deployment, the bridle attachment produces antispin rolling moment. At recovery, parachute forces are in the aircraft plane of symmetry.

Attachment	Parachute Diameter, ft (m)	Turns for Recovery
Single	30.9 (9.4)	6, 6¼
Single	37.4 (11.3)	3½, 4, 4¼
Bridle	20.8 (6.3)	6½, 6½, 8
Bridle	25.2 (7.8)	3, 3½, 4½

Smaller Parachutes attached by the bridle configuration are as effective in spin recovery as larger parachutes attached at a single point.

Compact Antispin Parachute System

Costs and complexity of parachute system are greatly reduced.

Langley Research Center, Hampton, Virginia

Antispin parachutes used for emergency spin recovery of aircraft during flight testing can be improved with a rigid towline. The towline (see figure) may be either fixed or extendable, the extendable version being either telescoping or unfolding.

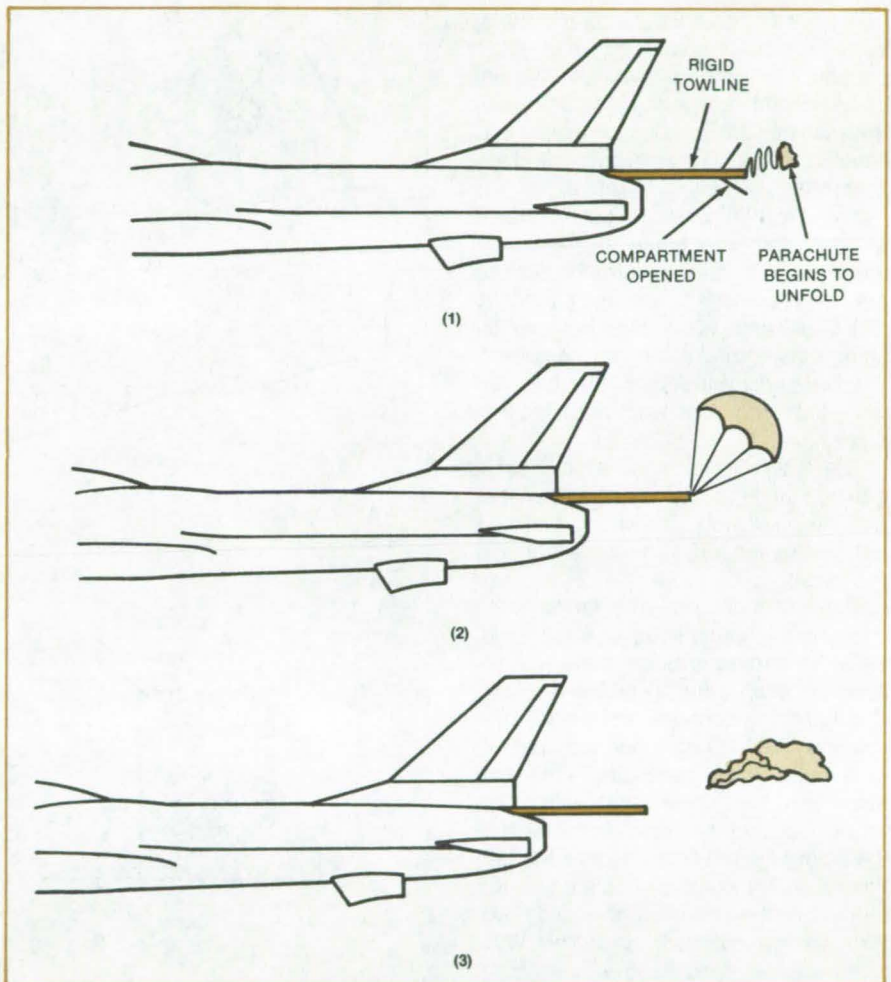
The advantage of this towline system is that it allows the use of a much smaller parachute, reducing the design loads on the structural reinforcement. Also, complex pyrotechnic-deployment or jettison systems are no longer necessary. Because of the reduced parachute size and the elimination of the deployment system, the parachute can be stored in a small compartment at the end of the rigid towline, rather than within the aircraft tail section.

The size of the antispin parachute and the length of the rigid towline are determined for each aircraft configuration by model tests in a vertical spin tunnel. Vertical-spin-tunnel test results from a fighter model, which has a fast flat spin, are compared in the table.

In test 1, the existing system as a baseline demonstrated unsatisfactory recoveries. A comparison with test 2 shows how a smaller parachute used with the rigid-towline system and entailing about half the design load produced acceptable recoveries. Test 3 shows results equivalent to test 1 except with a very small parachute on a rigid towline at less than 15 percent of the baseline design load.

This work was done by Raymond D. Whipple of Langley Research Center. For further information, Circle 115 on the TSP Request Card.

This invention is owned by NASA, and a patent application has been filed. Inquiries concerning nonexclusive or exclusive license for its commercial development should be addressed to the Patent Counsel, Langley Research Center [see page A5]. Refer to LAR-12979.



A Rigid-Towline Parachute System operates in three steps: (1) When the aircraft begins to spin, the parachute compartment is opened up, and the parachute unfolds; (2) the parachute is deployed and the spin terminated; and (3) the parachute is released.

Test	System	Parachute Diameter (ft)	Towline Length (ft)	Turns ⁽³⁾ for Recovery	Parachute Design Load (lb)
1	Conventional ⁽¹⁾	26	74 ⁽²⁾	14 ⁽⁴⁾	24,500
2	Rigid-Towline	18.5	12	5	12,400
3	Rigid-Towline	9.4	9	13	3,300

- (1) Implemented on flight-test aircraft
- (2) Flexible nylon line
- (3) Number of turns for spin recovery after parachute deployment; all control motions identical in all cases
- (4) Unsatisfactory: supplemental systems are required.

Test Results show how the rigid-towline antispin parachute compares with the conventional system. Tests 2 and 3 demonstrate the size and performance advantages over the conventional system used in test 1.

Garter Valves

Small subvalves are opened and closed simultaneously.

Marshall Space Flight Center, Alabama

A valve concept would control many inlets or outlets dispersed around the periphery of a cylindrical vessel. Radial or conical influx or efflux could be controlled evenly for combustion mixing and sampling. Such a valve might control the flow rate of fuel into a burner.

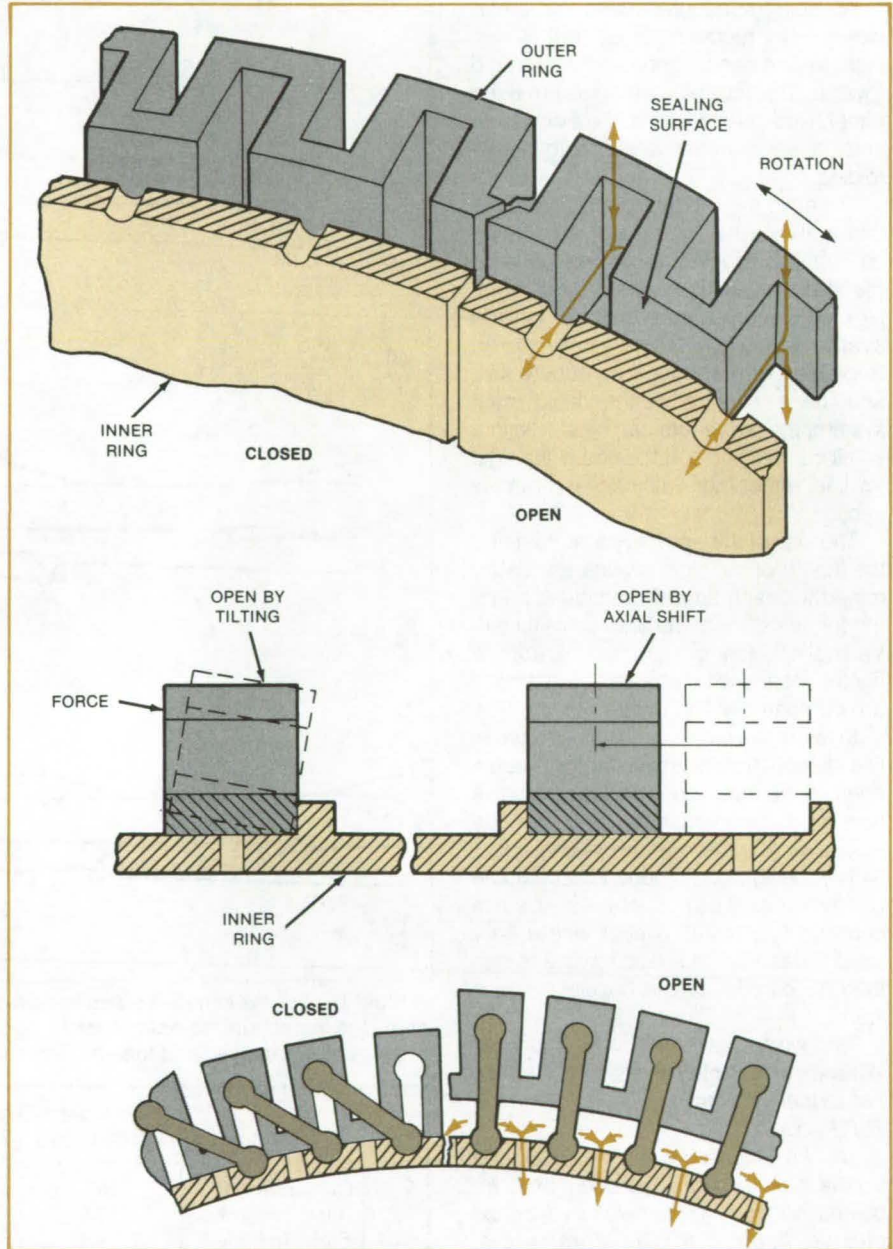
The essential parts of such a valve are two rings machined to precise dimensions, with holes to form the desired orifices, control surfaces, and channels. One of the rings is machined with weakening cuts to make it more compliant. The two rings fit together at mating surfaces that are lapped to conform to each other.

The inner ring is made slightly oversize so that it must be spring-force-fitted into the outer ring. The spring force on the mating lapped surfaces assures a tight seal.

Three of many possible versions are shown in the figure. In the one at the top, the inner and outer rings rotate with respect to each other in sliding contact. The inner ring contains radial holes, the spacing of which matches the spacing of channels in the outer ring. When the inner-ring holes are on the sealing surfaces midway between the channels of the outer ring, the flow is blocked. When the inner-ring holes are rotated to the centers of the channels, the fluid flows through the holes. Intermediate flow rates are obtained as the holes pass across the edges of the channels.

In the version at the middle of the figure, the more-compliant outer ring is held by the spring force against the holes in the inner ring, thereby blocking the flow. The outer ring can be either deformed and tilted by an axial force or else displaced axially to uncover the holes.

In the version at the bottom, the expandable outer ring is pushed outward and away from the holes by counterrotating the rings against small rods that pivot in both rings. A similar arrangement could be used to push one ring away from the other by opposing axial displacements.



Precisely-Machined Mating Rings act as valves. The rings seal against each other to stop fluid flow. The rings are deformed or moved relative to each other to uncover the holes and permit the flow.

This work was done by P. Jencek of Rockwell International Corp. for Marshall Space Flight Center. For further information, Circle 116 on the TSP Request Card.

Inquiries concerning rights for the commercial use of this invention should be addressed to the Patent Counsel, Marshall Space Flight Center [see page A5]. Refer to MFS-19899.

Degreaser Reduces Solvent Loss

Escape of solvent is minimized by a second cooling coil.

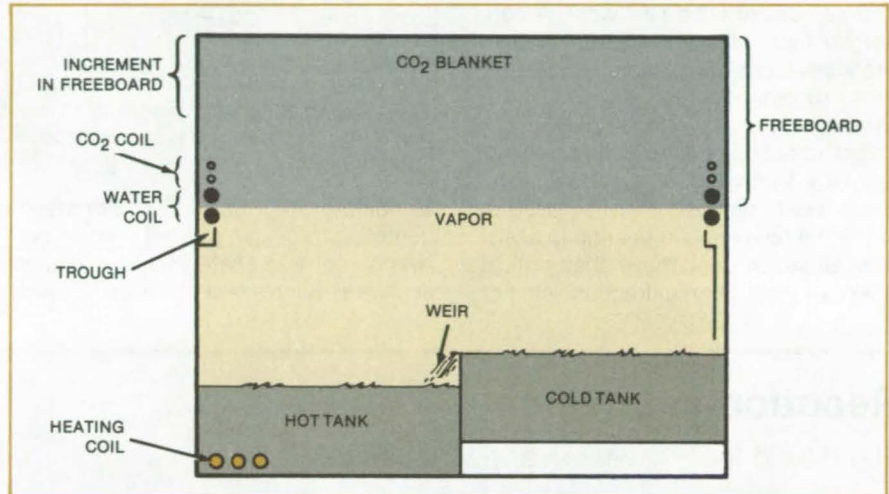
NASA's Jet Propulsion Laboratory, Pasadena, California

In the improved degreaser shown in the figure, the freeboard height above the water-filled cooling coil is increased by about 1 ft (30 cm) above that of earlier versions. A second cooling coil above the water-filled cooling coil operates at a lower temperature: It could circulate a recyclable refrigerant, such as liquid CO₂, brine, Freon, or ammonia. The new design minimizes loss of the solvent.

In one version, the refrigerant is CO₂ and is not recycled. Instead, it flows through the second coil, which is open at its lower end. As the CO₂ flows, it expands, cooling the coil, and emerges in the gaseous state to replenish the gas blanket in the vapor space.

The CO₂ lid is stable because the densest gas is the degreasing compound (molecular weight 131.4 for trichloroethylene, a typical degreaser). The next densest gas is CO₂ (molecular weight 44), followed by air (average molecular weight about 29). The density of the CO₂ relative to that of air is increased by the cooling coils.

Most of the solvent vapor condenses on the water-cooled coil. The lower portion of the gas blanket is mixed with the solvent vapor by turbulence created as the parts basket is raised or lowered. The lower portion of the blanket is partially purified by buoyant forces. The purification process is completed by a slow convection that brings the CO₂/sol-



An Improved Vapor Degreaser suppresses solvent-vapor loss through parts-basket dragout and air drafts. Within the CO₂ blanket, convection repeatedly exposes the CO₂/solvent mixture to the cold spot created by the CO₂ coil. Solvent vapor condenses, then runs down via the trough to the cold tank.

vent mixture to the upper cooling coil. There, the solvent condenses and runs down a trough. The cold purified CO₂ slowly descends to the lower edge of the blanket.

The rate of CO₂ use is small, since most of the solvent vapor is condensed on the water coil (as in other degreasers). The CO₂ coil removes only the small fraction of vapor that would otherwise escape into the atmosphere. This small expenditure of CO₂ never-

theless minimizes health and environmental hazards.

This work was done by Eugene R. du Fresne of Caltech for NASA's Jet Propulsion Laboratory. For further information, Circle 117 on the TSP Request Card.

Inquiries concerning rights for the commercial use of this invention should be addressed to the Patent Counsel, NASA Resident Office-JPL [see page A5]. Refer to NPO-16128.

Tapered Ring Seal

Centering force is maximized by decreased seal clearance in the flow direction.

Lewis Research Center, Cleveland, Ohio

An optimum-geometry ring seal has been designed that maximizes the seal centering force generated by the sealed fluid. Ring seals are commonly used to restrict fluid leakage between a rotating shaft and a nonrotating housing. Seals may be either fixed to the housing or floating, in order to accommodate shaft misalignment and vibration.

In the convergent tapered ring seal, the seal clearance decreases in the direction of flow (see figure). The fluid flow through the clearance space produces a centering force that tends to keep the shaft centered in the seal. The centering force is produced by the pressure distribution in the seal clearance. Pressure within the seal, in

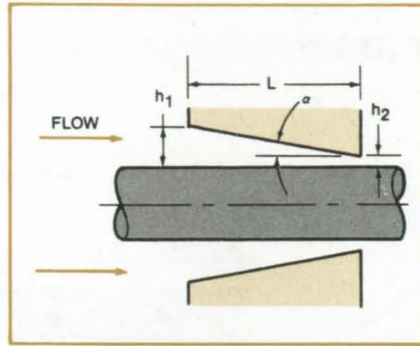
turn, depends on the sum of Bernoulli pressure drop (due to fluid-velocity increase) and friction pressure drop. When the seal is eccentric, pressure is higher on the low-clearance side (due to relatively smaller Bernoulli pressure drop) resulting in a centering force.

(continued on next page)



Existing seals have straight bores and produce much smaller centering forces than convergent tapered seals. For sealing a liquid, experiments have shown that the centering force in a convergent tapered seal is 40 percent or more greater than in a straight-bore seal. For a compressible fluid, a straight-bore seal may actually have a decentering force that can cause rapid seal wear. A convergent tapered seal, in contrast, always produces a positive self-centering force; thus, rubbing contact and wear are avoided.

The convergent tapered ring seal is a significant advance in seal technology. For a fixed ring seal, it can be used to serve the function of a bearing to assist in shaft support and move shaft critical speeds to less harmful frequencies. For



The Tapered Ring Seal produces higher centering forces than conventional straight seals.

a floating ring seal, the increased centering force can prevent contact between seal and shaft, thus eliminating seal wear. Such a seal is now being used

in the Space Shuttle main engine oxygen pump; the previously used seal wore severely, whereas the convergent tapered seal performs well over the life of the pump.

This work was done by David P. Fleming of **Lewis Research Center**. Further information may be found in NASA TP-1646 [N80-19495/NSP], "Damping in Tapered Annular Seals for an Incompressible Fluid" [\$7]. A copy may be purchased [prepayment required] from the National Technical Information Service, Springfield, Virginia 22161.

Inquiries concerning rights for the commercial use of this invention should be addressed to the Patent Counsel, Lewis Research Center [see page A5]. Refer to LEW-14055.

Reactionless Winch

Hand-held tool serves a variety of uses.

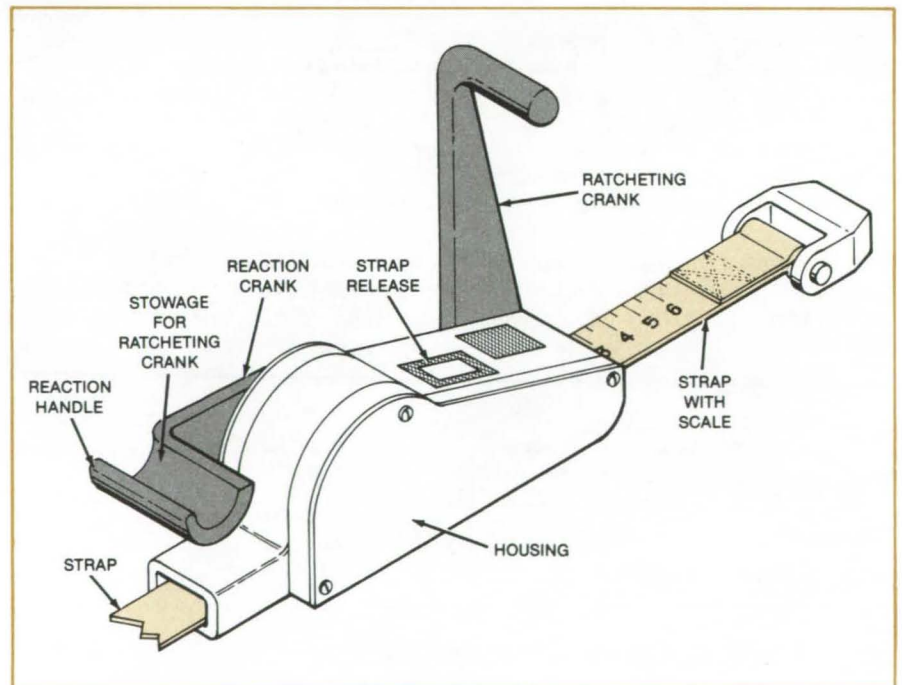
Lyndon B. Johnson Space Center, Houston, Texas

A lightweight, hand-held winch designed for use by astronauts on the Space Shuttle has a reaction crank braced against the housing, in addition to a ratcheting crank. To pull on the load, the operator squeezes handles of the two cranks toward each other (as with pliers or scissors). Since all forces are thereby reacted into the tool, there is no need to restrain or brace the operator against an external object.

The winch features retracting polyester straps instead of the cables and pulleys found on "come-along" ratcheting pullers. In its present form, the total length is adjustable out to 15 ft (4.6 m). The ends of the straps are equipped with pintle hooks.

In one version, the reaction crank can be rotated between its operating position and a storage position in which it protrudes less from the housing. In another version (see figure), the reaction crank could be either stowable or fixed to the housing, and the ratcheting crank handle nests in the reaction-crank handle.

The winch could be used by divers working underwater. It also might be used for pulling vehicles out of mud, lifting heavy objects, or tightening cables.



The Housing of the Winch includes simple controls and a reaction handle that also serves as stowage for the ratcheting-crank handle.

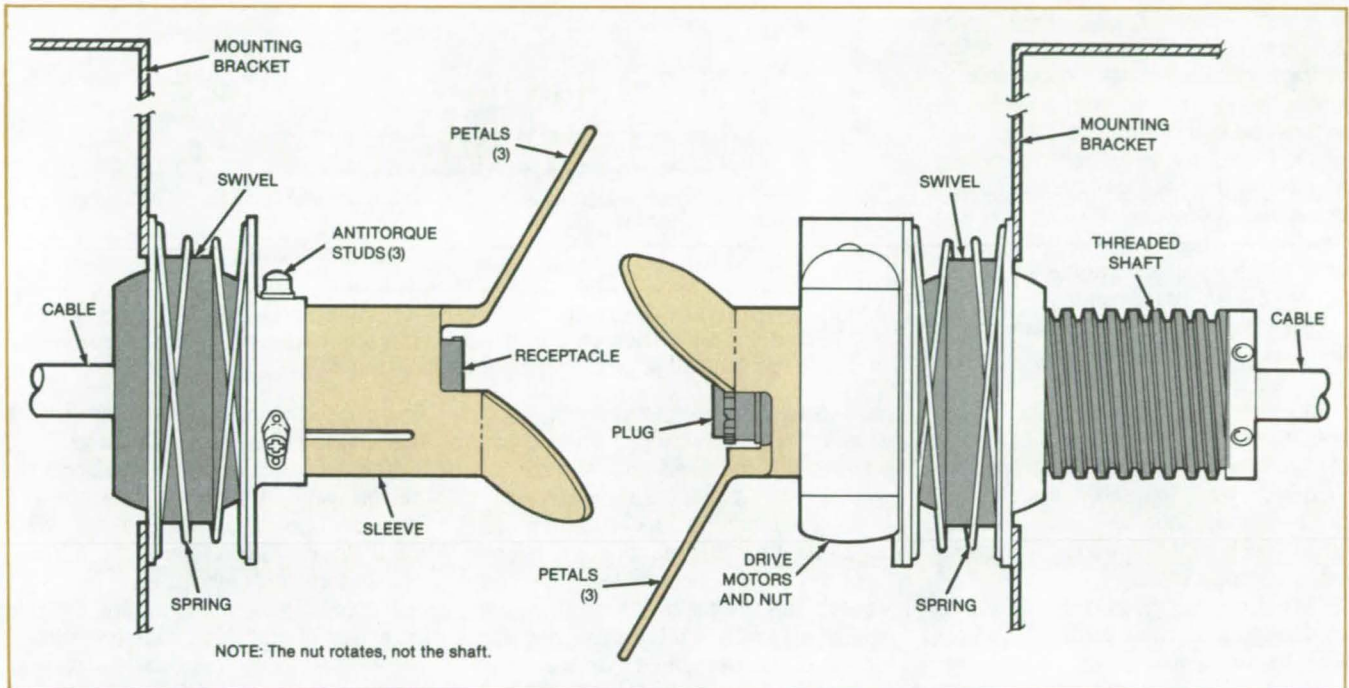
This work was done by Barry E. Boswell of McDonnell Douglas Corp. for **Johnson Space Center**. For further in-

formation, Circle 118 on the TSP Request Card. MSC-20440

Remote Coupling of Electrical Connectors

Device aligns a plug and receptacle axially and radially.

Lyndon B. Johnson Space Center, Houston, Texas



A Standard Multiple-Pin Plug and Socket are mounted in the mechanism. As the threaded shaft moves out from its mounting bracket (to the left in this view), the two sets of petals engage each other and correct misalignment. The misalignment is absorbed by the spring-mounted swivels.

An automatic mechanism connects and disconnects a self-aligning electrical plug and receptacle. Designed for umbilical cables between the Space Shuttle and a payload, the mechanism is adaptable to other remote or hazardous situations in which a human is not available to connect mating parts by hand — underwater or in poisonous atmospheres, for example. A principal advantage is that precise prealignment of the mating parts is not necessary. The parts are merely brought near each other, after which sets of petals and swivels align the parts as one is inserted in the other.

Conventional flanged plugs and sockets are used with the mechanism (see figure). The usual coupling ring is not required. The plug and the receptacle are mounted on swivel joints, each of which functions in combination with a counterwound conical compression spring to orient the part approximately perpendicular to its mounting bracket. The large diameter of the springs in relation

to their length ensures that they offer minimal resistance to the swiveling freedom of the joint. At the same time, the counterwound configuration of the springs ensures that the swivel joints resist torsion equally in either a clockwise or counterclockwise direction.

Extending from either half of the connector are three equally spaced petals. The plug and its petals are mounted on a threaded shaft. Electrical motors turn a large nut around the shaft, thus extending or retracting the plug.

As the plug extends, its petals engage those of the receptacle. Each petal trio adjusts its position to accommodate the other. With further extension of the screw, axial and radial misalignment of the connector halves is taken up by the swivels.

When the force exerted by the plug on the receptacle reaches a predetermined value, the receptacle spring yields, and the sleeve starts to retract. When the sleeve has traveled about halfway

toward its mounting bracket, a limit switch stops the drive motors. The connector parts are then in the mated position. In combination, the springs and swivels tolerate sizable changes in the relative position of the connector mounting brackets without affecting the electrical connection.

Demating the connectors is an uncomplicated process. Reversing the direction of the drive motors retracts the plug screw until the plug and receptacle are disengaged.

This work was done by Richard T. Barbour of Rockwell International Corp. for Johnson Space Center. For further information, Circle 119 on the TSP Request Card.

Inquiries concerning rights for the commercial use of this invention should be addressed to the Patent Counsel, Johnson Space Center [see page A5]. Refer to MSC-20414.



Tool for Inserting and Removing Tube Plugs

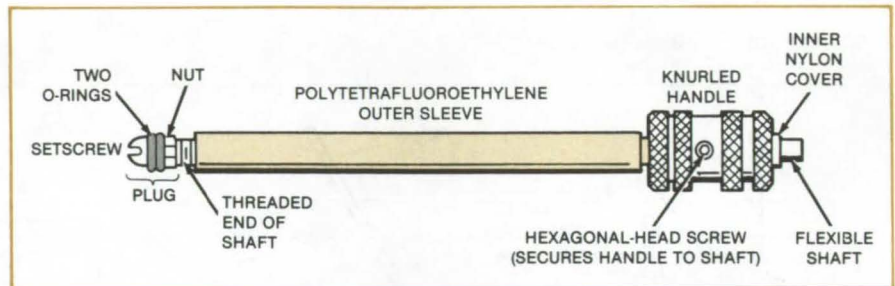
Simple handtool can be used with both straight and bent tubes.

Marshall Space Flight Center, Alabama

A tool inserts a plug deep inside a tube to protect the innermost section of the tube from contamination during inspection or testing. With the plug inserted, the end of the tube can be subjected to inspection by penetrant dyes, to grinding, the casting of internal molds, and other operations. After debris and residue have been rinsed away by a solvent, the tool is used to remove the plug, leaving the entire tube clean.

The plug includes two expandable fluoroelastomer O-rings on a short threaded shaft. The O-rings are axially compressed by turning a setscrew or nut, thereby radially expanding the O-rings to make a tight seal against the tube inner wall. The end of the plug opposite the screwhead has a threaded hole to receive the threaded end of the flexible shaft.

The plug is screwed onto the end of the flexible shaft, then is inserted in the tube to the required depth. The user rotates the handle to unscrew the shaft from the plug. The tool can then be



A Plug Consisting of Two Expandable O-Rings is pushed into or pulled out of a tube with this flexible tool. The flexible shaft of the tool is threaded at the inner (plug) end to engage or disengage the plug when the knurled handle is turned.

pulled out of the tube, leaving the plug inside. To remove the plug, the user simply screws the threaded end of the shaft into the plug, then pulls the plug out.

So that it can be used in bent as well as straight tubes, the tool has a flexible shaft made of speedometer cable (see figure). The shaft is sheathed in a nylon sleeve, which in turn is surrounded by a polytetrafluoroethylene sleeve. This combination results in exceptionally low friction between the shaft and the tube

and allows the insertion and removal of the plug to be carefully controlled.

This work was done by Orlando G. Molina and Antonio G. Pascua of Rockwell International Corp. for Marshall Space Flight Center. No further documentation is available.

Inquiries concerning rights for the commercial use of this invention should be addressed to the Patent Counsel, Marshall Space Flight Center [see page A5]. Refer to MFS-19871.

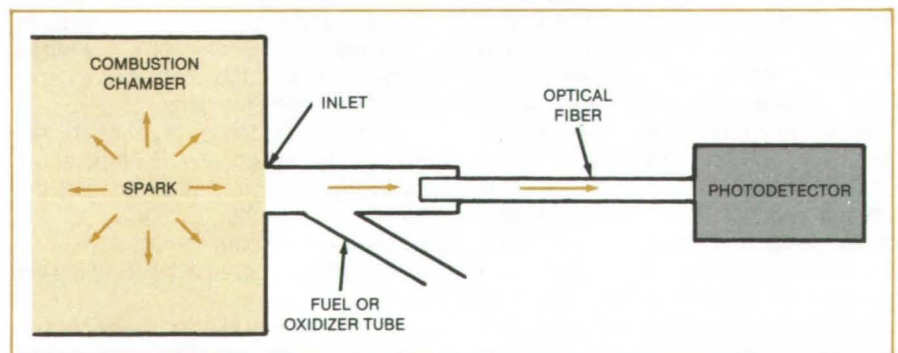
Ignition-Spark Detector for Engine Testing

An optical fiber views sparks directly.

Marshall Space Flight Center, Alabama

A photodetector linked by optical fiber to a combustion chamber determines whether or not an ignition spark has occurred. Useful in engine testing, the detector helps determine the reason for engine failure. If no spark is observed, then the problem is probably in the ignition circuit. If a spark is detected, it is likely that the problem is in the fuel system.

The optical-fiber is inserted in a fuel or oxidizer tube through a Y-shaped tube near the inlet to the combustion chamber (see figure). The cable is positioned so that it has the best possible line



In a Fuel or Oxidizer Tube, an optical fiber collects light from an ignition spark. The fibers can also be used to collect light from combustion reactions for spectrographic analysis.

of sight to the igniter tip to collect the maximum amount of light. Light from the spark travels through the fuel or oxidizer and reflects from the tube wall into the cable. The optical-fiber cable carries the light to a photodetector circuit, which registers the occurrence of the spark.

The detector was originally developed for igniters in the Space Shuttle main engine. Its principle is adaptable to industrial or residential furnaces or to engines for internal-combustion research. It also might be possible to replace the photodetector with a spec-

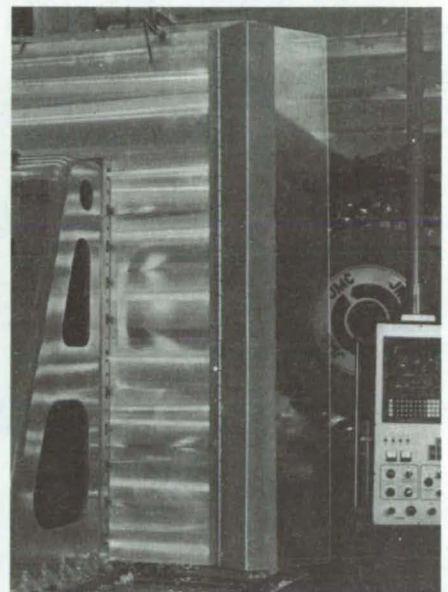
trograph for combustion studies.

This work was done by George Kuhr of Rockwell International Corp. for Marshall Space Flight Center. No further documentation is available.
MFS-19890

Hinged Shields for Machine Tools

Flaps guard against flying chips, but fold away for tool setup.

Goddard Space Flight Center, Greenbelt, Maryland



A Clear Plastic Shield is in position to intercept flying chips from a machine tool (left) and retracted to give the operator access to the workpiece (middle). The view from behind the platen (right) shows the hinge. Machine shops can readily make such shields for their own use.

A hinged shield deflects flying chips on a horizontal-spindle milling machine. Made of clear plastic, it allows the operator to view the machining process.

The shield is permanently mounted on a vertical platen (see figure). When the

machine operator requires access to the workpiece, the shield is folded back out of the way. In contrast, some commercial shields tested for this NASA application had to be continually repositioned to intercept flying chips. They also

had to be lifted on and off the machine tool to allow access to the workpiece.

This work was done by John B. Lallande, Woodrow W. Poland, and Stuart Tull of Goddard Space Flight Center. No further documentation is available.
GSC-12915



Advanced dc-Traction-Motor Control System

A proposed motor control for battery-powered vehicles includes separate excitation of the motor windings in traction and in regenerative braking. The power-conditioning subsystem operates under the control of a computer that coordinates traction, braking, and protective functions. The computer control is through a drive-logic unit.

(See page 449.)

Proximity Indicator for Remote Manipulator

A display indicates the pitch, yaw, and distance of a remote manipulator with respect to an object to be grasped. When the errors in position and orientation are small enough to ensure a successful grasp, the unit alerts the operator with audible and visible signals. The display unit is intended for a four-claw hand.

(See page 468.)

Improved Coulomb-Friction Damper

An improved coulomb (sliding) friction damper resists motion equally on both the forward and reverse strokes. The damper has two Belleville springs — one on either end of a piston wedge. The wedge therefore pushes the friction pad outward against the cylinder with equal force in both directions of travel.

(See page 515.)

Holding Cargo in Place With Foam

Foam would fill the entire container to protect cargo from shock and vibration.

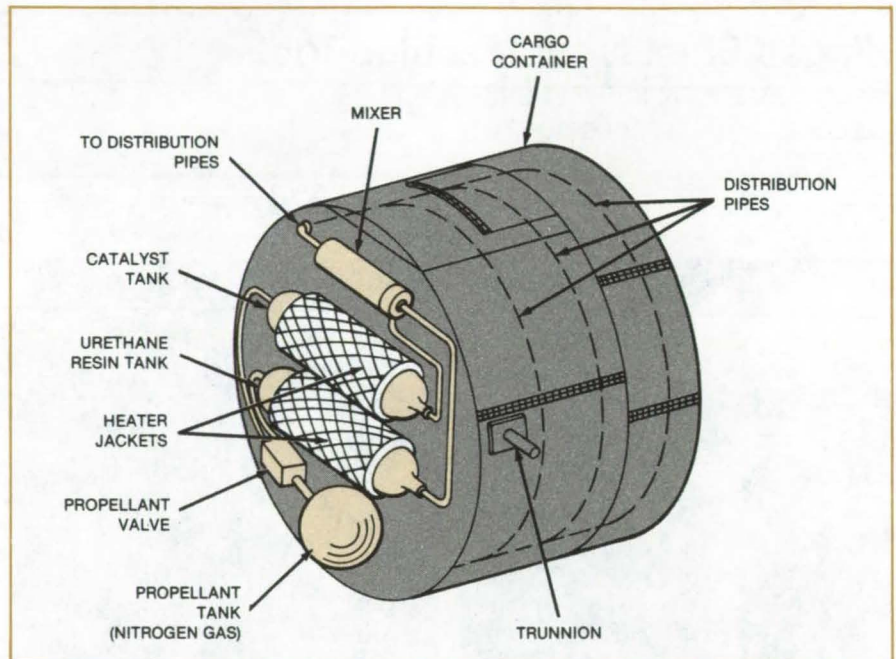
Lyndon B. Johnson Space Center, Houston, Texas

A proposed foam-in-place encapsulation method would secure cargoes for transportation from remote locations. The method requires two basic elements: an enclosure large enough to accommodate the cargo and an encapsulating material to support the cargo and resist the forces imposed on it during transportation. Originally developed for stowing space debris and spent satellites in the Space Shuttle for return to Earth, the encapsulation concept is also suitable for preparing shipments to be carried by truck, boat, or airplane.

The shipping container would support the equipment necessary to fill the spaces around the cargo with polyurethane foam (see figure). This equipment includes tanks for the resin and catalyst, a propellant-gas tank, a mixing chamber, a distribution network of piping and orifices within the container, and valves, meters, and control devices for automatic operation.

Before the foaming operation, the cargo can be supported by netting. The density of the foam can be modified to accommodate different cargo masses and shapes.

This work was done by Thomas T. Fisher of Lockheed Missiles & Space Co., Inc., for Johnson Space Center. No further documentation is available. MSC-20723



This **Cylindrical Cargo Compartment** contains equipment that automatically injects polyurethane foam into its interior to hold cargo securely in place. A container of rectangular or other cross section could be built to match the shape of the vehicle in which it is to be used.

Automatic Robot Safety Shutdown System

Robot is turned off if its acceleration exceeds a preset value.

Marshall Space Flight Center, Alabama

A safety controller monitors the movements of a robot and shuts it down if they do not conform to a previously established pattern. The unit could control other machines that perform repetitive movements, including rotary tables, tracked vehicles, conveyor lines, and elevators.

A three-axis piezoelectric accelerometer is mounted on the robot arm. The analog accelerometer outputs are transmitted to a computer where they are digitized and sampled 60 times per second (see figure). To set the acceleration limits, an operator runs the robot through one "good" cycle of its routine,

and the computer stores the resulting accelerometer data.

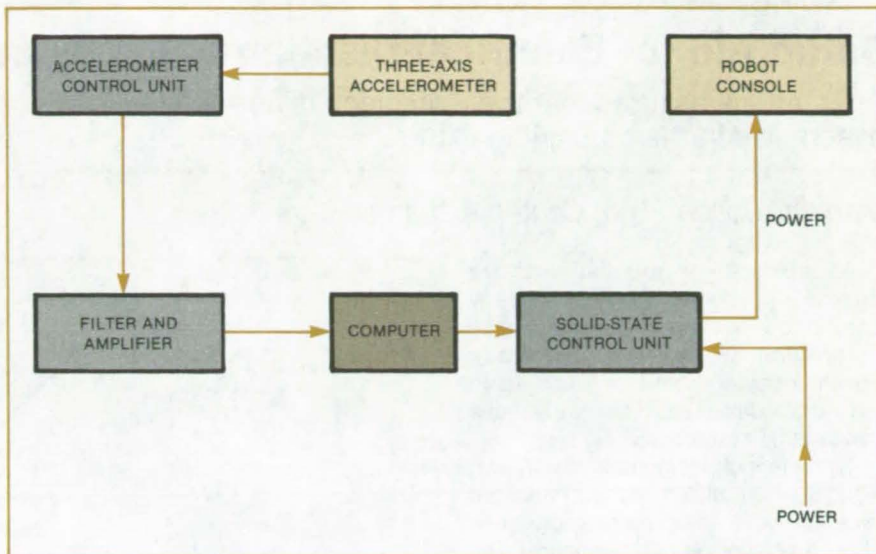
During succeeding work cycles, the computer samples the accelerometer signals and compares them with the stored data. When it detects a deviation of more than a preset amount, the computer generates a shutdown signal,

energizing a solid-state relay that interrupts power to the robot.

In one test on an industrial robot, motion was stopped within about 1 inch (2.5 cm) of the point at which nonconforming motion started. The response time could be shortened by increasing the sampling rate. However, a larger computer memory would then be needed to store the sampled data. In principle, sensors other than accelerometers could be used. For example, capacitive or ultrasonic sensors might be substituted.

This work was done by M. J. Lirette of Martin Marietta Corp. for Marshall Space Flight Center. For further information, Circle 120 on the TSP Request Card.

Inquiries concerning rights for the commercial use of this invention should be addressed to the Patent Counsel, Marshall Space Flight Center [see page A5]. Refer to MFS-25969.



Signals From an Accelerometer on a robot arm pass through a filter and amplifier, which eliminate high-frequency noise and hydraulic-pump pulsations. Data are then digitized and processed in the computer.

EDM Electrode for Internal Grooves

Electroerosive process is an inexpensive alternative to broaching.

Marshall Space Flight Center, Alabama

An inexpensive tool allows electric-discharge machining (EDM) of lengthwise grooves on the internal surfaces of tubular parts. The tool can be used on tubes already in place in equipment.

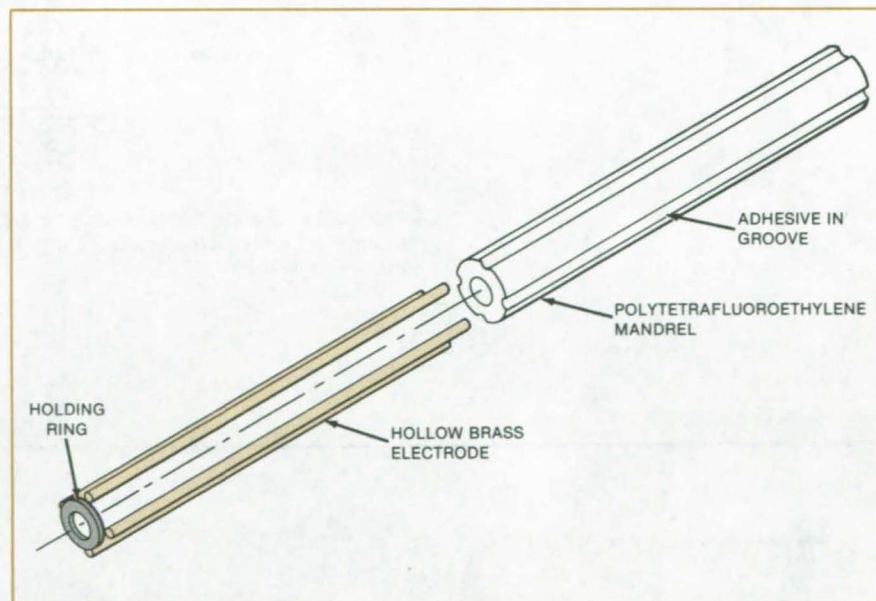
The tool consists of thin tubular brass electrodes bonded by an epoxy adhesive in premachined grooves in a polytetrafluoroethylene mandrel. The tool is inserted in a part to form grooves on the inside surface adjacent to the brass electrodes.

Attempts to use ceramic or glass for the mandrel were unsuccessful. Polytetrafluoroethylene was selected because it is nonconducting, readily machined, and easily bonded to the brass electrodes.

The tool can be redesigned for electric-discharge machining of grooves on outside surfaces. In this case, the electrodes would be bonded in grooves on the inside surface of a tubular mandrel.

This work was done by Ven Ramani and Al Werner of Rockwell International Corp. for Marshall Space Flight Center. No further documentation is available.

MFS-19733



Hollow Brass Electrodes, soldered at one end to a stainless-steel holding ring, are held in grooves in the mandrel. These electrodes are used to machine grooves electrically in a stainless-steel tube three-eighths inch (9.5 millimeters) in diameter.

Setup Aid for Electrical-Discharge Machining

An interlock assures that the workpiece is correctly assembled in the machining fixture.

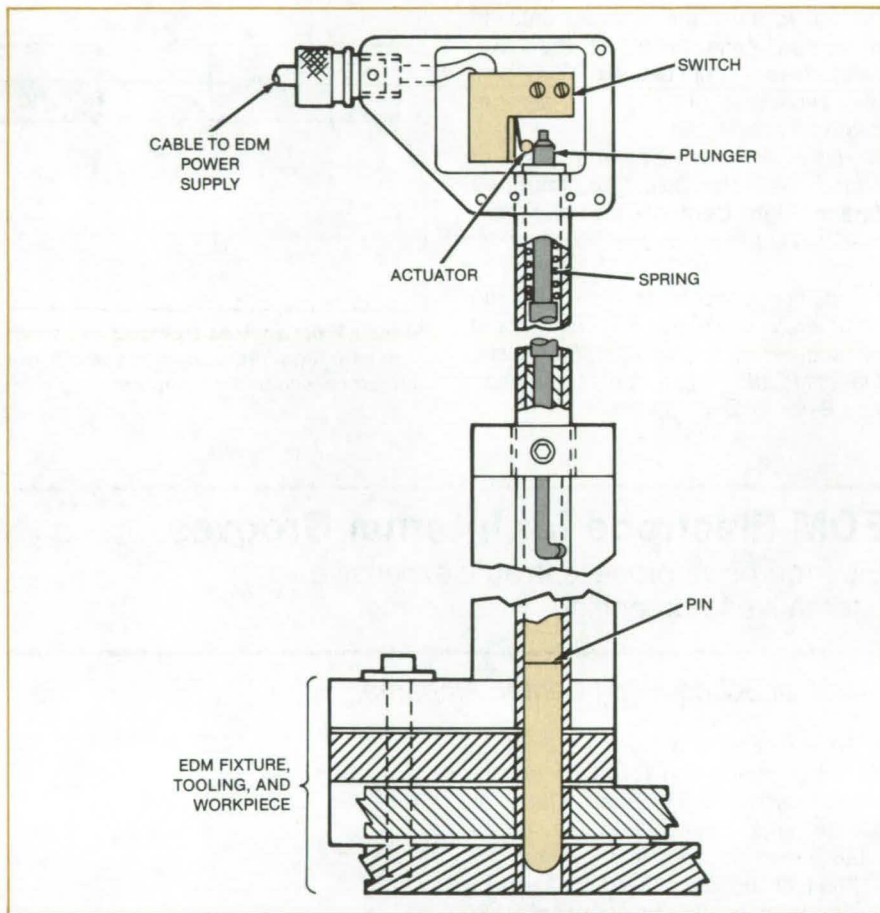
Marshall Space Flight Center, Alabama

An interlock ensures that parts are completely assembled and properly positioned for electrical-discharge machining (EDM). The interlock prevents power from being applied to the electrodes unless the parts have been set up correctly.

The interlock includes a switch that signals when all the mating parts are assembled in their correct positions about a positioning pin (see figure). The pin can be fully inserted only if the parts are in the correct orientation. When fully inserted, the positioning pin pushes against a plunger that moves against the switch actuator, thereby turning on the current.

This work was done by Gerald Lines and John Duca of Rockwell International Corp. for Marshall Space Flight Center. No further documentation is available.

MFS-19874



A Plunger in a Hollow Shaft actuates a switch, allowing a power supply to produce current for electrical-discharge machining. The plunger operates only when the necessary parts are in position.

Computer Programs

These programs may be obtained at very reasonable cost from COSMIC, a facility sponsored by NASA to make new programs available to the public. For information on program price, size, and availability, circle the reference letter on the COSMIC Request Card in this issue.

Propeller Design Program

Planform and propeller twist with minimum induced loss are calculated.

The theoretical basis for the design of propellers was well developed by 1920 and has been further refined in succeeding years. Most propellers, however, have been designed using empirical methods. The theoretical approach has been neglected because of the complex nature of the problem and the lack of a theory

combining the important contributions of various investigators.

Now a new theoretical treatment that combines the classical theories of Betz-Prandtl, Goldstein, and Glauert is easily applied to the problem of determining the propeller blade geometry for minimum induced loss. The analysis is applicable at subsonic flight speeds and neglects structural considerations in the propeller design.

This propeller design method has been programed for the HP9820 desk top calculator and the HP9830 desk top computer. The HP9820 desk top calculator uses its own machine language for programing. For this calculator, the propeller design program requires as input: Thrust, airspeed, rotational speed, air density, diameter, number of blades, and blade-section characteristics (angle-of-attack, lift coefficient, and lift-to-drag ratio) as a function of radial station along the blade. As output, the program provides propeller blade plan-

form, pitch distribution, torque, and efficiency. A plotting option draws the propeller-blade-developed planform and top and side views of the blade.

Additional capabilities were programed in BASIC program language for the HP9830 desk top computer. Input to this program may be either thrust or absorbed power, airspeed, rotational speed, altitude, diameter, number of blades, and blade section characteristics (angle-of-attack, lift coefficient, and drag-to-lift ratio) as a function of radial station along the blade.

The program output is blade planform, pitch distribution, slipstream displacement velocity, propeller efficiency, and, as a function of radial station along the blade, mach number and Reynolds number. The program draws the propeller-developed blade planform and top and side views of the blade. It also plots blade angle, mach number, and Reynolds number as a function of radial position along the blade.

These programs were written by

William H. Phillips of Langley Research Center. The theoretical development was done by E. Eugene Larrabee of the Massachusetts Institute of Technology. The theory for the HP9820 program is found in the Symposium of the National Free-Flight Society, 1977. A copy may be purchased from NFFS Plans and Publications, c/o Fred Terzian, 4858 Moorpark Ave., San Jose CA 95129. The theory for the HP9830 program is given in the following paper: Larrabee, E. Eugene, "Practical Design of Minimum Induced Loss Propellers," SAE Paper 790585, 1979. A copy may be purchased from the Society of Automotive Engineers, Inc., 400 Commonwealth Drive, Warrendale, PA 15096. For user instructions and a listing of the HP9820 program, Circle 165 on the TSP Request Card. For user instructions and a listing of the HP9830 program, Circle 166 on the TSP Request Card. LAR-13141 and LAR-13142

MiniBriefs describe NASA innovations and reports in an abbreviated format. Readers desiring additional information on these items should request the Technical Support Packages (TSP's), available in most cases, which can be obtained by using the TSP Request Card at the back of this issue.

Hybrid-Vehicle Transmission System

Internal-combustion engines and electric motors are coupled by a variable transmission.

A continuously-variable transmission system for hybrid vehicles couples the internal-combustion engine and the electric motor section, either individually or in parallel, to power the vehicle wheels during steering and braking. An onboard computer controls a high-pressure hydraulic system that carries power from the combustion engine to the wheels via a converter and steel belt and provides the necessary vehicle power to function during electric-only operation. Belt tension and transmission-ratio variation are changed by means of a solenoid valve that modulates oil pressure of the hydraulic system.

This work was done by Giorgio Lupo and Giulio Dotti of Centro Ricerche Fiat S. p. A. for NASA's Jet Propulsion Laboratory. For further information, Circle 121 on the TSP Request Card. NPO-16119

Evening Flow Distribution Through Parallel Tubes

Flow nonuniformity in parallel tubes can be reduced by introducing pressure drops.

Nonuniform distribution of gas or liquid flow through parallel-path equipment such as those found in solar-powered heat pumps or low-pressure refrigerants can be reduced by introducing additional pressure drops to each of the parallel tubes. If the added pressure drop is large compared to the difference in pressure drops for all-liquid and all-

vapor flows through the tubes, then uniform flow will result.

Flow constrictors such as check valves introduced into each tube increase the pressure drop through that tube and improve the uniformity in flow distribution. Total flow is maintained and controlled by varying the main inlet-valve position.

This work was done by Steven C. Bray, Peter W. Dietz, and Heinz Jaster of General Electric Co. for Marshall Space Flight Center. For further information, Circle 122 on the TSP Request Card.

Inquiries concerning rights for the commercial use of this invention should be addressed to the Patent Counsel, Marshall Space Flight Center [see page A5]. Refer to MFS-23936.



Linear Boom Actuator

Angular supports for spacecraft components are varied to control wobble.

A linear actuator that controls spacecraft wobble may have applications in rotating systems on Earth. The actuator stabilizes spacecraft spin by varying the length of support struts that hold the spacecraft booms. The variation changes the spin axis and controls wobble.

The actuator uses redundant low-torque steel spur gears and bearings impregnated with perfluoroalkylpolyether lubricant. When the stepper motors are deenergized, a magnetic detent prevents the gear train from being back-driven and eliminates the need for either a clutch or brake. The housing maintains a positive pressure to protect the internal components from the environment.

This work was done by Edgar F. Koch of Caltech for NASA's Jet Propulsion Laboratory. For further information, Circle 123 on the TSP Request Card. NPO-16099

Safety Evaluation Methodology for Mining Systems

Methodology evaluates the design of proposed mining systems.

A study made for the coal mining industry, but which is generally applicable to the mining of other minerals, has developed practical, qualitative, and quantitative evaluation methodologies to assist the designer in determining whether proposed advanced extraction systems will be safer than existing systems. The analysis tests the proposed mining systems against the specifications and hazards of existing similar systems, examines the soundness of the new design in terms of reducing or eliminating major health and

safety hazards, and identifies major design weaknesses. This methodology provides the mining designer with a means for establishing the approximate impact of the proposed system on reducing morbidity and injury levels.

This work was done by Wayne F. Zimmerman of Caltech for NASA's Jet Propulsion Laboratory. For further information, Circle 124 on the TSP Request Card. NPO-15831

High-Temperature Pump

Heat exchanger in water-cooled pumps allows high-temperature operation.

A pump that circulates fluid at high temperatures uses a tubular heat exchanger to water-cool the impeller, bearings, and face seals. Internal passages carry water through the turbine wheel for cooling. The drive motor and pump are connected by magnetic coupling, which allows mounting and disassembly of the motor without affecting the closed water-cooled system. The increased operating temperature allows for an increase in thermodynamic efficiency.

This work was done by Robert R. Hale and Allan R. McDougal of Caltech for NASA's Jet Propulsion Laboratory. For further information, Circle 125 on the TSP Request Card. NPO-15783

Power Train for Hybrid Electric Vehicle

The engine and motor run at nearly constant speed for high efficiency.

The power train of a proposed hybrid electric vehicle would enable the internal-combustion engine and the electric motor to operate near the same constant speed except when off or idling. The engine and motor would be

optimized with respect to power, weight, emissions, and vibration at that speed.

The engine and motor are connected through a clutch and are disengaged except when engine power is needed to charge the battery or to relieve the motor when it is overheated. Regenerative braking is used. The vehicle speed is varied in response to accelerator and brake commands, which are fed through a control system to a continuously variable transmission.

This work was done by Howard C. Vivian of Caltech for NASA's Jet Propulsion Laboratory. For further information, Circle 126 on the TSP Request Card. NPO-15742

Adjustable Tuning Spring for Bellows Pump

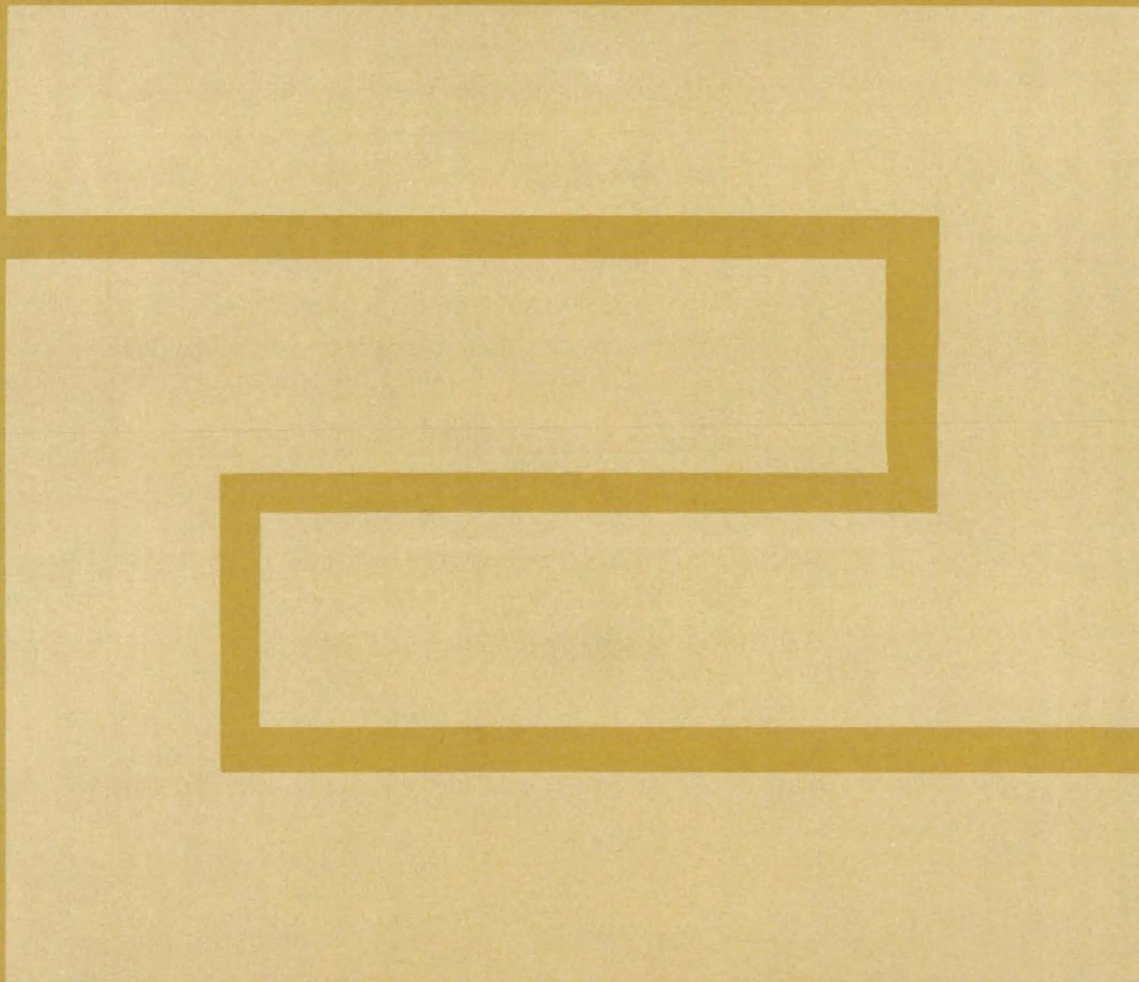
An adjustable leaf spring increased the maximum operating pressure of the pump from 2 to over 60 psi (13 to over 400 kN/m²).

A small commercial bellows pump that uses an ac-powered electromagnet to vibrate a bellows at mechanical resonance has been modified to operate over a wider pressure range. Before modification, the pump operated only at gas pressures below 2 psi (13 kN/m²). At higher pressures the bellows expanded, shifting the resonant frequency and stopping the pump.

A leaf spring with an adjustment screw was added to apply an adjustable force to the bellows to counteract the higher bellows pressure and retune the resonance back to powerline frequency. The modified pump can be tuned to operate at any pressure up to 60 psi (400 kN/m²).

This work was done by Gary L. Green, Doan Duc Tu and S. L. Hooper of Pan American World Airways, Inc., for Johnson Space Center. For further information, Circle 127 on the TSP Request Card. MSC-20512

Fabrication Technology



Hardware, Techniques, and Processes

- 553 Optical-Fiber-Welding Machine
- 554 Roof Polishing of Optical Fibers
- 555 Fabricating Underwater Electroacoustic Transducers
- 556 Prestressed Thermal-Protection Panels
- 557 Sorting Titanium Welding Rods
- 558 Fluorescent Gage Indication
- 558 Solar-Array Substrate From Glass-Reinforced Concrete
- 559 Bonding Technique for Stiffened-Skin Structures
- 559 Solder Bonding for Power Transistors
- 560 Edge Labels for Multilayer Circuit Boards
- 561 Glass/Epoxy Door Panel for Automobiles
- 561 Stripping the Sheath From Stranded Cables
- 562 Gravitational Effects on Crystal Growth by Vapor Transport
- 563 Making Cubic Silicon Carbide Semiconductors
- 564 Gas Atmospheres Improve Silicon-Ribbon Quality
- 565 Contoured Orifice for Silicon-Ribbon Die
- 565 Top-Coating Silicon Onto Ceramic
- 566 Bonding Heat-Resistant Fabric to Tile
- 567 Explosive Welding for Remote Applications
- 568 Welding Many Thin Metal Layers

MiniBriefs

569

Optical-Fiber-Welding Machine

Technique yields joints with average transmissivity of 91.6 percent.

NASA's Jet Propulsion Laboratory, Pasadena, California

Single-mode optical fibers are joined by a technique that combines fusion arc welding with micromanipulation. The technique was demonstrated with stepped-index glass fibers of 80- μm outside diameter and 4.5- μm core diameter. The transmissivities of 60 experimental joints ranged from 70 to 98 percent, with an average of 91.6 percent. As a result of these experiments, a practical welding machine under development will enable the heretofore delicate and tedious joining operation to be performed routinely.

The machine (see Figure 1) includes all the equipment necessary for manipulation, preparation, and fusion of the fibers. A fiber is prepared by bending, then scoring with a diamond cutter to produce an end that is as flat and as perpendicular to the axis as possible. After preparation, each of two fibers to be joined is placed in a vacuum chuck on one of a pair of three-axis micrometer stages.

The fiber ends are observed through a microscope equipped with a beam splitter and mirrors that permit simultaneous viewing of the fiber ends along a horizontal axis and a vertical axis, both of which are perpendicular to the fiber axis. The micrometer stages are adjusted to bring the fibers into precise lateral alignment and abutment. The fibers are then pushed together axially to compress them slightly. It was found experimentally that the correct amount of compression is that which causes the fibers to displace laterally by 140 μm , leaving a wedge-shaped airgap between the end faces with the two ends touching at only one point.

The arc-welding apparatus includes two 30° conical tungsten electrodes 3.18 mm in diameter facing each other across a 2-mm gap. The discharge is fed by a 0- to 6-kV variable power supply through a current-limiting resistor and a milliammeter. The electrodes are mounted on a motorized micropositioner so that the discharge passes across the fibers at the joint (see Figure 2). The best welds are obtained

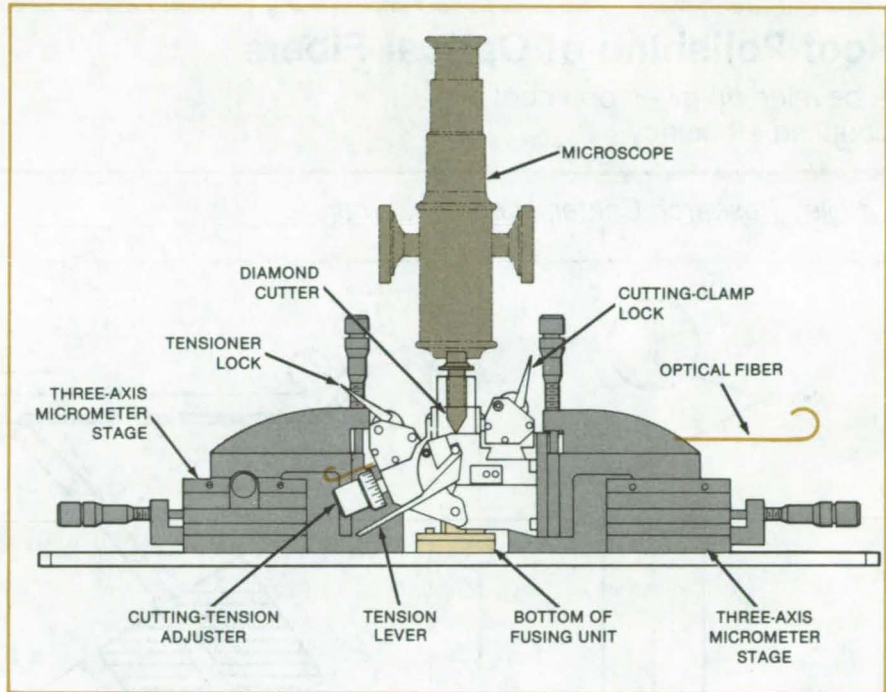


Figure 1. The **Optical-Fiber-Welding Machine** includes all the equipment needed to join two glass optical fibers.

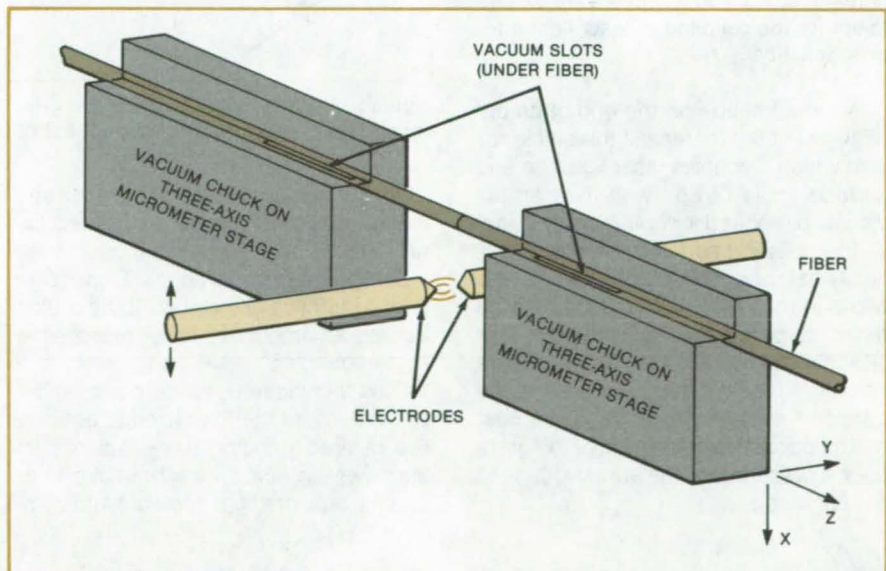


Figure 2. An **Electric Arc** is passed over the butted fiber ends to melt them together. The maximum optical transmissivity of the joint is achieved with an optimum choice of discharge current, translation speed, and axial compression of the fibers.

when the moving arc starts across the fibers from the side where the ends touch. Once the fibers start melting, the compressed ends move back into place.

There appears to be some diffusional mixing of the core and the cladding during the melting process. To minimize

the time available for diffusion and to maximize the transmissivity, it is best to use a high arc current and a rapid (1.25-mm/s-or-faster) arc translation. At 1.25 mm/s, the optimal current is about 16 mA: Higher currents deform or burn through the junction.

This work was done by Willis C. Goss, Wolfgang A. Mann, and Raymond Goldstein of Caltech for NASA's Jet Propulsion Laboratory. For further information, Circle 128 on the TSP Request Card. NPO-15004

Roof Polishing of Optical Fibers

A beveled tip gives optimum coupling efficiency.

Langley Research Center, Hampton, Virginia

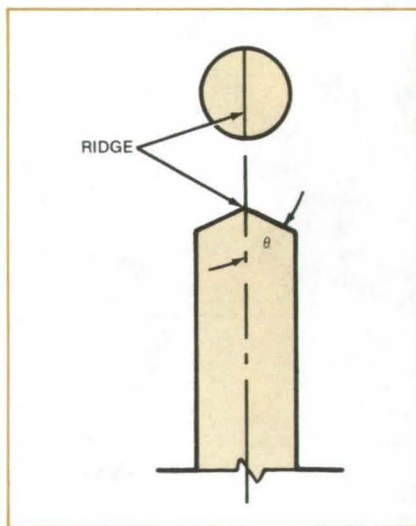


Figure 1. A Roof Angle of $\theta = 65^\circ$ is optimum for the coupling of laser light into an optical fiber.

A "roof" shape on the end of an optical glass fiber increases the efficiency with which it couples laser light. An end surface angle of 65° with the perpendicular is required for optimum coupling.

The polished surfaces should be optically flat, and the ridge formed by the two surfaces (see Figure 1) should be free of chips larger than 0.1 micron. This is achieved by using a silicon carbide abrasive lapping tape on an audio transport system. The tape is run past two guideposts, and the end of the glass fiber is presented to the abrasive tape at the 65° angle.

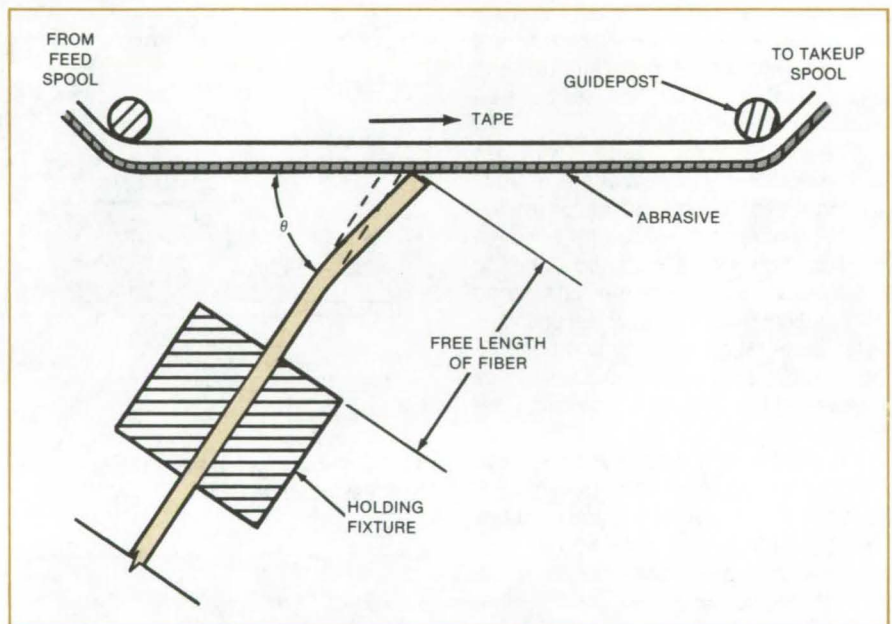


Figure 2. An Abrasive Tape is used to grind the tip of the optical fiber. The grinding force depends on the stiffness of the optical fiber.

As shown in Figure 2, the "free" length of fiber is outside the holding fixture. As the fiber is pushed closer to the tape, the free length bends. Depending on the stiffness of the fiber, this bending applies an amount of force responsible for the grinding.

This technique uses the compliance, or stiffness, of the fiber itself to achieve the desired grinding force against an abrasive surface. Since both the fiber and the tape are light in weight and com-

pliant, the ridge is defect-free, and chipping on the fiber edge is totally eliminated.

This work was done by Anil Ramniklal Dholakia of RCA Corp. for Langley Research Center. No further documentation is available.

Title to this invention has been waived under the provisions of the National Aeronautics and Space Act [42 U.S.C. 2457(f)], to the RCA Corporation, Princeton, NJ 08540. LAR-13070

Fabricating Underwater Electroacoustic Transducers

Use of retainer ring instead of adhesives simplifies assembly and disassembly.

Langley Research Center, Hampton, Virginia

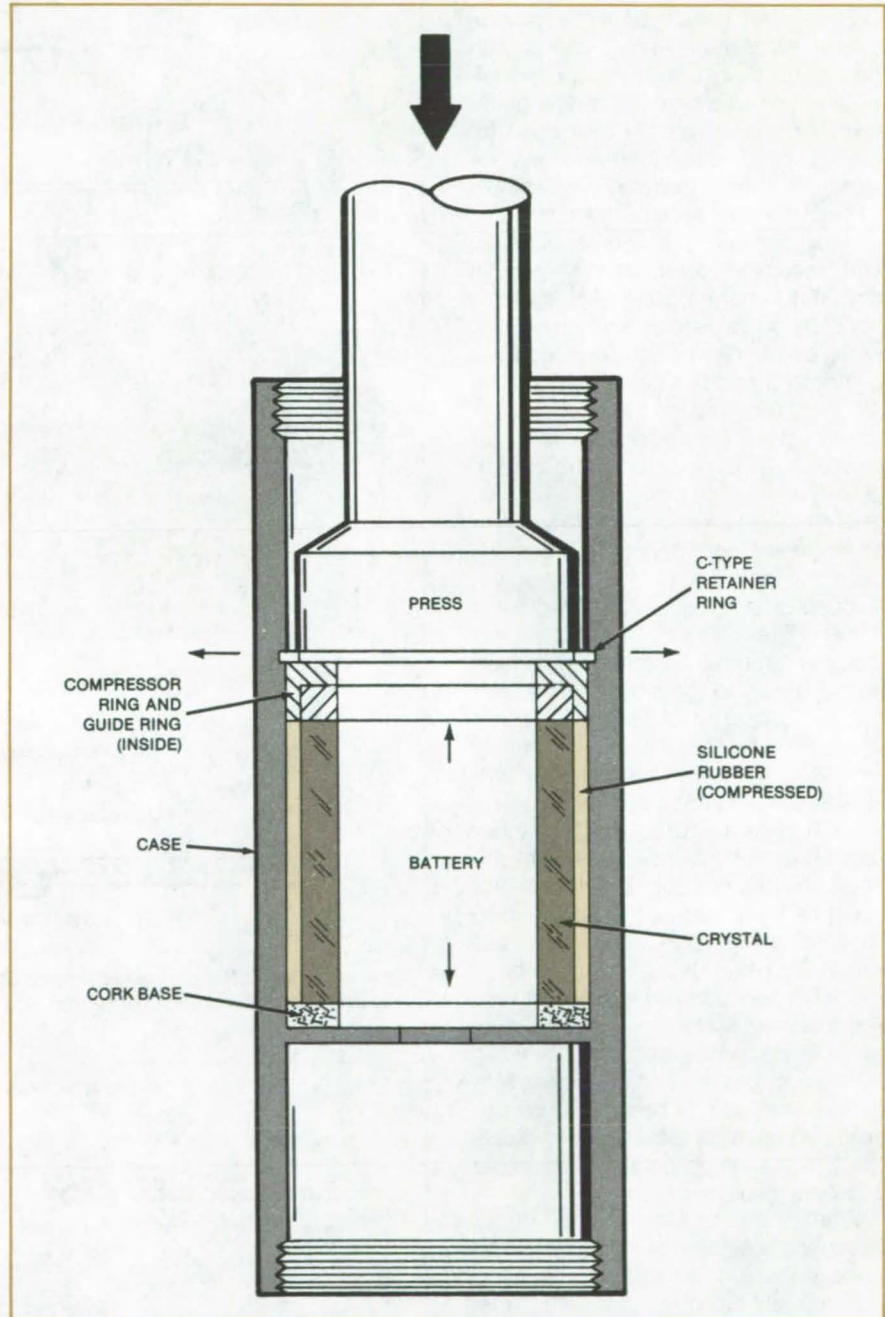
An underwater electroacoustical transducer assembly uses a precast silicone rubber compressed between the ceramic crystal and metal container. A removable retainer ring holds the assembly in place. This method provides for proper stress loading, speed and ease of assembly, and a way of removing the transducer without damaging the crystal.

Conventional fabrication of underwater electroacoustical transducers typically involves bonding a piezoceramic crystal driving assembly to the inner surface of a rugged pressure vessel to provide an electromechanical transfer of acoustic energy into the water. The adhesive is usually cast in place with a catalyzed liquid and allowed to cure at room temperature. Some problems presented by this technique include difficult removal of entrapped gas or voids, weak surface bonding at interfaces, long cure time, high failure rates, and inability to remove or salvage crystal assemblies.

The new fabrication method achieves a superior coupling coefficient and avoids the problems of in-place casting. Precast silicone rubber with a high durometer reading and suitable temperature characteristics is forced under extreme pressure between the crystal and the container (see figure). The radial thickness is undersized for ease of assembly, and the length is oversized to provide the extra material needed to compensate for the undersized thickness. A press expands the rubber between the crystal and the container, forcing out any voids or trapped gas.

The crystal assembly and compressed rubber are held in place by an internal C-type retainer ring. The whole assembly may be removed easily by releasing the retainer ring.

This work was done by Robert L. Ferguson and Ray W. Lovelady of Langley Research Center. No further documentation is available.
LAR-13007



A Precast Silicone-Rubber Cylindrical Shell is forced between the crystal and outer container and held in place by an internal C-type retainer ring.

Prestressed Thermal-Protection Panels

Panels are held securely with a minimum of mounting hardware.

Lyndon B. Johnson Space Center, Houston, Texas

Hexagonal panels of high-temperature-resistant composite material can be mounted in a prestressed condition to prevent vibration or distortion under load. Although originally developed for the Space Shuttle thermal-protection system, the technique may be adaptable to industrial thermal-protection systems as well. Furthermore, the panel shape and mounting arrangement are not limited to thermal-protection systems but can also be used on aircraft, building walls, or wherever large surfaces must be covered with stiff, flat sheets that can be easily removed for maintenance.

The panels in this case are made of an advanced 12-ply carbon/carbon composite with a thickness of 0.14 in. (3.6 mm). Each panel has stepped edges (see Figure 1). In the assembly, each stepped edge underlies an unstepped abutting edge of an adjacent panel. The panels therefore nest together, presenting a smooth outer surface interrupted only by a hexagonal pattern of cracks. There are no unobstructed gaps between the panels that would expose the substructure directly to high temperatures.

Each panel is fastened in a manner reminiscent of that used to mount the covers of automobile air filters. The panel as fabricated has a convex dish shape (see Figure 2). A depression or hub in the center has a hole for a high-temperature-resistant mounting screw. Thermally-insulating spacer bars support the stepped edge of the panel in question or of an adjacent overlapping panel. A low-density batt insulation (for example, alumina/silica fibers in nickel foil) fills the space between the panel and the substructure.

When the screw is tightened in the threaded receptacle in the central insulating stanchion, the panel is flattened from its dished configuration. The panel is thus placed in bending stress; the spacer bars, in compression; and the insulating stanchion, in tension. The screw is tightened until the panel becomes flat and flush with the specified outer surface. The prestress is sufficient to resist

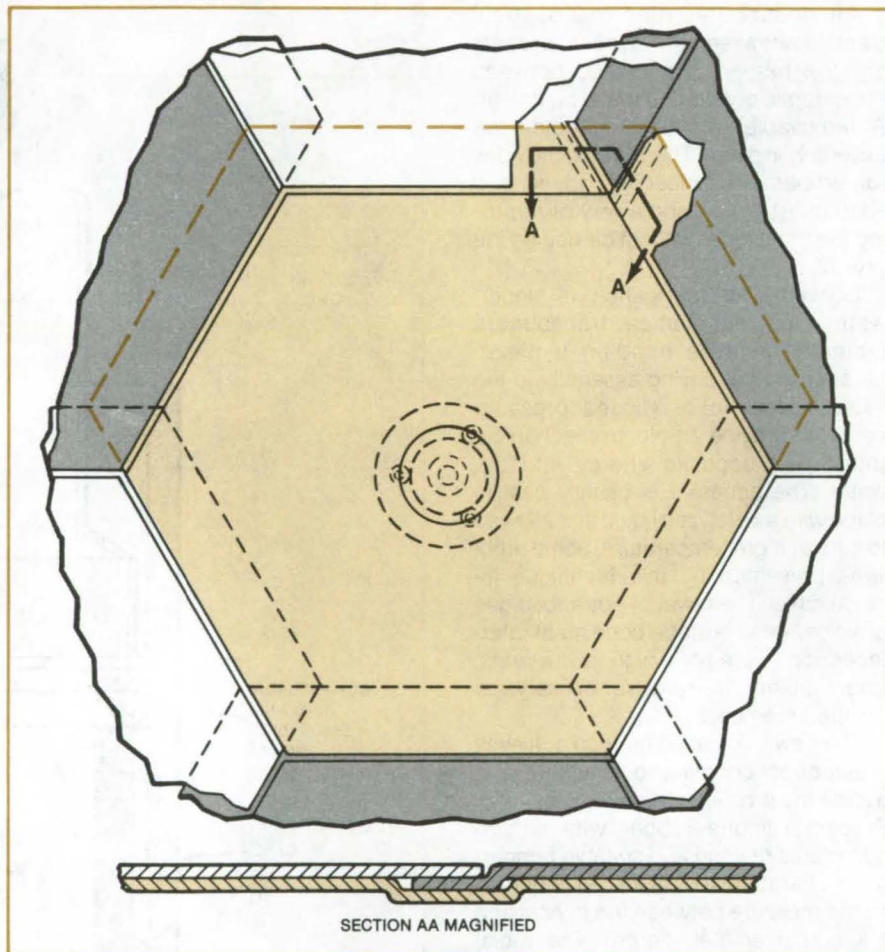


Figure 1. **Adjacent Panels Have Stepped Edges** so that they nest together in a hexagonal array and present a smooth outer surface.

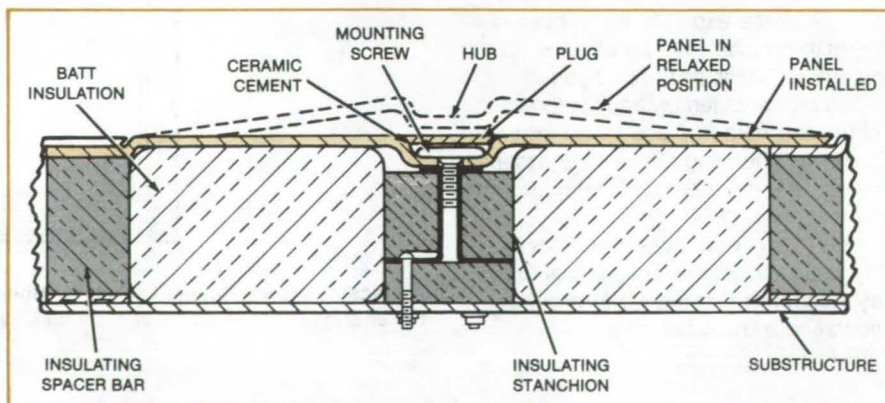


Figure 2. **Each Panel Is Held in Place** by a single screw that pulls it into a flat shape from its original shallow-dish shape. This shape and the prestressing make the panel stiff so that it resists vibration and withstands large mechanical loads.

distortion of the panel under normal operating loads.

After tightening, the screwhead is given some protection from oxidation by covering it with a carbon/carbon plug, the top of which is flush with the outer surface. The plug is held in place with a

ceramic cement in a toroidal cavity around the edge of the hole.

This work was done by Thomas J. Dunn of Johnson Space Center. For further information, Circle 129 on the TSP Request Card.

This invention is owned by NASA, and a patent application has been filed. Inquires concerning nonexclusive or exclusive license for its commercial development should be addressed to the Patent Counsel, Johnson Space Center [see page A5]. Refer to MSC-20254.

Sorting Titanium Welding Rods

Three types of titanium welding wires are identified by their resistance to current flow.

Lyndon B. Johnson Space Center, Houston, Texas

An instrument sorts out titanium-alloy welding wires by monitoring the current that flows when an aluminum cathode contacts the wire. Each of the three alloys (Ti40, 5Al-2.5 5n, and 6Al-4U) produces a different electrical response, permitting positive identification.

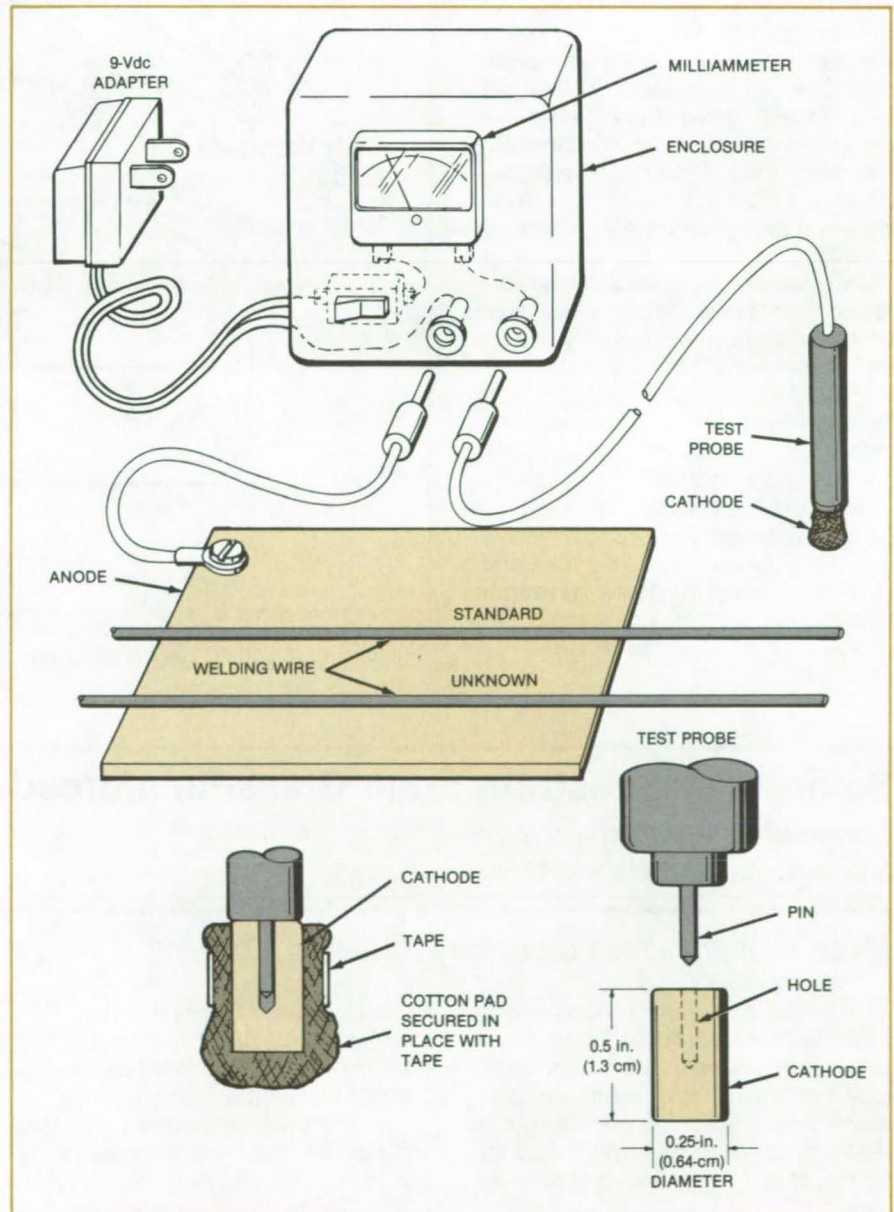
Shown in the figure, the tester includes a 9-Vdc source, a milliammeter (0 to 100 mA), an anode, and an aluminum cathode tipped with a cotton pad that has been moistened with an electrolyte (4 percent by weight ammonium nitrate). The welding wire closes the path for electric-current flow.

The anode is a rectangular copper plate measuring approximately 5 by 10 inches (12.7 by 25.4 cm). It rests on a tabletop in front of the operator. The cathode is a standard pin-jack test probe with an aluminum tip. A small pad of cotton, taped over the tip, holds the electrolyte.

The operator places clean welding wires on the anode plate, with the wire ends extending beyond the edge of the plate. He or she then wets the cotton tip of the cathode with the electrolyte and touches it to the wires. The alloy is identified by comparing the meter response with the response when the cathode is touched to a known standard.

This work was done by Wylie D. Ross, Jr., and Robert L. Brown of Rockwell International Corp. for Johnson Space Center. For further information, Circle 130 on the TSP Request Card.

Inquiries concerning rights for the commercial use of this invention should be addressed to the Patent Counsel, Johnson Space Center [see page A5]. Refer to MSC-20588.



The **Welding-Wire Tester** quickly identifies an unknown titanium-alloy wire by touching the wire with the test probe and comparing the meter response with the standard response. Before touching the wire, the tip of the test probe is dipped into an electrolyte.

Fluorescent Gage Indication

Transfer of dye shows the quality of contact between two mating parts.

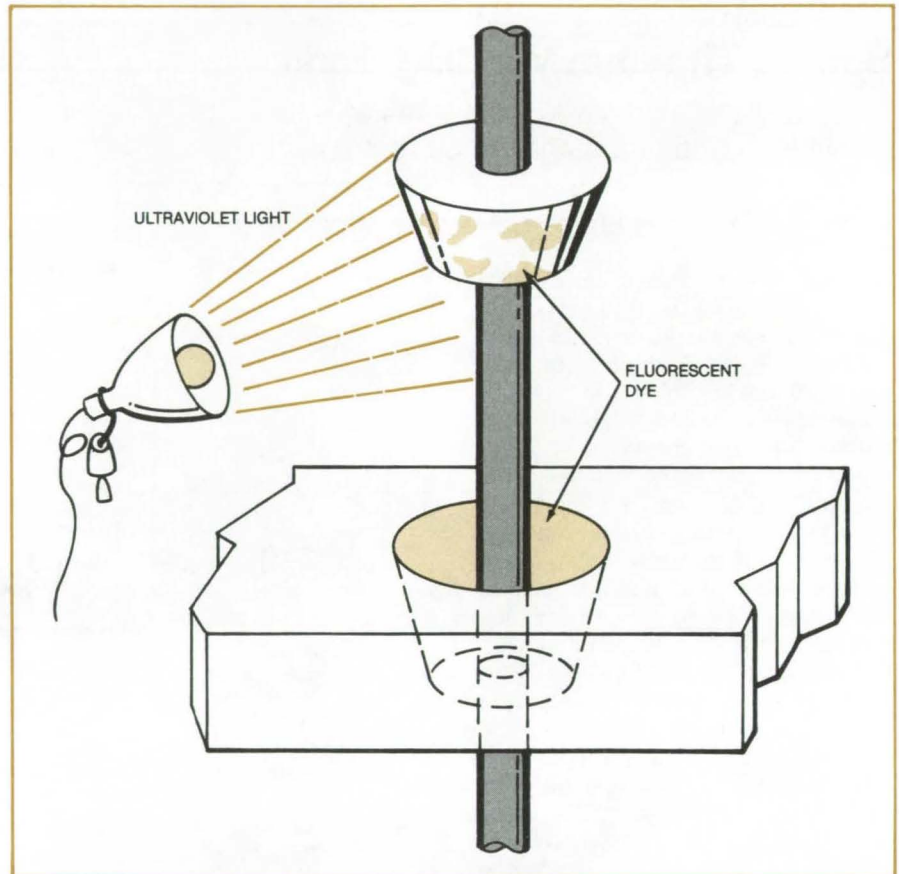
Ames Research Center, Moffett Field, California

Fluorescent dye may replace red-lead powder as the visible component in a contact transfer coating used to check the fit of machined parts. The dye offers greater visibility under ultraviolet illumination, allowing a better indication of how precisely the parts match and what areas interfere.

The fluorescent dye powder is mixed in light machine oil and applied to one of two mating parts in a thin film. The parts are then lightly fitted together, separated (see figure), and examined for the indications of contact. Under UV light — from a dye-penetrant analysis lamp, for example — any of the dye powder that transfers from the coated surface to the uncoated part glows brightly, indicating contact.

The extent of the contact can be estimated from the portion of the total gage area that glows, and the quality of contact is seen in the pattern or spottiness of that glowing area. The brightness of the dye makes it possible to take photographs for reference in the subsequent machining operations.

This work was done by Chris E. Barns, Bruce L. Gilbaugh, Bobby Gin, William L. Holt, Peter Lesak, Ronald Mancini, and Harry F. Spencer of Ames Research Center. For further information, Circle 131 on the TSP Request Card. ARC-11397



Mating Parts are checked for fit by spreading fluorescent dye on one, making brief light contact with the other, and then looking (under UV light) for transferred dye.

Solar-Array Substrate From Glass-Reinforced Concrete

Design eliminates a glass superstrate and associated metal framing.

NASA's Jet Propulsion Laboratory, Pasadena, California

A strong glass-reinforced concrete panel has a smooth flat surface suitable for a solar substrate. It includes structural bracing for rigidity and a design adaptable to mass production. The glass-reinforced panel might also be used for solar concentrators and exterior wall panels.

The panel has two trapezoidal stiffening ribs for structural support. The strategic placement of the ribs with

embedded support tubes (standard PVC tubing) minimizes bending moments and resulting stresses produced by installation and windloads.

The four-point panel support system includes (a) four wooden posts [6- by 6-in. (15.2- by 15.2-cm)] of pressure-treated fir, each serving two separate panels; (b) four simple post brackets (6- by 6-in.) of standard square structural-steel tubing, each serving two

separate panels; and (c) two support bars of standard 1-in. (2.54-cm) schedule 40 galvanized pipe with No. 7 reinforcing-steel bars inserted in the pipe ends as bracket connectors.

This work was done by James L. Eirls of MB Associates for NASA's Jet Propulsion Laboratory. For further information, Circle 132 on the TSP Request Card. NPO-15077

Bonding Technique for Stiffened-Skin Structures

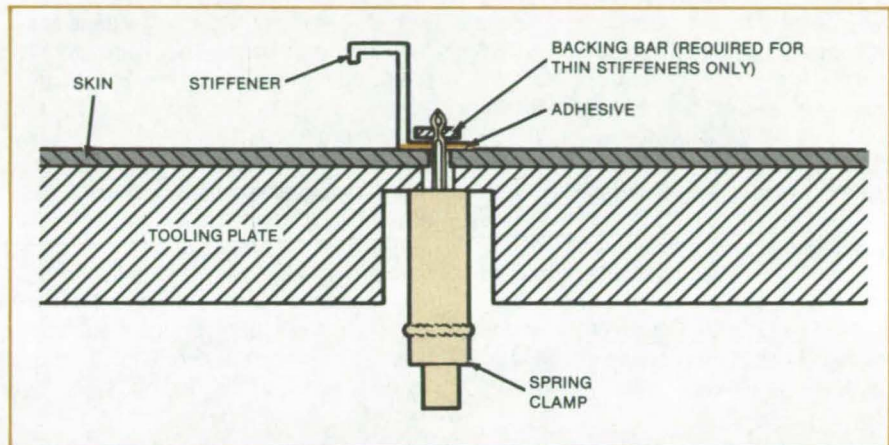
Consistent bond thickness is achieved even in large, complicated parts.

NASA's Jet Propulsion Laboratory, Pasadena, California

An adhesive bonding technique uses commercially-available spring clamps to hold stiffened-skin structures together during adhesive cure. It is useful in the fabrication of large and small rib-stiffened structures. This method provides controlled and constant pressure during cure, resulting in consistent bondline thickness.

The technique involves temporarily replacing the rivets in a structure with spring clamps that fit through the rivet holes. First, the pattern of rivet holes is transferred from the skin to an aluminum tooling plate. The holes are drilled in the tooling plate, then counter-bored from the back. The depth of each counterbore is determined by the desired clamping force and grip range of the spring clamp.

Adhesive is applied to the stiffeners, and a mold-release agent is applied to the tooling plate and clamps. Next, the stiffeners, the skin, and the backing bars (where necessary) are assembled on the tooling plate using the clamps as shown in the figure. Thermal distortions resulting from high-temperature cure cycle may be minimized by using tooling mate-



A **Spring Clamp** positions and holds the parts to be assembled on a tooling plate. The stiffener and backing bar are held against the adhesive layer by the clamp. The spring action of the clamp keeps a steady force on the pieces as they cure, thereby insuring a consistent bond thickness.

rials with similar coefficients of thermal expansion as the bonded structure.

The adhesive is then cured. After the cure, the tooling plate and clamps are removed. Then the clamps are replaced with rivets. The clamps may be soaked in adhesive stripper to remove the residual adhesive.

This work was done by Peter O. Frickland, Eugene L. Headrick, and Takashi Hasegawa of Caltech for NASA's Jet Propulsion Laboratory. For further information, Circle 133 on the TSP Request Card. NPO-15994

Solder Bonding for Power Transistors

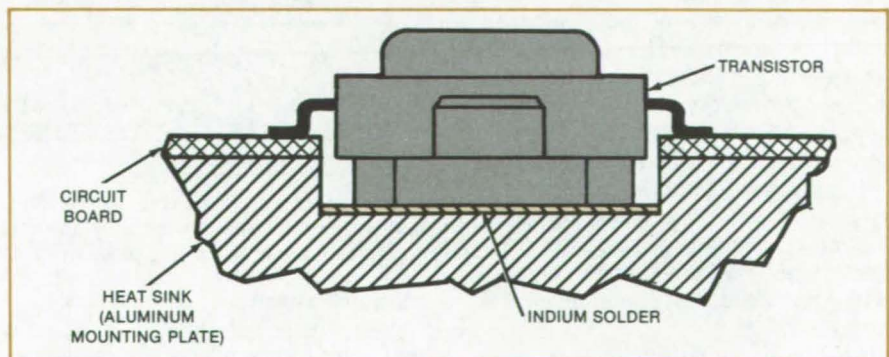
Indium solder boosts power rating and facilitates circuit changes.

Lyndon B. Johnson Space Center, Houston, Texas

Mounting power transistors with indium solder allows the devices to be operated at higher power levels than does conventional attachment by screws. At the same time, the low melting point of indium solder (141°C) allows a power transistor to be removed, if the circuit must be reworked, without disturbing other components mounted with ordinary solder that melts at 181°C .

The indium-solder bond is located between the bottom surface of the transistor and the mounting plate (see figure).

(continued on next page)



Efficient Heat Conduction from a power transistor to a heat sink is provided by a layer of indium solder.

The mounting plate serves as a heat sink: It removes heat from the transistor, protecting the device from thermal runaway. The intimate contact provided by the indium solder reduces the thermal resistance between the transistor and the mounting board. The thermal resistance after mounting is less than it is with heat-sink compounds sometimes used in conjunction with screw fastening. Moreover, the indium solder does not evaporate and contaminate surrounding components as do heat-sink compounds.

The transistor is prepared for soldering by cleaning in a vapor degreaser. Then it is placed in a holding fixture with the bottom facing up. Diluted flux is brushed on the transistor bottom surface. Indium solder is melted and spread over the surface with a soldering iron set at 700° F (371° C). The tip of the iron is moved swiftly so that it does not build up excessive heat at any point. The transis-

tor is degreased again, and burned flux is cleaned away with a chlorofluorocarbon solvent agitated with a bristle brush.

A preform is cut with a knife and a template in indium foil 0.0015 inch (0.0381 mm) thick. The preform is slightly larger than the transistor base surface. The preform, the bottom of the transistor, and the mounting plate are brushed with flux and put together in their final mounting positions. The transistor is temporarily fastened to the board with screws so that it presses gently on the preform.

A thermocouple is taped to the mounting-plate surface; and the assembly, consisting of the plate, circuit, preform, and transistor, is placed on a hotplate at 450° F (232° C). When the thermocouple gage indicates 290° F (143° C), the solder preform starts to flow. The temperature must not be allowed to exceed 329° F (165° C).

When a solder fillet forms around the transistor, the mounting screws are tightened lightly to compress the solder and complete the seating of the transistor. The assembly is then removed from the hotplate. When the board has cooled, the screws are removed. The transistor leads are attached to the circuit with conventional solder.

To remove a transistor from a board, flux is first applied to the leads, which are then unsoldered with a soldering iron. The assembly is then placed on a hotplate and instrumented with a thermocouple as before. As soon as the indium solder melts, the transistor is pulled away.

This work was done by Henri A. Snytsheuvel and Harold Mandel of TRW, Inc., for Johnson Space Center. For further information, including a specification for indium solder bonding, Circle 134 on the TSP Request Card. MSC-20570

Edge Labels for Multilayer Circuit Boards

A quick visual inspection identifies out-of-place layers.

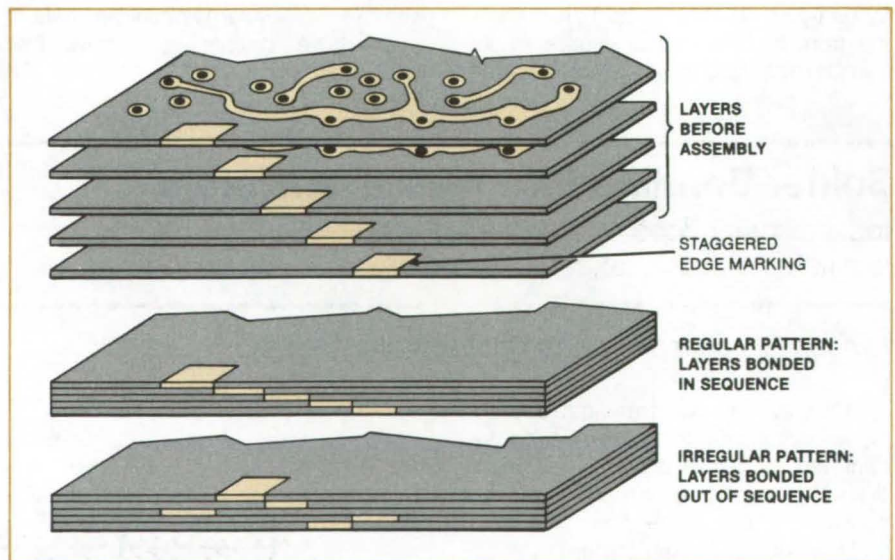
Lyndon B. Johnson Space Center, Houston, Texas

Position-coded edge labels added to stacked printed-circuit boards make it easy to determine whether the boards have been assembled in the correct order. It is essential that the proper sequence of layers be maintained during assembly, or else electromagnetic interference can occur between layers.

In the new method, a small marker is affixed before assembly to each layer of a multilayer circuit board, at a predetermined location on the edge of that layer. The positions of markers on subsequent layers are staggered in sequence so that the layer sequence of the assembled board can be checked by visual inspection (see figure). If the marker pattern is regular, the layers are correctly assembled while a marker out of the pattern indicates a layer out of sequence.

This is a nondestructive method of inspection. It adds little or nothing to the cost of manufacturing, since the edge markers can be formed during electroplating of the circuit patterns on the layers.

Previously, X-ray inspection was used, but was not always reliable in finding out-of-sequence layers. Alternatively, a small hole was drilled into the board



Small Copper Pads or Other Labels on layers (top) present a regular pattern if the multilayer circuit board is properly assembled (middle) and an irregular pattern if one or more layers are in the wrong place (bottom).

at a specific location to a depth at which a given circuit path should be found. After it was ascertained that the path was there, the drill hole had to be repaired. The new method is faster, cheaper, and more reliable than either

of the earlier methods.

This work was done by Peter J. Rossi of Rockwell International Corp. for Johnson Space Center. No further documentation is available. MSC-20704

Glass/Epoxy Door Panel for Automobiles

Lightweight panel is cost-effective.

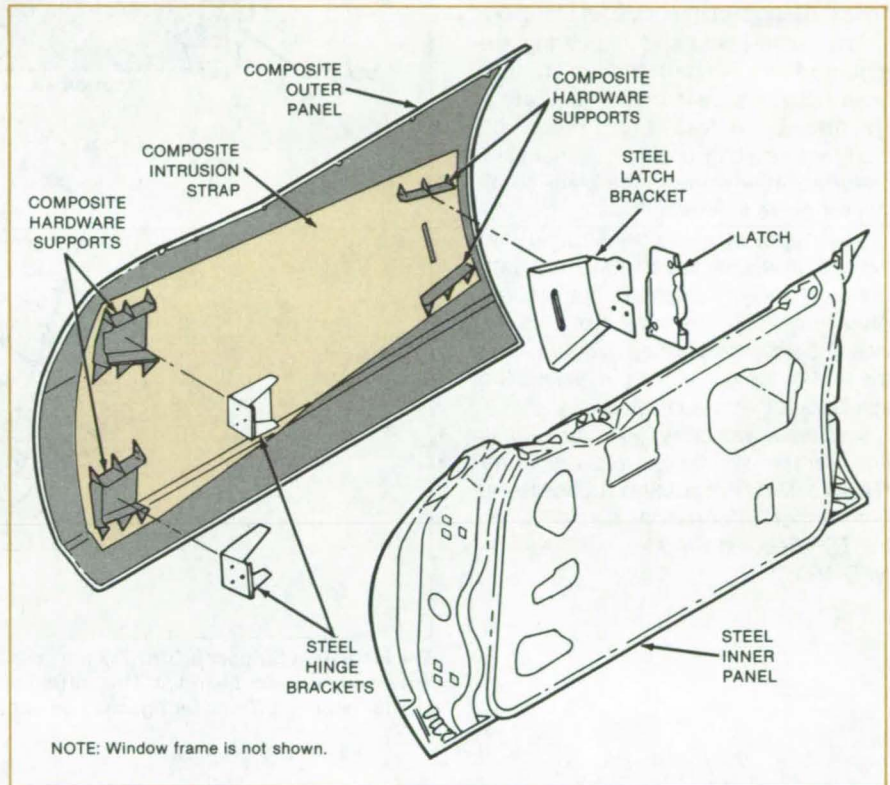
NASA's Jet Propulsion Laboratory, Pasadena, California

An experimental outer panel for an automobile door, made of a glass/epoxy composite material, is lighter than a conventional steel door panel, meets the same strength requirements, and is less expensive. With a weight of 14.6 pounds (6.6 kilograms), the panel weighs 43 percent less than its steel counterpart.

The composite panel (see figure) consists of a contoured epoxy sheet filled with chopped glass fibers and comolded with an intrusion strap of continuous glass fibers. The intrusion strap helps to protect occupants from side collisions. It replaces the intrusion beam of the steel door and accounts for the thickness reduction and a large part of the weight reduction in the composite panel.

The composite outer panel is designed for use with a conventional steel inner panel, latch, window frame, and hinges. The composite was not selected for the inner panel because it could fail catastrophically and injure occupants if penetrated in a collision. Although an intrusion strap like the one shown in the outer panel would prevent such failure, it would drive the cost up excessively. The attachment of hardware to the inner panel could also be more expensive because of the need for metal inserts.

Prototype composite outer-panel parts were made in a zinc-alloy compression mold. Sheets of chopped glass/epoxy, a sheet of continuous glass fiber/epoxy, and slugs of chopped glass/epoxy (to fill ribs) were molded simultaneously. The chopped-fiber material has the smooth surface finish required for automotive use.



The **Integrally-Molded Intrusion Strap** is a key feature of the composite outer door panel. This strap replaces the bulky and heavy steel intrusion beam of a conventional door. In the prototype composite door shown here, a standard steel inner panel was used for demonstration purposes. A door redesigned to exploit the advantages of the composite outer panel would be thinner.

This work was done by Jerome L. Bauer, Jr., of Caltech for **NASA's Jet Propulsion Laboratory**. For further information, Circle 135 on the TSP Request Card.

Inquiries concerning rights for the commercial use of this invention should be addressed to the Patent Counsel, NASA Resident Office-JPL [see page A5]. Refer to NPO-15057.

Stripping the Sheath From Stranded Cables

A device similar to a tubing cutter removes the tough plastic cover.

NASA's Jet Propulsion Laboratory, Pasadena, California

A new cable stripper uses a rotary cutter and two bearings to remove Kapton (or equivalent) plastic sheathing from a multiwire stranded cable without damaging the insulation of the individual

conductors. The sheath is cut part of the way through by the cutter, and the insulation is then "worked" off the end of the wire by hand.

Some newer types of stranded cables

are covered with a tough plastic sheath. Two or more wires are twisted together to form a cable, producing a cross section that is not quite circular. This shape
(continued on next page)

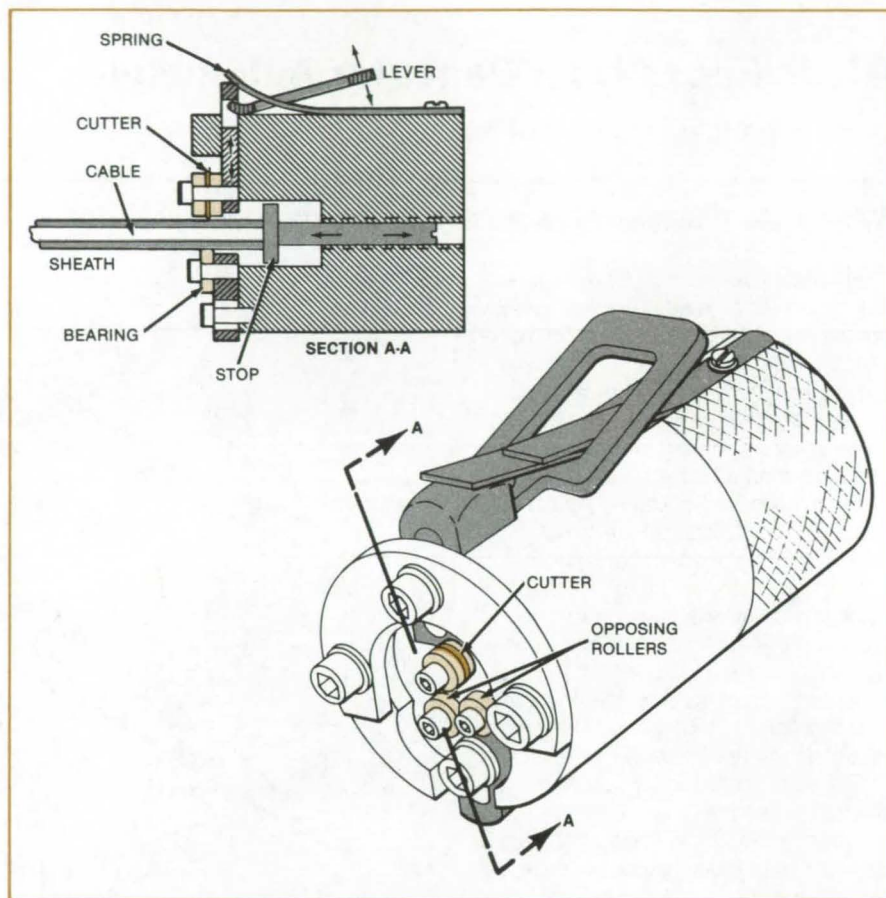
makes conventional wire strippers unsuitable for removing the sheaths.

The new device shown in the figure resembles a tubing or pipe cutter. The cutter blade is spring-urged to engage the cable that is inserted between the blade and the rollers. The blade can be lifted away manually so that the cable can be inserted. An adjustable stop defines the length of the cable for stripping.

The cutter blade and its bearing are mounted on a shaft that is in turn mounted on a slide journaled for translation radially. A leaf spring urges the blade into cutting position. A manually operated lever retracts the blade to allow for cable insertion.

The depth of blade penetration into the sheath is selected so that the sheath is almost but not completely cut through. After removal of the cable from the device, the sheathing is manually wrung off the end of the cable without nicking the insulation of individual wires.

This work was done by Arthur L. Prisk and James W. Rotta of Caltech for NASA's Jet Propulsion Laboratory. For further information, Circle 136 on the TSP Request Card. NPO-15082



The **Insulation Stripper** is 3 in. (7.6 cm) long and 1.5 in. (3.8 cm) in diameter. The two rollers are small-diameter bearings. The cutter blade is journaled for rotation between a pair of similar bearings. The bearings may be either pin or ball types of suitable dimensions.

Gravitational Effects on Crystal Growth by Vapor Transport

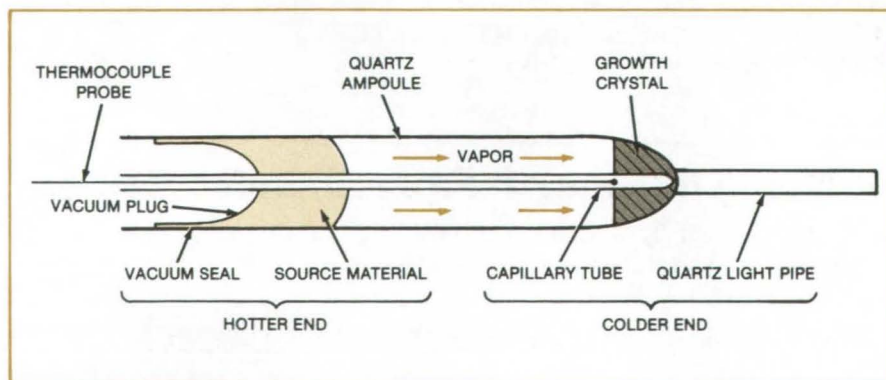
A transparent crystal-growth apparatus can be operated in any orientation.

NASA's Jet Propulsion Laboratory, Pasadena, California

A crystal-growth apparatus makes it possible to measure growth rates in three directions: up, down, and horizontal. The apparatus allows the effect of gravity on crystal growth to be determined quantitatively.

The system consists of a transparent quartz ampoule (see figure) in a cylindrical transparent furnace. A capillary tube along the axis of the ampoule allows the internal temperature profile to be measured with a thermocouple. The entire apparatus can be rotated to any angle with respect to the vertical.

The thermocouple in the capillary tube measures not only temperature but also the position of the growing crystal



Sealed in a Quartz Ampoule, a charge of source material vaporizes and condenses in the crystalline state at the colder end of the tube.

surface. For this purpose, the thermocouple is attached to a vernier caliper. When the tip of the thermocouple is manually set at the crystal surface, the vernier indicates the growth-surface position with an accuracy of 0.1 millimeter.

The apparatus has been used to study the growth of lead telluride (PbTe), a material used in infrared laser diodes and detectors. The PbTe is loaded and sealed into the growth ampoule under vacuum. When the ampoule is heated in the furnace, the source material gradually vaporizes and collects as

crystalline PbTe at the cooler end of the ampoule. The temperature profile is varied by moving the ampoule to different positions in the furnace.

In the PbTe growth experiments, the downward and horizontal material transport growth rates reach a maximum with increasing source-to-crystal temperature difference consistent with diffusion-limited growth. The horizontal growth rates appear to be somewhat larger than the downward-transport growth rates for the same temperature difference. For large temperature dif-

ferences ($\geq 20^\circ\text{C}$), the upward-transport growth rate is greater than that of the other two orientations. At small temperature differences, the horizontal and downward-transport growth rates fall off more slowly with decreasing temperature difference, and the upward-transport growth rates are lower than those of the other two orientations.

This work was done by John A. Zoutendyk and Wesley M. Akutagawa of Caltech for NASA's Jet Propulsion Laboratory. For further information, Circle 137 on the TSP Request Card. NPO-15853

Making Cubic Silicon Carbide Semiconductors

A thin buffer layer of SiC minimizes the effects of lattice mismatch.

Lewis Research Center, Cleveland, Ohio

A reproducible process has been developed for the production of large-area single-crystal wafers of cubic silicon carbide (SiC) for semiconductor devices. The process can also be used to make the devices themselves. Potential applications include electronics for high temperatures (up to 900°C) and electronics for very high frequencies.

The approach consists of growing a single-crystal layer of cubic SiC on a single-crystal silicon (Si) wafer by chemical-vapor deposition (CVD). This has been tried many times previously; but the results have never been satisfactory, largely because of a 20 percent difference in the atomic spacing of SiC and Si crystals. In the new process, a thin intermediate buffer layer is grown between the SiC and the Si to minimize the effects of this lattice mismatch.

The CVD system is of conventional design with special attention to system cleanliness and reproducibility of growth conditions. Deposition takes place at atmospheric pressure. The sources of silicon and carbon are silane and propane in a purified hydrogen carrier gas. The reaction tube is a horizontal water-cooled quartz tube. The Si substrate is placed on an RF-heated graphite susceptor as shown in Figure 1.

The process of growing the SiC layer consists of three steps as shown in Figure 2. The etching step cleans the substrate prior to growth. The buffer layer step provides a 20-nm-thick layer
(continued on next page)

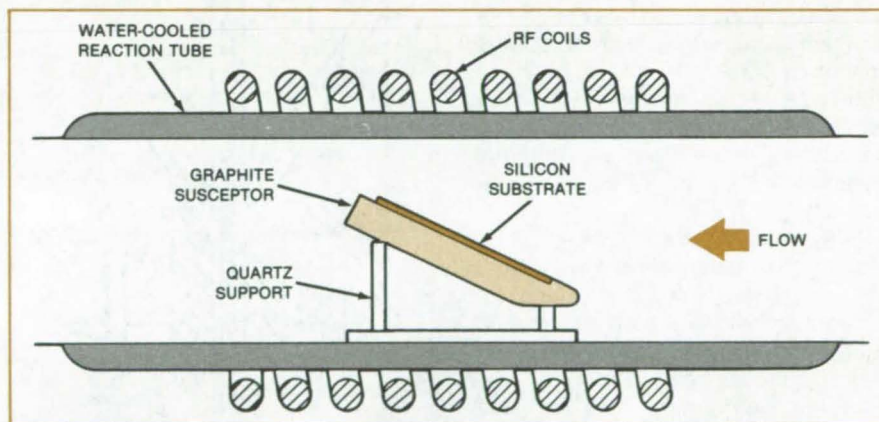


Figure 1. In the Reaction Chamber for the SiC Crystal Growth, the sources of silicon and carbon are silane and propane in a purified hydrogen carrier gas.

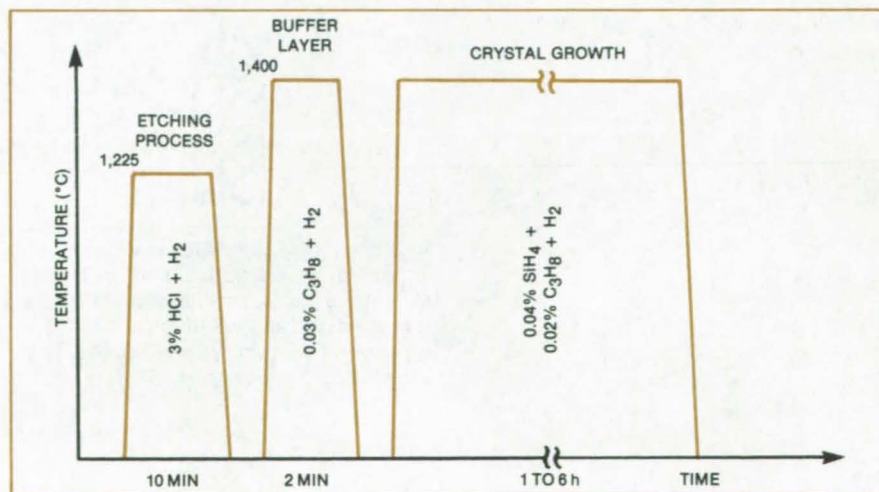


Figure 2. The SiC Single-Crystal Layer is grown in three steps. The growth rate is about $5\ \mu\text{m/h}$.

of SiC that is necessary for the subsequent single-crystal growth. With the conditions listed for the crystal-growth step, the growth rate of the SiC single-crystal layer is about 5 $\mu\text{m}/\text{hour}$.

In this process it is important to minimize premature deposition upstream of the susceptor and to minimize the recirculation of gaseous reaction products over the Si substrate. The process has consistently yielded high-

quality single-crystal layers with areas of several cm^2 and thicknesses up to 34 μm . The Si substrate can be removed by chemical etching leaving a thin SiC wafer. By adding dopant gases during the crystal-growth step, pn junctions have been formed. Hence, the process can also be used to fabricate devices.

X-ray diffraction measurements and electron channeling patterns obtained from the cubic SiC wafers verify that they are high quality single crystals. Hall

measurements have yielded electron mobilities up to 380 $\text{cm}^2/\text{V}\cdot\text{s}$.

This work was done by J. A. Powell and H. A. Will of Lewis Research Center and S. Nishino of Kyoto University. For further information, Circle 138 on the TSP Request Card.

Inquiries concerning rights for the commercial use of this invention should be addressed to the Patent Counsel, Lewis Research Center [see page A5]. Refer to LEW-14018.

Gas Atmospheres Improve Silicon-Ribbon Quality

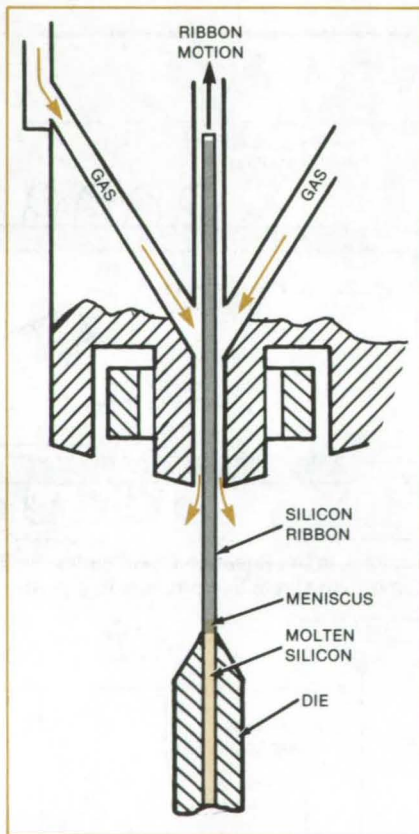
The growing crystal is surrounded by a gas containing carbon or oxygen.

NASA's Jet Propulsion Laboratory, Pasadena, California

The quality of silicon ribbon grown from molten silicon may be improved if a gas containing oxygen, carbon, or both surrounds the emerging ribbon. This conclusion is suggested by experiments in which silicon grown in atmospheres containing CO or CO₂ had a longer diffusion length and contained fewer large silicon carbide particles on the surface. Solar cells made from the material should have superior performance as a result.

In the modified process, CO₂, CO, or CH₄ mixed with argon is introduced into the growth slot near the interface between the liquid and solid silicon (see figure). The gas flow rate is 100 to 5,000 cubic centimeters per minute.

In the experiments, the diffusion length of ribbons grown in CO₂/Ar atmospheres ranged from 45 to 50 μm , while that for ribbons grown in Ar alone was 30 to 35 μm . Similar results were obtained with CO.



A Ribbon of Solid Silicon, viewed here edgewise, grows from a pool of molten silicon in a die. Gases flowing through the orifice ensure longer diffusion length and less contamination by carbide particles in the product.

The gases reduce the size and number of silicon carbide particles that grow on the die top and become entrained in the ribbon. These particles tend to make growth erratic and to degrade ribbon quality. It is estimated that CO₂, CO, or CH₄ in concentrations from 100 to 10,000 parts per million, suppresses particle formation on the die top. Instead, very fine SiC particles form on the meniscus at the growth interface. These particles do not penetrate the ribbon, but cling to the ribbon surface in a SiC/SiO_x film. This film can be removed easily by standard etchants.

This work was done by Fritz V. Wald and Juris P. Kalejs of Mobil Tyco Solar Energy Corp. for NASA's Jet Propulsion Laboratory. For further information, Circle 139 on the TSP Request Card.

NPO-15129

Contoured Orifice for Silicon-Ribbon Die

Die configuration encourages purity and stable growth.

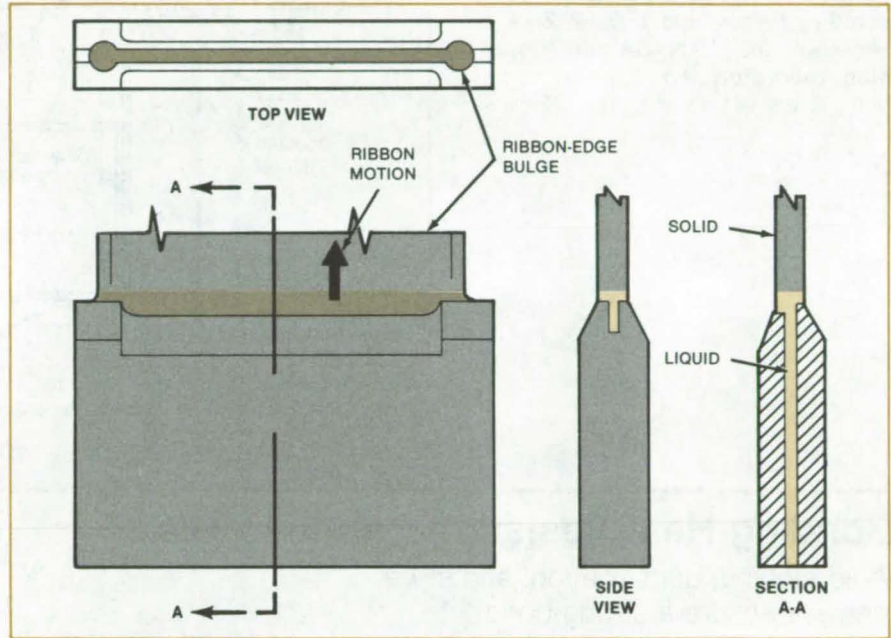
NASA's Jet Propulsion Laboratory, Pasadena, California

A die for silicon ribbon growth has an unusual shape. Over most of the orifice, the tips are vertically displaced from one another. At the ends of the orifice, however, the tips are flush (see figure).

The die is part of a furnace being developed to produce high-quality, low-cost material for solar cells. It shapes the silicon into a ribbon as the silicon is pulled from the die.

The tip displacement ensures that carbon impurities are segregated to one side of the ribbon. The flush tips at the die ends cause the ribbon to form bulges at its edges: The bulges ensure that stable growth occurs at the edges, without ripples in the ribbon width.

This work was done by Brian H. Mackintosh of Mobil Tyco Solar Energy Corp. for NASA's Jet Propulsion Laboratory. For further information, Circle 140 on the TSP Request Card. NPO-15126



The Contour of the Die Orifice changes near the ribbon edges. As a result, the silicon ribbon has nearly constant width and little carbon contamination.

Top-Coating Silicon Onto Ceramic

Polycrystalline silicon for solar cells may be produced at low cost.

NASA's Jet Propulsion Laboratory, Pasadena, California

In a promising new method of making silicon for solar cells, molten silicon is poured on a moving substrate. The molten material solidifies to form a sheet of polycrystalline silicon having a photo-voltaic conversion efficiency greater than 10 percent. The method produces 100- μ m-thick silicon coatings at a speed of 0.15 centimeter per second.

The substrate is a carbon-coated, silicon dioxide rich, aluminum silicate ceramic, selected for its similarity to silicon in thermal expansion. This ensures that there is minimal strain in the solidified silicon layer. The ceramic is in the form of a long, narrow strip and is

coated with graphite so that the molten silicon will wet it.

The hot substrate is pulled under a trough holding the molten silicon (see figure). The silicon is slowly poured on the moving substrate. A doctor blade at 1,420°C wipes the poured liquid silicon, forming a uniform coating. The doctor blade is a quartz-covered graphite rod that is electrically heated by an electric current through the graphite. A jet of gas cools the substrate from underneath, thereby solidifying the silicon layer.

Pouring molten silicon proved to be difficult to control because of the large surface tension of the material. As the

trough was tipped, a high meniscus developed; and when pouring finally started, the quantity of silicon delivered was larger than desired. However, even with too much molten silicon on the substrate, the liquid did not flow outside the boundaries of the carbon coating. (The carbon coating did not extend to the edges of the ceramic sheet.) Thus, keeping the liquid from spilling off the substrate is unlikely to be a problem in production.

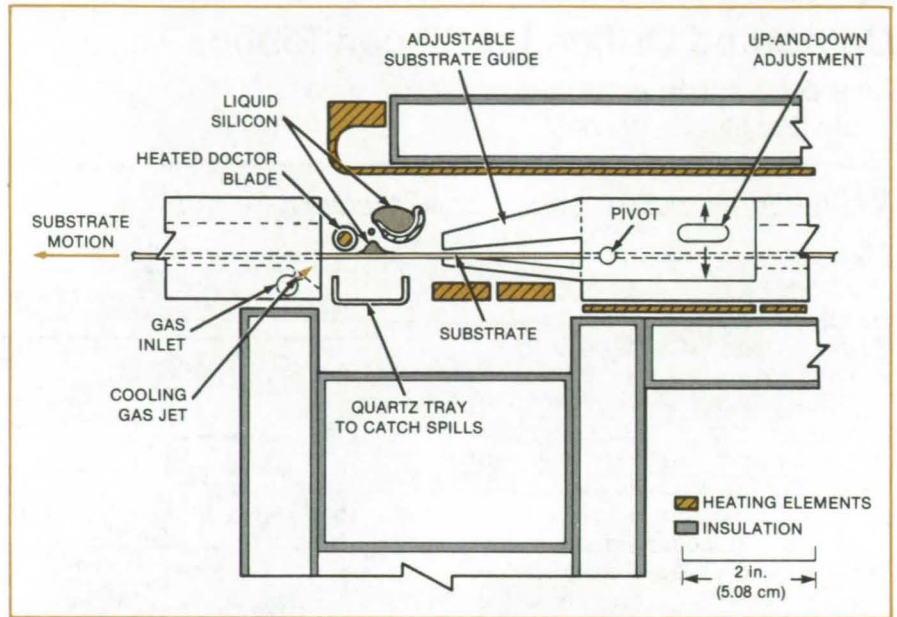
An alternative silicon dispenser will be evaluated. Instead of being poured over
(continued on next page)



the brim of the trough, molten silicon would be applied through a long, narrow slot in the bottom of the trough. Provided that the liquid silicon in the trough does not exceed a certain height, the liquid will not drain from the trough all at once, but will instead be drawn smoothly from the trough by the moving substrate.

This work was done by J. Don Heaps, Leroy D. Nelson, and J. David Zook of Honeywell, Inc., for NASA's Jet Propulsion Laboratory. For further information, Circle 141 on the TSP Request Card.

NPO-15125



Molten Silicon is poured from a quartz trough onto a moving carbon-coated ceramic substrate. A doctor blade spreads the liquid silicon evenly over the substrate.

Bonding Heat-Resistant Fabric to Tile

Acid etching, densification, and silica cement ensure a strong bond.

Lyndon B. Johnson Space Center, Houston, Texas

Procedures have been developed for bonding quartz fabric to silica tiles, both glazed and unglazed. The procedures use high-temperature materials exclusively and are therefore suitable for securing flexible seals and heat barriers around doors and viewing ports in furnaces and kilns.

The bond withstands temperatures in excess of 1,200° F (650° C). It provides a peel strength of 3 pounds per linear inch (500 N/m) on glazed tile and 7.4 pounds per linear inch (1.3 kN/m) on unglazed tile. Previously, the tile and fabric were joined with a room-temperature-vulcanizing adhesive that was limited to service temperatures below 600° F (316° C).

The key step in the preparation for bonding to glazed tile is etching the quartz fabric and the tile with acid: This increases the adhesion of the silica cement used to form the bond.

Major steps in preparing the quartz fabric for bonding are as follows:

- Application of a liberal coat of isopropyl alcohol to the contact surface,
 - Application of three coats of 0.10 normal hydrochloric acid,
 - Rinsing, and
 - Coating with a wetting agent.
- Glazed tile is prepared by the following steps:
- Masking with tape so that only the bond contact area is exposed,
 - Application of a thick coating of paste imbued with hydrofluoric acid for 10 minutes,
 - Rinsing, and
 - Removal of the masking tape.

Bonding of the quartz fabric to the tile must be done within 4 hours after the tile glaze has been etched. Silica cement is applied to the prepared areas of the fabric and the tile. The cement should form a fillet along the edges of the fabric contact area. The fabric is applied to the

tile and held in place with tape. The cement is allowed to dry in air for 48 hours, after which the bond is complete.

The key step in bonding to unglazed tile is densification of the tile to create a stronger joint. The tile is masked with tape to expose only the contact area. The exposed area is densified by repeated brushings of colloidal silica slurry, then is allowed to dry. The area is waterproofed by brushing on three coats of a silane solution. The surface is then lightly sanded.

The quartz fabric is prepared in the same way as for bonding to glazed tile. The bonding of fabric to tile with silica cement is also performed in the same way as for glazed tile.

This work was done by Jack W. Holt and Laurence W. Smiser of Rockwell International Corp. for **Johnson Space Center**. For further information, Circle 142 on the TSP Request Card. MSC-20540.

Explosive Welding for Remote Applications

Explosive seam welding produces up to 100-percent joint strength.

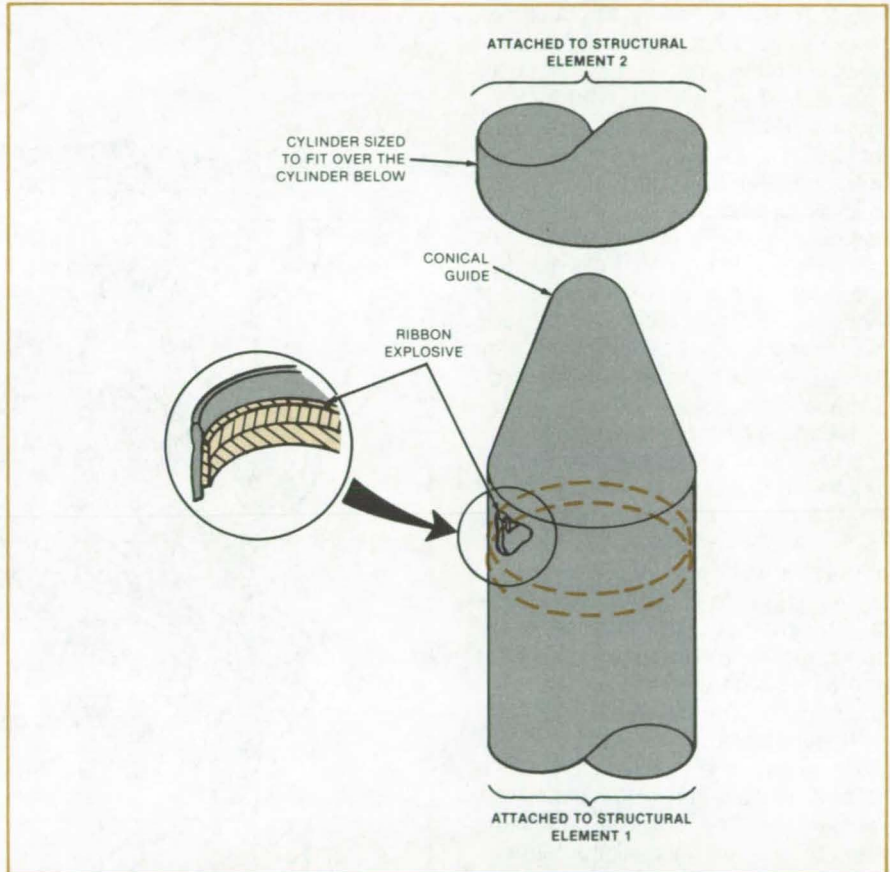
Langley Research Center, Hampton, Virginia

The figure illustrates a fully contained method to join structures remotely for such applications as structural assembly in toxic atmospheres and in radioactive or otherwise hazardous environments. Ribbon explosive is installed inside a cylinder on a "V"-notched welding interface. The conical apex aligns and receives a second cylinder and closes off the cylinder. The opposite end of the first cylinder is closed and attached to one of the two structural elements to be joined. The second cylinder, attached to the other structural element, slides over the conical guide and covers the area opposite the ribbon explosive.

The explosive can be activated by a variety of methods, including electrical detonation, to form an explosively welded joint between the cylinders, thus joining the two structural elements. All explosive products, such as flame, debris, smoke, and sound, are contained within the closed volume. The joint is metallurgically complete, yielding a hermetic seal. Unbalanced forces are minimal and, once the gases in the closed volume have cooled, little gas pressure remains.

An added advantage of this method is that the cylinders could be telescoping over considerable lengths so that the joint could be made at any point on the cylinders to allow precise adjustment of the lengths of the structural elements prior to joining. The table gives data on the joining of like and unlike metals by this technique.

This work was done by Laurence J. Bement of Langley Research Center. For further information, Circle 143 on the TSP Request Card. LAR-13119



Ribbon Explosive Activated by a Remote Energy Source produces a metallurgically sound joint. The success of the technique has been verified for joints between like metals and joints between two different metals.

Metal	Thickness Range (inch)
Iron or Steel (Low-carbon to 300 and 400 stainless)	0.001 to 0.050
Aluminum (Any fully annealed alloy and all age- and work-hardened alloys except 2024 and 7075)	0.010 to 0.188
Copper or Brass	0.010 to 0.150
Titanium (Ti-6Al-4V, each plate prebent 5°)	0.005 to 0.050

- Low-carbon to series 300 and 400 stainless steel are joinable in any combination.
- All aluminum alloys and conditions are joinable to each other except a combination of 2024-T3, T4, etc., and 7075-T3, T6, etc.
- Any combination of copper, aluminum, and brass can be joined.

The Metals Identified at the Top of this Table were used in both halves of explosively welded joints. Such joints between like metals were tested at 100-percent strength. At the bottom of the table are results of tests of joints consisting of different metals.

Welding Many Thin Metal Layers

Electron-beam welding yields reliable, leakproof joints.

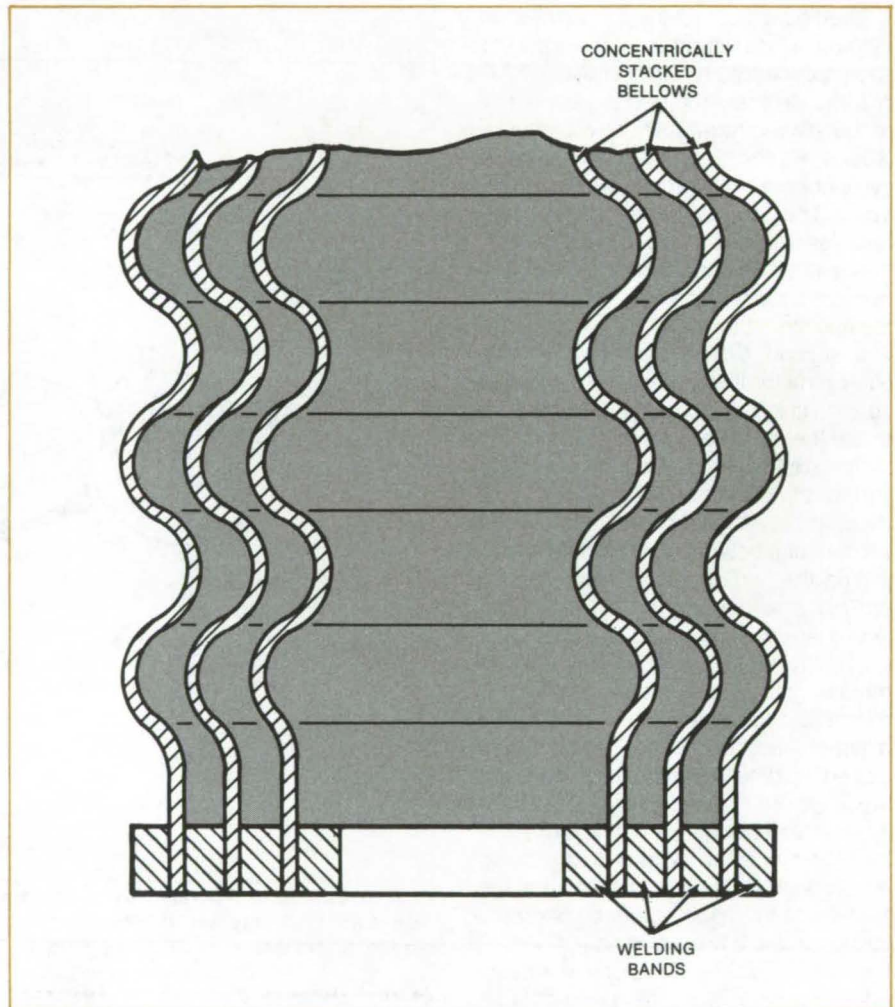
Lyndon B. Johnson Space Center, Houston, Texas

Electron-beam welding has been proposed as a substitute for resistance welding of the ends of concentrically stacked sheet-metal cylinders or bellows. The technique was developed for fuel lines in which metal bellows are used at restrained-pin or gimballed joints to allow for stress- or heat-induced motion between parts. So that the bellows can withstand many cycles of expansion and contraction, they are made of two or more plies of sheet metal — for example, a nickel alloy 0.006 in. (0.15 mm) thick. The new technique ensures repeatable leakproof assemblies.

In conventional practice, the "skirts" or ends of thin multiple-ply metal bellows or tubes are resistance-welded to somewhat thicker interspersed plies. This creates a fused zone thick enough not to melt all the way through when welded to thicker parts (see figure). The skirt is then trimmed to the fused zone, which provides sufficient metal thickness for making a good fusion weld between the end of the bellows or tube and the supporting hardware.

However, the fused zone of a resistance weld cannot be directly inspected, even by X-rays. If part of the fused zone is poorly joined, the plies can delaminate when the skirt is trimmed. The delamination is undetectable, but can cause the plies to burn back during the fusion-welding step. A leaky joint will result.

Electron-beam welding of the thin metal layers results in a solid square-cross-section fused zone that has no tendency to delaminate during fusion welding. Thus, leak paths do not develop unless the entire zone is consumed by fusion welding. Moreover, the fusion weld is easier to make, since the welder does not have to be concerned about sudden delamination. The fusion weld is



Welding Bands (also called "doublers") are sandwiched between the layers to be welded to increase the final weld-section thickness.

also of better quality, since the electron-beam weld is made in vacuum, and therefore does not have the oxidation and flash characteristic of a resistance weld.

This work was done by Bruce O. Hartwell, Peter Caras, and Phil H. Hobbes of Ametek for Johnson Space Center. No further documentation is available. MSC-20698

MiniBriefs describe NASA innovations and reports in an abbreviated format. Readers desiring additional information on these items should request the Technical Support Packages (TSP's), available in most cases, which can be obtained by using the TSP Request Card at the back of this issue.

Strong, Lightweight Curved Panels

Sandwich construction gives panels structural efficiency.

Large panels with compound curvatures are formed from a honeycomb core faced with sheets of graphite/epoxy cloth and tape. The core is strong, lightweight, and easy to form in contoured areas. It also is corrosion-resistant.

The sandwich construction is as strong as solid graphite/epoxy laminates or stiffened metal skins, but is thinner and lighter. The filaments in the cloth and tape are oriented to withstand internal pressure and buckling loads. Originally developed for a pod on the Space Shuttle, the construction can readily be adapted to curved skin panels on cars, trucks, and airplanes.

*This work was done by Ralph Molho and Henry L. Bestor of McDonnell Douglas Corp. for **Johnson Space Center**. For further information, Circle 144 on the TSP Request Card. MSC-16278*

Tape-Mounted Thermocouple

Thermocouple junctions soldered to copper-foil adhesives allow easy assembly.

Copper-foil tape is used to attach thermocouples to hardware. The thermocouple junction is soft-soldered to a copper-foil tape that has an acrylic pressure-sensitive adhesive backing. The thermocouple is mounted on the surface by simply pressing and smoothing it in place. The entire assembly is then covered by a piece of aluminized glass or dielectric Kapton, or equivalent, tape. The adhesive couplings may be easily removed.

*This work was done by Kenton S. MacDavid of Caltech for **NASA's Jet Propulsion Laboratory**. For further information, Circle 145 on the TSP Request Card. NPO-16291*

Connector-Array Attachment Matrix

Factory-assembled electrical/mechanical connectors on flexible sheets improve installation efficiency.

Multiple combinations of electrical/mechanical connectors typically found in photovoltaic modules can be attached to rollable and foldable sheets and then factory-assembled under controlled conditions for easy installation to structural supports such as roofs. The prespaced connectors, which are attached to plastic-film sheets, cloth tape, or other flexible materials should improve photovoltaic-module installation and fieldwork quality by simplifying the placement of the multiple connectors. When the flexible sheet is placed on the support, all of the connectors are already in place.

*This work was done by Timothy J. Maloney of AIA Research Corp. for **NASA's Jet Propulsion Laboratory**. For further information, Circle 146 on the TSP Request Card. NPO-15778*

Snapping Quick Fastener

A snapping fastener allows quick attachment and detachment of solar panels.

An inexpensive quick fastener for attaching and detaching solar-panel modules to a support consists of a large single snapping having multiple sinusoidally curved sections in a generally rectangular configuration formed from brass, stainless steel, or plastic. The giant sinusoidally configured locking is distorted readily when the unit is used for latching solar panels. The springy structure can be bent to fit any recess, making solar-panel removal or repair extremely simple.

*This work was done by Abraham H. Wilson of Caltech for **NASA's Jet Propulsion Laboratory**. For further information, Circle 147 on the TSP Request Card. NPO-15724*

Splicing Efficiently Couples Optical Fibers

Coupling losses between the joined optical-fiber ends are only 0.1 dB.

A method of splicing single-mode optical fibers results in very low transmission losses through the joined fiber ends. Transmission losses are only 0.1 dB, as opposed to 1.0 dB attained by conventional chemical-bond-splicing methods.

The fiber ends, coated with ultraviolet-curable epoxy, are guided toward each other in a short glass tube. The ends are aligned with a micropositioner. An optical time-domain reflectometer is used in monitoring the joint to assure that the ends are aligned for a minimal transmission loss. The method needs no special operator training.

*This work was done by George F. Lutes of Caltech for **NASA's Jet Propulsion Laboratory**. For further information, Circle 148 on the TSP Request Card. NPO-16294*

Automated Solar-Panel Fabricator

System takes raw components and assembles solar panels.

An automated computer-controlled system based on a standard commercial industrial robot takes solar cells and other raw materials and assembles them into completed solar panels. The system can be broken into three substations: The cell-stringing station takes the solar cells, interconnecting ribbons, and solder paste and solders the ribbons to the cells in a two-dimensional array. The lamination station encapsulates the string of cells into a laminate. Finally, an edge-sealing and framing station applies a hot-melt seal to the finished module.

*This work was done by John J. Hagerty of MB Associates for **NASA's Jet Propulsion Laboratory**. For further information, Circle 149 on the TSP Request Card. NPO-16205*

Close-Out Plugs

Externally-applied circular plug seals holes in walls up to 0.44 in. (12 mm) in diameter.

A plug assembly can be installed externally through a port in a wall to mechanically seal off the 0.44-in. (12-mm) inspection hole. The elongated circular flanged plug is inserted through the hole and rotated by 90°. In this position the plug cannot be pulled out. A tubular retainer held by an integral shoulder holds the plug in place. To prevent rotation of the plug, the retainer and plug are keyed together.

This work was done by T. C. Adams of Rockwell International Corp. for Marshall Space Flight Center. For further information, Circle 150 on the TSP Request Card.
MFS-19370

Acoustic Levitation System

A high-powered siren/reflector system levitates dense materials.

Dense materials, such as steel balls, can be continuously levitated with the energy provided by an efficient high-powered siren in combination with a shaped reflector. The motor-driven variable-frequency siren has its acoustic impedance matched to the impedance of the air in the chamber by an exponential horn.

A reflector system, consisting of a curved top reflector and a flat lower

reflector, eliminates instability in the spatial positioning of the sample. The optimum reflector shapes for the chamber are determined empirically. The siren and levitation chambers are enclosed in a special enclosure with acoustic insulation to reduce external sound levels. Temperature and pressure of the gas in the chamber, as well as the moisture, can be controlled externally before the gas is applied to the siren.

This work was done by Paul M. Gammell, Taylor G. Wang, Arvid Croonquist, and Mark C. Lee of Caltech for NASA's Jet Propulsion Laboratory. For further information, Circle 151 on the TSP Request Card.
NPO-16146

Acoustic Position Servosystem

A servosystem automatically centers levitated objects within a given volume.

A positioning system automatically centers solid samples in high-temperature levitation chambers. The closed-loop servosystem monitors the frequency shift from the sample as it drifts. The instantaneous relative frequency shift for each of the three chamber axes, which is indicative of the change in position of the sample in the chambers, is monitored by frequency counters. When the arbitrarily-set spatial boundaries, such as the furnace area, are exceeded, the closed frequency-to-acoustic power loop is automatically turned on to provide enough power to recenter the object in the chamber.

This work was done by Emily W. Leung, Chun Ping Lee, and Taylor G. Wang of Caltech for NASA's Jet Propulsion Laboratory. For further information, Circle 152 on the TSP Request Card.
NPO-15936

Heat-Shield Gap Filler

Ceramic cloth strips provide a flexible, easily replaceable insulating filler.

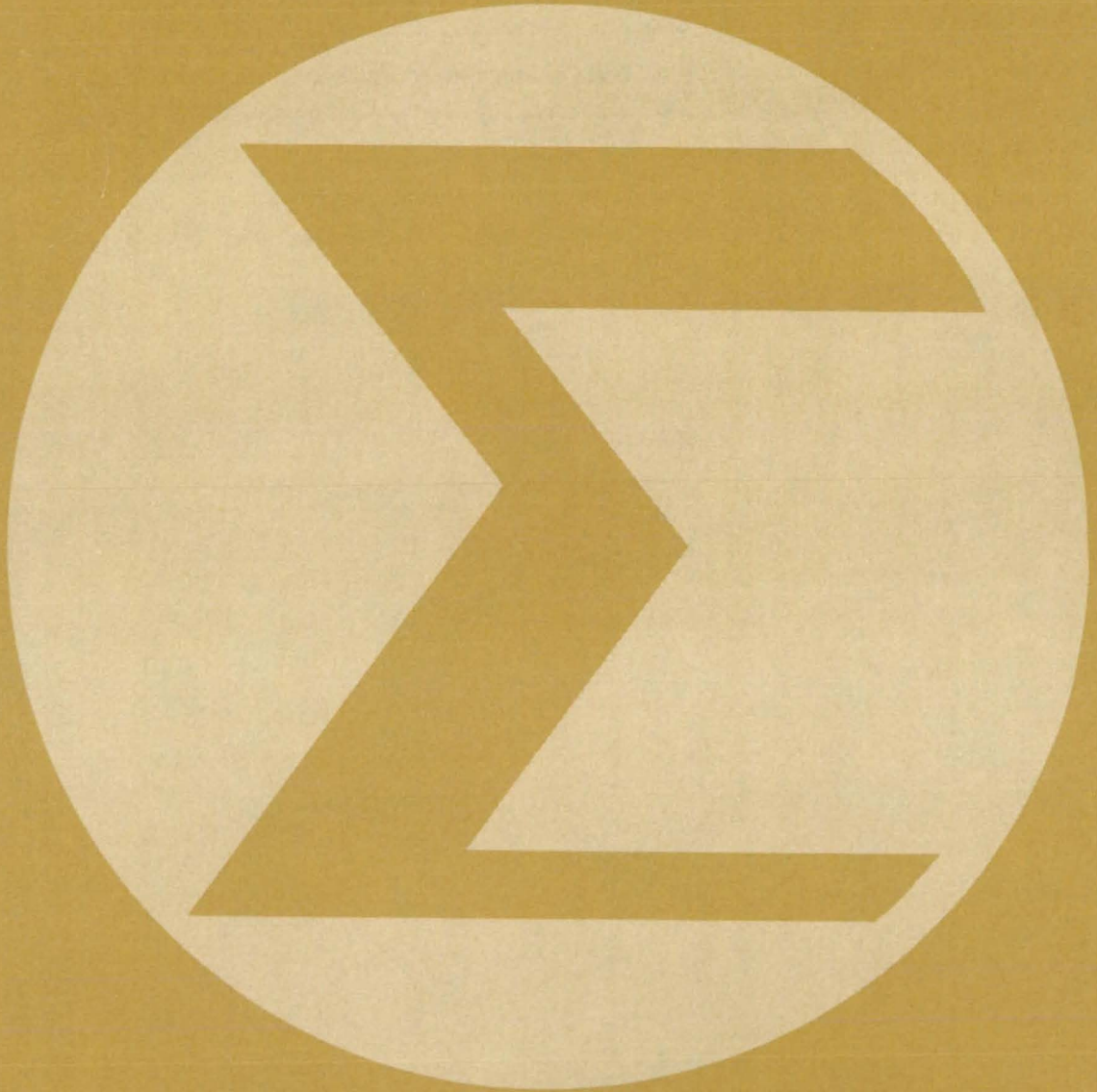
Strips of ceramic cloth are used to fill the gaps between heat-resistant blocks or tiles. This filler prevents hot gas from flowing between heat-shield tiles while allowing space for thermal expansion and contraction.

The filler strip is formed from superimposed layers of ceramic cloth with a ceramo-organic high-emittance coating. The strip is inserted into the gap to be filled and attached at the bottom with silicone rubber adhesive. The filler can accommodate gaps of less than 0.1 in. (2.54 mm). The strips can be easily replaced when necessary.

This work was done by Daniel B. Leiser, David A. Stewart, Marnell Smith, Carlos Estrella, and Howard E. Goldstein of Ames Research Center. For further information, Circle 153 on the TSP Request Card.

This invention has been patented by NASA (U.S. Patent No. 4,308,309). Inquiries concerning nonexclusive or exclusive license for its commercial development should be addressed to the Patent Counsel, Ames Research Center [see page A5]. Refer to ARC-11310.

Mathematics and Information Sciences



**Hardware,
Techniques, and
Processes**

- 573 Flight-Stability Extremes Calculated From the Uncertainty Ellipse
- 574 Predicting the Reliability of Solar-Cell Interconnections
- 575 Predicting Severe Duststorms

Books and Reports

- 576 Cost Considerations in Nonlinear Finite-Element Computing
- 576 Source Pre-Processor or Interface-Specification Language

Computer Programs

- 576 Library Information-Processing System
- 577 Orbital and Geodetic Error Analysis

Minibriefs

- 577

Flight-Stability Extremes Calculated From the Uncertainty Ellipse

Tangents and normals to the ellipse are useful in control-system calculations.

Lyndon B. Johnson Space Center, Houston, Texas

Expressions for tangents and normals to ellipses were derived for situations with two correlated aerodynamic force or moment variables having normally (Gaussian) distributed uncertainty. However, the expressions describe basic geometrical properties of an ellipse arbitrarily located and oriented in a plane. Thus they could also be useful in other problems involving ellipses.

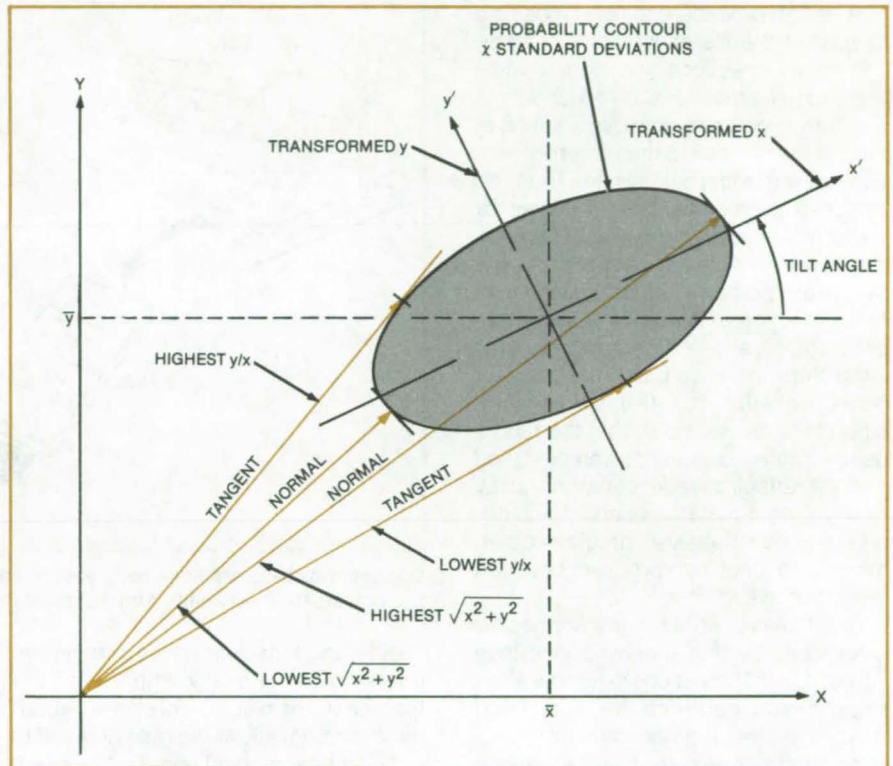
Suppose that x and y represent the two correlated random variables with standard deviations σ_x and σ_y , respectively. Let ρ = the correlation coefficient between x and y . The probability contour that surrounds all points lying within X standard deviations of the mean values \bar{x} and \bar{y} is described by the equation

$$\frac{1}{1 - \rho^2} \left[\left(\frac{x - \bar{x}}{\sigma_x} \right)^2 + \left(\frac{y - \bar{y}}{\sigma_y} \right)^2 - 2\rho \left(\frac{x - \bar{x}}{\sigma_x} \right) \left(\frac{y - \bar{y}}{\sigma_y} \right) \right] = X^2$$

This equation has the same form as that for a tilted ellipse centered at \bar{x}, \bar{y} in the x - y plane (see figure).

Four quantities are often of great interest for control and stability purposes: These are the high and low extremes of the y/x ratio and the greatest and smallest magnitude, $\sqrt{x^2 + y^2}$, of the x, y vector on the 3σ contour. The y/x ratios are just the slopes of the tangents to the $X = 3$ ellipse drawn from the origin (unless the origin is inside the ellipse). The magnitudes are just the lengths of the perpendiculars to the ellipse drawn from the origin.

To simplify the calculation, the x - y plane is transformed into one in which the center of the ellipse lies at the new origin and its axes correspond to the coordinate axes. The transformation includes a translation of $(-\bar{x}, -\bar{y})$ and a rota-



A Tilted Ellipse surrounds all points x, y within X standard deviations of the mean x, y . The vectors drawn from the origin are tangents and normals to the ellipse that are of interest in control and stability analysis.

tion that brings the tilt back to zero, the tilt angle being calculated by one of three alternate expressions depending on the values of ρ , σ_x , and σ_y . The tangents and normals emanating from the transformed old origin are calculated in the transformed coordinate system, then retransformed back into the original coordinates. The desired ratios and magnitudes are obtained from these tangents and normals.

Although the transformations and vector calculations are tedious when

done by hand, the equations are in closed form and give rapid results when performed by computers or programmable desk calculators. The probability extremes of the ratios and magnitude are thus obtained directly, without repeated table lookup or other complication.

This work was done by Daniel F. Dominik of Rockwell International Corp. for Johnson Space Center. For further information, Circle 154 on the TSP Request Card.
MSC-20308



Predicting the Reliability of Solar-Cell Interconnections

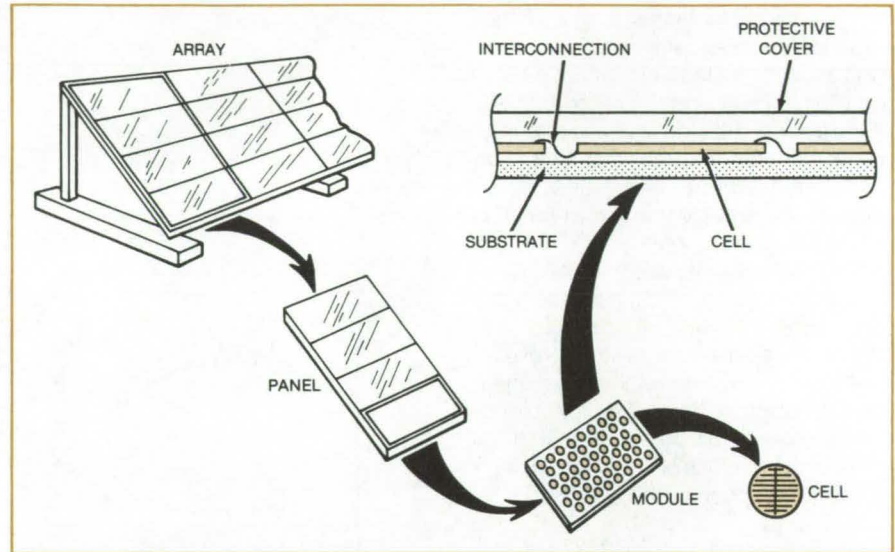
The reduction of life expectancy by thermal cycling is calculated during design.

NASA's Jet Propulsion Laboratory, Pasadena, California

A design procedure makes it possible to predict the life expectancy of solar-cell interconnections and to determine the cost-effectiveness of redundancy. The new procedure employs a series of algorithms for calculating interconnection displacement and strain. Then, on the basis of empirical fatigue curves for the interconnection material (copper), the displacements are used to calculate the failure probabilities for individual interconnections. The individual failure probabilities are used in another algorithm for predicting the loss of power output for the array. The algorithms are set up so that the redundancy in interconnections can be varied and the effect of redundancy on array power output can be observed. Finally, an energy/cost analysis program determines the best compromise between redundancy and cost.

Solar cells in an array are connected electrically by thin metal ribbons (see figure). Daily fluctuations in temperature expand and contract the array and thereby subject the ribbon interconnections to stress cycles. In time, fatigue cracks can develop in the interconnections and ultimately cause failure. If enough interconnections fail, entire segments of an array can be lost. Redundant interconnections reduce the problem, but add to the cost of the array.

The procedure enables a solar-cell-module manufacturer to calculate the interconnection strain levels for a particular interconnection configuration. The manufacturer will be able to predict the cumulative interconnection failures at the end of the expected array lifetime, to estimate the degradation in power output over the array lifetime, and to determine the degree of interconnection



Connections between solar cells are critical parts of solar-cell arrays for generating electric power. Their reliability affects the life expectancy of modules, panels, and arrays.

redundancy necessary for minimum energy cost. Equally important, the manufacturer will be able to establish the maximum allowable ratio of failed to unfailed interconnections. This ratio will provide a realistic standard in an accelerated thermal-cycling test.

The procedure can be used for materials other than copper if fatigue curves are available. When applied to aluminum, for example, the procedure shows that its fatigue behavior is not as good as that of copper. This plus the limited weldability and solderability of aluminum may limit its use as a solar-cell interconnection material. Connections of copper-clad Invar (or equivalent nickel/iron alloy) are more expensive to manufacture than are those of aluminum, but are more resistant to fatigue failure at lower levels of redundancy.

The procedure is not limited to solar-cell interconnections. It can be used to predict the stress-cycle lifetimes of such structures as arches, walkways, cylindrical ribbing of aircraft fuselages and submarine hulls, and pipeline expansion loops. In automobile design, for instance, a few samples of a new dashboard could be fatigue-cycle tested in a laboratory instead of being built into cars that would be cycled and tested as units. Testing costs might be reduced by about 90 percent.

This work was done by Gordon R. Mon, Donald M. Moore, and Ronald G. Ross, Jr., of Caltech for NASA's Jet Propulsion Laboratory. For further information, Circle 155 on the TSP Request Card.
NPO-15976

Priority Queuing on a Parallel Data Bus

A queuing strategy for communications along a shared data bus minimizes the number of data lines while always assuring that the user of highest priority is given access to the bus. The algorithm thus provides maximum service with a minimum number of wires. (See page 471.)

Active Pulse Suppression of Structural Vibrations

An algorithm for controlling the reactions of buildings and other structures to Earthquakes initiates counterpulses when incoming shock pulses exceed a threshold level. The control needs less computation effort than do comparable closed-loop systems. (See page 522.)

Fuel-Conservative Descents Using a Programmable Calculator

An algorithm compatible with time-based metering and profile-descent procedures accurately delivers an airplane to a metering fix at a time, altitude, and airspeed designated by the air-traffic control system. (See page 515.)

Predicting Severe Duststorms

Combined human/machine forecasting technique shows promise.

NASA's Jet Propulsion Laboratory, Pasadena, California

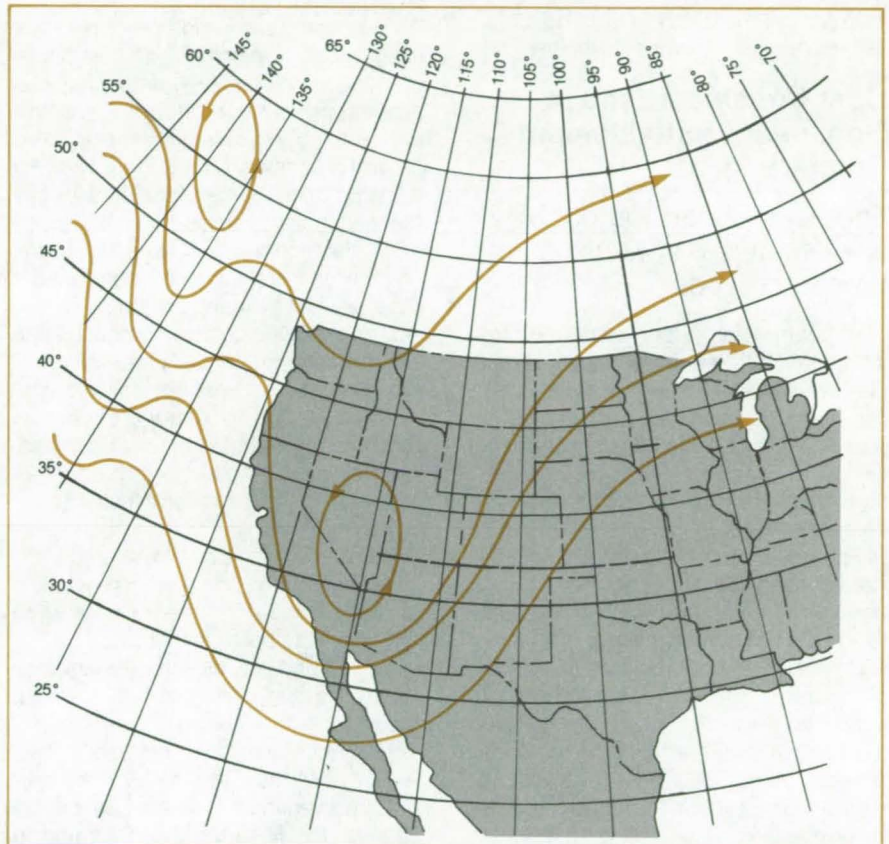
Severe duststorms in the Great Plains can be forecast with fair reliability. The forecasts are derived from a combination of human expertise and a variety of meteorological information sources, including all current and recent weather observations, standard National Meteorological Center (NMC) computer analyses for surface and upper air, and the NMC 12-, 24-, 36-, and 48-hour prognostication charts generated by the Limited Fine Mesh computer model.

The forecasts depend on a knowledge of synoptic weather conditions associated with severe duststorms. A study of 50 storms during the years 1968 through 1977 revealed a set of meteorological features common to all of them. These are as follows:

- Windspeed ≥ 40 knots (20.6 m/s) at altitudes where the pressure is 700 or 850 mbar (70 or 85 kN/m²);
- Windspeed ≥ 60 knots (30.9 m/s) at altitudes of 500-mbar (50-kN/m²) pressure;
- Subsidence region in certain vertical-velocity and local-vorticity-change computer forecasts;
- Cyclogenesis deepening at ≥ 1 mbar (100 N/m²) per hour;
- Jet streaks;
- A dry adiabatic lapse rate from the surface to the altitude where the pressure is 500 mbar (50 kN/m²); and
- Satellite photographs showing comma-shaped clouds and typical dustcloud patterns.

Taking these features into account, a hierarchy of observational data, computer outputs, and analysis techniques was developed for severe-duststorm forecasting. Analyses and numerical forecasts are blended in a human/machine process to arrive at the finished duststorm forecast.

The information sources and techniques required in a particular situation depend on the spatial and temporal



This Flow Pattern at altitudes where the pressure is 500 mbar (50 kN/m²) is conducive to the development of a major cyclogenetic duststorm over the central and southern plains states.

resolution required of the forecast. Seasonal predictions depend on soil and rainfall history. For predictions 3 days or longer in advance, general hemispheric flow patterns are important (see figure). Forecasting in the 12- to 48-hour range depends heavily on special upper-air analyses and computer output. Short-range forecasts rely on radar, satellite, and instrumentation readings and reports of human observers.

The forecasting method was verified by the prediction of seven duststorms in the central and southern Great Plains

during the months of October 1976 through April 1977. Of the seven predictions, six were correct and one was a false alarm. In contrast, a forecast based purely on computer outputs showed only three of these six storms and incorrectly predicted others with a false-alarm rate of 60 percent.

This work was done by Peter M. Woicheshyn of Caltech for NASA's Jet Propulsion Laboratory. For further information, Circle 156 on the TSP Request Card. NPO-14999



Books and Reports

These reports, studies, and handbooks are available from NASA as Technical Support Packages (TSP's) when a Request Card number is cited; otherwise they are available from one of NASA's Industrial Application Centers or the National Technical Information Service.

Cost Considerations in Nonlinear Finite-Element Computing

The quasi-linear approach is evaluated in various computer types.

A conference paper discusses the computational requirements for finite-element analysis using the quasi-linear approach to nonlinear problems. The paper evaluates the computational efficiency of different computer architectural types in terms of relative cost and computing time.

The nonlinear problems of particular interest are those of mechanical equilibrium or vibrations in complicated structures. The solution algorithms involve the computation of the deflections and forces at discrete times by Newton-Raphson iterations. To establish the feasibility of the quasi-linear method for nonlinear analysis, each step of an iteration is shown to correspond to the solution of a linear problem.

The authors emphasize substructuring; that is, the mathematical partitioning of a physical structure into pieces that are loosely coupled to each other but are

internally tightly coupled. (Sometimes a solution can be aided by further partitioning a substructure at a lower level of computation.) They show how to analyze an algorithm and a computer for the optimum number of partitions to be used in systematic substructuring with respect to processor and memory usage and execution speed.

The organization and flow of data are described for five computer types: single-processor/single-level-memory, single-processor/two-level-memory, vector-processor/two-level-memory, and parallel-processor, both without and with substructuring. Some of the conclusions reached in the paper are as follows:

- The developments in substructuring techniques appear to be beneficial in the efficient use of single-processor/two-level-memory computers and in preparing for parallel processing.
- As the cost of the primary memory decreases and its size increases, the need for substructuring may decrease.
- As the cost of peripheral processors decreases, the need for substructuring may increase.
- In substructuring a particular algorithm, one should consider the computation-price structure of the computer on which it is to be implemented.
- Parallel and vector processing may decrease the running time of a job but not necessarily its cost.

This work was done by Senol Utku, Robert J. Melosh, and Munirul Islam of Duke University and Moktar Salama of Caltech for NASA's Jet Propulsion Laboratory. To obtain a copy of the paper, Circle 157 on the TSP Request Card.

NPO-16237

Source Pre-Processor or Interface-Specification Language

Design aid for data structures works in combination with a source program pre-processor.

A user's guide is now available for the source program pre-processor (SPP) method for producing descriptions of data structures or records. The SPP enhances the usefulness of Program Design Language (PDL) — a software-design tool that decreases debugging time and improves the quality of source programs.

By itself, PDL stresses control and processing actions in software design. The new method provides a way of integrating data and procedural designs and performing cross-references between the two.

The SPP employs a pseudolanguage to describe a record structure and build a language processor to convert the record structure to both human-readable documentation and machine-readable access parameters. The method enables the separation of code, design language, and structure-definition language and thus makes it possible to maintain all documentation in a single source module. The human-readable documentation can be further processed by PDL.

This work was done by William J. C. Luebker of Telos Computing, Inc., for NASA's Jet Propulsion Laboratory. To obtain a copy of the user's guide, Circle 158 on the TSP Request Card.

NPO-15814

Computer Programs

These programs may be obtained at very reasonable cost from COSMIC, a facility sponsored by NASA to make new programs available to the public. For information on program price, size, and availability, circle the reference letter on the COSMIC Request Card in this issue.

Library Information-Processing System

System works with the Library of Congress MARC II format.

The Library Information-Processing System was developed to support library facilities at Goddard Space Flight Center. The system is composed of subsys-

tems that provide a wide range of library information-processing capabilities. The system is designed to work with data in the Library of Congress MARC II communications format, which is the American National Standards Institute (ANSI) format for machine-readable bibliographic data. This library information-processing system should be adaptable to any medium-to-large library.

The Bibliographic Products Subsystem provides library users and staff with in-depth easy access to the library collection through catalogs, keyword indexes, and control tables. Several methods of information access are provided, including call number, author/title, subject, keyword, and control field. Output from this subsystem includes both hard-copy reports and tapes for computer-output microfilm. These output products direct users and staff to items contained in the library book collection and to other products from the system. This subsystem also generates the cataloger's shelf list, which provides a working tool for the cataloging staff. MARC II-compatible data records can be added, changed, or deleted at the word, subfield, tagged field, or record level.

The Book Acquisition Subsystem provides a front-end tracking system for materials ordered by the library but not yet on the shelves. Order status is tracked from order placement through the cataloging operation. The subsystem provides both financial accountability and order followup mechanisms. Staff can quickly ascertain the status of individual orders and verify items on order, thus avoiding duplication. The Journal Acquisition Subsystem provides similar tracking procedures for journal orders. Additional reports include a master vendor list that serves as a backup to individual purchase orders. The journal system provides brief cataloging records for journals acquired and held by the library and provides an inventory of all bound journal volumes in the collection.

The Library Statistics Subsystem provides the library with management information relating to holdings and use as well as aging characteristics of the book collection. Reports generated by this subsystem include the Circulation/Holding Report, the Holdings Profile, and the

Call Number/Imprint Report. The Audit Subsystem can be used to track the work done by the library staff. It generates reports that display types of requests, how and where material is obtained, completion time, and source of requests for various types of materials. This subsystem utilizes SAS, a commercial software system, to generate cross-tabulated and graphical displays.

The programs in the Library Information-Processing System are written in ANS COBOL (Level 3 or 4) and OS Assembler. The system is designed for batch execution, has been implemented on an IBM 370-compatible computer with OS/MVT or OS/MVS, and has a minimum central-memory requirement of approximately 150K of 8-bit bytes. This library system was last updated in 1982.

This program was written by Informatics General Corp. for Goddard Space Flight Center. For further information, Circle C on the COSMIC Request Card.
GSC-12861

Orbital and Geodetic Error Analysis

Results that previously required several runs are determined in a more computer-efficient manner.

ERODYN is an orbital and geodetic error-analysis program designed specifically to be operated as a companion to the COSMIC program GEODYN. To perform an error analysis of a proposed or actual GEODYN parameter-estimation run, ERODYN requires as input the normal ("E") matrix and, for some options, the variational partials ("V") matrix as computed within GEODYN. To examine various partitionings of the total parame-

ter set into adjusted and unadjusted parameters, the initial GEODYN run must have all parameters of interest adjusted. However, only one estimator iteration is required using "nominal" initial conditions to generate the required normal matrix and variational partials matrix. These matrices are subdivided within ERODYN into the appropriate adjusted and unadjusted partitions as specified by the ERODYN user.

The ERODYN approach has proved to be extremely efficient. A typical analysis problem requires multiple runs of an error-analysis program using the same tracking schedule and problem geometry but with different partitionings of the parameter set. With the ERODYN approach, the operations that are common to these multiple runs are performed only once with GEODYN and stored on tape. ERODYN then performs the matrix partitioning and linear algebra required for each individual error-analysis run. In some cases, the iteration feature of ERODYN can be used to achieve results in a single run that would otherwise require several error-analysis runs.

The ERODYN program is written in FORTRAN IV and OS Assembler for batch execution and has been implemented on an IBM 370-series computer with an overlaid central-memory requirement of approximately 140K of 8-bit bytes. The ERODYN concept and design have undergone continuous evolution since 1974 based on user requirements. The most current version of ERODYN was developed in 1982.

This program was developed by Ted Felsentreger of Goddard Space Flight Center and Paul Maresca and Ron Estes of Business Technological Systems. For further information, Circle D on the COSMIC Request Card.
GSC-12768

MiniBriefs describe NASA innovations and reports in an abbreviated format. Readers desiring additional information on these items should request the Technical Support Packages (TSP's), available in most cases, which can be obtained by using the TSP Request Card at the back of this issue.

Managing Software Design and Design Changes

Specialized computer system makes design and development faster and more accurate.

A microprocessor-based system for document production, work scheduling, and change control and management information aids in design, development, and control of software. The system provides text-editing and record-keeping capability for the software designers. For managers, the system immediately shows the effects of changes, including

effects on work force, schedules, development status, and system configuration. When software changes have been approved, the requirements and project plans are instantly updated.

The system operates on an automated office-data center. The main components are a Z80 microprocessor, (continued on next page)



floppy-disk and hard-disk drives, and a character printer. The system may be linked to a large computer. Major software components are a control program monitor (CP/M), a text-editing and word-processing system, a work-breakdown-schedule processor, and a data-base management tool.

This work was done by Robert E. Loesh of Caltech for NASA's Jet Propulsion Laboratory. For further information, Circle 159 on the TSP Request Card.
NPO-15331

Error Correction for Tandem Data-Transmission Paths

The optimum number of repeaters required for digital links is computed.

A mathematical analysis for digital data transmission calculates the optimum number of binary error-correcting repeaters to install in a given number of wideband channel links. For a large number, L , of tandem links in series, the optimum number of required decoders typically approaches \sqrt{L} asymptotically. This error-control strategy gives guidance as to whether each wideband link should be separately coded and terminated by an error-correcting repeater or whether to use just one decoder for an entire series of L links. The asymptotic results are compared to computed numerical results.

This work was done by Edward C. Posner and Arthur L. Rubin of Caltech for NASA's Jet Propulsion Laboratory. For further information, Circle 160 on the TSP Request Card.
NPO-16125

Simplified Convolution Codes

A simple recursive algorithm efficiently calculates minimum-weight error vectors using Diophantine equations.

An improved, simplified algorithm carries out the final stages of decoding convolutional error-correcting codes for data transmission over noisy channels by determining what patterns of bit er-

rors have probably occurred. The least-weight error is found by a Viterbi-like algorithm but requires fewer comparisons, is simpler, and detects errors more readily. The recursive algorithm uses the general solution of the polynomial linear Diophantine equation to determine the minimum-weight error polynomial vector in the equation in polynomial space.

This work was done by Trieu-Kie Truong and Irving S. Reed of Caltech for NASA's Jet Propulsion Laboratory. For further information, Circle 161 on the TSP Request Card.
NPO-16251

Predictive Smoothing-Convolution Algorithm

Signal estimate is continually updated with or without phase correction.

Samples of a noisy waveform are numerically filtered with a moving-convolution technique. The technique is useful where the signal varies slowly with respect to the sampling rate.

The technique is based on a variable-coefficient, n -degree-polynomial approximation of the noise-free signal. The polynomial coefficients are obtained anew at each time step by a convolution over the preceding m time steps, with a convolution algorithm chosen so that the resulting coefficients produce the least-square error between the polynomial and the m waveform samples. Applications of this algorithm include predicting the next waveform sample and smoothing to filter out noise with or without correction for phase delay.

This work was done by Jose C. Alvarez of Ford Aerospace & Communications Corp. for Johnson Space Center. For further information, Circle 162 on the TSP Request Card.
MSC-20604

Parallel VLSI Architecture

A Fermat number transformation convolutes two digital data sequences.

In very-large-scale integration (VLSI) applications, such as image and radar signal processing, X-ray reconstruction, and spectrum shaping, linear convolution of two digital data sequences of ar-

bitrary lengths can be accomplished using a Fermat number transform (FNT). A pipeline structure is designed to compute a 128-point FNT in which only additions and bit rotations are required. The bit rotations are implemented by modification of a standard barrel shifter. This method alleviates the usual dynamic range limitations in FNT's of long transform lengths.

This work was done by Trieu-Kie Truong of Caltech and I. S. Reed, C. S. Yeh, and H. M. Shao of the University of Southern California for NASA's Jet Propulsion Laboratory. For further information, Circle 163 on the TSP Request Card.
NPO-16124

Computing Tridiagonal Matrices

Tridiagonal matrices are recomputed when the computer memory is full.

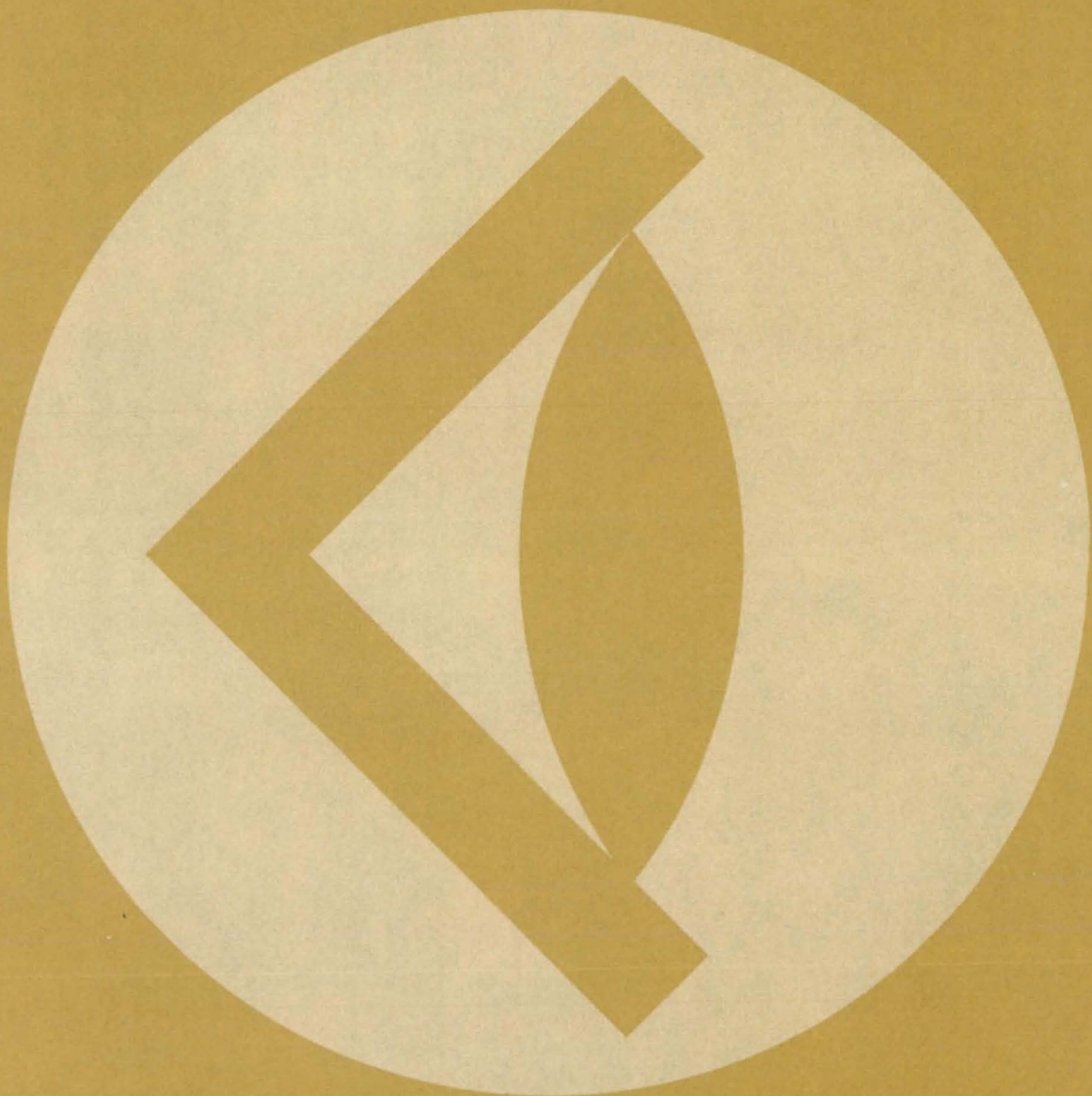
An algorithm applying Gaussian elimination helps computers in processing tridiagonal matrices. It is useful when a computer memory cannot accommodate a relatively large system of linear equations. When the memory is full, the algorithm resorts to recomputation. When enough memory capacity is available, the algorithm reduces to the standard solution form.

The algorithm is included as a subroutine to the main matrix-processing program. The user specifies with one parameter exactly how much storage is available in the primary memory, and the subroutine minimizes the computation subject to this constraint. The approach can be extended to periodic and pentadiagonal matrices and in general to any computation with a forward and backward sweep that saves the intermediate results.

This work was done by Marshal L. Merriam of Ames Research Center. For further information, Circle 164 on the TSP Request Card.

Inquiries concerning rights for the commercial use of this invention should be addressed to the Patent Counsel, Ames Research Center [see page A5]. Refer to ARC-11476.

SUBJECT INDEX



ABRASION			
Cleaning the walls of a silane reactor			
page 499	NPO-15851		
ACOUSTIC LEVITATION			
Applying uniform polymer coatings to microspheres			
page 496	NPO-16075		
Acoustic levitation system			
page 570	NPO-16146		
Acoustic position servosystem			
page 570	NPO-15936		
ACOUSTIC MEASUREMENT			
Interferometer for measuring acoustic signals			
page 484	LAR-13030		
ACTUATORS			
Linear boom actuator			
page 550	NPO-16099		
ADHESION TESTS			
Insulation debond detection			
page 508	MFS-25862		
ADHESIVE BONDING			
Bonding technique for stiffened-skin structures			
page 559	NPO-15994		
Bonding heat-resistant fabric to tile			
page 566	MSC-20540		
Tape-mounted thermocouple			
page 569	NPO-16291		
AERODYNAMIC FORCES			
Flight-stability extremes calculated from uncertainty ellipse			
page 573	MSC-20308		
AIRCRAFT DESIGN			
Propeller design program			
page 548	LAR-13141		
AIR TRAFFIC CONTROL			
Fuel-conservative descents using a programmable calculator			
page 515	LAR-13138		
ALGORITHMS			
Cost considerations in nonlinear finite-element computing			
page 576	NPO-16237		
ANNEALING			
Activated internal gettering			
page 499	NPO-15530		
ANTENNA DESIGN			
Antenna subreflector fed by a line source			
page 456	MSC-20626		
Ellipsoidal balloon antenna			
page 457	NPO-15931		
Efficient reflector antenna			
page 458	NPO-16262		
Theoretical investigation of dielectric-horn antennas			
page 462	GSC-12876		
ARCHITECTURE			
Parallel VLSI architecture			
page 578	NPO-16124		
ARITHMETIC AND LOGIC UNITS			
Digital ratiometer			
page 478	NPO-15396		
ASSEMBLING			
Connector-array attachment matrix			
page 569	NPO-15778		
Automated solar-panel fabricator			
page 569	NPO-16205		
AUTOMATED RADAR TERMINAL SYSTEM			
Synchronized radar-target simulator			
page 472	MSC-20240		
AUTOMATIC FREQUENCY CONTROL			
Temperature compensation for a frequency modulated oscillator			
page 463	MSC-20556		
BALLOONS			
Ellipsoidal balloon antenna			
page 457	NPO-15931		
BARRIER LAYERS			
Reusable thermal barrier for insulation gaps			
page 512	MSC-20519		
BERNOULLI THEOREM			
Tapered ring seal			
page 541	LEW-14055		
BLOOD VESSELS			
Probe follower for moving blood vessels			
page 503	NPO-15898		
BOILERS			
Microphone detects boiler-tube leaks			
page 529	NPO-16027		
BOLTS			
Acousto-optic extensometer for bolts			
page 518	MFS-19914		
BONDING			
Solder bonding for power transistors			
page 559	MSC-20570		
BOOMS (EQUIPMENT)			
Linear boom actuator			
page 550	NPO-16099		
BRAKES (FOR ARRESTING MOTION)			
Safety pedal for foot-operated machinery			
page 537	MSC-20535		
BY-PRODUCTS			
Inhibiting wet oxidation of ammonia			
page 496	ARC-11407		
CABLES (ROPES)			
Stripping the sheath from stranded cables			
page 561	NPO-15082		
CALIBRATING			
Dynamic calibration of pressure transducers			
page 517	LAR-13094		
In-place calibration of instrumentation microphones			
page 530	ARC-11463		
CAMERAS			
High-resolution charge-coupled-device camera			
page 478	NPO-15086		
Instrumentation for solar oscillation measurements			
page 488	NPO-15687		
CAPACITORS			
High-frequency, high-power capacitor			
page 445	LEW-14034		
CARGO			
Holding cargo in place with foam			
page 546	MSC-20723		
CARRIAGES			
Thermal compensator for paraboloidal reflector			
page 490	NPO-16145		
CATALOGS (PUBLICATIONS)			
Library information-processing system			
page 576	GSC-12861		
CATHODES			
Elastomeric cathode binder			
page 499	NPO-15424		
CELL ANODES			
High-cycle-life lithium cell			
page 451	NPO-15921		
CERAMICS			
A ceramic heat exchanger for solar receivers			
page 489	NPO-15771		
Stabilized aluminum titanate			
page 499	NPO-16227		
CHANNELS (DATA TRANSMISSION)			
Priority queuing on a parallel data bus			
page 471	NPO-15005		
CHARGE COUPLED DEVICES			
Quicker selection of CCD images			
page 478	NPO-15345		
High-resolution charge-coupled-device camera			
page 478	NPO-15086		
CHARGE EXCHANGE			
Measuring air-ionizer output			
page 461	NPO-16058		
CHEMICAL TESTS			
Integrated exhaust-gas-analysis system			
page 519	LEW-14062		
CHLORINATION			
Preparing InSb substrates			
page 499	NPO-16127		
CIRCUIT BOARDS			
Edge labels for multilayer circuit boards			
page 560	MSC-20704		
CIRCUIT PROTECTION			
Hall-effect ground-fault interruptor			
page 464	NPO-15915		
CLAMPS			
Bonding technique for stiffened-skin structures			
page 559	NPO-15994		
CLASSIFIERS			
Differential-coil eddy-current material sorter			
page 451	MFS-19872		
CLEANING			
Cleaning the walls of a silane reactor			
page 499	NPO-15851		
CLEARANCES			
Measuring clearance indirectly			
page 534	MFS-19875		
CLOSED LOOP SYSTEMS			
Acoustic position servosystem			
page 570	NPO-15936		
CLOSURES			
Close-out plugs			
page 570	MFS-19370		
CLUTCHES			
Power train for hybrid electric vehicles			
page 550	NPO-15742		
COAL DERIVED GASES			
Solar heated gasifier			
page 489	NPO-15071		
Integrated fuel cell/coal gasifier			
page 498	NPO-16062		
COAL UTILIZATION			
Desulfurization of coal in fluidized beds			
page 493	NPO-15924		
COATING			
Top-coating silicon onto ceramic			
page 565	NPO-15125		
COMMUNICATION NETWORKS			
Priority queuing on a parallel data bus			
page 471	NPO-15005		
Short-range digital optical links			
page 477	NPO-15999		
COMPARATORS			
Digital ratiometer			
page 478	NPO-15396		
COMPENSATORS			
Thermal compensator for paraboloidal reflector			
page 490	NPO-16145		
COMPOSITE STRUCTURES			
Glass/epoxy door panel for automobiles			
page 561	NPO-15057		
COMPRESSED AIR			
Adjustable tuning spring for bellows pump			
page 550	MSC-20512		
COMPRESSIBLE FLOW			
Hot-wire probe for compressible subsonic flow			
page 524	LAR-13051		



COMPUTER PROGRAMS

Source preprocessor or interface-specification language page 576 NPO-15814
 Managing software design and design changes page 577 NPO-15331

CONCRETE STRUCTURES

Solar-array substrate from glass-reinforced concrete page 558 NPO-15077

CONDUCTIVITY METERS

Differential-coil eddy-current material sorter page 451 MFS-19872

CONNECTORS

Connector-array attachment matrix page 569 NPO-15778

CONSTRUCTION INDUSTRY

Automated solar-panel fabricator page 569 NPO-16205

CONTACT RESISTANCE

Measuring the contact resistances of photovoltaic cells page 459 NPO-16168

CONTAINERS

Holding cargo in place with foam page 546 MSC-20723

CONTAMINATION

Laser pollutant-measuring systems page 487 NPO-16101

CONTROL EQUIPMENT

Fiber-optic equipment for power-system control page 476 NPO-15968
 Deployable geodesic truss page 532 LAR-13113

CONTROLLED ATMOSPHERES

Gas atmospheres improve silicon-ribbon quality page 564 NPO-15129

COPOLYMERS

Elastomeric cathode binder page 499 NPO-15424

CORRELATION

Estimates of small signal/noise ratios page 468 NPO-15653

COUPLING

High-pressure coupling for open-ended tubes page 510 MSC-20451
 Remote coupling of electrical connectors page 543 MSC-20414
 Hybrid-vehicle transmission system page 549 NPO-16119

CROSSTALK

Convolutionally-coded unbalanced QPSK systems page 476 NPO-15566

CRYSTAL DEFECTS

Defect chemistry of $Hg_{1-x}Cd_xTe$ page 497 MFS-25851

CRYSTAL GROWTH

Observing gravitational effects on crystal growth by vapor page 562 NPO-15853
 Contoured orifice for silicon-ribbon die page 565 NPO-15126

CURRENT REGULATORS

Hall-effect ground-fault interruptor page 464 NPO-15915

CURVED PANELS

Prestressed thermal-protection panels page 556 MSC-20254
 Strong, lightweight curved panels page 569 MSC-16278

CUTTERS

Stripping the sheath from stranded cables page 561 NPO-15082

CYLINDRICAL SHELLS

Quick-change holder for aeronautical-research microphones page 528 FRC-11072

DAMAGE

Reversing optical damage in $LiNbO_3$ switches page 447 NPO-16239

DAMPING

Improved coulomb-friction damper page 515 MSC-20505

DATA PROCESSING

Computing tridiagonal matrices page 578 ARC-11476

DECODERS

Real-time Reed-Solomon decoder page 448 NPO-15982
 Simplified convolution codes page 578 NPO-16251

DELAMINATING

Welding thin metal layers page 568 MSC-20698

DENSITY MEASUREMENT

Gas-density gage page 534 MFS-28011

DESCENT TRAJECTORIES

Fuel-conservative descents using a programmable calculator page 515 LAR-13138

DESIGN ANALYSIS

Ellipsoidal balloon antenna page 457 NPO-15931
 Paraboloidal-dish power modules page 490 NPO-16100

DESULFURIZING

Desulfurization of coal in fluidized beds page 493 NPO-15924

DIELECTRICS

Theoretical investigation of dielectric-horn antennas page 462 GSC-12876

DIES

Contoured orifice for silicon-ribbon die page 565 NPO-15126

DIFFERENTIAL PRESSURE

Differential pressure helps seal ball valve page 513 MSC-20615

DIFFERENTIAL THERMAL ANALYSIS

Platinum-resistor differential temperature sensor page 464 NPO-15666

DIGITAL DATA

Parallel VLSI architecture page 578 NPO-16124

DIOPHANTINE EQUATION

Simplified convolution codes page 578 NPO-16251

DIRECT POWER GENERATORS

Integrated fuel cell/coal gasifier page 498 NPO-16062

DISTANCE MEASURING EQUIPMENT

Measuring clearance indirectly page 534 MFS-19875

DOORS

Glass/epoxy door panel for automobiles page 561 NPO-15057

DOPPLER EFFECT

Estimating Doppler shifts for synthetic-aperture radar page 473 NPO-15990

DUST STORMS

Predicting severe duststorms page 575 NPO-14999

DYNAMIC PRESSURE

Dynamic calibration of pressure transducers page 517 LAR-13094

EARTHQUAKE RESISTANT STRUCTURES

Active-pulse suppression of structural vibrations page 522 NPO-15788

EDDY CURRENT

Differential-coil eddy-current material sorter page 451 MFS-19872

ELASTOMERS

Predicting polymer/liquid interactions page 498 NPO-14874
 Elastomeric cathode binder page 499 NPO-15424

ELECTRIC BRIDGES

Platinum-resistor differential temperature sensor page 464 NPO-15666

ELECTRIC HYBRID VEHICLES

Hybrid-vehicle transmission system page 549 NPO-16119
 Power train for hybrid electric vehicles page 550 NPO-15742

ELECTRIC MOTOR VEHICLES

Batteries for electric vehicles page 462 NPO-15142

ELECTRIC MOTORS

Advanced dc-traction-motor control system page 449 NPO-16118

ELECTRIC PULSES

Pulsed-current transducers page 464 NPO-14048

ELECTRIC RELAYS

Solid-state latching relay page 464 NPO-15028

ELECTRIC WIRE

Calculating strain-relief in electronic-component leads page 463 MSC-20416

ELECTRICAL GROUNDING

Estimation of grounding-strap resistances page 460 MSC-20694

ELECTRICAL RESISTIVITY

Measuring the contact resistances of photovoltaic cells page 459 NPO-16168
 Estimation of grounding-strap resistances page 460 MSC-20694

ELECTROACOUSTIC TRANSDUCERS

Fabricating underwater electroacoustic transducers page 555 LAR-13007

ELECTROCHEMICAL CELLS

High-cycle-life lithium cell page 451 NPO-15921

ELECTRODES

EDM electrode for internal grooves page 547 MFS-19733

ELECTROLYSIS

Molten-salt electrolysis page 499 NPO-15535

ELECTRON ATTACHMENT

Electron-attachment profiles page 490 NPO-14865

ELECTRON BEAM WELDING

Welding thin metal layers page 568 MSC-20698

ELECTRON MICROSCOPES

Specimen holder for analytical electron microscopes page 514 MSC-20398

ELECTRONIC CONTROL

Advanced dc-traction-motor control system page 449 NPO-16118

ELECTRONIC MODULES

Real-time Reed-Solomon decoder page 448 NPO-15982

ELECTROPLATING

Increasing the ductility of electroplated metals page 494 MFS-19873

ELLIPTIC FUNCTIONS

Flight-stability extremes calculated from uncertainty ellipse page 573 MSC-20308

ENDOSCOPES

Imaging system for high-temperature processes page 478 NPO-15945

ENERGY CONSERVATION

Reducing stepping-motor power consumption
page 463 MFS-25119

ENGINE TESTS

Ignition-spark detector for engine testing
page 544 MFS-19890

ENVIRONMENTAL TESTS

Determining the life expectancy of
photovoltaic systems
page 464 NPO-15683

ERROR ANALYSIS

Convolutionally-coded unbalanced QPSK
systems
page 476 NPO-15566

Determining the slope error of a parabolic
reflector
page 484 NPO-15713

Orbital and geodetic error analysis
page 577 GSC-12768

ERROR CORRECTING CODES

Simplified convolution codes
page 578 NPO-16251

ERROR CORRECTING DEVICES

Error correction for tandem data-
transmission paths
page 578 NPO-16125

EUTECTIC COMPOSITES

Heat storage and transport
page 488 NPO-15468

Eutectic contact inks for solar cells
page 494 NPO-15171

EVALUATION

Safety evaluation methodology for mining
systems
page 550 NPO-15831

EXHAUST GASES

Integrated exhaust-gas-analysis system
page 519 LEW-14062

EXPLOSIVE WELDING

Explosive welding for remote applications
page 567 LAR-13119

EXTENSOMETERS

Acousto-optic extensometer for bolts
page 518 MFS-19914

EXTRACTION

Low-temperature extraction of oil from shale
page 498 NPO-15656

EYE EXAMINATIONS

Photographic screening for eye defects
page 504 MFS-27045

FABRICS

Heat-shield gap filler
page 570 ARC-11310

FAN BLADES

Propeller design program
page 548 LAR-13141

FASTENERS

Tape-mounted thermocouple
page 569 NPO-16291

FIBER OPTICS

Fiber-optic equipment for power-system
control
page 476 NPO-15968

Optical-fiber-welding machine
page 554 NPO-15004

Roof polishing of optical fibers
page 554 LAR-13070

Splicing efficiently couples optical fibers
page 569 NPO-16294

FILLERS

Reusable thermal barrier for insulation gaps
page 512 MSC-20519

Heat-shield gap filler
page 570 ARC-11310

FINITE ELEMENT METHOD

Cost considerations in nonlinear finite-
element computing
page 576 NPO-16237

FITTING

Fluorescent gage indication
page 558 ARC-11397

FLAT CONDUCTORS

Estimation of grounding-strap resistances
page 460 MSC-20694

FLATNESS

Thermal-balance strip for fluted LFC panels
page 527 LAR-12991

FLIGHT CHARACTERISTICS

Flight-stability extremes calculated from
uncertainty ellipse
page 573 MSC-20308

FLOCCULATING

Purification of solar ponds
page 489 NPO-15397

FLOW DISTRIBUTION

Sting-mounted flow survey apparatus
page 516 LAR-13157

Hot-wire probe for compressible subsonic
flow
page 524 LAR-13051

Evening flow distribution through parallel
tubes
page 549 MFS-23936

FLUORESCENCE

Fluorescent gage indication
page 558 ARC-11397

FOCUSING

Point-focusing solar-power distributed
receivers
page 489 NPO-15578

FOLDING STRUCTURES

Synchronously deployable truss
page 531 LAR-13117

Deployable geodesic truss
page 532 LAR-13113

FORECASTING

Predicting the reliability of solar-cell
interconnections
page 574 NPO-15976

Predicting severe duststorms
page 575 NPO-14999

FORMING TECHNIQUES

Silicon formation for solar cells
page 498 NPO-14973

FREQUENCY DISCRIMINATORS

Discriminator aids phase-lock acquisition
page 452 NPO-14311

FREQUENCY MEASUREMENT

Instrumentation for solar oscillation
measurements
page 488 NPO-15687

Insulation debond detection
page 508 MFS-25862

FREQUENCY MODULATION

Temperature compensation for a frequency
modulated oscillator
page 463 MSC-20556

FRESNEL LENSES

Fresnel-lens/heat-storage system
page 488 NPO-16242

FUEL CELLS

Integrated fuel cell/coal gasifier
page 498 NPO-16062

FUEL CONSUMPTION

Fuel-conservative descents using a
programmable calculator
page 515 LAR-13138

FUEL TESTS

Rapid freezing-point measurement
page 483 LEW-14019

FUEL VALVES

Garner valves
page 540 MFS-19899

FUSELAGES

Continuous-filament isogrid composite panel
page 526 LAR-12975

FUSION WELDING

Optical-fiber-welding machine
page 554 NPO-15004

GAS ANALYSIS

Laser pollutant-measuring systems
page 487 NPO-16101

Electron-attachment profiles
page 490 NPO-14865

Integrated exhaust-gas-analysis system
page 519 LEW-14062

GAS DENSITY

Gas-density gage
page 534 MFS-28011

GAS DYNAMICS

Measuring the liquid content of a gas
page 525 MFS-25990

GAS FLOW

Constant-operating-resistance hot-wire probe
page 523 LAR-13144

GASIFICATION

Solar heated gasifier
page 489 NPO-15071

GETTERS

Activated internal gettering
page 499 NPO-15530

GRAPHITE-EPOXY COMPOSITES

Strong, lightweight curved panels
page 569 MSC-16278

GRAVITATIONAL EFFECTS

Observing gravitational effects on crystal
growth by vapor
page 562 NPO-15853

GUARDS (SHIELDS)

Guard for fuse caps
page 461 KSC-11283

Hinged chip shields for machine tools
page 545 GSC-12915

HALL EFFECT

Hall-effect ground-fault interruptor
page 464 NPO-15915

HEAT EXCHANGERS

A ceramic heat exchanger for solar receivers
page 489 NPO-15771

HEAT OF VAPORIZATION

Solar-power system produces high-pressure
steam
page 488 NPO-15434

HEAT REJECTION DEVICES

Solar shutter
page 489 NPO-15428

HEAT RESISTANCE

Lightweight high-temperature thermal
insulation
page 495 MFS-19754

Bonding heat-resistant fabric to tile
page 566 MSC-20540

HEAT STORAGE

Heat storage and transport
page 488 NPO-15468

Fresnel-lens/heat-storage system
page 488 NPO-16242

HIGH PRESSURE

High-pressure coupling for open-ended tubes
page 510 MSC-20451

HIGH TEMPERATURE FLUIDS

High-temperature pump
page 550 NPO-15783

HIGH TEMPERATURE TESTS

Brazing alloys indicate turbomachinery
temperatures
page 511 MFS-19792

HOLDERS

Specimen holder for analytical electron
microscopes
page 514 MSC-20398

Quick-change holder for aeronautical-
research microphones
page 528 FRC-11072

HORN ANTENNAS

Efficient reflector antenna
page 458 NPO-16262



Theoretical investigation of dielectric-horn antennas page 462	GSC-12876		
HOT PRESSING Increasing the ductility of electroplated metals page 494	MFS-19873		
HOT WIRE ANEMOMETERS Constant-operating-resistance hot-wire probe page 523	LAR-13144		
Measuring the liquid content of a gas page 525	MFS-25990		
HOUSINGS Guard for fuse caps page 461	KSC-11283		
IGNITERS Ignition-spark detector for engine testing page 544	MFS-19890		
IMAGING TECHNIQUES Measuring tracking accuracy of CCD imagers page 470	NPO-15665		
Quicker selection of CCD images page 478	NPO-15345		
Imaging system for high-temperature processes page 478	NPO-15945		
High-resolution charge-coupled-device camera page 478	NPO-15086		
Reflecting Schmidt/Littrow prism imaging spectrometer page 481	NPO-15801		
IMPACT TESTS Insulation debond detection page 508	MFS-25862		
INFORMATION FLOW Interactive digital signal processor page 477	GSC-12862		
Communication program emulates switchboard page 477	MFS-19917		
Packet telemetry and packet telecommand page 478	NPO-16301		
Library information-processing system page 576	GSC-12861		
Managing software design and design changes page 577	NPO-15331		
INFRARED TRACKING Integrated laser and light detector page 450	NPO-15943		
INJECTION LASERS Integrated laser and light detector page 450	NPO-15943		
INORGANIC COATINGS High-temperature coating for titanium page 498	NPO-16222		
INPUT/OUTPUT ROUTINES Communication program emulates switchboard page 477	MFS-19917		
INSERTION Tool for inserting and removing tube plugs page 544	MFS-19871		
INSPECTION Fluorescent gage indication page 558	ARC-11397		
Edge labels for multilayer circuit boards page 560	MSC-20704		
INSTALLING Connector-array attachment matrix page 569	NPO-15778		
INSTRUCTION SETS (COMPUTERS) Computing tridiagonal matrices page 578	ARC-11476		
INTEGRATED CIRCUITS Parallel VLSI architecture page 578	NPO-16124		
INTERFEROMETERS Interferometer for measuring acoustic signals page 484	LAR-13030		
INTERPROCESSOR COMMUNICATION Communication program emulates switchboard page 477	MFS-19917		
IONIZERS Measuring air-ionizer output page 461	NPO-16058		
IONOSPHERIC CROSS MODULATION Calibrating for ionospheric phase delays page 489	NPO-15430		
IRRADIANCE Ten thousand solar constants radiometer page 488	NPO-15922		
ISOLATORS Stable optocoupler page 447	MFS-25927		
LAMINATES Improved optical keyboard page 464	NPO-15132		
LASER APPLICATIONS Acousto-optic extensometer for bolts page 518	MFS-19914		
LASER RANGE FINDERS Laser rangefinder and remote profilometer page 482	NPO-15865		
LASERS Laser pollutant-measuring systems page 487	NPO-16101		
LATCHES Solid-state latching relay page 464	NPO-15028		
Snapping quick fastener page 569	NPO-15724		
LEAKAGE Microphone detects boiler-tube leaks page 529	NPO-16027		
LIBRARIES Library information-processing system page 576	GSC-12861		
LIFE (DURABILITY) High-cycle-life lithium cell page 451	NPO-15921		
Determining the life expectancy of photovoltaic systems page 464	NPO-15683		
LIGHTNING Detecting the polarity of lightning strikes page 463	NPO-16063		
LINEAR CIRCUITS Pulsed-current transducers page 464	NPO-14048		
LINKAGES Capture-range indicator page 534	MFS-28008		
LOCKING Setup aid for electrical-discharge machining page 548	MFS-19874		
MACHINE TOOLS Hinged chip shields for machine tools page 545	GSC-12915		
MAGIC TEES Magic-T-coupled magnetrons page 454	NPO-15061		
MAGNETIC RECORDING Detecting the polarity of lightning strikes page 463	NPO-16063		
MAGNETRONS Magic-T-coupled magnetrons page 454	NPO-15061		
MAPPING Contour-mapping synthetic-aperture radar page 474	NPO-15939		
MARKING Edge labels for multilayer circuit boards page 560	MSC-20704		
MATERIAL ABSORPTION Predicting polymer/liquid interactions page 498	NPO-14874		
MATERIALS RECOVERY Inhibiting wet oxidation of ammonia page 496	ARC-11407		
MATRICES (MATHEMATICS) Computing tridiagonal matrices page 578	ARC-11476		
MEASURING INSTRUMENTS Measuring the contact resistances of photovoltaic cells page 459	NPO-16168		
MECHANICAL DRIVES Remote coupling of electrical connectors page 543	MSC-20414		
MEDICAL EQUIPMENT Probe follower for moving blood vessels page 503	NPO-15898		
Photographic screening for eye defects page 504	MFS-27045		
MELTING POINTS Rapid freezing-point measurement page 483	LEW-14019		
METAL FOILS Brazing alloys indicate turbomachinery temperatures page 511	MFS-19792		
MICROPHONES Microphone detects boiler-tube leaks page 529	NPO-16027		
In-place calibration of instrumentation microphones page 530	ARC-11463		
MICROWAVE COUPLING Magic-T-coupled magnetrons page 454	NPO-15061		
MICROWAVE SWITCHING Light-activated microwave device page 453	NPO-16112		
MINING Safety evaluation methodology for mining systems page 550	NPO-15831		
MINORITY CARRIERS Activated internal gettering page 499	NPO-15530		
MISALIGNMENT X-ray determination of weld misalignment page 507	MSC-20418		
MIXTURES Eutectic contact inks for solar cells page 494	NPO-15171		
MOLECULAR BEAM EPITAXY Preparing InSb substrates page 499	NPO-16127		
MOLTEN SALTS Molten-salt electrolysis page 499	NPO-15535		
MOTION PERCEPTION Probe follower for moving blood vessels page 503	NPO-15898		
MOUNTING Quick-change holder for aeronautical-research microphones page 528	FRC-11072		
Solder bonding for power transistors page 559	MSC-20570		
MULTIPROCESSING (COMPUTERS) Controlling solar-power systems with distributed processors page 469	NPO-15101		
MULTISTATIC RADAR Bistatic synthetic-aperture radar page 478	NPO-15619		

NEWTON-RAPHSON METHOD			
Cost considerations in nonlinear finite-element computing			
page 576	NPO-16237		
NICKEL-IRON BATTERIES			
Batteries for electric vehicles			
page 462	NPO-15142		
NICKEL-ZINC BATTERIES			
Batteries for electric vehicles			
page 462	NPO-15142		
NOISE PREDICTION			
Predictive smoothing-convolution algorithm			
page 578	MSC-20604		
O RING SEALS			
Tapered ring seal			
page 541	LEW-14055		
OPTICAL COMMUNICATION			
Direct photon detection communications			
page 467	NPO-15905		
Short-range digital optical links			
page 477	NPO-15999		
OPTICAL CORRECTION PROCEDURE			
Reversing optical damage in LiNbO ₃ switches			
page 447	NPO-16239		
OPTICAL COUPLING			
Stable optocoupler			
page 447	MFS-25927		
Multipurpose photonic transducers			
page 520	NPO-15135		
Optical-fiber-welding machine			
page 554	NPO-15004		
Roof polishing of optical fibers			
page 554	LAR-13070		
Splicing efficiently couples optical fibers			
page 569	NPO-16294		
OPTICAL REFLECTION			
Improved optical keyboard			
page 464	NPO-15132		
Reflecting Schmidt/Littrow prism imaging spectrometer			
page 481	NPO-15801		
OPTICAL TRACKING			
Integrated laser and light detector			
page 450	NPO-15943		
Laser rangefinder and remote profilometer			
page 482	NPO-15865		
ORBITAL ELEMENTS			
Orbital and geodetic error analysis			
page 577	GSC-12768		
ORIFICES			
Contoured orifice for silicon-ribbon die			
page 565	NPO-15126		
OSCILLATORS			
Discriminator aids phase-lock acquisition			
page 452	NPO-14311		
OXIDATION			
Inhibiting wet oxidation of ammonia			
page 496	ARC-11407		
PACKAGING			
Holding cargo in place with foam			
page 546	MSC-20723		
PACKET TRANSMISSION			
Packet telemetry and packet telecommand			
page 478	NPO-16301		
PANELS			
Continuous-filament isogrid composite panel			
page 526	LAR-12975		
Thermal-balance strip for fluted LFC panels			
page 527	LAR-12991		
Glass/epoxy door panel for automobiles			
page 561	NPO-15057		
PARABOLIC REFLECTORS			
Determining the slope error of a parabolic reflector			
page 484	NPO-15713		
Paraboloidal-dish power modules			
page 490	NPO-16100		
PARALLEL FLOW			
Evening flow distribution through parallel tubes			
page 549	MFS-23936		
PARAMETER IDENTIFICATION			
Retrieval of geophysical parameters from radiometric data			
page 488	NPO-16266		
PARTITIONS (MATHEMATICS)			
Orbital and geodetic error analysis			
page 577	GSC-12768		
PAYLOAD TRANSFER			
Capture-range indicator			
page 534	MFS-28008		
PEDALS			
Safety pedal for foot-operated machinery			
page 537	MSC-20535		
PERFORMANCE PREDICTION			
Safety evaluation methodology for mining systems			
page 550	NPO-15831		
PHASE ERROR			
Convolutionally-coded unbalanced QPSK systems			
page 476	NPO-15566		
Calibrating for ionospheric phase delays			
page 489	NPO-15430		
PHASE LOCKED SYSTEMS			
Discriminator aids phase-lock acquisition			
page 452	NPO-14311		
PHASE SHIFT			
Estimating Doppler shifts for synthetic-aperture radar			
page 473	NPO-15990		
PHOTOELECTRIC GENERATORS			
Controlling solar-power systems with distributed processors			
page 469	NPO-15101		
PHOTOELECTRON SPECTROSCOPY			
Electron-attachment profiles			
page 490	NPO-14865		
PHOTOGRAPHIC EQUIPMENT			
Photographic screening for eye defects			
page 504	MFS-27045		
PHOTOMETERS			
Ignition-spark detector for engine testing			
page 544	MFS-19890		
PHOTONICS			
Direct photon detection communications			
page 467	NPO-15905		
Multipurpose photonic transducers			
page 520	NPO-15135		
PHOTOVOLTAIC CELLS			
Determining the life expectancy of photovoltaic systems			
page 464	NPO-15683		
PHYSIOCHEMISTRY			
Defect chemistry of Hg _{1-x} Cd _x Te			
page 497	MFS-25851		
PLASTIC COATINGS			
Applying uniform polymer coatings to microspheres			
page 496	NPO-16075		
PLATES (STRUCTURAL MEMBERS)			
Snapring quick fastener			
page 569	NPO-15724		
PLUGGING			
Tool for inserting and removing tube plugs			
page 544	MFS-19871		
PLUGS			
Close-out plugs			
page 570	MFS-19370		
POLARITY			
Detecting the polarity of lightning strikes			
page 463	NPO-16063		
POLISHING			
Roof polishing of optical fibers			
page 554	LAR-13070		
POLYNOMIALS			
Predictive smoothing-convolution algorithm			
page 578	MSC-20604		
POROUS BOUNDARY LAYER CONTROL			
Increasing the ductility of electroplated metals			
page 494	MFS-19873		
POSITION INDICATORS			
Capture-range indicator			
page 534	MFS-28008		
POSITIONING DEVICES (MACHINERY)			
Setup aid for electrical-discharge machining			
page 548	MFS-19874		
POWER CONDITIONING			
Advanced dc-traction-motor control system			
page 449	NPO-16118		
POWER EFFICIENCY			
Maximum outputs of solar photovoltaic arrays			
page 487	NPO-15966		
POWER MODULES (STS)			
Paraboloidal-dish power modules			
page 490	NPO-16100		
POWER SUPPLY CIRCUITS			
Lightweight regulated power supply			
page 455	NPO-15977		
Controlling solar-power systems with distributed processors			
page 469	NPO-15101		
PRESSURE MEASUREMENT			
Gas-density gage			
page 534	MFS-28011		
PRESSURE REDUCTION			
Evening flow distribution through parallel tubes			
page 549	MFS-23936		
PRESSURE SENSORS			
Dynamic calibration of pressure transducers			
page 517	LAR-13094		
PRESTRESSING			
Prestressed thermal-protection panels			
page 556	MSC-20254		
PRISMS			
Composite spectrometer prisms			
page 490	NPO-16060		
PRODUCTION ENGINEERING			
Top-coating silicon onto ceramic			
page 565	NPO-15125		
PROFILOMETERS			
Laser rangefinder and remote profilometer			
page 482	NPO-15865		
PROGRAM VERIFICATION (COMPUTERS)			
Source preprocessor or interface-specification language			
page 576	NPO-15814		
PROPELLERS			
Over-the-wing propeller reduces wing drag			
page 512	LAR-13134		
Propeller design program			
page 548	LAR-13141		
PROXIMITY			
Proximity indicator for remote manipulator			
page 468	NPO-15064		
PULLING			
Reactionless winch			
page 542	MSC-20440		
PULSE GENERATORS			
Light-activated microwave device			
page 453	NPO-16112		
PULSE POSITION MODULATION			
Direct photon detection communications			
page 467	NPO-15905		
PUMPS			
High-temperature pump			
page 550	NPO-15783		
Adjustable tuning spring for bellows pump			
page 550	MSC-20512		
PURIFICATION			
Purification of solar ponds			
page 489	NPO-15397		



Degreaser reduces solvent loss page 541	NPO-16128	RESOLUTION Measuring tracking accuracy of CCD imagers page 470	NPO-15665	SHALE OIL Low-temperature extraction of oil from shale page 498	NPO-15656
PYROLYSIS Low-temperature extraction of oil from shale page 498	NPO-15656	RESONANCE Adjustable tuning spring for bellows pump page 550	MSC-20512	SHIELDING Telescoping shield for point-focusing solar concentrators page 486	NPO-16236
QUEUEING THEORY Priority queuing on a parallel data bus page 471	NPO-15005	RIBBONS Gas atmospheres improve silicon-ribbon quality page 564	NPO-15129	SHOCK ABSORBERS Improved coulomb-friction damper page 515	MSC-20505
RADAR IMAGERY Target simulator for synthetic-aperture radars page 472	NPO-15024	RING STRUCTURES Garter valves page 540	MFS-19899	SHUTDOWNS Automatic robot safety shutdown system page 546	MFS-25969
Estimating Doppler shifts for synthetic- aperture radar page 473	NPO-15990	Snapping quick fastener page 569	NPO-15724	SIGNAL ANALYSIS Calibrating for ionospheric phase delays page 489	NPO-15430
Bistatic synthetic-aperture radar page 478	NPO-15619	ROBOTS Automatic robot safety shutdown system page 546	MFS-25969	Predictive smoothing-convolution algorithm page 578	MSC-20604
RADIATION DETECTORS Determining thermal diffusivities of radiating specimens page 510	NPO-15436	ROLLING MOMENTS Bridle attachment for aircraft spin-recovery parachute page 538	LAR-13076	SIGNAL PROCESSING Interactive digital signal processor page 477	GSC-12862
RADIO COMMUNICATION Real-time Reed-Solomon decoder page 448	NPO-15982	ROOFS Roof overhangs for solar houses page 485	LAR-13140	SIGNAL TO NOISE RATIOS Estimates of small signal/noise ratios page 468	NPO-15653
RATIOMETERS Digital ratiometer page 478	NPO-15396	RUBBER Predicting polymer/liquid interactions page 498	NPO-14874	SILICON Silicon formation for solar cells page 498	NPO-14973
READERS Managing software design and design changes page 577	NPO-15331	SAFETY DEVICES Guard for fuse caps page 461	KSC-11283	Making cubic silicon carbide semiconductors page 563	LEW-14018
RECOVERY PARACHUTES Bridle attachment for aircraft spin-recovery parachutes page 538	LAR-13076	Safety pedal for foot-operated machinery page 537	MSC-20535	Gas atmospheres improve silicon-ribbon quality page 564	NPO-15129
Compact antispin parachute system page 539	LAR-12979	Hinged chip shields for machine tools page 545	GSC-12915	Top-coating silicon onto ceramic page 565	NPO-15125
REFLECTORS Efficient reflector antenna page 458	NPO-16262	Automatic robot safety shutdown system page 546	MFS-25969	SILICONE RUBBER Silicone-rubber tooling for hollow panels page 527	LAR-12974
Acoustic levitation system page 570	NPO-16146	SAMPLING DEVICES Sorting titanium welding rods page 557	MSC-20588	SINTERING Lightweight high-temperature thermal insulation page 495	MFS-19754
REGRESSION ANALYSIS Retrieval of geophysical parameters from radiometric data page 488	NPO-16266	SANDWICH CONSTRUCTION Strong, lightweight curved panels page 569	MSC-16278	SIRENS Acoustic levitation system page 570	NPO-16146
REINFORCEMENT (STRUCTURES) Continuous-filament isogrid composite panel page 526	LAR-12975	SATELLITE TRANSMISSION Retrieval of geophysical parameters from radiometric data page 488	NPO-16266	SLIDING FRICTION Improved coulomb-friction damper page 515	MSC-20505
RELIABILITY ANALYSIS Deriving strain modes from vibrational tests page 521	MSC-20587	SATURABLE REACTORS Lightweight regulated power supply page 455	NPO-15977	SLOPES Determining the slope error of a parabolic reflector page 484	NPO-15713
Predicting the reliability of solar-cell interconnections page 574	NPO-15976	SCRAPERS Cleaning the walls of a silane reactor page 499	NPO-15851	SOLAR ARRAYS Maximum outputs of solar photovoltaic arrays page 487	NPO-15966
REMOTE HANDLING Adjustable mount page 534	LAR-13100	SEALING Differential pressure helps seal ball valve page 513	MSC-20615	Eutectic contact inks for solar cells page 494	NPO-15171
Explosive welding for remote applications page 567	LAR-13119	SEALS (STOPPERS) Tapered ring seal page 541	LEW-14055	Solar-array substrate from glass-reinforced concrete page 558	NPO-15077
REMOTE MANIPULATOR SYSTEM Proximity indicator for remote manipulator page 468	NPO-15064	Close-out plugs page 570	MFS-19370	Automated solar-panel fabricator page 569	NPO-16205
REMOTE SENSORS General design considerations for remote sensors page 490	NPO-15930	SEMICONDUCTOR DEVICES Light-activated microwave device page 453	NPO-16112	Predicting the reliability of solar-cell interconnections page 574	NPO-15976
REMOVAL Stripping the sheath from stranded cables page 561	NPO-15082	Making cubic silicon carbide semiconductors page 563	LEW-14018	SOLAR COLLECTORS Roof overhangs for solar houses page 485	LAR-13140
REPEATERS Error correction for tandem data- transmission paths page 578	NPO-16125	SEMICONDUCTOR LASERS Short-range digital optical links page 477	NPO-15999	Telescoping shield for point-focusing solar concentrators page 486	NPO-16236
		SEPARATORS Molten-salt electrolysis page 499	NPO-15535	Solar-power system produces high-pressure steam page 488	NPO-15434
		SERVOMECHANISMS Acoustic position servosystem page 570	NPO-15936	Heat storage and transport page 488	NPO-15468
				Ten thousand solar constants radiometer page 488	NPO-15922

Fresnel-lens/heat-storage system page 488	NPO-16242	STABILITY AUGMENTATION Stable optocoupler page 447	MFS-25927	SYSTEMS ANALYSIS Fiber-optic equipment for power-system control page 476	NPO-15968
Solar heated gasifier page 489	NPO-15071	STATIC DISCHARGERS Setup aid for electrical-discharge machining page 548	MFS-19874	TARGET SIMULATORS Target simulator for synthetic-aperture radars page 472	NPO-15024
Solar shutter page 489	NPO-15428	STATIC ELECTRICITY Measuring air-ionizer output page 461	NPO-16058	Synchronized radar-target simulator page 472	MSC-20240
Point-focusing solar-power distributed receivers page 489	NPO-15578	STEAM Solar-power system produces high-pressure steam page 488	NPO-15434	TELEMETRY Estimates of small signal/noise ratios page 468	NPO-15653
A ceramic heat exchanger for solar receivers page 489	NPO-15771	STEERABLE ANTENNAS Synchronized radar-target simulator page 472	MSC-20240	Packet telemetry and packet telecommand page 478	NPO-16301
SOLAR OSCILLATIONS Instrumentation for solar oscillation measurements page 488	NPO-15687	STEPPING MOTORS Reducing stepping-motor power consumption page 463	MFS-25119	TEMPERATURE CONTROL Telescoping shield for point-focusing solar concentrators page 486	NPO-16236
SOLAR PONDS (HEAT STORAGE) Purification of solar ponds page 489	NPO-15397	STRESS ANALYSIS Calculating strain-relief in electronic- component leads page 463	MSC-20416	Solar shutter page 489	NPO-15428
SOLDERING Solder bonding for power transistors page 559	MSC-20570	STRESSED-SKIN STRUCTURES Bonding technique for stiffened-skin structures page 559	NPO-15994	TEMPERATURE MEASUREMENT Rapid freezing-point measurement page 483	LEW-14019
SOLID STATE DEVICES High-frequency, high-power capacitor page 445	LEW-14034	STRUCTURAL DESIGN Roof overhangs for solar houses page 485	LAR-13140	Brazing alloys indicate turbomachinery temperatures page 511	MFS-19792
Solid-state latching relay page 464	NPO-15028	STRUCTURAL VIBRATION Active-pulse suppression of structural vibrations page 522	NPO-15788	TEMPERATURE SENSORS Platinum-resistor differential temperature sensors page 464	NPO-15666
SOLVENT RETENTION Degreaser reduces solvent loss page 541	NPO-16128	STRUTS Synchronously deployable truss page 531	LAR-13117	TEST STANDS Adjustable mount page 534	LAR-13100
SOUND GENERATORS In-place calibration of instrumentation microphones page 530	ARC-11463	SUBREFLECTORS Antenna subreflector fed by a line source page 456	MSC-20626	THERMAL CONTROL COATINGS High-temperature coating for titanium page 498	NPO-16222
SOURCE PROGRAMS Source preprocessor or interface- specification language page 576	NPO-15814	SUBSONIC FLOW Hot-wire probe for compressible subsonic flow page 524	LAR-13051	THERMAL DIFFUSIVITY Determining thermal diffusivities of radiating specimens page 510	NPO-15436
SPACE PERCEPTION Proximity indicator for remote manipulator page 468	NPO-15064	SUBSTRATES Preparing InSb substrates page 499	NPO-16127	THERMAL EXPANSION Stabilized aluminum titanate page 499	NPO-16227
SPARK MACHINING EDM electrode for internal grooves page 547	MFS-19733	Solar-array substrate from glass-reinforced concrete page 558	NPO-15077	THERMAL INSULATION Lightweight high-temperature thermal insulation page 495	MFS-19754
SPATIAL RESOLUTION General design considerations for remote sensors page 490	NPO-15930	SUPPORTS Adjustable mount page 534	LAR-13100	Reusable thermal barrier for insulation gaps page 512	MSC-20519
SPECTROMETERS Reflecting Schmidt/Littrow prism imaging spectrometer page 481	NPO-15801	SURFACE ACOUSTIC WAVE DEVICES Interferometer for measuring acoustic signals page 484	LAR-13030	Heat-shield gap filler page 570	ARC-11310
Composite spectrometer prisms page 490	NPO-16060	SURVEYS Sting-mounted flow survey apparatus page 516	LAR-13157	THERMAL PROTECTION Prestressed thermal-protection panels page 556	MSC-20254
SPECTORADIOMETERS Ten thousand solar constants radiometer page 488	NPO-15922	SWITCHES Reversing optical damage in LiNbO ₃ switches page 447	NPO-16239	THERMAL RESISTANCE Constant-operating-resistance hot-wire probe page 523	LAR-13144
SPHERICAL SHELLS Applying uniform polymer coatings to microspheres page 496	NPO-16075	SWITCHING CIRCUITS Reducing stepping-motor power consumption page 463	MFS-25119	THERMAL STABILITY Thermal compensator for paraboloidal reflector page 490	NPO-16145
SPIN REDUCTION Bridle attachment for aircraft spin-recovery parachute page 538	LAR-13076	SYNCHRONIZERS Power train for hybrid electric vehicles page 550	NPO-15742	THERMISTORS Temperature compensation for a frequency modulated oscillator page 463	MSC-20556
Compact antispin parachute system page 539	LAR-12979	SYNTHETIC APERTURE RADAR Target simulator for synthetic-aperture radar page 472	NPO-15024	THERMOCOUPLES Tape-mounted thermocouple page 569	NPO-16291
SPIN STABILIZATION Linear boom actuator page 550	NPO-16099	Contour-mapping synthetic-aperture radar page 474	NPO-15939	THRESHOLD DETECTORS (DOSIMETERS) Quicker selection of CCD images page 478	NPO-15345
SPlicing Splicing efficiently couples optical fibers page 569	NPO-16294	Bistatic synthetic-aperture radar page 478	NPO-15619	TILES Bonding heat-resistant fabric to tile page 566	MSC-20540
SPRAYED COATINGS High-temperature coating for titanium page 498	NPO-16222	TIME SERIES ANALYSIS Interactive digital signal processor page 477	GSC-12862		
SPRAYING Silicon formation for solar cells page 498	NPO-14973				



TITANATES			
Stabilized aluminum titanate			
page 499	NPO-16227		
TITANIUM ALLOYS			
Sorting titanium welding rods			
page 557	MSC-20588		
TOOLING			
Silicone-rubber tooling for hollow panels			
page 527	LAR-12974		
TOOLS			
Measuring clearance indirectly			
page 534	MFS-19875		
Reactionless winch			
page 542	MSC-20440		
Tool for inserting and removing tube plugs			
page 544	MFS-19871		
EDM electrode for internal grooves			
page 547	MFS-19733		
TOPOGRAPHY			
Contour-mapping synthetic-aperture radar			
page 474	NPO-15939		
TOWING			
Compact antispin parachute system			
page 539	LAR-12979		
TOXIC HAZARDS			
Desulfurization of coal in fluidized beds			
page 493	NPO-15924		
TRACKING (POSITION)			
Measuring tracking accuracy of CCD imagers			
page 470	NPO-15665		
TRANSDUCERS			
Pulsed-current transducers			
page 464	NPO-14048		
Multipurpose photonic transducers			
page 520	NPO-15135		
Fabricating underwater electroacoustic transducers			
page 555	LAR-13007		
TRANSMISSION LOSS			
Error correction for tandem data-transmission paths			
page 578	NPO-16125		
TRANSMISSIONS (MACHINE ELEMENTS)			
Hybrid-vehicle transmission system			
page 549	NPO-16119		
TRUSSES			
Synchronously deployable truss			
page 531	LAR-13117		
Deployable geodesic truss			
page 532	LAR-13113		
TUBE HEAT EXCHANGERS			
High-temperature pump			
page 550	NPO-15783		
TUBING			
High-pressure coupling for open-ended tubes			
page 510	MSC-20451		
UMBILICAL CONNECTORS			
Remote coupling of electrical connectors			
page 543	MSC-20414		
UNDERWATER ACOUSTICS			
Fabricating underwater electroacoustic transducers			
page 555	LAR-13007		
VACUUM TESTS			
High-frequency, high-power capacitor			
page 445	LEW-14034		
VALVES			
Differential pressure helps seal ball valve			
page 513	MSC-20615		
Garner valves			
page 540	MFS-19899		
VAPOR DEPOSITION			
Observing gravitational effects on crystal growth by vapor			
page 562	NPO-15853		
VAPORIZERS			
Degreaser reduces solvent loss			
page 541	NPO-16128		
VIBRATION ISOLATORS			
Active-pulse suppression of structural vibrations			
page 522	NPO-15788		
VIBRATIONAL STRESS			
Deriving strain modes from vibrational tests			
page 521	MSC-20587		
VIEWING			
Imaging system for high-temperature processes			
page 478	NPO-15945		
VOLTAGE REGULATORS			
Lightweight regulated power supply			
page 455	NPO-15977		
WAFERS			
Making cubic silicon carbide semiconductors			
page 563	LEW-14018		
WARPAGE			
Thermal-balance strip for fluted LFC panels			
page 527	LAR-12991		
WAVE DISPERSION			
Composite spectrometer prisms			
page 490	NPO-16060		
WAVE FRONTS			
Antenna subreflector fed by a line source			
page 456	MSC-20626		
WEATHER			
Predicting severe duststorms			
page 575	NPO-14999		
WELD STRENGTH			
Explosive welding for remote applications			
page 567	LAR-13119		
WELD TESTS			
Sorting titanium welding rods			
page 557	MSC-20588		
WELDED JOINTS			
X-ray determination of weld misalignment			
page 507	MSC-20418		
WELDING			
Welding thin metal layers			
page 568	MSC-20698		
WINCHES			
Reactionless winch			
page 542	MSC-20440		
WIND EFFECTS			
Over-the-wing propeller reduces wing drag			
page 512	LAR-13134		
WIND TUNNEL APPARATUS			
Sting-mounted flow survey apparatus			
page 516	LAR-13157		
WING PANELS			
Silicone-rubber tooling for hollow panels			
page 527	LAR-12974		
X RAY FLUORESCENCE			
Specimen holder for analytical electron microscopes			
page 514	MSC-20398		
X RAY INSPECTION			
X-ray determination of weld misalignment			
page 507	MSC-20418		

National Aeronautics and
Space Administration


Washington, D.C.
20546

Official Business
Penalty for Private Use \$300

THIRD-CLASS BULK

THIRD-CLASS BULK RATE
POSTAGE & FEES PAID
NASA
WASHINGTON, D.C.
PERMIT No. G27

NASA



This two-person submersible vehicle is powered by five brushless dc motors, each of which employs an electronic controller developed in a joint NASA/Department of Energy project. Among the advantages of the new motor system are high reliability — there are no brushes to replace — and high performance in relation to size and weight. [See the bottom of page A1.]